

UNIVERSITY OF BIRMINGHAM

Luminescent metal nanoparticles for antigen targeting

By

SARAH OGHENEFEGO AKPONASA

A Thesis submitted to

The University of Birmingham

For the degree of

DOCTOR OF PHILOSOPHY

2022

UNIVERSITY OF
BIRMINGHAM

University of Birmingham Research Archive

e-theses repository

This unpublished thesis/dissertation is copyright of the author and/or third parties. The intellectual property rights of the author or third parties in respect of this work are as defined by The Copyright Designs and Patents Act 1988 or as modified by any successor legislation.

Any use made of information contained in this thesis/dissertation must be in accordance with that legislation and must be properly acknowledged. Further distribution or reproduction in any format is prohibited without the permission of the copyright holder.

Abstract

Gold nanoparticles are important as a delivery vehicle for different moieties. Here in this thesis, different gold nanoparticles have been examined as a vehicle for delivery for luminescent iridium(III) complexes in cells. The characteristics and potential uses of three iridium(III) complexes **IrpqSS**, **IrpqSH** and **Irpqbpy** with 2-phenylquinoline cyclometalated ligands will be discussed, to show that these probes are suitable luminescent complexes for use as imaging agents on their own and when conjugated onto gold nanoparticle surfaces. Gold nanoparticle sizes of 15 nm coated with the longer organic chain complex **IrpqSS** and shorter organic chain complex **IrpqSH** were shown to be monodisperse and luminescent with μs-length luminescence lifetimes. The different iridium(III) complex chain lengths were chosen to investigate the effect that the chain length has on the luminescence. The nanoparticles were studied in pancreatic cancer cell lines MiaPaca-2 and CFPAC-1 in combination with a variety of surfactants, showing the imaging capabilities of the nanoparticles as well as the surfactant-dependent localisation of the nanoparticles in different sub-cellular organelles. Four different surfactants were chosen with the aim of investigating the effect of PEG-based surfactants and fluorinated surfactants on nanoparticle cell luminescence and uptake, showing potential for engineering nanoparticles to target specific sub-cellular organelles. Directional conjugation of anti-mesothelin antibodies to nanoparticles of size 19 nm displayed targeting of the mesothelin surface protein with slow internalisation. This showed that anti-mesothelin antibody-AuNP nanoconjugates present a potential for use as diagnostic agents due to cell membrane binding of nanoparticles in pancreatic cancer cell lines overexpressing mesothelin.

Acknowledgements

Firstly, thank you to my parents Benjamin Akponasa and Gladys Akponasa for instilling in me a love of learning from an early age that led me to this point. Thank you to my brothers Ben Jr. Akponasa and Caleb Akponasa for your support during this time. Many thanks to MIBTP and BBSRC for funding this project and to the University of Birmingham Chemistry department for providing the facilities, instruments and software licences for data collection and processing. Many thanks to my supervisors Professor Zoe Pikramenou and Dr Nikolas Hodges and to past and present members of the Pikramenou and Hodges group for their support, guidance and expertise. Thank you to the analytical facility in the CEM and IBR, particularly to Theresa Morris who helped significantly with sample preparation for TEM image collection. Thank you to my BICC family, without which I would have struggled to settle in Birmingham or had the energy do research. Lastly, thank you God for giving me the strength to finish.

Where then does wisdom come from? Where does understanding dwell?
It is hidden from the eyes of every living thing, concealed even from the birds in the sky.
Destruction and Death say, "Only a rumour of it has reached our ears."
God understands the way to it and he alone knows where it dwells,
for he views the ends of the earth and sees everything under the heavens.
When he established the force of the wind and measured out the waters,
when he made a decree for the rain and a path for the thunderstorm,
then he looked at wisdom and appraised it; he confirmed it and tested it.
And he said to the human race,
"The fear of the Lord—that is wisdom,
and to shun evil is understanding."

~ Job 28:20-28

Contents

1. Introduction 1

1.1 Pancreatic cancer 1

1.1.1 Pancreatic cancer therapies 4

1.2 Nanomaterials 7

1.3 Gold Nanoparticles 9

1.3.1 Cellular uptake of gold nanoparticles 10

1.4 Techniques for gold nanoparticle characterisation 10

1.4.1 Dynamic Light Scattering 11

1.4.2 Nanoparticle Tracking Analysis 13

1.4.3 Transmission Electron Microscopy 14

1.4.4 UV-vis absorbance 15

1.5 Techniques for photophysical characterisation of luminescent metal complexes 16

1.5.1 UV-vis absorbance 16

1.5.2 Luminescence 17

1.5.3 Quantum yields 17

1.5.4 Luminescence Lifetimes 17

1.6 Thesis outline – aims and objectives 18

1.7 References 19

2. Synthesis and characterisation of luminescent iridium(III) complexes and their AuNP conjugates 23

2.1 Introduction 23

2.1.1 Iridium(III) cyclometalated complexes 23

2.1.2 Chapter summary 30

2.2 Synthesis of IrpqSS, IrpqSH and Irpqbpy cyclometalated iridium(III) complexes for the coating of colloidal gold nanoparticles 31

2.3 Photophysical properties of IrpqSS, IrpqSH and Irpqbpy cyclometalated iridium(III) complexes 36

2.4 Synthesis and characterisation of colloidal gold nanoparticles 47

2.5 Surfactant coating of gold nanoparticles with LPEG, SPEG, Zonyl-FSA and TFD-S 52

2.6 Synthesis and characterisation of IrpqSS- and IrpqSH-coated AuNPs 58

2.7 Photophysical characterisation of IrpqSS- and IrpqSH-coated AuNPs 70

2.8 Conclusions 74

2.9 Further Studies 75

2.10 Experimental 76

2.11 Six-step synthesis of bpySS ligand 77

2.11.1 Synthesis of N-(Boc)-5-amino-1-pentanol *(2)* 77

2.11.2 Synthesis of N-(Boc)-5-amino-1-tosylpentane *(3)* 78

2.11.3 Synthesis of 4,4'-dihydroxy-2,2'-bipyridine *(4)* 79

2.11.4 Synthesis of 4,4'-di-(N-(Boc)-5-amino-1-pentoxy)-2,2'-bipyridine *(5)* 80

2.11.5 Synthesis of 4,4'-di-(5-amino-1-pentoxy)-2,2'-bipyridine *(6)* 81

2.11.6 Synthesis of 4,4'-di-(5-lipoamido-1-pentoxy)-2,2'-bipyridine *(7)* 82

2.12 Synthesis of $[Ir(pq)_2Cl]_2$ dimer 83

2.13 Synthesis of $[Ir(pq)_2bpySS]PF_6$ complex *[IrpqSS]PF6* 84

2.14 Two-step synthesis of bpySH ligand 85

2.14.1 Synthesis of 5,5'-Bis(bromomethyl)-2,2'-bipyridine *(9)* 85

2.14.2 Synthesis of 5,5'-Bis(mercaptomethyl)-2,2'bipyridine *(10)* 86

2.15 Synthesis of [Ir(pq)$_2$bpySH]PF6 complex *[IrpqSH]PF6* 87

2.16 Synthesis of [Ir(pq)$_2$bpy]PF6 complex *[Irpqbpy]PF6* 88

2.17 Dowex ion exchange to form IrpqSS, IrpqSH and Irpqbpy from the PF6- salts 89

2.18 Gold nanoparticle synthesis *(AuNP13)* 90

2.19 Gold nanoparticle synthesis *(AuNP25)* 90

2.20 Synthesis of N-(2-(ethylthio)ethyl) tricosafluorododecanamide) surfactant *(TFD-S)* 91

2.21 Coating of AuNP13 and AuNP25 with LPEG, SPEG, Zonyl-FSA and TFD-S surfactants 91

2.22 Coating of LPEG.AuNP, SPEG.AuNP, Zonyl.AuNP and TFD-S.AuNP with IrpqSS and IrpqSH complexes 93

2.23 Preparing AuNPs for TEM imaging 93

2.24 Preparing samples for Quantum yield measurements 94

2.25 Preparing samples for ICP-MS analysis 94

2.26 References 94

2.27 Appendix 98

3. Investigating the surfactant-dependent luminescence and localisation of iridium-coated nanoparticles 127

3.1 Introduction 127

3.1.1 Iridium-coated nanoparticles for cell imaging 127

3.1.2 Effect of surfactants on nanoparticle stability, functionalisation, and uptake 130

3.1.2.1 PEG nanoparticle coating 130

3.1.2.2 Fluorinated compound nanoparticle coating 135

3.1.3 TEM characterisation of subcellular components for localisation studies 136

3.1.4 Chapter Summary 140

3.2 Uptake of coated AuNPs and Irpqbpy in A549 cells 140

3.3 Cell survival assays in MiaPaca-2 and CFPAC-1 cells 145

3.4 Uptake and localisation of coated AuNPs and Irpqbpy in pancreatic cancer cells 147

3.4.1 Confocal luminescence of nanoparticles in MiaPaca-2 and CFPAC-1 cell lines 147

3.4.2 Quantification of confocal luminescence 153

3.4.2.1 MiaPaca-2 vs. CFPAC-1: cell line comparison 154

3.4.2.2 CFPAC-1: nanoparticle comparison 155

3.4.2.3 MiaPaca-2: nanoparticle comparison 156

3.4.3 Flow cytometry of nanoparticles in MiaPaca-2 and CFPAC-1 cell lines 157

3.4.4 Quantification of nanoparticle uptake using ICP-MS 161

3.4.4.1 MiaPaca-2 vs. CFPAC-1: cell line comparison 161

3.4.4.2 CFPAC-1: nanoparticle comparison 163

3.4.4.3 MiaPaca-2: nanoparticle comparison 165

3.4.5 Localisation of nanoparticles in TEM images 167

3.4.6 Gold nanoparticle interaction with cell media 175

3.4.7 Photophysical studies of AuNPs in cells 179

3.5 Conclusions 181

3.6 Further Studies 182

3.7 Experimental 182

3.7.1 Cell Culture 183

3.7.2 MTT assays 183

3.7.3 Confocal Microscopy Imaging 183

3.7.4 Transmission Electron Microscopy 184

3.7.5 Flow Cytometry 184

3.7.6 Inductively Coupled Plasma Mass Spectrometry (ICP-MS) 185

3.7.7 Incubation of cells for luminescence lifetime measurements 185

3.8 References 186

3.9 Appendix 189

4. Directional conjugation of anti-mesothelin antibodies to gold nanoparticles for diagnostic labelling of pancreatic cancer cells 203

4.1 Introduction 203

4.1.1 Directional conjugation of antibodies on gold nanoparticle surfaces 203

4.1.2 Pancreatic cancer tumour markers 204

4.1.3 Antibodies for pancreatic cancer targeting 206

4.1.4 Chapter Summary 210

4.2 Synthesis and characterisation of IrpqSS- and IrpqSH-coated AuNP19s 211

4.3 Photophysical characterisation of IrpqSS- and IrpqSH-coated AuNP19s 217

4.4 Selection of pancreatic cancer cell lines for cell studies 218

4.5 Uptake of AuNP19s in pancreatic cancer cells 222

4.5.1 Cell survival assays 222

4.5.2 Confocal images 223

4.5.3 Flow Cytometry 226

4.5.4 ICP-MS gold quantification 228

4.5.5 TEM localisation of gold nanoparticles 231

4.5.6 Reactive Oxygen Species (ROS) assays 241

4.5.7 Effect of gold nanoparticle interaction with cell media 242

4.6 Conclusions 244

4.7 Further Studies 245

4.8 Experimental 246

4.8.1 Colloidal AuNP synthesis *(AuNP19)* 246

4.8.2 Attachment of antibodies to a directional PEG linker 246

4.8.3 Coating of *AuNP19*s with antibody-linker solution 247

4.8.4 Coating of MAB.AuNP19s with IrpqSS and IrpqSH complexes 247

4.8.5 Preparing samples for ICP-MS analysis of AuNPs 248

4.8.6 Cell Culture 248
4.8.7 MTT assays 248
4.8.8 Confocal Microscopy Imaging 249
4.8.9 Transmission Electron Microscopy 250
4.8.10 Flow Cytometry 250
4.8.11 Preparing samples for ICP-MS analysis of AuNPs in cells 250
4.8.12 Reactive Oxygen Species (ROS) assay 251
4.8.13 qPCR of BxPC-3, MiaPaca-2 and CFPAC-1 cell lines 251

4.9 References 252

4.10 Appendix 256

5. General Conclusions 272

Abbreviations

^{13}C NMR	Carbon Nuclear Magnetic Resonance
^{1}H NMR	Proton Nuclear Magnetic Resonance
ADC	Antibody-Drug Conjugate
ADCC	Antibody Dependent Cell Cytotoxicity
AFM	Atomic Force Microscopy
AIE	Aggregation Induced Emission
AUC	Analytical Ultracentrifugation
AuNP	Gold nanoparticle
BPEI	Branched Polyethylenimine
BSA	Bovine Serum Albumin
COSY	Correlation Spectroscopy
CT	Computed Tomography
DCM	Dichloromethane
DCFDA	2',7'-dichlorodihydrofluorescein diacetate
DLS	Dynamic Light Scattering
DMEM	Dulbecco's Modified Eagle Medium
DMF	Dimethyl Formaldehyde
DMSO	Dimethyl Sulfoxide
ECM	Extracellular Matrix
EDC	1-Ethyl-3-(3-dimethylaminopropyl)carbodiimide
EDTA	Ethylenediaminetetraacetic acid
ELS	Electrophoretic light scattering
Et_2O	Diethyl ether
EUS	Endoscopic Ultrasound
FBS	Fetal Bovine Serum

FCS	Fluorescence Correlation Spectroscopy
FFF	Field-Flow Fractionation
HMBC	Heteronuclear Multiple-Bond Correlation spectroscopy
HOMO	Highest Occupied Molecular Orbital
HSQC	Heteronuclear Single-Quantum Correlation spectroscopy
ICP-MS	Inductively coupled plasma mass spectrometry
IR	Infrared Spectroscopy
IRF	Instrument Response Function
KRAS	Kirsten Rat Sarcoma virus
LC	Ligand Centre Transfer
LLCT	Ligand to Ligand Charge Transfer
LUMO	Lowest Unoccupied Molecular Orbital
MeCN	Acetonitrile
MLCT	Metal to Ligand Charge Transfer
MRI	Magnetic Resonance Imaging
MS	Mass Spectrometry
MSLN	Mesothelin
MTT	(3-(4, 5-dimethylthiazolyl-2)-2, 5-diphenyltetrazolium bromide)
NIR	Near Infra-red
NP	Nanoparticle
NTA	Nanoparticle Tracking analysis
PCC	Pancreatic Cancer Cells
PDAC	Pancreatic Ductal Adenocarcinoma
PDI	Polydispersity index
PDT	Photodynamic Therapy
PEG	Polyethylene glycol
Pq	2-phenylquinoline
PSC	Pancreatic Stellate Cells

QY	Quantum Yield
RF	Radio Frequency
RON	Recepteur d'Origine Nantais
ROS	Reactive Oxygen Species
RPMI	Roswell Park Memorial Institute
SAXS	Small-Angle X-Ray Scattering
SEC	Size Exclusion Chromatography
SEM	Scanning electron microscopy
SERS	Surface Enhanced Raman Spectroscopy
siRNA	Small interfering RNA
SLS	Static Light Scattering
SOP	Standard Operating Procedure
SPR	Surface Plasmon Resonance
TCSPC	Time Correlated Single Photon Counting
TEM	Transmission electron microscopy
TFA	Trifluoroacetic Acid
THF	Tetrahydrofuran
TOF	Time of flight
TRPS	Tunable Resistive Pulse Sensing
UV	Ultraviolet
Vis	Visible Spectrum
XPS	X-ray photoelectron spectroscopy
XRD	X-Ray Diffraction
ε	Molar Absorptivity
ζ-potential	Zeta potential
λmax	Wavelength at Maximum Intensity
τ	Luminescence lifetime
Φ	Luminescence Quantum Yield

Chapter 1

1. Introduction

Pancreatic cancer treatments to show the most recent advances involving nanotherapeutics in recent years will be outlined. The use of gold nanoparticles (AuNPs) as a therapeutic agent and the most common techniques for the characterisation of nanomaterials and luminescent metal complexes will be discussed and explained, in addition to the different uptake methods for AuNPs into cells.

1.1 Pancreatic cancer

In the human body, the pancreas is an organ of approximately six inches, located behind the stomach. The head of the pancreas is connected to the duodenum via the pancreatic duct, while the pancreas tail is located on the left-hand side of the body. The function of the pancreas is the secretion of enzymes of digestive juices into the small intestine, as well as producing insulin. Therefore the pancreas serves as both an exocrine and endocrine gland (Figure 1.1).[1]

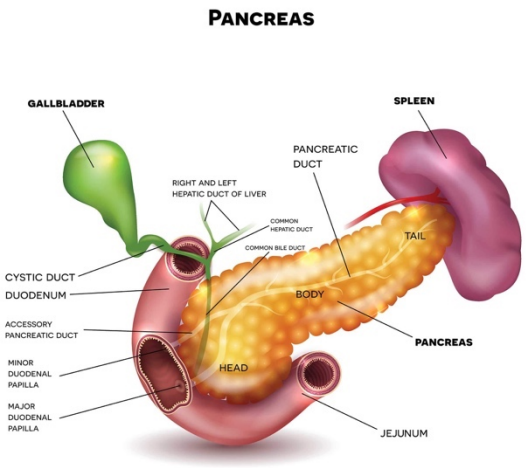


Figure 1.1. Diagram of a human pancreas, with its attachment to the small intestine, gall bladder and spleen shown. Image obtained from https://www.hopkinsmedicine.org/health/conditions-and-diseases/pancreatic-cancer/pancreatic-cancer-types.

When things go wrong in the body, conditions that affect the pancreas include diabetes 1 and 2, cystic fibrosis, pancreatitis, pancreatic pseudocyst, and pancreatic cancer. Pancreatic cancer has two types. Exocrine tumours are the most common, with adenocarcinoma as the most regular form of exocrine tumour. Adenocarcinomas normally begin in the ducts, hence why they are called ductal adenocarcinomas. The second type of pancreatic cancer is endocrine tumours, also called islet cell tumours. In this project, the focus will be on the most common form of pancreatic cancer, Pancreatic Ductal Adenocarcinoma (PDAC).

Pancreatic ductal adenocarcinoma (PDAC) makes up 90% of pancreatic cancers.[2, 3] Survival rates from the treatment of the disease has not significantly improved within the last 20 years[4, 5] (only an increase from 5% to 8%) despite improvements in methods of treatments, making PDAC one of the most aggressive and fatal cancers. The main challenges are a lack of effective therapeutics and a lack of early diagnostic tools. Few chemotherapy agents for pancreatic cancer such as gemcitabine are available. And even the efficacy and penetration of these drugs is not very high due to the dense stroma of cells that surround the tumours to form an extracellular matrix (Figure 1.2).[6] This dense stroma consists of pancreatic stellate cells and many other extracellular components such as type I collagen which may contribute to the survival of the tumour cells. The efficacy of drugs such as gemcitabine (Figure 1.3A)[7] is reduced as a result of this microenvironment and connective tissue growth factor which is produced in the stroma helps to keep the stroma strong and prevent the penetration and activity of the drug by creating barriers. In addition, the high interstitial pressure of the stroma impairs drug delivery due to reduced blood flow. The method of action of gemcitabine is to replace the nucleoside cytidine, causing apoptosis. Other drugs used to treat PDAC are 5-fluorouracil (5-Fu) (Figure 1.3B),[7] cisplatin[8] and capecitabine.[9] Before gemcitabine became popular, 5-Fu was what was used most frequently. In addition to the extracellular matrix, there is a low density of blood vessels in PDAC tumours, resulting in hypoxia and low levels of nutrients. Fibroblasts that form lead to immunosuppressive signalling and immune cells take part in inflammatory signalling.

Diagnosis of PDAC usually occurs in older patients, those over 40 years of age[6] and at late stages, at which point the disease has usually already reached metastasis. Screening techniques such as CT (Computerized Tomography), EUS (Endoscopic Ultrasound) and MRI (Magnetic Resonance Imaging) are not advanced enough to accurately detect the stage of the cancers, so it is difficult to target specific treatment for different stages of the cancer. In addition, screening for premalignant or early malignant tumours is successful in less than 25% of cases.[10] The death rate will continue to increase if good treatments cannot be found, especially at early stages where there is a higher chance of preventing metastasis.

PDAC has mutations in the KRAS gene. This mutation causes the cells to proliferate continuously due to hindered proliferation control from the KRAS gene. This proliferation then often leads to cancer. Patients with pancreatic cancer have a variety of obvious symptoms such as abdominal pain, weight loss, asthenia, anorexia, jaundice and diabetes. These symptoms are related to the location of the cancer in the pancreas, whether the head, or the body and tail. Location of metastasis is usually to the liver, abdomen and lungs.

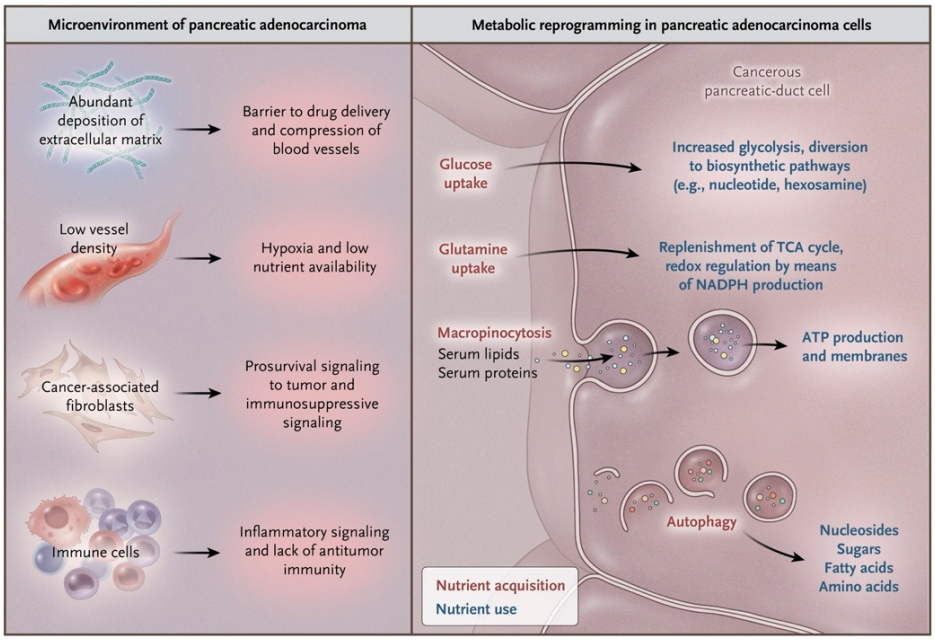


Figure 1.2. The microenvironment of PDAC cell tumours, showing different aspects that contribute to the dense stroma surrounding PDAC tumours. Image obtained from ***D. P. Ryan et al., New England Journal of Medicine, 2014, 371, 1039-1049.***

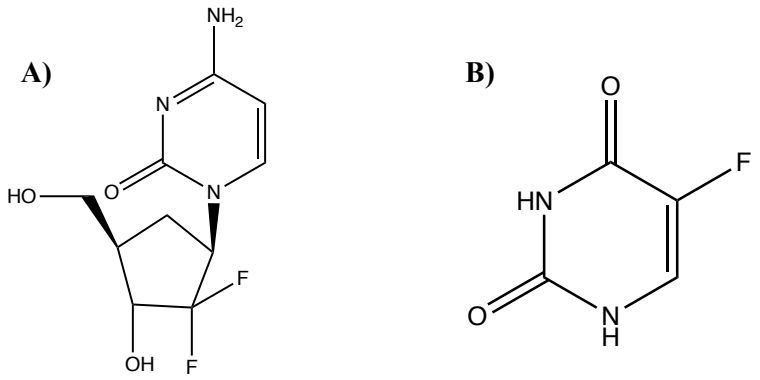


*Figure 1.3. Structures of pancreatic cancer drugs **(A)** gemcitabine in pro-drug form before conversion to the triphosphate active drug and **(B)** 5-fluorouracil.*

1.1.1 Pancreatic cancer therapies

Depending on the stages of the cancer, different treatments are available. The four stages are surgically resectable pancreatic cancer (Stage 1 & 2), unresectable pancreatic cancer that is locally advanced (Stage 3) and metastatic pancreatic cancer (Stage 4). Due to most cases of pancreatic cancer being diagnosed at stages 3 and 4, better diagnosis and treatment methods are required for the early stages. Most therapies to date consist of surgical resection, chemotherapeutics and combination therapy, with gemcitabine-radiation combination therapy and gemcitabine-capecitabine as some examples of adjuvant treatments.[1] Other therapies include nanotechnology, immunotoxins/antibody-drug conjugates and vaccines. For stage 1 and 2 PDAC, surgical resection is possible because the tumours are localised and not advanced. However, due to the late-stage diagnosis of most cases, surgical resection is not as common a treatment as might be expected. For stage 3 and 4, chemotherapy drugs are the first line of treatment. However, due to the dense stroma of cells surrounding the tumours as mentioned in section 1.1, the penetration of drugs such as gemcitabine is reduced. Adjuvant treatment with chemotherapy drugs are also available; for example gemcitabine-radiation combination is one of the best neo-adjuvant treatments. Another combination is with surgical resection and chemotherapy drugs.

Due to lack of early diagnostic tools, PDAC is normally detected at late stages, when metastasis has already occurred. There is a great need for early diagnostic tools and better treatment of the PDAC. Currently, drug gemcitabine has poor efficacy due to rapid clearance by the body[11, 12] and the dense

stroma that surrounds PDAC tumours, impairing delivery of the drug. Folfirinox, a combination of folinic acid, fluorouracil, irinotecan and oxaliplatin drugs has been shown to be a treatment option for patients upon failure of other chemotherapy drugs.[13, 14] Nanotechnology in recent years has shown significant potential in the targeting of cancers. The advantage of using nanotechnologies such as gold nanoparticles, is site specificity in the body and enhanced drug permeability as well as controlled drug release rate. Circulation time of drugs increase upon loading them onto nanoparticles because eradication of the drug by liver and kidneys is avoided.

Research conducted with AuNPs using the antibody Cetuximab as a targeting agent, provided a delivery vehicle for gemcitabine which resulted in inhibition of PDAC cell proliferation both in vivo and vitro, showing that improved efficiency of drug delivery in pancreatic cancer using AuNPs is possible[15, 16] (Chapter 4). This was later supported by the research of Spadavecchia *et al*. in 2016 that showed improved efficacy when PEGylated AuNPs were used as a drug carrier for the cancer drug doxorubicin. The EC_{50} of doxorubicin dropped by more than 30 times compared to the free drug in PDAC cell lines.[17, 18] AuNPs with targeting antibodies have been shown to release energy as heat in cancer cells after absorbing nonionizing radio frequency (RF) radiation. The production of heat led to cytotoxic hyperthermal activity and normal cells were unaffected despite whole-body RF field exposure.[19, 20] This technique is different from the typical cytotoxicity simulation, however, still provides an interesting alternative to the classical apoptosis pathway.

Other research that explores a different apoptosis pathway in cancer cells is the work of Borkowska *et al*. in mixed-charge nanoparticles.[21] This research highlights the influence of the positive-to-negative charge ratio on targeting lysosomes in cancer cells that leads to lysosome swelling and eventual cell death. This research is interesting because it demonstrates that apoptosis may not necessarily be through the normal caspase-dependent mechanism and any cell death seen from NP uptake in cells must be carefully investigated before conclusions are made about the effect that the NPs have had. This is because most NPs are used as delivery vehicles, so moieties added for functionalisation could change the surface charge.

Research has shown that the microenvironment of the tumour cells suppresses immune response by favouring immune suppressor cells instead of immune effector cells.[22] Han *et al*.[23] reported a new application of gold nanoparticles in the microenvironment of tumour cells, for the re-education of pancreatic stellate cells. Pancreatic stellate cells (PSC) assist greatly with the stromal aspect of PDAC and targeting them could reduce the resistance of tumours to chemotherapy, as drugs such as gemcitabine could be more easily delivered. A nanosystem was constructed that would respond to the acidic microenvironment of the PDAC cells. This nanosystem consisted of PEGylated polyethylenimine-coated gold nanoparticles, loaded with siRNA targeting heat shock protein 47 and all-*trans* retinoic acid, both of which contribute to pancreatic stellate cell quiescence. Their work aimed at targeting activated pancreatic stellate cells to change the tumour surroundings to a more penetrable environment for chemotherapy drugs. By using a detachable linker for the PEG coating, they were able to enhance cellular uptake because the acidic tumour microenvironment caused the PEG to detach and once the nanoparticle was in the cell, the siRNA and retinoic acid were detached to work on reducing the effect of the PSCs. Their conclusions were that they succeeded in transforming the PSC, transforming activated PSCs into quiescent PSCs, reducing the extracellular matrix (ECM) production and suppressing the progression of tumour growth by combining their nanosystem with chemotherapy drugs for improved penetration. By successfully re-educating the PSCs, this shows potential for further combination therapy with chemotherapeutics. In other research, plain citrate AuNPs of 20 nm were shown to sensitise PDAC cells to gemcitabine by inhibiting migration and colony formation of cells.[24]

Recently one of the main drives in PDAC research is to find overexpressed markers. Overexpressed PDAC cell markers could provide a way of specifically targeting the tumours and eliminating them without killing healthy cells. This is because overexpressed PDAC cell antigens that are targeted by an antibody could lead to Antibody Dependent Cell Cytotoxicity (ADCC). In addition, coupling an antibody to a toxin to make ADCs (Antibody-Drug conjugates)/Immunotoxins[25, 26] provides another route to cancer cell death due to uptake into the cell by endocytosis. Release of the drug/toxin leads to cell apoptosis. Due to the large size of ADCs, they escape from circulation slowly, therefore the cancer

cells are exposed to high levels of the immunotoxin. Some immunotoxins have even reached Phase II trials (NCT01362790).

For this project, finding an overexpressed antigen on the surface of pancreatic ductal adenocarcinoma cells that could be targeted by an antibody would be a perfect way of delivering gold nanoparticles to cancer cells together with iridium(III) photodynamic complexes. The antigen used should be expressed only in the tumour, or minimally expressed in healthy cells[22] for specificity towards the cancer cells. Research has shown overexpressed antigens with corresponding antibodies that are specific,[27-30] however some of these antibodies are non-human. Although some non-human antibodies have reached clinical trials, higher immunogenicity of the non-human antibodies indicates that human-antibodies may be the best.[31] This is discussed further in Chapter 4.

Vaccination against tumour antigens, so that the body can recognise them and destroy them before the cancer advances is the method for vaccine treatment. The antigen used must only be expressed on tumour cell surfaces, or minimally expressed in healthy cells. However not many immune responses have been seen in patients using this method. Vaccination with whole-cells[32] is another technique that removes the need for identification of an overexpressed antigen and immunity against multiple antigens could be obtained. Other forms of vaccines include peptide vaccines, DNA vaccines and vaccines with microorganisms.[33] Some vaccines have also reached clinical trials.[34]

1.2 Nanomaterials

In recent years, research in the nanotherapeutics field has revealed the potential of nanomaterials for promoting more efficient drug delivery, tumour permeability and controlled drug release as well as improved targeting specificity. The advantage of nanotherapeutics over other treatments is that nanomaterials can be functionalised with targeting moieties such as antibodies, DNA fragments, nucleic acids and aptamers. These tend to accumulate in cancer cells over normal cells due to more specific targeting and faster uptake in the cancer cells. Nanomaterials have the potential to have high loading of

compounds attached, enabling delivery of high concentrations of compounds compared to free compounds in solution. There are different kinds of nanomaterials such as nanoparticles,[16] nanorods,[35] nanocages,[36] nanostars,[37] and quantum dots.[7] They are also made from a variety of materials such as gold,[38, 39] silver,[40, 41] platinum,[41] palladium,[42] ruthenium,[41] iron oxide,[43] silica,[44] carbon[45] and a range of polymers[46] (Figure 1.4).[47] Other potential treatments on the nanoscale include polymer-drug conjugates, amphiphilic polymers and albumin.[7] Each material has advantages and disadvantages depending on the function.

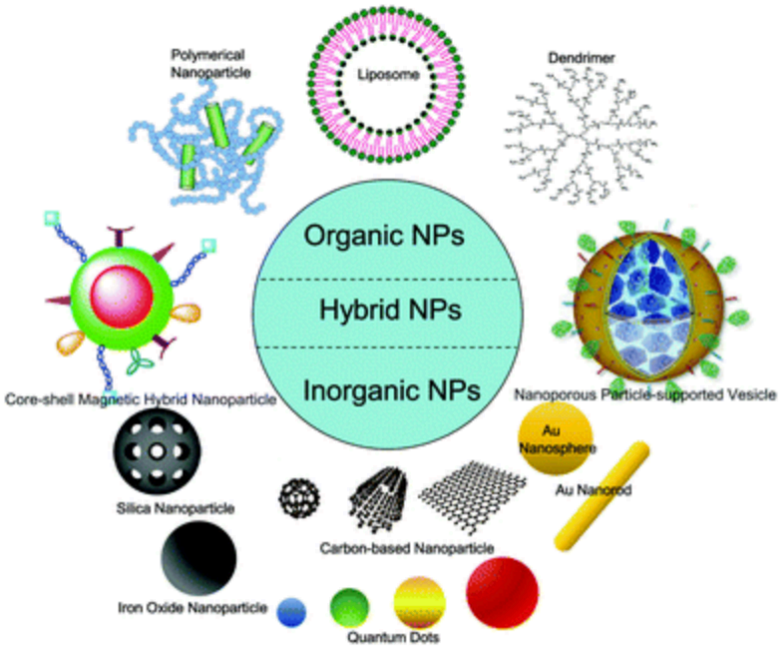


Figure 1.4. Image to show the various type of nanomaterials used for diagnostics, imaging or treatment. Image obtained from ***H.-m. Ding and Y.-q. Ma, Nanoscale Horizons, 2018, 3, 6-27.***

Amongst all the nanomaterials that exist, gold nanoparticles (AuNPs) are popular due to their biocompatibility, ease of synthesis, shape and size tunability, ease of characterisation and strong Au-S bonds. Up to thousands of metal complexes can be attached to the surface for imaging, meaning that lower concentrations are required compared to free probes in solution. AuNPs can hold multiple different components on their surfaces due to the strong gold-thiol/amine interaction that promotes surface functionalisation. Hence, different targeting bodies can be loaded onto the surface of AuNPs, ensuring target specificity for the nanoparticles that act as vehicles for different moieties. Hence, this

thesis will focus on AuNPs and the methods of optimisation in order to make them useful for potential treatments.

1.3 Gold Nanoparticles

As the size of gold decreases from bulk gold to the macroscale, microscale and then nanoscale, the properties of the gold change. One of the properties are the optical colour, of which bulk gold is yellow and nanoscale gold has a red colour, based on the interaction with light. AuNPs interact with light, forming surface plasmons (Section 1.4.4). Gold nanoparticle shape and size can be altered by modification of the synthesis process. They can be used in optical imaging, fluorescence imaging, PDT (Photodynamic Therapy),[48] photothermal and photoacoustic therapy, magnetic resonance, SERS (Surface Enhanced Raman Spectroscopy) and computed tomography (Figure 1.5).[49] AuNPs from 5 – 80 nm have been used for anti-tumour applications,[50] and in a variety of clinical trials as gold nanoparticles (NCT02782026, NCT01420588), gold nanocrystals (NCT02755870), silica-gold nanoparticles (NCT01270139), silica-gold nanoshells (NCT02680535, NCT00848042, NCT01679470) and Spherical Nucleic Acid (SNA) Gold Nanoparticles (NCT03020017).

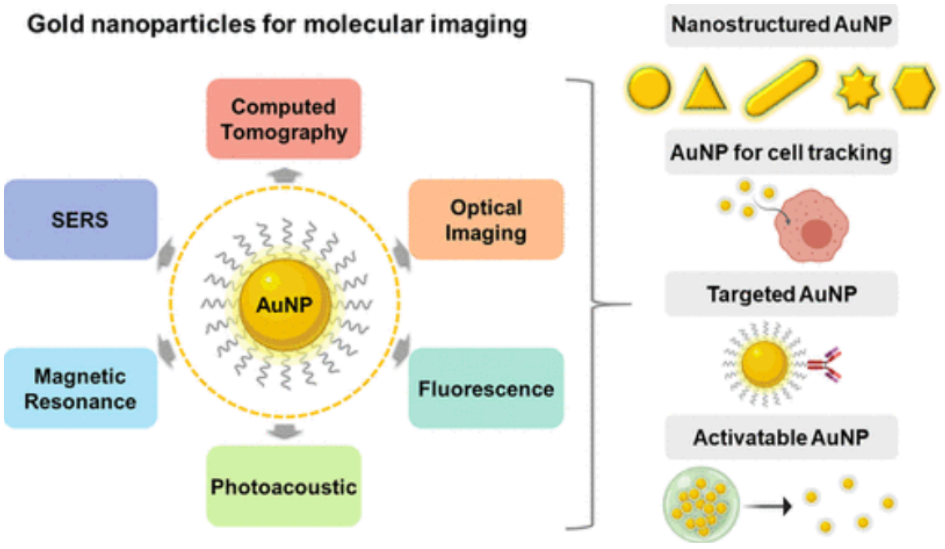


Figure 1.5. Uses of gold nanoparticles such as optical imaging, fluorescence imaging, photothermal and photoacoustic therapy, magnetic resonance, SERS (Surface Enhanced Raman Spectroscopy) and computed tomography. Image obtained from ***M. Bouché et al., Bioconjugate Chemistry, 2020, 31, 303-314.***

1.3.1 Cellular uptake of gold nanoparticles

There are various ways for AuNP uptake in cells (Figure 1.6).[51] Passive uptake and translocation (A) occurs when the samples pass through the membrane and accumulate in different sub-cellular organelles depending on AuNP lipophilicity. Clathrin-mediated endocytosis (B), where AuNPs bind to a receptor at the cell surface causing the membrane to fold inwards forming a vesicle that fuses with endosomes and later multivesicular bodies is the second method of uptake. Lastly, macropinocytosis, where the cell membrane protrudes from the bulk of the cell forming membrane ruffles (C) is the third method.

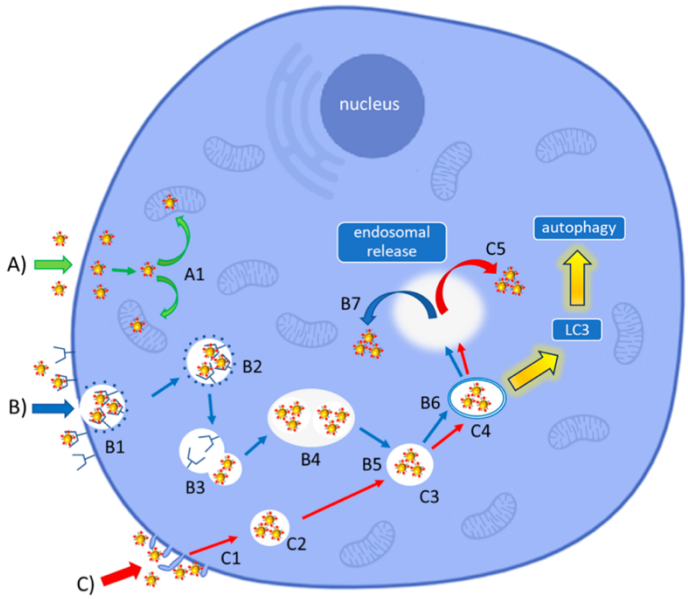


Figure 1.6. Schematic showing cellular uptake in cells.. Image was obtained from ***A. N. Dosumu et al., JACS Au, 2021, 1, 174-186.***

Depending on the type of uptake method of a particular cell line or a particular treatment of cells, the localisation of AuNPs can vary, as will be seen in Chapters 3 and 4.

1.4 Techniques for gold nanoparticle characterisation

For reliability and reproducibility of synthesis of AuNPs, certain characterisation methods should be used to confirm the formation of the AuNPs[52-55] as well as their stability. In this section, methods used to characterise AuNPs within this project are outlined. Dry techniques and suspension techniques can

both be used to ensure uniformity of AuNPs in different environments, confirming stability due to different preparation methods.

1.4.1 Dynamic Light Scattering

DLS (Dynamic Light Scattering) is a suspension technique that calculates the size of nanoparticles from Brownian motion. It is a quick and cheap first-hand technique that can indicate whether further optimisation/purification is needed in a sample before moving on to other more expensive size analysis techniques. Equation 1.1 shows the Stokes-Einstein equation for the diffusion of spherical particles, where particle size is obtained from the diffusion coefficient D. k_B is Boltzmann's constant, T is the absolute temperature, η is the dynamic viscosity, and R_h is the hydrodynamic radius.

There are some disadvantages to using DLS as a characterisation method. There is temperature sensitivity and sensitivity to solvent viscosity. Smaller particles move faster than larger ones, hence the speed of diffusion through the solvent by Brownian motion depends on the size. An increase/decrease in temperature as well as solvent-particle friction can affect the final calculated size of the particles. The size of the NPs affects the scattering intensity to the 6th power of the size of the particle. So larger NPs scatter more light and this means that impurities could scatter light as well and skew the size distribution. Due to the nature of the technique, optimisation of concentration may be necessary because the signal obtained will depend on the size of the particle and the concentration, as a transparent sample is needed for this technique.

$$D = \frac{k_B T}{6\pi\eta R_h} \qquad \textit{Equation 1.1}$$

The first order result obtained by DLS is the scattering intensity. Then from the Mie theory, size by volume distribution is obtained. Size by volume assumes that all the NPs are spherical and homogeneous and that the scattering intensity has no error. Another assumption is that then optical

properties of the sample are known. Many of the parameters for DLS are input in the standard operating procedure (SOP) at the start of the experiment, so the conditions can be changed, depending on the sample. If human error causes an incorrect setting to be input in the SOP, the final NP size will be incorrect. The third order result obtained by DLS is the size by number, which measures the number of particles at a particular size, rather than measuring the scattering intensity and volume taken up by the particles. Hence, size by intensity, size by volume and size by number are the three distributions obtained from DLS, for comparative purposes. Z-average and Polydispersity index (PDI) are also obtained. Z-average is the mean hydrodynamic size obtained from the scattering intensity, and PDI is the polydispersity index, a measure of the monodispersity of the sample. PDI values of 0.2 indicate monodisperse samples, as previously recorded. PDI is obtained from the square of the standard deviation divided by the average particle diameter.

Due to DLS being a solution technique, R_h is the hydrodynamic radius, which is the radius of the particle in addition to a hydration layer that surrounds the particle. This hydration layer is formed from solvent molecules in solution that interact with adsorbed ions on particle surfaces and diffuse alongside the particle in an identical manner (Figure 1.7), as though they were part of the particle. Therefore, R_h in the scattering intensity distribution is usually larger than the the actual radius of the particle being measured. It was found in this study that size by volume was more representative of the true size, when comparing with Transmission Electron Microscopy (TEM), a solid-state size analysis technique. The layer between the adsorbed ions at a NP surface and diffuse ions in solution is called the Stern layer[53]. At the point that the hydrodynamic radius stops and the fluid is mobile, this is called the slipping plane. Zeta potential can then be calculated, as it is the potential difference between the slipping plane and the solution.[53]

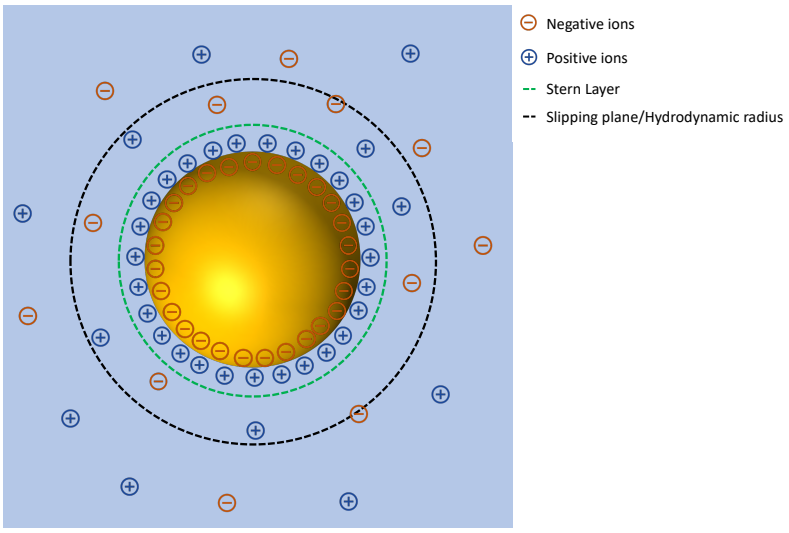


*Figure 1.7. A schematic of an **AuNP** in H_2O with a representation of the ions present on the NP surface and in solution. The Stern Layer and Slipping plane are represented in green and black,*

1.4.2 Nanoparticle Tracking Analysis

NTA (Nanoparticle Tracking Analysis) is another solution-based technique used to measure the NP size (Figure 1.8). Unlike DLS, NTA allows the visualisation of the NPs in real time via a microscope camera and can also measure fluorescence of the AuNPs due to the camera. NTA can used in combination with DLS to confirm sizes of the AuNPs. In addition to DLS and NTA, other suspension techniques for measuring AuNP size include SLS (Static Light Scattering), AUC (Analytical Ultracentrifugation), SEC (Size Exclusion Chromatography), FFF (Field-Flow Fractionation), FCS (Fluorescence Correlation Spectroscopy), TRPS (Tunable Resistive Pulse Sensing) and ELS (Electrophoretic light scattering).

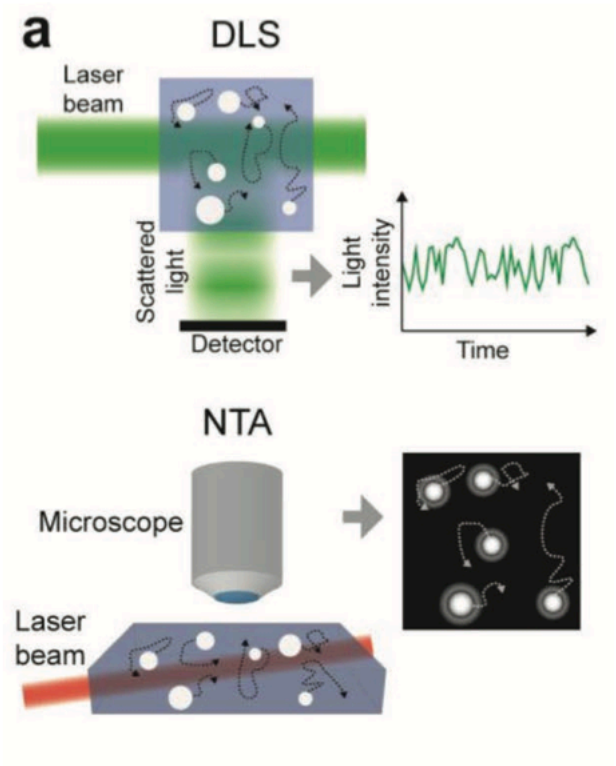


Figure 1.8. Illustration of DLS (top) and NTA (bottom) techniques showing the scattered light collection from DLS and the video acquisition of nanoparticles by NTA. Image obtained from ***M. M. Modena et al., Advanced Materials, 2019, 31, 1901556.***

1.4.3 Transmission Electron Microscopy

TEM is a solid-state dry technique for visualising single NPs and measuring their size. The microscopes use an electron beam to obtain magnified images of high resolution (Figure 1.9).[53] As the name suggests, the electron beam passes through the sample (transmit) if the sample has lower density, and the image is brighter. Where the sample has a high density, the electrons don't pass through as well and the image is darker. Therefore, TEM works well with samples of high density to get better contrast compared to the background signal. TEM is costly due to maintenance costs and highly trained users are required for efficient maintenance. Other dry characterisation techniques for AuNPs include SEM (Scanning Electron Microscopy), AFM (Atomic Force Microscopy), XRD (X-Ray Diffraction), SAXS (Small-Angle X-Ray Scattering), MS (Mass Spectrometry) and gas sorption.

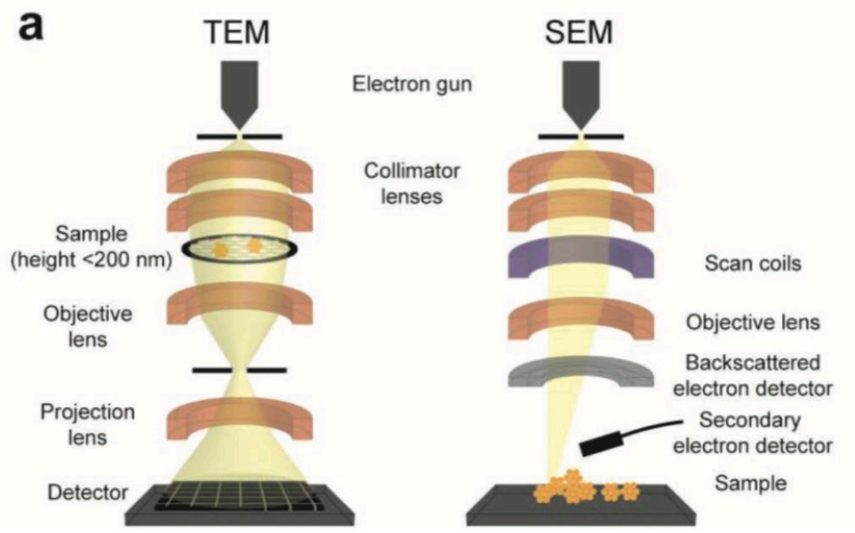


Figure 1.9. Schematic for TEM and SEM instruments. Images obtained from ***M. M. Modena et al., Advanced Materials, 2019, 31, 1901556.***

1.4.4 UV-vis absorbance

Surface Plasmon Resonance (SPR) occurs when electrons on a metal surface are excited by light to form surface plasmon polaritons (oscillating electrons) from the oscillating electric field (Figure 1.10). These electromagnetic waves travel in a direction that is parallel to the metal surface, hence they are sensitive to any changes that occur at the metal/H_2O medium interface, i.e. adsorption, bond formation, ion interaction.

For AuNPs, these waves are termed Localised Surface Plasmon Resonance (LSPR), because the surface plasmon is localised on the AuNP that has a size the same or smaller than that of the wavelength of light used to excite the AuNP. The frequency of oscillation of the electrons is determined by the density of the electrons, the mass of the electrons, distribution of the electron charge and the shape of the AuNP. An AuNP will display maximum absorption at the frequency of the plasmon resonance. When AuNP surfaces are modified, the frequency of oscillation will change, confirming modification. Other techniques that can be used for characterisation of functionalised AuNPs[56] are gel electrophoresis, circular dichroism spectroscopy and DLS.

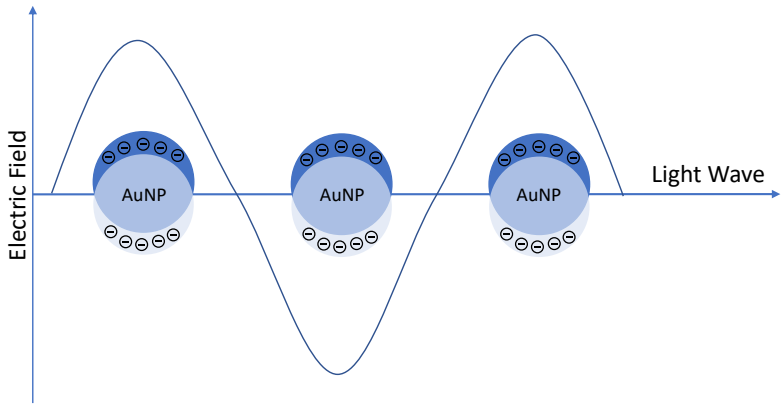


Figure 1.10. Localised Surface Plasmon Resonance (LSPR) of AuNPs in the presence of an electric field and a light wave. Oscillating cloud of electrons shown within the AuNPs.

1.5 Techniques for photophysical characterisation of luminescent metal complexes

1.5.1 UV-vis absorbance

From UV-vis absorbance spectra, the extinction coefficient (ε / $M^{-1}cm^{-1}$) of iridium(III) cyclometalated complexes can be obtained from the Beer-Lambert law (Equation 1.2) when the concentration (c/M) and path length (l/cm) of the cuvette is known.

$$A = \varepsilon cl \qquad \textit{Equation 1.2}$$

Extinction coefficients measure how strongly a compound absorbs light at a specific wavelength, so a higher value corresponds to greater absorbance at that wavelength. Calculation of the extinction coefficient is important when selecting a complex, as complexes that efficiently absorb light can emit when excited with light of lower intensity.

1.5.2 Luminescence

Excitation and emission spectra of iridium(III) cyclometalated complexes are also important in their characterisation. Excitation spectra show the emission intensity at fixed emission wavelength, as the excitation wavelength is varied. It probes the excited states, but only those that lead to emission. Emission spectra indicate the colour of the emission when in the complex is used for imaging. In different solvents, the emission wavelength can also shift, which gives an indication of how different solvent affect the ground state/excite energies of the complexes.

When a compound obeys Kasha's rule and Vavilov's rule, the excitation and UV-vis spectra will be identical. Kasha's rule states that within a multiplicity, the level from where emission occurs is the lowest excited state level.[57, 58] Vavilov's rule states that the quantum yield of luminescence is independent of the excitation light wavelength[59]. When the excitation and UV-vis spectra differ, this means that not all the electrons excited by the absorbance wavelength led to emission.

1.5.3 Quantum yields

The formula for calculation of the quantum yields using an integrating sphere can be seen in Equation 1.3,[60] where E_c = emission of the sample, A = absorbance of the sample at excitation wavelength, E_b = integrated luminescence from the sample caused by indirect luminescence from the sphere, L_a = scatter of the blank solvent and L_c = scatter of the sample.

$$\phi = \frac{E_c - (1 - A) \cdot E_b}{L_a \cdot A} = \frac{E_c - E_a}{L_a - L_c} \qquad \textit{Equation 1.3}$$

1.5.4 Luminescence Lifetimes

For the collection of luminescence lifetimes, the sample is excited by a laser and the emitted photons are counted using Time Correlated Single Photon Counting (TCSPC), to create an exponential curve of

counts vs time. The exponential curve is run through a fitting software to generate the luminescence lifetime. The number of counts falls exponentially with time, so the equation used assumes all data fitted is an exponential curve. Therefore, the residuals showing the quality of the fitting curve need to be observed to ensure good quality of data, as will be seen for all luminescence lifetime data collected in Chapters 2, 3 and 4.

1.6 Thesis outline – aims and objectives

The aim of this thesis was to show that monodisperse nanoparticles coated with surfactants and luminescent iridium(III) complexes can be used to image PDAC cells, and that different surfactants influence the imaging, uptake and localisation of the nanoparticles in cells. A secondary aim was to show that monodisperse nanoparticles coated with anti-mesothelin antibodies and iridium(III) complexes can be used to target PDAC cells overexpressing mesothelin, as opposed to PDAC cells with low levels of mesothelin.

In Chapter 2, synthesis of the three iridium(III) complexes **IrpqSS**, **IrpqSH** and **Irpqbpy** as well as the synthesis of colloidal 15 nm AuNPs will be discussed. Coating of the AuNPs with the complexes and the suitability of the final iridium-AuNP samples for imaging in cells will be proven. In Chapter 3, the influence of four different surfactants (two PEG-based surfactants and two fluorinated surfactants) on the surface of the AuNPs will be compared, as well as localisation in different subcellular components with TEM. In Chapter 4, directional conjugation of anti-mesothelin antibodies to the surface of 19 nm size AuNPs will show the capability of these antibodies for diagnosis of cell lines overexpressing mesothelin.

1.7 References

1. John Hopkins Medicine, Pancreatic Cancer Types, https://www.hopkinsmedicine.org/health/conditions-and-diseases/pancreatic-cancer/pancreatic-cancer-types, (accessed March 19, 2022).
2. A. Adamska, A. Domenichini and M. Falasca, *Int. J. Mol. Sci.*, 2017, **18**.
3. M. Orth, P. Metzger, S. Gerum, J. Mayerle, G. Schneider, C. Belka, M. Schnurr and K. Lauber, *Radiat. Oncol.*, 2019, **14**, 141.
4. R. Goess and H. Friess, *Expert Rev. Anticancer Ther.*, 2018, **18**, 295-304.
5. A. Bengtsson, R. Andersson and D. Ansari, *Sci. Rep.*, 2020, **10**, 16425.
6. D. P. Ryan, T. S. Hong and N. Bardeesy, *N. Engl. J. Med.*, 2014, **371**, 1039-1049.
7. A. Manzur, A. Oluwasanmi, D. Moss, A. Curtis and C. Hoskins, *Pharmaceutics*, 2017, **9**, 39-39.
8. V. Heinemann, H. Wilke, H. G. Mergenthaler, M. Clemens, H. König, H. J. Illiger, M. Arning, A. Schalhorn, K. Possinger and U. Fink, *Ann. Oncol.*, 2000, **11**, 1399-1403.
9. P. Grierson, A. Teague, R. Suresh, K. H. Lim, M. Amin, K. Pedersen, B. Tan, J. Huffman, N. Boice, L. Du, J. Liu, A. C. Lockhart and A. Wang-Gillam, *J. Gastrointest. Oncol.*, 2020, **11**, 61-67.
10. G. Capurso, M. Signoretti, R. Valente, U. Arnelo, M. Lohr, J.-W. Poley, G. Delle Fave and M. Del Chiaro, *World J. Gastrointest. Endosc.*, 2015, **7**, 833-842.
11. C. R. Patra, R. Bhattacharya, D. Mukhopadhyay and P. Mukherjee, *Adv. Drug Del. Rev.*, 2010, **62**, 346-361.
12. A. M. Storniolo, S. R. Allerheiligen and H. L. Pearce, *Semin. Oncol.*, 1997, **24**, S7-2-S7-7.
13. A. Belkouz, J. de Vos-Geelen, R. A. A. Mathôt, F. Eskens, T. M. van Gulik, M. G. H. van Oijen, C. J. A. Punt, J. W. Wilmink and H. J. Klümpen, *Br. J. Cancer*, 2020, **122**, 634-639.
14. M. Sawada, A. Kasuga, T. Mie, T. Furukawa, T. Taniguchi, K. Fukuda, Y. Yamada, T. Takeda, R. Kanata, M. Matsuyama, T. Sasaki, M. Ozaka and N. Sasahira, *BMC Cancer*, 2020, **20**, 449.
15. C. R. Patra, R. Bhattacharya, E. Wang, A. Katarya, J. S. Lau, S. Dutta, M. Muders, S. Wang, S. A. Buhrow, S. L. Safgren, M. J. Yaszemski, J. M. Reid, M. M. Ames, P. Mukherjee and D. Mukhopadhyay, *Cancer Res.*, 2008, **68**, 1970-1978.
16. J. A. Khan, R. A. Kudgus, A. Szabolcs, S. Dutta, E. Wang, S. Cao, G. L. Curran, V. Shah, S. Curley, D. Mukhopadhyay, J. D. Robertson, R. Bhattacharya and P. Mukherjee, *PLoS One*, 2011, **6**, e20347-e20347.
17. J. Spadavecchia, D. Movia, C. Moore, C. Manus Maguire, H. Moustaoui, S. Casale, Y. Volkov and A. Prina-Mello, *Int. J. Nanomedicine*, 2016, **11**, 791-822.

18. H. Moustaoui, D. Movia, N. Dupont, N. Bouchemal, S. Casale, N. Djaker, P. Savarin, A. Prina-Mello, M. L. de la Chapelle and J. Spadavecchia, *ACS Appl. Mater. Interfaces*, 2016, **8**, 19946-19957.
19. E. S. Glazer, K. L. Massey, C. Zhu and S. A. Curley, *Surgery*, 2010, **148**, 319-324.
20. E. S. Glazer, C. Zhu, K. L. Massey, C. S. Thompson, W. D. Kaluarachchi, A. N. Hamir and S. A. Curley, *Clin. Cancer Res.*, 2010, **16**, 5712-5721.
21. M. Borkowska, M. Siek, D. V. Kolygina, Y. I. Sobolev, S. Lach, S. Kumar, Y.-K. Cho, K. Kandere-Grzybowska and B. A. Grzybowski, *Nat. Nanotechnol.*, 2020, **15**, 331-341.
22. L. F. Dodson, W. G. Hawkins and P. Goedegebuure, *Immunotherapy*, 2011, **3**, 517-537.
23. X. Han, Y. Li, Y. Xu, X. Zhao, Y. Zhang, X. Yang, Y. Wang, R. Zhao, G. J. Anderson, Y. Zhao and G. Nie, *Nat. Commun.*, 2018, **9**, 3390-3390.
24. Y. Huai, Y. Zhang, X. Xiong, S. Das, R. Bhattacharya and P. Mukherjee, *Cell stress*, 2019, **3**, 267-279.
25. N. Kommineni, P. Pandi, N. Chella, A. J. Domb and W. Khan, *Polym. Adv. Technol.*, 2020, **31**, 1177– 1193.
26. I. Pastan, R. Hassan, D. J. FitzGerald and R. J. Kreitman, *Annu. Rev. Med.*, 2007, **58**, 221-237.
27. M. Ho, M. Feng, R. J. Fisher, C. Rader and I. Pastan, *Int. J. Cancer*, 2011, **128**, 2020-2030.
28. Y. Feng, X. Xiao, Z. Zhu, E. Streaker, M. Ho, I. Pastan and D. S. Dimitrov, *Mol. Cancer Ther.*, 2009, **8**, 1113-1118.
29. R. Hassan, W. Ebel, E. L. Routhier, R. Patel, J. B. Kline, J. Zhang, Q. Chao, S. Jacob, H. Turchin, L. Gibbs, M. D. Phillips, S. Mudali, C. Iacobuzio-Donahue, E. M. Jaffee, M. Moreno, I. Pastan, P. M. Sass, N. C. Nicolaides and L. Grasso, *Cancer Immun.*, 2007, **7**, 20.
30. Y.-F. Zhang, Y. Phung, W. Gao, S. Kawa, R. Hassan, I. Pastan and M. Ho, *Sci. Rep.*, 2015, **5**, 9928.
31. G. A. Huls, I. A. Heijnen, M. E. Cuomo, J. C. Koningsberger, L. Wiegman, E. Boel, A. R. van der Vuurst de Vries, S. A. Loyson, W. Helfrich, G. P. van Berge Henegouwen, M. van Meijer, J. de Kruif and T. Logtenberg, *Nat. Biotechnol.*, 1999, **17**, 276-281.
32. J. Yang, A. Eresen, J. Shangguan, Q. Ma, Z. Zhang and V. Yaghmai, *Am. J. Cancer Res.*, 2020, **10**, 3911-3919.
33. X. Huang, G. Zhang, T. Tang and T. Liang, *Mol. Cancer*, 2021, **20**, 44.
34. A. Paniccia, J. Merkow, B. H. Edil and Y. Zhu, *Chin. J. Cancer Res.*, 2015, **27**, 376-391.
35. E. Darrigues, Z. A. Nima, D. A. Nedosekin, F. Watanabe, K. M. Alghazali, V. P. Zharov and A. S. Biris, *Sci. Rep.*, 2020, **10**, 3362-3362.
36. W. Qiu, R. Chen, X. Chen, H. Zhang, L. Song, W. Cui, J. Zhang, D. Ye, Y. Zhang and Z. Wang, *Int. J. Nanomedicine*, 2018, **13**, 6809-6827.
37. L. Xing, X. Li, Z. Xing, F. Li, M. Shen, H. Wang, X. Shi and L. Du, *Chem. Eng. J.*, 2020, **382**, 122949-122949.

38. J. Pérez-Juste, I. Pastoriza-Santos, L. M. Liz-Marzán and P. Mulvaney, *Coord. Chem. Rev.*, 2005, **249**, 1870-1901.
39. X. Hu, Y. Zhang, T. Ding, J. Liu and H. Zhao, *Front. Bioeng. Biotechnol.*, 2020, **8**, 990-990.
40. R. Foulkes, M. Ali Asgari, A. Curtis and C. Hoskins, *ACS Appl. Nano Mater.*, 2019, **2**, 1758-1772.
41. M. Azharuddin, G. H. Zhu, D. Das, E. Ozgur, L. Uzun, A. P. F. Turner and H. K. Patra, *Chem. Commun.*, 2019, **55**, 6964-6996.
42. S. B. Yaqoob, R. Adnan, R. M. Rameez Khan and M. Rashid, *Front. Chem.*, 2020, **8**, 376-376.
43. A. Ali, H. Zafar, M. Zia, I. Ul Haq, A. R. Phull, J. S. Ali and A. Hussain, *Nanotechnol Sci Appl*, 2016, **9**, 49-67.
44. J. G. Croissant, K. S. Butler, J. I. Zink and C. J. Brinker, *Nat. Rev. Mater.*, 2020, **5**, 886-909.
45. C. Testa, A. Zammataro, A. Pappalardo and G. Trusso Sfrazzetto, *RSC Adv.*, 2019, **9**, 27659-27664.
46. A. Zielińska, F. Carreiró, A. M. Oliveira, A. Neves, B. Pires, D. N. Venkatesh, A. Durazzo, M. Lucarini, P. Eder, A. M. Silva, A. Santini and E. B. Souto, *Molecules*, 2020, **25**.
47. H.-m. Ding and Y.-q. Ma, *Nanoscale Horiz.*, 2018, **3**, 6-27.
48. M. Sivasubramanian, Y. C. Chuang and L.-W. Lo, *Molecules*, 2019, **24**, 520-520.
49. M. Bouché, J. C. Hsu, Y. C. Dong, J. Kim, K. Taing and D. P. Cormode, *Bioconjug. Chem.*, 2020, **31**, 303-314.
50. P. Singh, S. Pandit, V. R. S. S. Mokkapati, A. Garg, V. Ravikumar and I. Mijakovic, *Int. J. Mol. Sci.*, 2018, **19**, 1979.
51. A. N. Dosumu, S. Claire, L. S. Watson, P. M. Girio, S. A. M. Osborne, Z. Pikramenou and N. J. Hodges, *JACS Au*, 2021, **1**, 174-186.
52. C. J. Murphy and J. M. Buriak, *Chem. Mater.*, 2015, **27**, 4911-4913.
53. M. M. Modena, B. Rühle, T. P. Burg and S. Wuttke, *Adv. Mater.*, 2019, **31**, 1901556.
54. C. Contado, D. Mehn, D. Gilliland and L. Calzolai, *J. Chromatogr. A*, 2019, **1606**, 460383-460383.
55. B. Zhang and B. Yan, *Anal. Bioanal. Chem.*, 2010, **396**, 973-982.
56. M. Yüce and H. Kurt, *RSC Adv.*, 2017, **7**, 49386-49403.
57. A. Demchenko, V. Tomin and P.-T. Chou, *Chem. Rev.*, 2017, **117**.
58. J. C. del Valle and J. Catalán, *Phys. Chem. Chem. Phys.*, 2019, **21**, 10061-10069.
59. Compiled by A. D. McNaught and A. Wilkinson, *IUPAC, Compendium of Chemical Terminology, 2nd ed. (the "Gold Book")*, Blackwell Scientific Publications, 1997.
60. Horiba, What are Luminescence Quantum Yields?, https://www.horiba.com/int/technology/spectroscopy/fluorescence-spectroscopy/what-are-luminescence-quantum-yields/, (accessed March 22, 2022).

Chapter 2

2. Synthesis and characterisation of luminescent iridium(III) complexes and their AuNP conjugates

2.1 Introduction

This introduction will outline various iridium(III) complexes that have been studied before and the different applications for them. The luminescent properties of iridium(III) complexes will also be discussed.

2.1.1 Iridium(III) cyclometalated complexes

Iridium(III) complexes attached to the surface of AuNPs for imaging have been studied previously with different carbon chain lengths.[1-3] Attachment of metal complexes to AuNPs has also been performed with ruthenium.[4, 5] Engineering of the iridium(III) complexes can be done by choosing suitable cyclometalated ligands (Figure 2.1, Figure 2.3) to modify excitation and emission wavelengths. The type of auxiliary ligand can also affect the luminescent properties. Cyclometalated ligands used for Ir(III) complex synthesis are typically aromatic, heterocyclic molecules with a carbon and a nitrogen available for interaction with the metal centre. The carbon donates two electrons to form a carbon-metal bond with the iridium centre. So cyclometalated ligands can also be refered to as C^N ligands on their own or N^C^- ligand when on the complex. Auxiliary ligands will not donate any electrons into the Ir(III) centre, but remain neutrally charged and can be referred to as N^N. A bis-cyclometalated complex (having two cyclometalated ligands) will result in an overall positive Ir(III) complex charge.

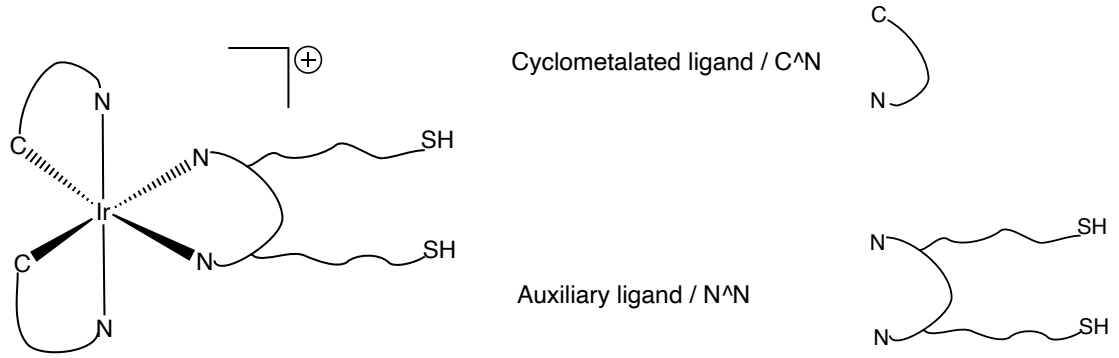


Figure 2.1. A schematic of a cyclometalated Ir(III) complex, with the C^N cyclometalated ligands forming carbon-metal bonds with the Ir(III) centre, and with the N^N auxiliary ligand containing thiol groups for attachment of the Ir(III) complex to gold nanoparticles. Black lines represent the rest of the ligand molecule. Some examples of cyclometalated ligands are shown in Figure 2.3.

The advantages of using iridium(III) to make complexes rather than other metals such as ruthenium(II) for example, is that the splitting energy of the d-orbitals (Δ_o) is larger in iridium(III) compared to ruthenium(II), due to iridium(III) being in period 6 and ruthenium(II) being in period 5 in the periodic table. Therefore, to raise the energy of the unoccupied e_g orbitals in ruthenium(II), strong field ligands are required, as these increase Δ_o. This ensures that the e_g orbital will be at a higher energy than the MLCT excited state, preventing non-radiative decay/quenching from metal-centred transitions. Due to this, ruthenium(II) complex synthesis is more limited compared to Ir(III) complex synthesis, as a smaller selection of ligands can be used in order to make a compound that will provide sufficient luminescence for the uses that they are designed for.

Iridium(III) complexes with sulphur containing groups are necessary for attachment to gold so that the complexes will not become detached. Thiol-metal bonds are strong[6, 7] so that makes gold nanoparticles and iridium(III) complexes with thiol groups a good combination for stable nanoconjugates. Evidence has shown that Au-S bonds can form due to chemisorption or physisorption and that in SAMs (self-assembled monolayers) physisorption occurs, where the hydrogen in the thiol functional group is

retained[8]. The strength of the Au-S bond depends on which attachment method is present at the surface. Distinguishing the type of Au-S bond at gold surfaces has not been studied to the point of being able to characterise whether physisorption of chemisorption is occurring, however the traditionally accepted method has been chemisorption[8].

There are a vast number of literature reports of cyclometalated iridium(III) complexes being used for imaging as they have many advantages compared to traditional organic probes. In fact, most inorganic probes have been found to have better properties than their organic counterparts. These advantages include larger Stokes shifts, longer luminescence lifetimes due to spin forbidden luminescence and greater photostability[9]. These advantages are necessary because Stokes shift ensures better separation between excited light and emission light. Long luminescence lifetimes of complexes mean that they will continue to display luminescence even when the light source has been removed. Photostability is necessary for retaining the structure of the compound because degradation could lead to loss of emissive properties. There are many examples of iridium(III) probes with varying auxiliary and cyclometalated ligands, and the luminescence colour and lifetime can be tuned based on which ligands are used[10]. In addition, solubility can be tuned to make these iridium(III) complexes more suitable for use in biological applications. Excitation and emission wavelengths and luminescence lifetimes of iridium(III) complexes can vary greatly due to the choice of the auxiliary and cyclometalated ligands (Figure 2.1). Current uses for luminescent iridium(III) complexes include as chemo-sensors, in biolabeling, tumour imaging, cell staining and for photoluminescence lifetime imaging (PLIM).[11-13] Two-photon imaging expands on the traditional luminescence imaging by combining the energy of two light sources of the same wavelength (NIR region) to excite a complex. The NIR light provides better tissue penetration than UV or visible light and is less destructive to tissues. It is hoped that complexes such as used in this project will promote this effect in future studies due to absorbing in the visible light region of the electromagnetic spectrum.

The excited state for cyclometalated Iridium(III) complexes is a mixture of triplet and singlet states, as indicated by DFT (Density Functional Theory)[14, 15], hence recombination from the excited state has a

timescale that is within the range of both fluorescence and phosphorescence (Figure 2.2), depending on solvent, ligands used for the iridium(III) complex and other factors. Therefore, recombination from the excited state should be referred to as luminescence when discussing iridium(III) cyclometalated complexes. As seen in the Jablonski diagram in Figure 2.2, ligand-centred ^{1}LC ($\pi \rightarrow \pi^*$) (auxiliary ligand (N^N) or cyclometalated ligand (N^C$^-$)) transitions are spin allowed intra-ligand transitions that occur within the same ligand. Ligand-to-ligand ^{1}LLCT ($\pi \rightarrow \pi^*$) (N^N or N^C$^-$) transitions are also spin allowed and occur between ligands. Metal-to-ligand ^{1}MLCT ($d\pi(Ir) \rightarrow \pi^*$(N^N and N^C$^-$)) transitions occur from the d orbital of the iridium(III) to the ligand on the iridium(III) complex. Metal-to-ligand ^{3}MLCT ($d\pi(Ir) \rightarrow \pi^*$(N^N and N^C$^-$)) transitions are spin forbidden. Transitions that occur without change in the number of unpaired electrons are allowed because the spin multiplicity does not change. Forbidden transitions have a low intensity because they involve a change in the number of unpaired electrons.

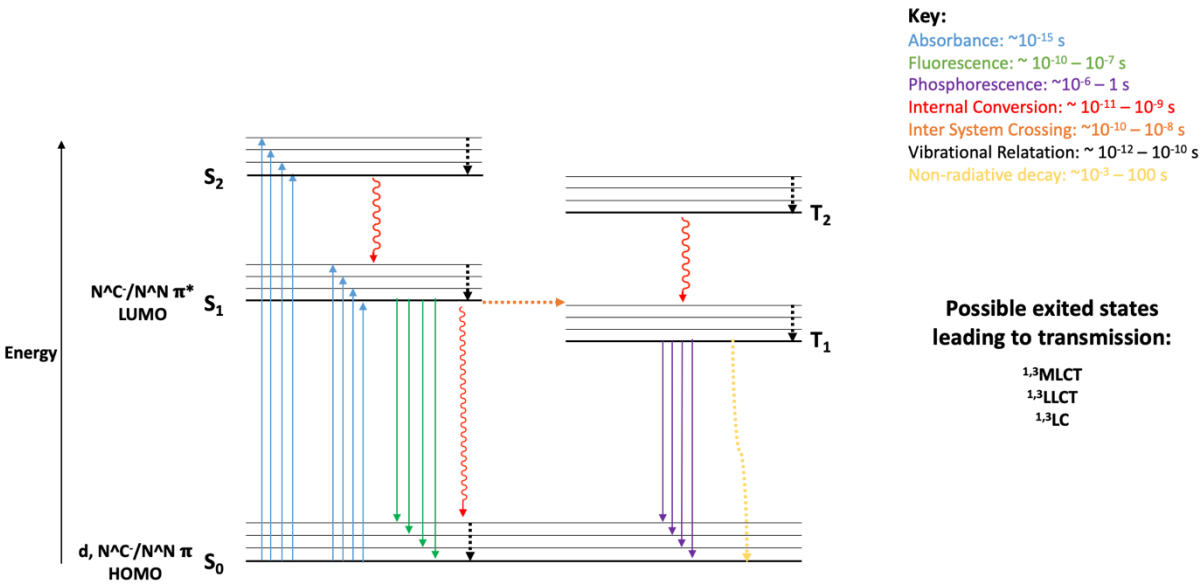


Figure 2.2. Jablonski diagram of transitions in iridium(III) cyclometalated complexes, along with a key showing the typical timescales of transitions.

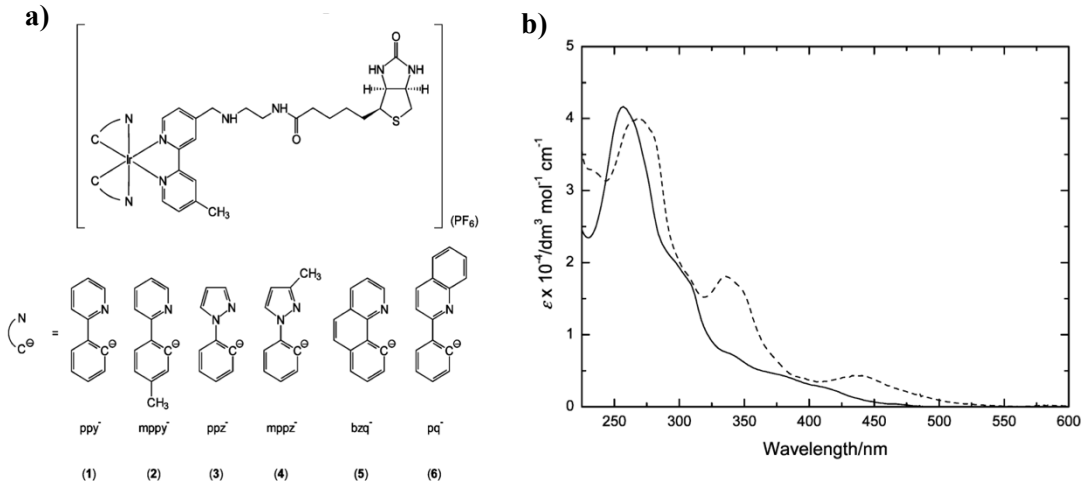


*Figure 2.3. Figure showing the ligands for the formation of cyclometalated iridium(III) complexes with a biotin moiety (**a**), where **1** = 2-phenylpyridine, **2** = 2-(4-methylphenyl)pyridine, **3** = 1-phenylpyrazole, **4** = 3-methyl-1-phenylpyrazole, **5** = 7,8-benzoquinoline and **6** = 2-phenylquinoline. The difference in absorption spectra for 2-phenylpyridine complex (–) and 2-phenylquinoline complex (---). Images were obtained from **K. K.-W. Lo, J. S.-W. Chan, L.-H. Lui and C.-K. Chung, Organometallics, 2004, 23, 3108-3116.***

Some of the cyclometalated ligands used for iridium(III) complex synthesis are 2-phenylpyridine, 2-(4-methylphenyl)pyridine, 1-phenylpyrazole, 3-methyl-1-phenylpyrazole, 7,8-benzoquinoline, 2-phenylquinoline (Figure 2.3a)[16]. 2-phenylpyridine is one of the most common cyclometalated ligands used for iridium(III) complexes, however complexes with this ligand have absorbance bands < 400 nm. To shift the wavelength of the absorbance band to the visible region (> 400 nm), another ligand such as 2-phenylquinoline must be used, to give an MLCT excitation band of > 400 nm (Figure 2.3b). 2-phenylquinoline complexes display intense absorption bands between around 235 – 310 nm, which correspond to spin-allowed ^{1}LLCT transitions. At around 310 – 400 nm, less intense bands corresponding to spin-allowed ^{1}MLCT transitions appear. Because of the extended conjugation of 2-phenylquinoline compared to 2-phenylpyridine, further ^{1}LLCT ($\pi \rightarrow \pi^*$) (N^C$^-$) and ^{1}MLCT transitions also exist at ~350 nm and 400 – 450 nm respectively. Extended conjugation of the N^C$^-$ ligands also show peaks at >400 nm[17], showing that extended conjugation of iridium(III) complex ligands may be a path to tuning the absorbance towards the visible. Absorption tails from 450 – 550 nm correspond to

spin-forbidden ^{3}MLCT and mixed ^{1,3}MCLT and ^{1,3}LLCT transitions[17]. When comparing different complexes with the same cyclometalated ligand and differing auxiliary ligands, interactions with the iridium(III) and the auxiliary ligand can be seen if there is a difference between the absorption bands, whereas if no difference is seen, this shows that the auxiliary ligand is not interacting with the iridium(III).

Iridium(III) cyclometalated complexes show intense orange to greenish-yellow luminescence in solution making them good complexes for imaging agents in different components of cells (Figure 2.4). There are a range of iridium(III) complexes for different application and for targeting various sub-cellular organelles.[12] Nucleolus staining[18] and nuclear staining was performed with a cationic complexes (Figure 2.4a, b)[19] that selectively lit up the nucleus of living cells. No neutral complexes have been developed. Staining of the cytoplasm was achieved with various complexes (Figure 2.4c, d)[12] and was used for the first time in 2008 with iridium(III) complexes[20]. Mitochondria staining was observed with iridium(III) complexes containing 2-phenylquinoline cyclometalated ligands and one phenanthroline auxiliary ligand[11, 21], which bound to biomolecules such as lysine and the N-terminal of proteins in mitochondria. Lysosomal and endosomal staining was performed with iridium(III) complexes that could withstand degradation, had low toxicity and long term localisation[12] (Figure 2.4e, f)[22]. This is because of the acidic environment of lysosomes. Hence the complexes had basic components to combat the acidity of the lysosomes. The Endoplasmic reticulum was targeted by iridium(III) complexes and imaged with one-and two-photon irradiation (Figure 2.4g, h)[23] for photodynamic therapy. Dendritic iridium(III) complexes have been shown to target the Golgi apparatus (Figure 2.4i, j).[24] Iridium(III) complexes for PLIM (Photoluminescence Lifetime Imaging) have also been developed[25, 26], due to utilisation of the longer lifetimes of iridium(III) complexes compared to background cell autofluorescence, which provides an alternative approach to traditional luminescence imaging. PDT (Photodynamic therapy) is an important function of iridium(III) complexes.[27] In PDT, ROS (Reactive Oxygen Species) are generated in cells due to the influence of a particular material upon irradiation with light. ROS are singlet oxygen radicals that can cause DNA damage to cells upon generation. Although all cells have some level of ROS[28], a high level of ROS can lead to apoptosis.

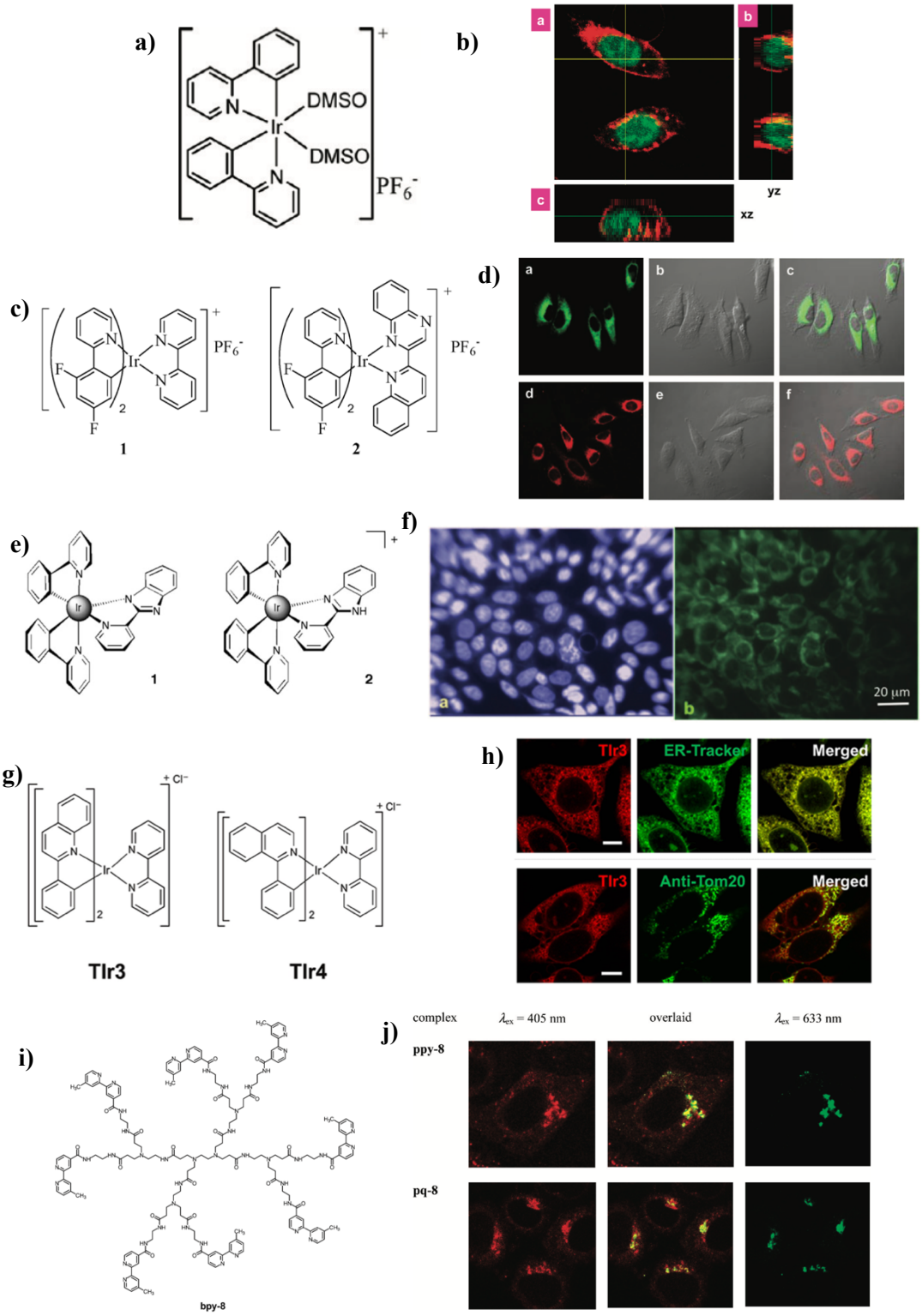


Figure 2.4. Iridium(III) complexes for imaging in cells for the nucleus ***(a, b)****, cytoplasm* ***(c, d)****, lysosomes* ***(e, f)****, Endoplasmic Reticulum* ***(g, h)*** *and Golgi apparatus* ***(i, j)****. Images obtained in order:* ***C. Li et al., Journal of the American Chemical Society, 2011, 133, 11231-11239; C. Caporale et al., Coordination Chemistry Reviews, 2018, 363, 71-91; L. Murphy et al., Chemical Communications, 2010, 46, 8743-8745; J. S. Nam et al., Journal of the American Chemical Society, 2016, 138, 10968-10977; K. Y. Zhang et al., Inorganic Chemistry, 2010, 49, 5432-5443.***

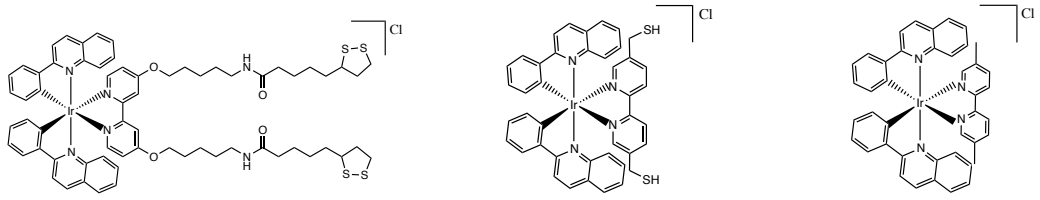
Zhang *et al*.[29] reported organoiridium photosensitizers that generated ROS within cancer cells and one was the first cyclometalated nucleus-targeting photosensitizer to be synthesized.[30] They performed this study in 2D and 3D models with one- and two-photon irradiation. PACT (Photoactivated Chemotherapy) of iridium(III) complexes despite their high photostability has also been explored[31] with Lo et al. reporting the only known example of an iridium(III) PACT compound[32]. Hypoxia monitoring is a method that can indicate possible tumours due to rapid proliferation causing high O_2 consumption in cancer cells. Iridium(III) complex cored polymer dots were synthesised for hypoxia imaging due to the sensitivity of the iridium(III) complex to oxygen.[33] In addition to detection of low O_2 levels by iridium(III) complexes, other molecules can also be detected, such as nuclear histidine[34] and human carboxylesterase 2.[13] Transition metal complexes have also been developed as aptamer-based optical diagnostic tools for certain proteins[35]. Iridium(III) complexes as photocytotoxic agents[36] and sandwich complexes of iridium(III) have been synthesised[37]. Iridium(III) complexes that show AIE (Aggregation Induced Emission) in different solvents[38], where the crystallization induces emission of the complex could be a way of detecting different environments.

2.1.2 Chapter summary

In this chapter, the synthesis of three cyclometalated iridium(III) complexes, **IrpqSS**, **IrpqSH** and **Irpqbpy** will be discussed, as well as the luminescent properties and the conjugation onto 15 nm AuNPs for subsequent imaging. This chapter will show that monodisperse AuNPs coated with luminescent iridium(III) cyclometalated complexes can be made and characterised to be suitable for imaging in cells.

2.2 Synthesis of IrpqSS, IrpqSH and Irpqbpy cyclometalated iridium(III) complexes for the coating of colloidal gold nanoparticles

The purpose of choosing these three iridium(III) complexes (Figure 2.5, Figure 2.6, Supplementary Figure 2.4, Supplementary Figure 2.5, Supplementary Figure 2.7, Supplementary Figure 2.8) was firstly, to compare the differences in the long- and short-chain auxiliary ligands of **IrpqSS** and **IrpqSH**, regarding their luminescent properties, their conjugation to AuNP surfaces, the effect of quenching by AuNPs and their interaction and uptake in cells. Secondly, it was to investigate the differences between 2-phenylquinoline cyclometalated complexes and 2-phenylpyridine cyclometalated complexes. 2-phenylquinoline cyclometalated complexes have been shown to absorb light in the visible region (Section 2.1.1), which has advantages in imaging for medical application, as this causes less damage to the DNA of cells upon excitation, compared to complexes that excite primarily in the UV region. A similar complex to **IrpqSS**, with 2-phenylpyridine cyclometalated ligands, and an identical auxiliary ligand **(7)** (Scheme 2.1, Figure 2.7) has been studied previously[3,2] , so this presents opportunity for comparison. Thirdly, the purpose for the **Irpqbpy** complex was to show that the Au-S bond is the covalent interaction by which the Ir(III) complexes bind to the AuNP surfaces. This complex is also used as a lone fluorophore for imaging in cell lines as complexes with thiol groups may interact with proteins and interfere with uptake. **IrpqSS** was a novel complex, reported here for the first time. The ligands for **IrpqSS** and **IrpqSH** were synthesised using published protocols and the final complexes were characterised by 1D NMR (Figure 2.6), 2D NMR, MS, UV-vis and IR (Sections 2.10 and 2.27).



IrpqSS **IrpqSH** **Irpqbpy**

*Figure 2.5. Structural images of **IrpqSS**, **IrpqSH** and **Irpqbpy** complexes with chloride counter ions.*

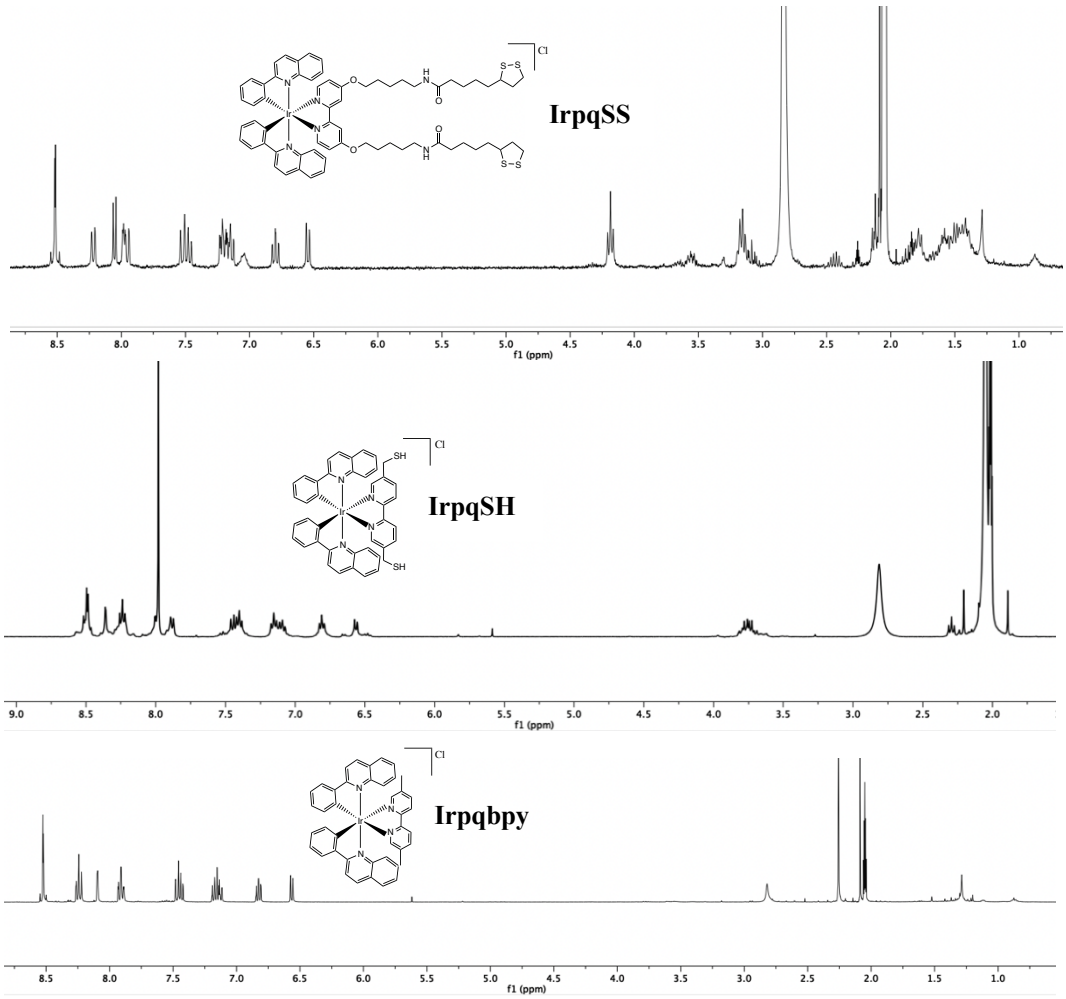
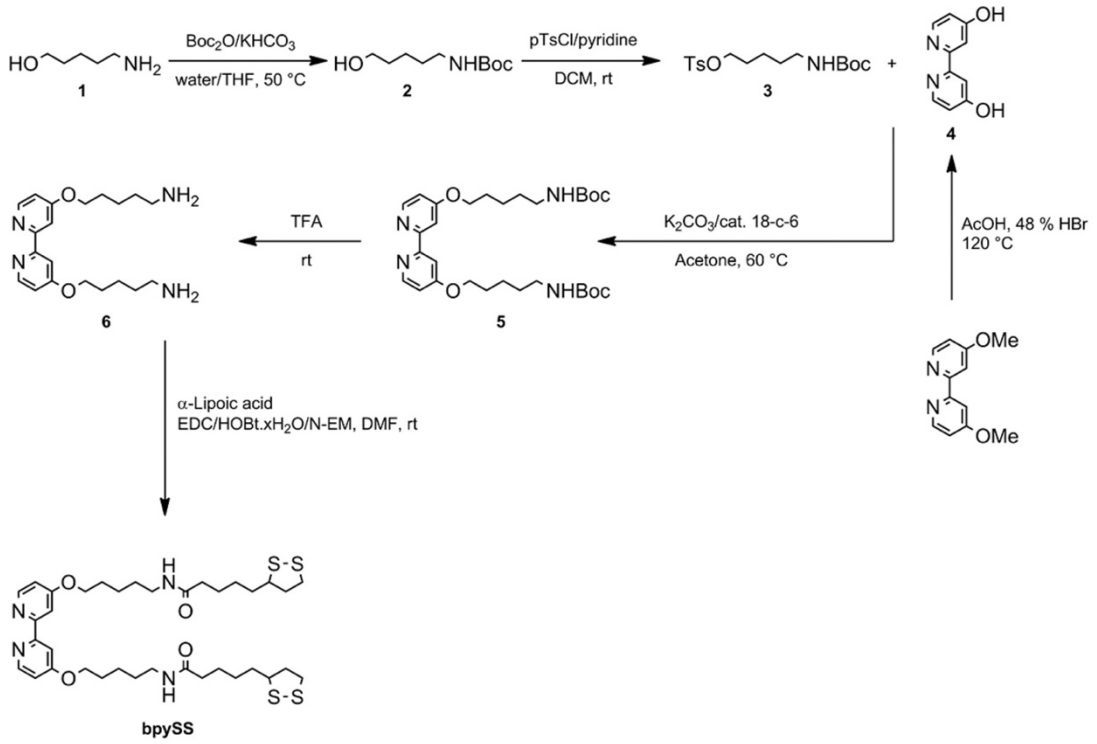


*Figure 2.6. Structures and ^{1}H NMR spectra of **IrpqSS**, **IrpqSH** and **Irpqbpy**, synthesized from a cyclometalated 2-phenylquinoline iridium(III) chloro-bridged dimer (400MHz, Acetone-d_6, 298K).*

A six-step synthesis was used to produce the ligand **(7)** (Scheme 2.1, Figure 2.7, Supplementary Figure 2.1, Supplementary Figure 2.2, Supplementary Figure 2.3) for the complex **IrpqSS**. When comparing ligand intermediates **(2)** and **(3)**, the ppm chemical shift for H-8 should move downfield, due to the electron withdrawing nature of the tosylate leaving group in **(3)**. As expected, the H-8 peak of **(2)** was found at 3.63 ppm, whereas the H-8 peak of **(3)** was found at 4.02 ppm. H-7 of ligand intermediate **(5)** had a chemical shift at 4.12 ppm. This means that the proton was more de-shielded than H-8 of ligand intermediate **(3)** due to the conjugated pyridine rings that allow delocalization into the pi system, and H-7 of ***(5)*** was more deshielded than **(3)**. The shifts for H-11 between **(5)** and **(6)** were 3.04 – 3.25ppm

and 2.53 – 2.77 ppm respectively. This is because the lone electron pair on the nitrogen in ligand **(5)** can be delocalized onto the carbonyl group, leaving H-11 more deshielded on **(5)** compared to **(6)**. Lastly, for **(7)**, the H-11 peak is 3.29 ppm, more de-shielded than H-11 of **(6)** because of the delocalization of the nitrogen lone pair onto the carbonyl group.



*Scheme 2.1. An outline showing the six-step formation of ligand **(7)** as previously studied before. Scheme obtained from **S. J. Adams et al.,** ACS Appl. Mater. Interfaces, **2014, 6, 11598-11608**.*

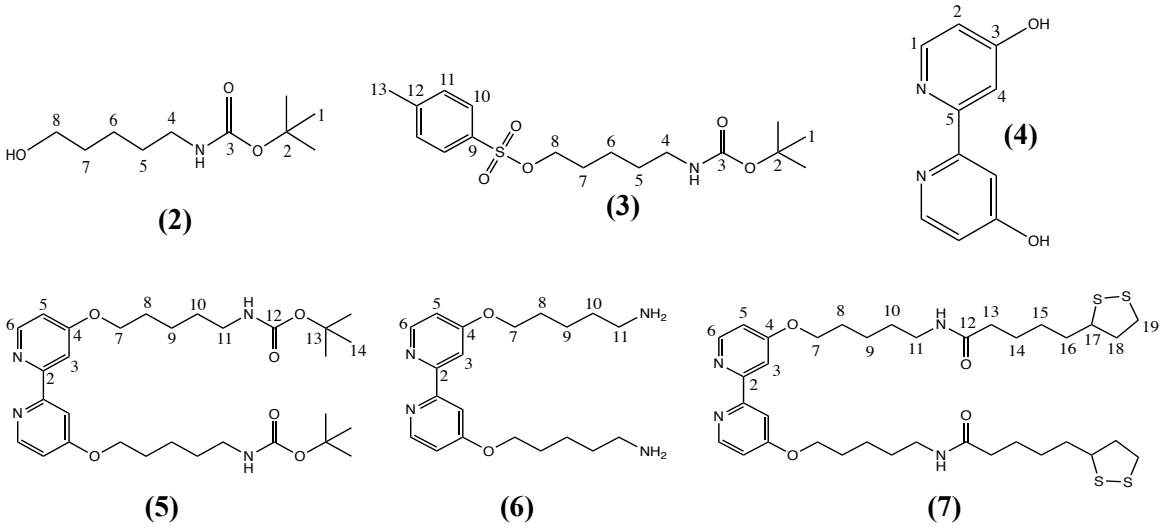
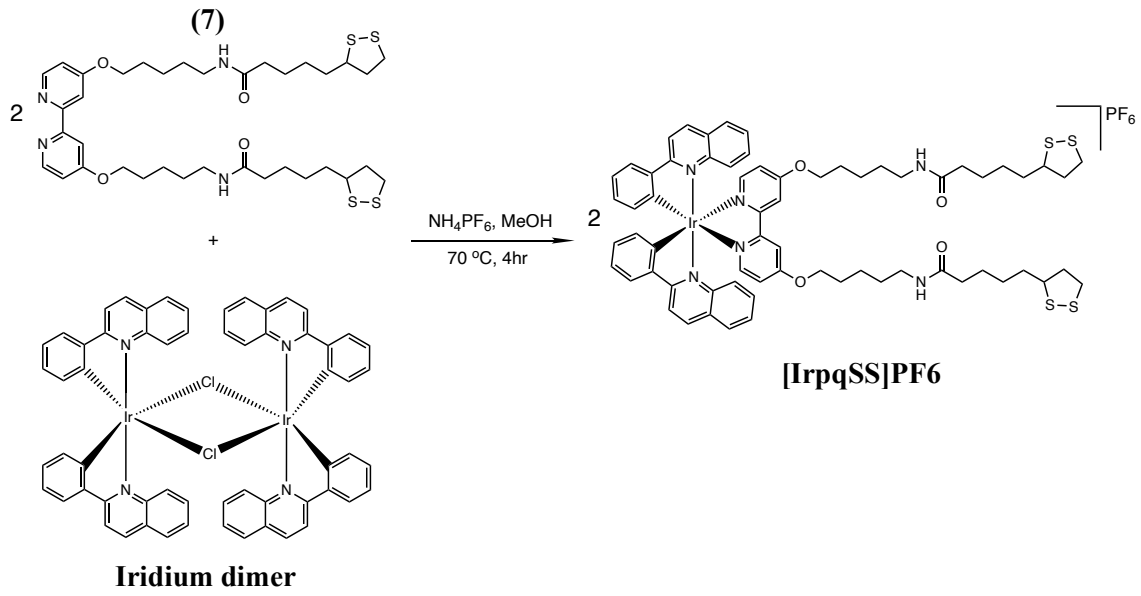
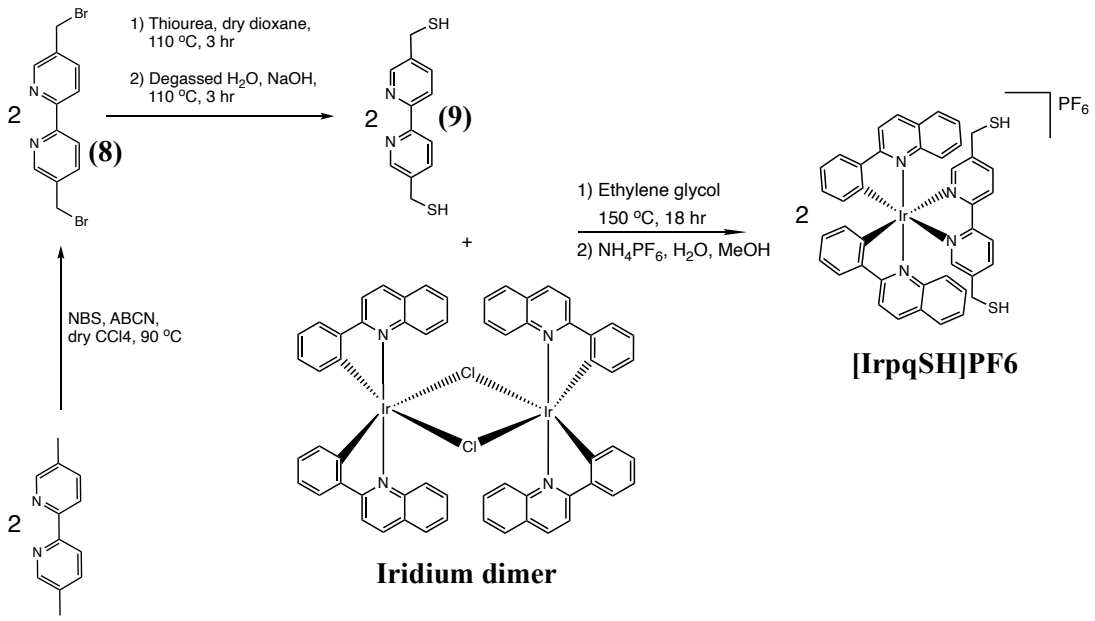


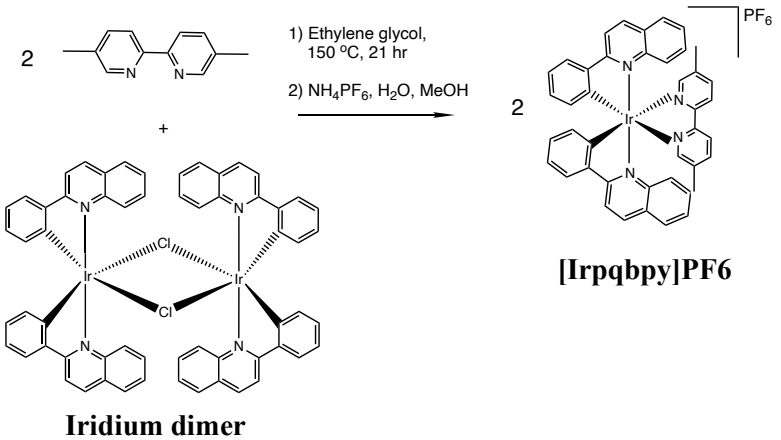
*Figure 2.7. Intermediate products for the synthesis of bpySS auxiliary ligand **(7)**. Labelled with numbers for the analysis of NMR chemical shifts.*

In the synthesis route for the **IrpqSH** ligands, it was found that monitoring the complete conversion of the di-methyl **(8)** starting material to the bis-bromo **(9)** intermediate (Scheme 2.2, Supplementary Figure 2.6) by monitoring with TLC and keeping a high reflux temperature of >85 ºC (Section 2.10) was important to eliminate the starting material. Although the boiling point of the reaction solvent CCl_4 is 77 ºC, a significant difference was observed in the rate of conversion of **(8)** to **(9)** when temperatures higher than 85 ºC were used. It is reported[39] that purification by column chromatography has been successful in the past, however **(8)** and **(9)** have very similar retention factors in a variety of different solvents mixtures, and separation even using flash chromatography was unsuccessful. However, a method that was successful in isolating the bis-bromo intermediate was recrystallisation. It is also reported[39] that a reaction time of 22 minutes was possible for conversion, which was found to be too short. This short timescale was to prevent over-bromination, however any over-brominated side products were successfully eliminated in the recrystallisation process, even when reaction times exceeded 2 hrs. The level of dryness for the solvent may have contributed to a longer reaction timescale needed for complete conversion.

The percentage yields for the final PF_6^- complexes (Scheme 2.2) were 48%, 23% and 32% for **[IrpqSS]PF6**, **[IrpqSH]PF6** and **[Irpqbpy]PF6** respectively. However, the chloride forms of these complexes were required because Cl^- is ubiquitous in biological systems and therefore is more compatible with biological studies. Infrared spectroscopy of the complexes before and after the Dowex PF_6^- to Cl^- ion exchange proved the success of the ion exchange as the infrared spectra show a disappearance of the P-F bond stretches (asymmetric and symmetric)[40], which appear between 820-850 cm^{-1} and 550-570cm^{-1} (Supplementary Figure 2.18). Dowex is a resin, used for the exchange of ions of a charge with different ions with the same charge. In **[IrpqSS]PF6**, the P-F peaks were found at 850 cm^{-1} (asymmetric) and 568 cm^{-1} (symmetric); in **[IrpqSH]PF6** these are found at 828 cm^{-1} (asymmetric) and 559 cm^{-1} (symmetric); in **[Irpqbpy]PF6** these were at 829 cm^{-1} (asymmetric) and 556 cm^{-1} (symmetric). The post dowex exchange Cl^- complexes will be referred to as **IrpqSS**, **IrpqSH** and **Irpqbpy** moving forward (Figure 2.5, Figure 2.6).







*Scheme 2.2. An outline of the reaction schemes to form **[IrpqSS]PF6** (top), **[IrpqSH]PF6** (middle) and **[Irpqbpy]PF6** (bottom).*

2.3 Photophysical properties of IrpqSS, IrpqSH and Irpqbpy cyclometalated iridium(III) complexes

IrpqSS displayed three absorbance peaks in the UV-vis spectrum in MeOH (Figure 2.8a) and H_2O (Figure 2.8b): λ_{max} (MeOH) / nm (ε / $dm^3mol^{-1}cm^{-1}$), 260 (36100), 335 (15600), and 440 (3200); λ_{max} (H_2O) / nm (ε / $dm^3mol^{-1}cm^{-1}$), 260 (27000), 335 (11600), and 440 (2300). The peak at 260 nm corresponds to the ^{1}LLCT band, 335 nm corresponds to the ^{1}MLCT band, and the 440 nm peak corresponds to mixed ^{1,3}MCLT and ^{1,3}LLCT transitions (Section 2.1.1). **IrpqSH** with chloride counter ions displays four absorbance peaks in the UV-vis absorbance spectrum in MeOH (Figure 2.8a) and H_2O (Figure 2.8b): λ_{max} (MeOH) / nm (ε / $dm^3mol^{-1}cm^{-1}$), 259 (16200), 280 (15900), 321 (10000), and 435 (1600); λ_{max} (H_2O) / nm (ε / $dm^3mol^{-1}cm^{-1}$), 257 (13300), 279 (13000), 317 (8000), and 430 (1300). The peaks at around 260 nm and around 280 nm correspond to the ^{1}LLCT band, the peak at around 320 nm corresponds to the ^{1}MLCT band and the peak at around 430 nm corresponds to mixed ^{1,3}MCLT and ^{1,3}LLCT transitions (Section 2.1.1). The difference in ^{1}MLCT band for **IrpqSH** compared to **IrpqSS** shows that the auxiliary ligands of the complexes participate in the ^{1}MLCT transitions, not 2-phenylquinoline only. **Irpqbpy** with chloride counter ions displays five absorbance peaks in the UV-vis absorbance spectrum of MeOH (Figure 2.8a) and H_2O (Figure 2.8b): λ_{max} (MeOH) / nm (ε / $dm^3mol^{-1}cm^{-1}$) 260 (32700), 280 (31100), 313 (16700), 334 (14200) and 438 (3100); λ_{max} (H_2O) / nm (ε / $dm^3mol^{-1}cm^{-1}$) 260 (31600), 280 (27900), 313 (15900), 334 (13200) and 438 (3000). The peak at 260 nm corresponds to the ^{1}LLCT band, the peak at around 313 nm and 334 nm correspond to the ^{1}MLCT bands and the peak at 438 nm corresponds to mixed ^{1,3}MCLT and ^{1,3}LLCT transitions (Section 2.1.1). The difference in ^{1}MLCT bands between the three complexes further confirm that the auxiliary ligands participate in the ^{1}MLCT transitions. The excitation spectra in the MeOH and H_2O for **IrpqSS**, **IrpqSH** and **Irpqbpy** follow the same patterns as the UV-vis absorbance spectra (Figure 2.9a, Supplementary Figure 2.28), showing that majority of the electrons excited by the absorbed light lead to emission and instead of non-emissive transitions.

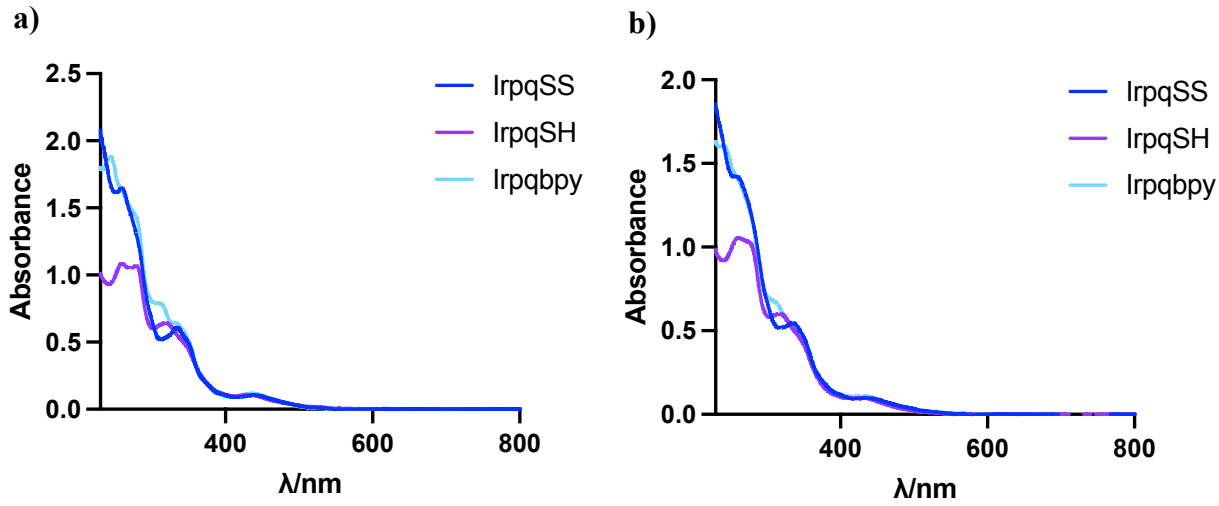


*Figure 2.8. UV-vis absorbance spectra for **IrpqSS, IrpqSH** and **Irpqbpy** in **a)** MeOH and **b)** H_2O at the concentrations used for quantum yield measurements, where the absorbance value for the MLCT band at 440nm was set to 0.1. This was equivalent to 31 μM, 63 μM and 32 μM in MeOH and 43 μM, 77 μM and 33 μM in H_2O for **IrpqSS, IrpqSH** and **Irpqbpy** respectively. The percentages of MeOH in the H_2O solutions were 4%, 8% and 3% for **IrpqSS, IrpqSH** and **Irpqbpy** respectively.*

Extinction coefficients were calculated from the Beer-Lambert law, because each solution was a known concentration (a stock solution of 1 mM iridium(III) complex with chloride counter ion in MeOH/H_2O was used to make solutions of different concentrations) from 10 μL additions (9.9 μM) to 50 μL additions (47.6 μM) (Supplementary Figure 2.19, Supplementary Figure 2.20, Supplementary Figure 2.21, Supplementary Figure 2.22). The extinction coefficients for **IrpqSS** and **Irpqbpy** are very similar, however the extinction coefficients for **IrpqSH** are approximately half that of the other two. For example, at λ_{abs} = 260 nm in MeOH, the extinction coefficient values were at around 30000 ε / $dm^3mol^{-1}cm^{-1}$ for **IrpqSS** and **Irpqbpy**, and at around 16000 ε / $dm^3mol^{-1}cm^{-1}$ for **IrpqSH**. This occurs in both MeOH (Figure 2.8a) and H_2O (Figure 2.8b), when the post-400nm peak at 440 nm was set to an absorbance value of 0.1 in order to the calculate the luminescent quantum yields (Table 2.2). The extinction coefficients for all three complexes agree with other cyclometalated iridium(III) complexes reported previously[41], and decreased in H_2O.

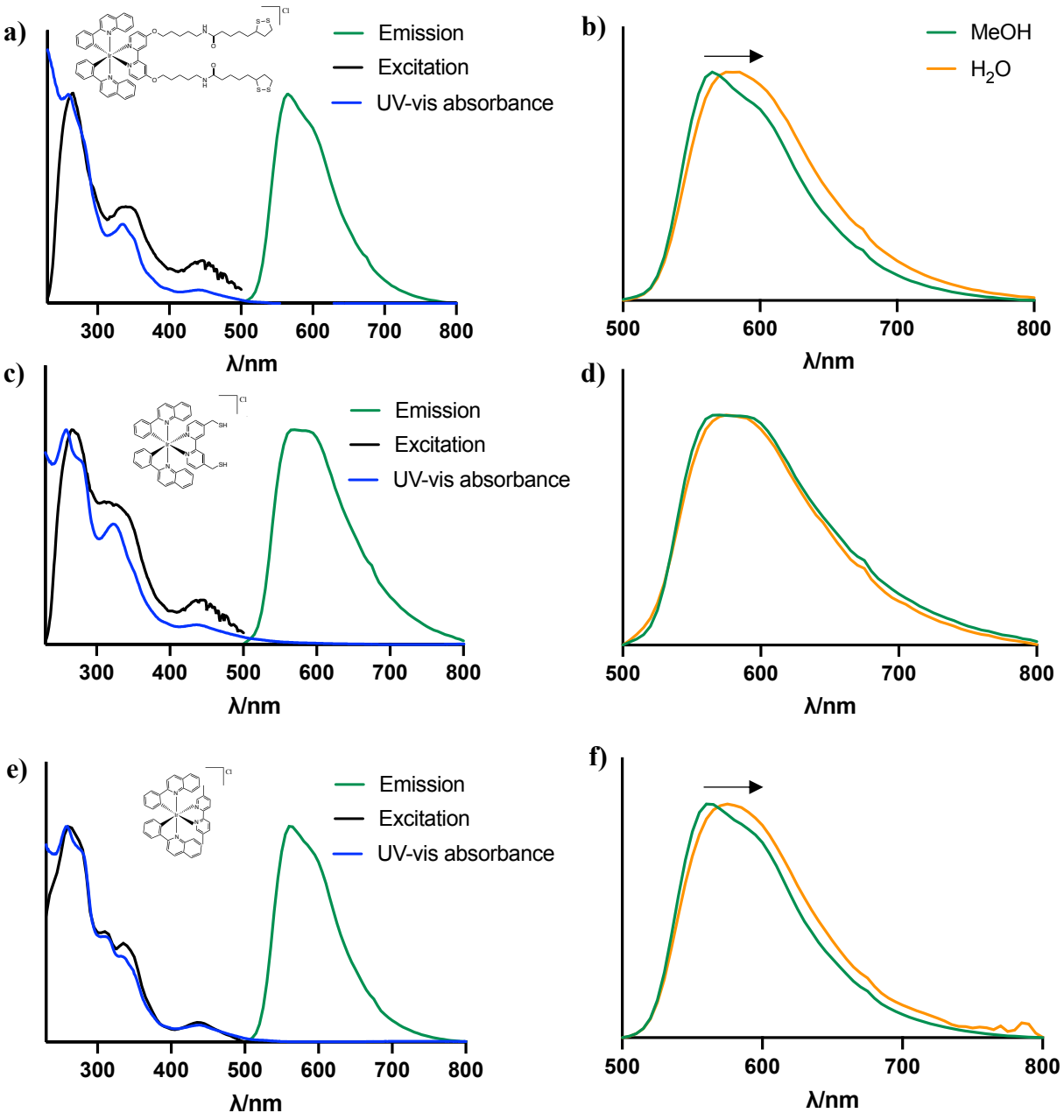


Figure 2.9. ***a), c), e)*** *UV-vis absorbance (blue), excitation (black) and emission (green) spectra of* ***IrpqSS***, ***IrpqSH*** *and* ***Irpqbpy*** *respectively in MeOH.* ***b), d), f)*** *Emission spectra in MeOH (green) and in H_2O (2% MeOH) (orange) of* ***IrpqSS***, ***IrpqSH*** *and* ***Irpqbpy*** *respectively. Concentrations of the solutions used for collection of spectra was 20 μM, obtained from dilution from a 1μM stock solution. Arrows in* ***b)*** *and* ***f)*** *show the bathochromic shift of the emission spectra between MeOH and H_2O for* ***IrpqSS*** *and* ***Irpqbpy***. *For the emission spectra, $\lambda_{ex} = 440nm$.*

Solvent effects are seen in the emission of these complexes. **IrpqSS** shows a bathochromic shift of 17 nm (Figure 2.9b) from 565 nm in MeOH to 582 nm in H_2O (2% MeOH). **IrpqSH** doesn't shift between the solvents (Figure 2.9d), but the peak remains at 578 nm. **Irpqbpy** shows a shift of 15 nm (Figure 2.9e) from 562 nm in MeOH to 577 nm in H_2O (2% MeOH). The shifts seen are caused by the increased polarity of H_2O, which stabilizes the LUMO of the complex.[42] More polar solvents such as H_2O form more hydrogen bonds than their less polar counterparts. Hence the energy level of the LUMO decreases, causing the final radiative recombination in H_2O to have a lower energy, corresponding to a longer wavelength of emission. **IrpqSH** does not show this shift, perhaps due to the thiol groups in the complex, which can form weak hydrogen bonds with other thiol groups and with the alcohol group in MeOH. Hence, the LUMO of the complex is already stabilised in MeOH and changing the solvent to H_2O does not have as much effect as on the other two complexes. This is shown by the fact that in MeOH, the **IrpqSH** emission peak is at 578nm, whereas that of **IrpqSS** and **Irpqbpy** are at 565 and 562 nm respectively.

Previously studied cyclometalated iridium(III) complexes (with 2-phenylquinoline and 2-phenylpyridine cyclometalated ligands) have shown that an increase in QY cause the luminescence lifetime to also increase.[16] However, for **IrpqSS**, **IrpqSH** and **Irpqbpy** (Figure 2.10a,c,e, Table 2.1, Table 2.2), the QY values decrease as the luminescence lifetime values increase. There is not a direct correlation between QY increase and lifetime increase because QY depends on the population of electrons promoted to the excited state and whether the relaxation is radiative or not, but decay of the excited state is a kinetic process and is the rate at which the electrons recombine from the excited state. There are many factors that can affect the percentage of radiative and non-radiative decay and the time that electrons spend in the excited state. These factors involve solvent polarity, rate of solvent relaxation, solvent viscosity, interaction with solvent molecules and inter-complex interactions, conformational changes, luminescent trap states, charge transfer and intersystem crossing rates among others.

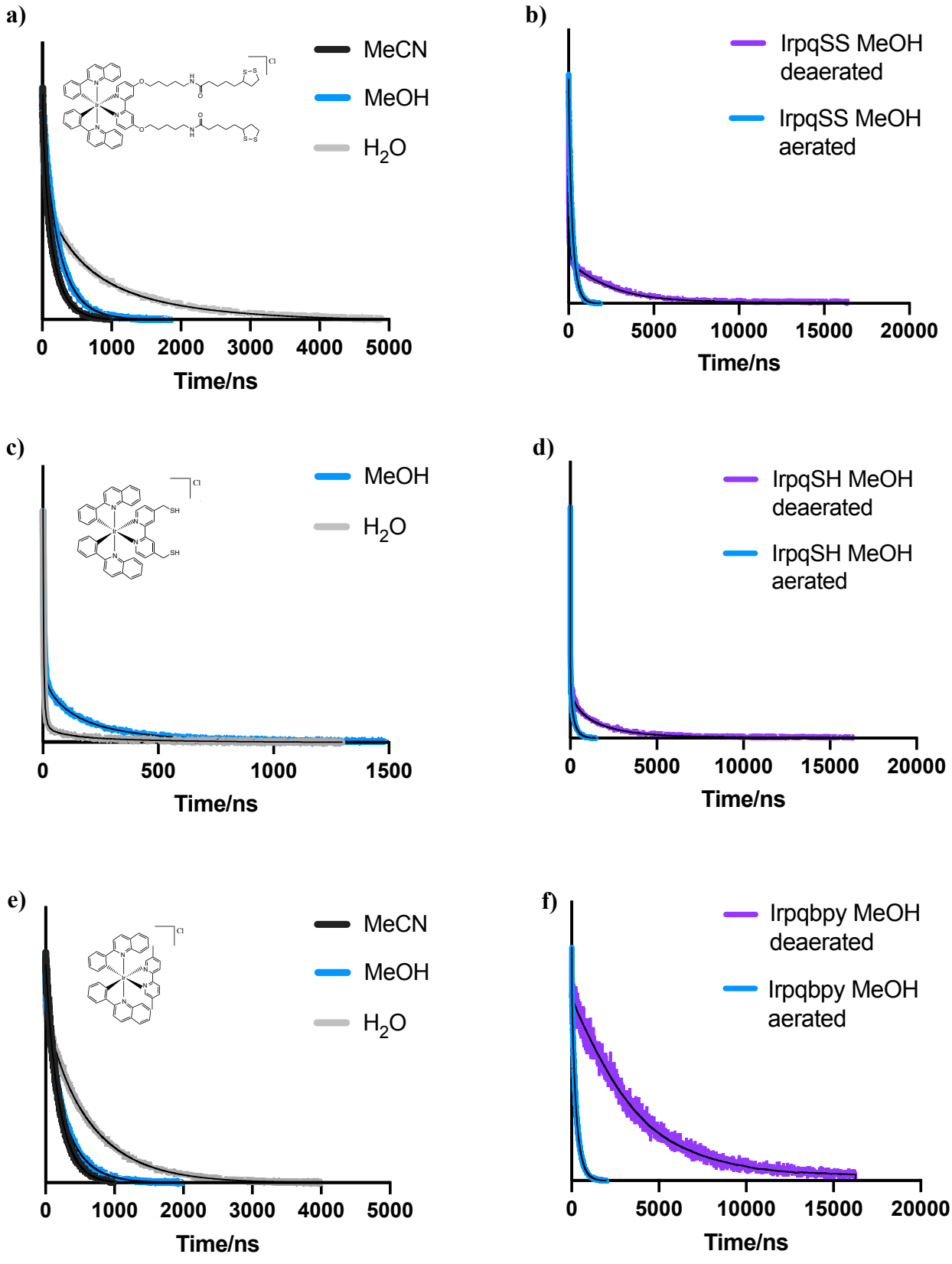


Figure 2.10. Luminescence lifetime decay curves with lifetime fitting at 20 μM of ***a) IrpqSS****,* ***c) IrpqSH*** *and* ***e) Irpqbpy*** *in MeCN, MeOH and H_2O (2% MeOH), and of* ***b) IrpqSS****,* ***d) IrpqSH*** *and* ***f) Irpqbpy*** *in deaerated and aerated MeOH. Laser excitation source was at 375 nm and collection wavelength of 570 nm, with a 475 nm filter. Decay curves for* ***a)****,* ***c)*** *and* ***e)*** *were fitted with χ^2 values of between 1 and 1.2. Decay curves for* ***b)****,* ***d)*** *and* ***f)*** *were fitted with χ^2 values of between 1 and 1.5. Final concentration was obtained from dilution of a 1μM stock solution.*

	IrpqSS						IrpqSH				Irpqbpy					
	MeCN		MeOH		H_2O		MeOH		H_2O		MeCN		MeOH		H_2O	
	%	τ / ns	%	τ / ns	%	τ / ns	%	τ / ns	%	τ / ns	%	τ / ns	%	τ / ns	%	τ / ns
Long component	78	**200**	79	**260**	49	**1410**	66	**280**	44	**420**	-	-	82	**300**	92	**680**

*Table 2.1. Luminescence lifetime values of **IrpqSS**, **IrpqSH** and **Irpqbpy** in MeCN, MeOH and H_2O (2% MeOH) at 20 μM, using a 375nm laser as an excitation source, a collection wavelength of 570nm and a 475 nm filter. Values for the long component are highlighted in **bold**.*

	Φ / %	
	MeOH	**H_2O**
IrpqSS	28	2
IrpqSH	3	0.5
Irpqbpy	22	12

*Table 2.2. Quantum yield values for **IrpqSS**, **IrpqSH** and **Irpqbpy**, collected using an integrating sphere, where the 440 nm MLCT band has an absorbance of 0.1 and the concentrations were 31 μM, 63 μM and 32 μM in MeOH and 43 μM, 77 μM and 33 μM in H_2O for **IrpqSS, IrpqSH** and **Irpqbpy** respectively. The percentages of MeOH in the H_2O solutions were 4%, 8% and 3% for **IrpqSS**, **IrpqSH** and **Irpqbpy** respectively.*

The luminescence lifetimes of the three iridium(III) complexes studied in this thesis follow an opposite trend from that of the quantum yields increasing in value with increasing polarity of the solvents. The luminescent quantum yield of a sample can be defined as the efficiency to emit radiative photons compared to the total number of photons absorbed, in other words, the ratio of emitted photons to absorbed photons. This can be shown as a relationship between the rate of radiative decay and the total decay rate (Equation 2.1). Therefore, in the unlikely event of a complex having 100% quantum yield, there would be a complete conversion of all absorbed photons into emitted photons, and the non-radiative and energy transfer processes would not contribute to the total decay rate. Experimentally obtained luminescence lifetime is defined as the inverse of the total decay rate (Equation 2.2). This includes radiative, non-radiative and energy transfer decay rates. Hence, a long luminescence lifetime may be long because the non-radiative decay is long, not necessarily because of the radiative decay rate. Radiative decay rate alone (and therefore radiative lifetimes) is difficult obtain experimentally, due to a variety of non-radiative processes and energy transfer processes that must be removed and discounted to quantify a reliable radiative decay value. An excited electron will live a certain time in its excited state before recombining through radiative or non-radiative processes. The rate of radiative recombination rate is the inverse of the radiative lifetime (Equation 2.3) and the rate of non-radiative recombination is the inverse of the non-radiative lifetime (Equation 2.4). Therefore, QY will increase by reducing the radiating lifetime while increasing the non-radiating lifetime.

$$\phi_l = \frac{k_r}{k_r + k_{nr} + k_t} \qquad \textit{Equation 2.1}$$

$$\tau = \frac{1}{k_r + k_{nr} + k_t} \qquad \textit{Equation 2.2}$$

$$k_r = \frac{1}{\tau_r} \qquad \textit{Equation 2.3}$$

$$k_{nr} = \frac{1}{\tau_{nr}} \qquad \textit{Equation 2.4}$$

$$\phi = \frac{{}^{1}/_{\tau_r}}{{}^{1}/_{\tau_r} + {}^{1}/_{\tau_{nr}}} \qquad \textit{Equation 2.5}$$

$$\phi = \frac{E_A - E_B}{S_B - S_A} \qquad \textit{Equation 2.6}$$

As QY decreases with increased solvent polarity, this means that there is an increase in k_{nr} and/or k_t and a decrease in k_r (Equation 2.1). Therefore, τ_{nr} decreases as an effect of k_{nr} increasing (Equation 2.4), and τ_r increases as an effect of k_r decreasing (Equation 2.3). For τ to increase with increasing polarity of solvents alongside the QY decreasing, k_r must decrease more than k_{nr} and k_t increase. This will be very difficult to quantify experimentally, however in the absence of experimental quantification, some theories can be presented as to what can decrease k_r and increase k_{nr} and k_t, among which are Stokes' losses and molecular oxygen quenching. Stokes losses are a loss of energy of complexes due to collision and interaction with solvent molecules. Stokes losses result in a lower energy level of the LUMO which is closer to the ground state of an excited electron. Therefore, the excited electrons are more stable in the excited state and remain longer at this state, and rate of radiative recombination (k_r) is decreased. Molecular oxygen quenching is well-known as molecular oxygen is dissolved in many solvents. The quenching process uses the energy of excited state complex to convert triplet state molecular oxygen to singlet state molecular oxygen. Singlet state molecular oxygen is commonly termed a reactive oxygen species (ROS) as it is a radical and harmful in biological systems. The generation of ROS will increase the rate of non-radiative decay through quenching.

Quantum yield values were obtained using an integrating sphere (Equation 2.6), where E_A and E_B are the emission intensities for the sample and the solvent respectively. S_A and S_B are the scatter from the lamp for the sample and the solvent respectively. The QY values (Table 2.2) as explained above decrease for all three complexes in more polar solvents (Supplementary Figure 2.31). **IrpqSS** has 93% reduction from 28% to 2% in MeOH and H_2O respectively. The next biggest reduction is that of **IrpqSH** – 83% reduction from 3% to 0.5%. Irpqbpy shows an 46% reduction from 22% to 12% in MeOH and H_2O respectively. Luminescence lifetimes of **IrpqSS**, **IrpqSH** and **Irpqbpy** were collected by TCSPC (Time correlated Single Photon Count) and fitted to multiple components using an Instrument Response Function (IRF) file, ensuring good fit in the residuals and χ^2 values of between 1 and 1.3 (Supplementary Figure 2.29, Supplementary Figure 2.30). Fitting of the lifetime curve with IRF generates more accurate lifetime values compared to exponential tail fitting, because it considers any variations from the solvent and the instrument that may arise. This ensures that the lifetime values are obtained from the sample alone. The errors are therefore typically smaller than for exponential tail fitting, which does not consider the solvent background. The long component of the lifetime for **IrpqSS** (Table 2.1) in H_2O (2% MeOH) was 1410 ns (49%), which decreased in MeOH to 260 ns (79%) and further decreases in MeCN to 200 ns (78%). It is interesting to note that this solvent effect in the luminescence lifetimes was seen for all three complexes. **IrpqSH** and **Irpqbpy** had long components in H_2O of 420 ns (44%) and 680 ns (92%) respectively. The lifetimes decreased in MeOH to 280 ns (66%) and 300 ns (82%) respectively. These lifetime values are typical of similar iridium(III) cyclometalated complexes[16] and indicate that the lifetimes of the complexes when attached to AuNPs in H_2O would also be long, presenting potential use for luminescence lifetime imaging, as the lifetimes values will be much longer than autofluorescence of cells. This is not a technique that is explored in this report, yet it is something that is worth investigating in the future. Another point is that because the luminescence lifetimes of these complexes cannot be fitted to a single component, this is an indication that there are multiple excited states from which the electrons are recombining from, for example in a typical Jablonski diagram for an iridium(III) complex (Section 2.1.1), intersystem crossing results in phosphorescence, and the mixing of fluorescence and phosphorescence is termed luminescence. Thus, when fitting to multiple components, not all photons have undergone intersystem crossing to the triplet

state, and hence the multiple lifetimes seen are a result of fluorescent and phosphorescent excited states. Hence, we can say that the MLCT excited state is a mixture of states (triplet/singlet) and there are multiple components in the luminescence lifetime for iridium(III) complexes.

Hence, when keeping the same complex as the constant, the luminescence lifetime increases, and the quantum yield decreases as solvent polarity increases. However, when keeping the solvent as the constant and removing molecular oxygen by deaerating the solvent, both the luminescence lifetime and the luminescent intensity for all three complexes increased (Figure 2.10b,d,f, Figure 2.11, Table 2.3, Table 2.4) due to reduced quenching by molecular oxygen. Although quantum yield was not measured directly in deaerated solvent for the three complexes, the 20 μM solutions of iridium(III) complex in MeOH were deaerated with N_2 for 5 minutes (to prevent solvent evaporation) and the area under the curve for emission spectra before and after degassing were compared (Table 2.4). In all three complexes, the luminescent intensity increased by a factor of more than 4 for all. **IrpqSS** increased in luminescence by 659%, **IrpqSH** by 411% and **Irpqbpy** by 853%.

For **IrpqSS**, the long component of the lifetime increases from 200 ns (78%) in aerated MeCN to 1950 ns (66%) in deaerated MeCN. The long component of the lifetime also increases from 260 ns (79%) in aerated MeOH to 1940 ns (66%) in deaerated MeOH. **IrpqSH** and **Irpqbpy** also follow the same pattern, as the lifetime for **IrpqSH** increases from 280 ns (66%) in aerated MeOH to 1890 ns in deaerated MeOH and the lifetime for **Irpqbpy** increases from 300 ns (82%) in aerated MeOH to 2763 ns in deaerated MeOH.

	IrpqSS								IrpqSH				Control			
	MeCN				MeOH				MeOH				MeOH			
	Aerated		Deaerated		Aerated		Deaerated		Aerated		Deaerated		Aerated		Deaerated	
	%	τ / ns	%	τ / ns	%	τ / ns	%	τ / ns	%	τ / ns	%	τ / ns	%	τ / ns	%	τ / ns
Long component	78	**200**	66	**1950**	79	**260**	95	**1940**	66	**280**	77	**1890**	82	**300**	62	**2760**

*Table 2.3. Luminescence lifetimes of **IrpqSS**, **IrpqSH** and **Irpqbpy** in aerated and deaerated solvents at 20 μM. Aerated solutions were bubbled with N_2 for 10 minutes before luminescence lifetimes were collected.*

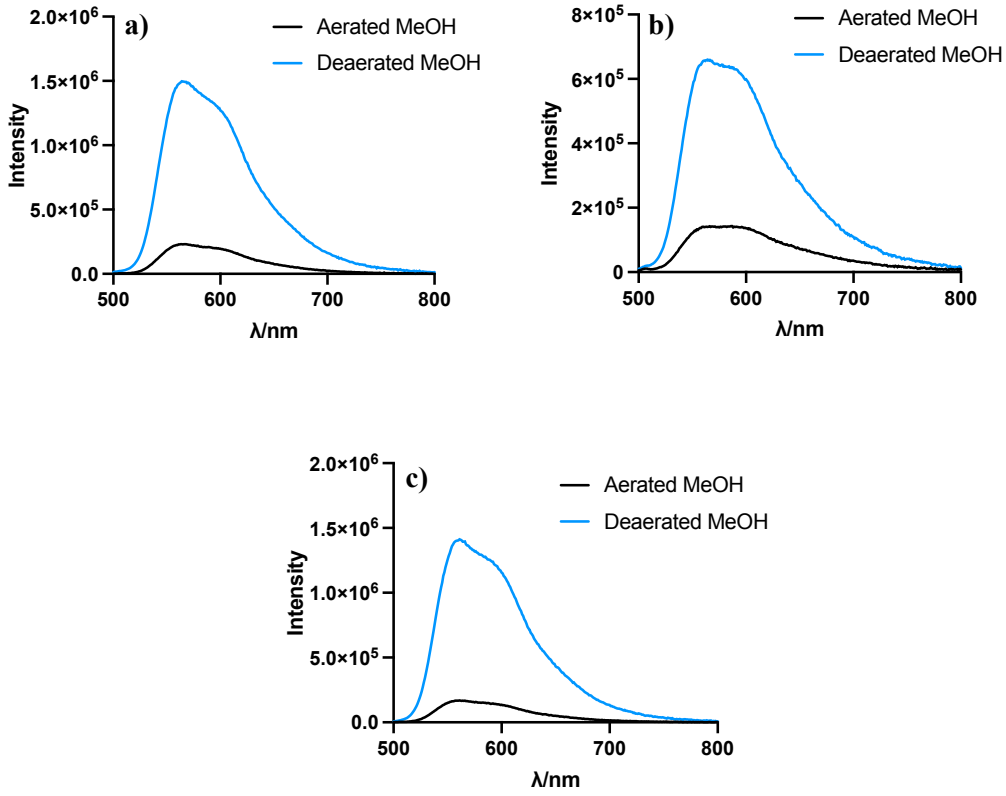


*Figure 2.11. Emission spectra in aerated (black) and deaerated (blue) MeOH at 20 μM for **a) IrpqSS**, **b) IrpqSH** and **c) Irpqbpy**. λ_{exc} = 440nm and filter of 475 nm used. Spectra were corrected for instrument response. Final concentration was obtained from dilution of a 1 μM stock solution.*

	Area under curve		
	IrpqSS	**IrpqSH**	**Irpqbpy**
Aerated MeOH	23,086,582	18,502,471	16,531,990
Deaerated MeOH	152,212,284	76,050,893	141,055,776

*Table 2.4. Area under curve of the emission spectra for the aerated and deaerated MeOH solutions of **IrpqSS, IrpqSH** and **Irpqbpy** at 20 μM.*

When comparing the **IrpqSS** complex to the previously studied 2-phenylpyridine version with the identical auxiliary ligand[3], the long component of the lifetime is reported as 25 ns (68%) in aerated MeCN, approximately 172 ns less than for **IrpqSS** in aerated MeCN. In addition, the quantum yield is 0.5% in MeCN, increasing to 3% in deaerated MeCN. If this complex were to follow the same trend seen in **IrpqSS**, **IrpqSH** and **Irpqbpy**, the QY would decrease further in MeOH and H_2O and would be lower than 0.5%. Hence, two advantages – increased QY and increased luminescence lifetimes – of using **IrpqSS** instead of the 2-phenylpyridine cyclometalated version of this complex in these studies can be seen.

2.4 Synthesis and characterisation of colloidal gold nanoparticles

Gold nanoparticles (labelled **AuNP13** and **AuNP25** for consistency to previously studied NPs[2, 4, 5, 43]) were synthesised following a previously studied protocol[44]. **AuNP13** and **AuNP25** sizes were 15 nm and 24 nm respectively (Figure 2.12a,b). The Zeta Potential (ζ-potential) of the NPs matches previously synthesised nanoparticles[4]. Cleaning of glassware used in the synthesis with fresh aqua regia was essential for the quality of the NPs produced as it cleaned any gold that stuck to the glassware. A time of three or more hours was determined as optimal to obtain the required quality.

In AuNP synthesis, EDTA acts as a base in the synthesis and promotes shape and size uniformity.[44] This is very important because larger sizes of NPs depend on the quality of **AuNP13**, because the larger sizes are made due to seeding more gold onto the smaller sized NPs. Multiple reactions for the synthesis of AuNP13 showed that when the concentration of EDTA was increased, this improved the polydispersity index (PDI), forming a more uniform solution of AuNPs with increased monodispersity. Citric acid is used to create a suitable pH for the formation of the NPs by forming a citrate buffer[45, 46] alongside trisodium citrate, which helps to reduce the Au^{3+} ion in the $HAuCl_4$ gold salt to produce CO_2, H^+ ions and Au^0. Once Au^0 is formed, the remaining gold seeds onto the neutral gold atoms, forming the desired nanoparticles. Ascorbic acid helps with the seeding process and is used as a reducing agent as well as a stabilising agent[47] in the seeding synthesis of AuNP25 and other larger sizes.

TEM and DLS comparison with different **AuNP13** and **AuNP25** samples showed that the volume distribution values are more closely matched to the nanoparticle diameters obtained from TEM image analysis compared to number and intensity distributions. For example, **AuNP13** and **AuNP25** of Figure 2.12a and Figure 2.12b respectively show nanoparticle diameters of 15 ± 2 nm and 24 ± 3 nm respectively from TEM images, corresponding to 16 ± 5 nm and 25 ± 10 nm in the DLS volume distribution (Figure 2.12e,f). In comparison, the number distributions are 13 ± 3 nm and 19 ± 6 nm respectively and the intensity distributions are 20 ± 6 nm and 39 ± 16 nm respectively. Thus, the number distribution tends to underestimate the size, whereas the intensity distribution overestimates, leaving volume distribution as the medium that closely resembles the nanoparticle diameter obtained from TEM images. The UV-vis absorbance shows SPR absorbance bands at 516 nm and 519 nm for **AuNP13** and **AuNP25** (Figure 2.12c,d). The reagents used in the synthesis remain in the solution and can be removed by centrifugation followed by removal of the supernatant and resuspension in H_2O. In Figure 2.12d, an absorbance band for the ascorbic acid used in **AuNP25** synthesis can be seen. After centrifugation, the ascorbic acid peak disappears (Figure 2.12g).

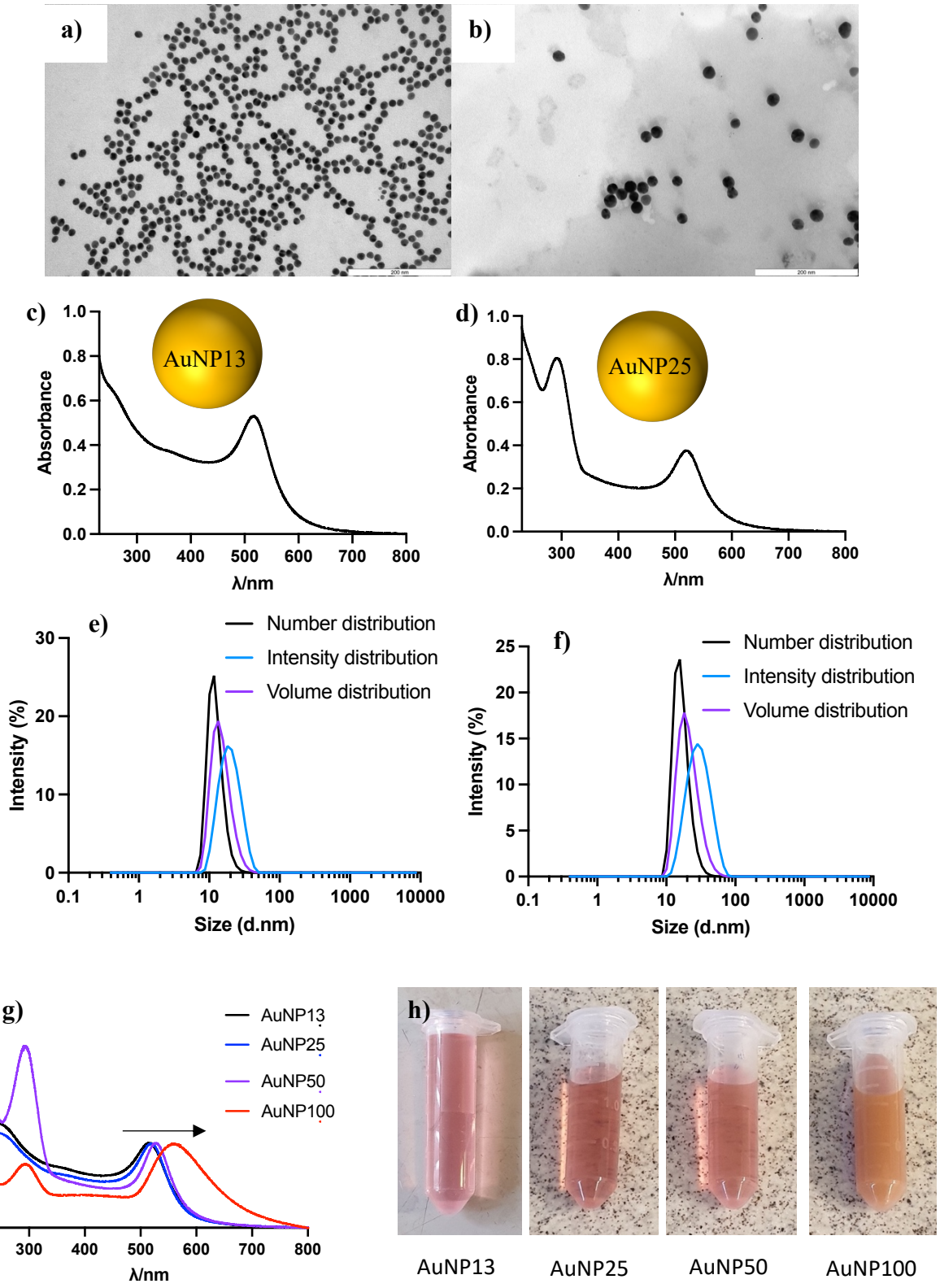


Figure 2.12. TEM images of ***a) AuNP13*** *of sizes 15.2 ± 1.8 nm and* ***b) AuNP25*** *of sizes 24.2 ± 2.7 nm. Nanoparticle diameters were calculated from an average of 20 NPs and processed using ImageJ software. Scale bars = 200 nm. UV-vis absorbance spectra of* ***c) AuNP13*** *and* ***d) AuNP25*** *in H_2O at concentration of 1.5 nM and 0.7 nM respectively.* ***e)*** *&* ***f)*** *show the number, volume and intensity DLS distributions for* ***AuNP13****s and* ***AuNP25****s respectively,* ***g)*** *shows the size-dependent AuNP red-shift and* ***h)*** *shows the different colours for the different AuNP sizes.*

Although **AuNP50** and **AuNP100** are not explored in depth in this report, comparison of the visual appearance of the NPs (Figure 2.12h) shows that at larger sizes, the NPs solution become less transparent as the size of the NPs becomes closer to that of bulk gold. The UV-vis absorbance peak also displays a red-shift in the spectrum (Figure 2.12g). This provides an interesting aspect into the property of gold nanoparticles, called SPR (Chapter 1, Section 1.4.4). Modification of the AuNP surface can be monitored by UV-vis absorbance. Surface plasmon resonance of AuNPs is the oscillation of electrons at the surface of the gold, that can change due to the coating of the gold. The coating of the gold affects the frequency of vibration of the electrons, leading to red or blue shifted absorbance spectrum, depending on the size of the NP and the coating on the surface (Chapter 1, Section 1.4.4).

The concentration (*C*) of NPs can be calculated using three different methods. Method 1 uses the quantity of gold and H_2O used in synthesis (Equation 2.7, Equation 2.8) when the diameter (*D*) is known from analysing TEM images[48,49]. This equation is derived from the density of gold. The number of gold atoms (*N*) can be calculated from *D*. Method 2 uses the absorbance of the NPs at 450 nm (*A*) in combination with the extinction coefficient (ε) of the NP size based on analysed TEM images (Equation 2.9)[50]. Method 3 uses Inductively Coupled Plasma Mass Spectrometry (ICP-MS). ICP-MS gives gold content in ppb values, from which the AuNPs concentration in nM can be obtained if a known volume of the NPs is used, and the diameter of the AuNPs is also known from the TEM images (Equation 2.10, Equation 2.11).

$$\mathrm{N} = 30.89685812 \times \mathrm{D}^3 \qquad \textit{Equation 2.7}$$

$$C = \frac{m_{i,Au}}{N\ x\ V\ x\ Mr} \qquad \textit{Equation 2.8}$$

$$C = \frac{A_{450}}{\varepsilon_{450}} \qquad \textit{Equation 2.9}$$

$$C(gL^{-1}) = C(nM)\ x\ Mr\ x\ N \qquad \textit{Equation 2.10}$$

$$C(ppb) = C(gL^{-1})\ x\ 10^6$$ *Equation 2.11*

Duplicate samples of **AuNP13** were analysed by ICP-MS in a 1:50 dilution and the final concentrations in nM were calculated and compared with methods 1 and 2. The concentrations were within a 10% error of each other (Table 2.5) and as such, the concentration of the **AuNP13s** can be stated to be 1.5 ± 0.15 nM. Subsequent concentrations of the coated **AuNP**s were calculated by the ratio of the colloidal **AuNP** absorbance to the coated **AuNP** absorbance.

	Concentration (Method 1)		**Concentration (Method 2)**		**Concentration (Method 3)**	
	ppb	**nM**	**ppb**	**nM**	**ppb**	**nM**
AuNP13	125	1.44	128	1.48	131	1.50
					136	1.56

*Table 2.5. Nanoparticle concentrations in ppb and nM, for the three methods of nanoparticle concentration calculation. 1.5 nM of **AuNP13** were diluted by a factor 250 to obtain the final ppb value by ICP-MS.*

2.5 Surfactant coating of gold nanoparticles with LPEG, SPEG, Zonyl-FSA and TFD-S

Surfactants are necessary for stabilisation of the NPs before addition of a charged complex. They reduce the surface tension between the NP and H_2O, preventing aggregation of the **AuNP**s. Aggregation occurs when the NPs lose their nanoscale properties and turn into bulk gold by clumping together to form larger particles that are not stable. Aggregated NPs have a more red-shifted SPR profile in UV-vis absorbance and a reduced absorbance. Neutral complexes such as many lanthanide complexes can be added to the NPs without the need for surfactant stabilisation.

It was found during the **AuNP** optimisation process that it was important to remove the excess reagents from **AuNP** synthesis, so that they will not interfere with the coating with the surfactants. Coating of the **AuNP**s with surfactant without removing the excess reagents affected the subsequent coating of the **AuNP**s with the iridium(III) complex. Brighter emission of the final iridium-coated nanoparticles was seen when the citrate **AuNP**s were centrifuged and resuspended in fresh H_2O before subsequent coating with surfactant and Ir(III) complexes. In addition, unexpectedly large sizes in DLS and nanosight were seen (Section 2.6) for the iridium-coated nanoparticles made from citrate **AuNP**s that had not been centrifuged and resuspended in H_2O prior to coating with surfactant and Ir(III) complexes. The surfactants used for the coating of **AuNP13** and **AuNP25** in this report consisted of per-fluorinated and PEG-based surfactants (Figure 2.13).

TFD-S was the only surfactant that was not commercially available. This compound was chosen as a comparison to the **Zonyl-FSA** at it contains the perfluorinated nature and sulfide bond as in in **Zonyl-FSA**. The synthesis of this compound presented many limitations. The purification was lengthy, requiring many different steps to remove the side reagents. The final crude product yield of 2 % was very low, however the pure product was obtained by HPLC in MeCN and H_2O. An improved synthesis method is needed for an effective production with higher yields. Increase in temperature, reaction time or reagents could all contribute to an improved synthesis (Section 2.9).

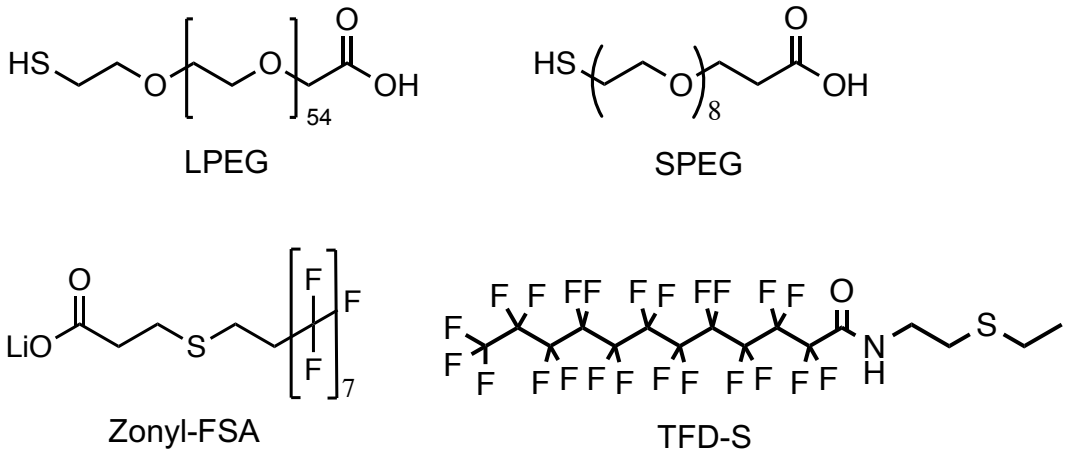


Figure 2.13. Structure of the four surfactants used to to coat the AuNPs before coating with the charged iridium(III) complexes. ***LPEG*** *= Poly(ethylene glycol) 2-mercaptoethyl ether acetic acid (M_n = 2100),* ***SPEG*** *= (α-Thio-ω-(propionic acid) octa(ethylene glycol),* ***Zonyl-FSA*** *= Lithium 3-[2-(perfluoroalkyl)ethylthio]propionate,* ***TFD-S*** *= N-(2-(ethylthio)ethyl)-2,2,3,3,4,4,5,5,6,6,7,7,8,8,9,9,10,10,11,11,12,12,12-tricosafluorododecanamide.*

The surfactants used for coating all have sulphur containing groups that could bind to the AuNPs. It was calculated from the binding curves (Figure 2.14) that 10 μM of LPEG, 30 μM of SPEG, and 6 μM of TFD-S were determined as the optimal concentrations of surfactant to add to 2.6 nM of NPs. Zonyl has been studied extensively in the past so the concentrations to add were obtained from previous studies[2], hence 10 μM of Zonyl-FSA was determined as optimal. The binding curves show the change in the SPR peak vs concentration in μM. Strength of binding to the **AuNP13** surface is referred to as the binding constant, which is the inverse of the dissociation constant. As seen in Figure 2.14, the surfactants bind to the AuNP surface in such a way as to cause a saturation (most clearly seen in LPEG). For SPEG and TFD-S, there is a plateau, and then the SPR band continues to shift until aggregation is reached at more red-shifted wavelengths or the increase in SPR becomes less prominent than the first shift prior to the first plateau. When nonlinear regression was performed on these points at the first plateau (Supplementary Figure 2.25, Supplementary Table 2.1), the dissociation constant and maximum specific binding for LPEG, SPEG and TFD-S enabled the binding constant calculation of 453926 M^{-1},

19478 M^{-1} and 552792 M^{-1} for LPEG, SPEG and TFD-S respectively. Hence the concentrations of surfactant required for coating of **AuNP13** decreases as the binding constant improves. **AuNP25** are approximately half the concentration of and double the surface area of **AuNP13** – the same concentration of surfactant was found to be suitable coverage.

DLS size distributions increased for all the NPs with surfactants (Figure 2.15). **TFD-S.AuNP13** had the smallest increase from 16 ± 5 nm of **AuNP13** to 17 ± 7 nm for **TFD-S.AuNP13**. **LPEG.AuNP13**, **SPEG.AuNP13** and **Zonyl.AuNP13** had a size of 27 ± 8 nm, 19 ± 6 nm and 21 ± 7 nm respectively. The different sizes can be attributed to the different sizes of hydrodynamic diameter caused by the size of the surfactants. **LPEG** is a large surfactant that is approximately 6 nm in length (Figure 2.16). SPEG and **Zonyl-FSA** are smaller, around 2 and 1 nm in diameter respectively, however due to **Zonyl-FSA** being a polymer, it wraps around the NP causing a larger hydrodynamic diameter in **Zonyl.AuNP13** than for **SPEG.AuNP13**. TFD-S surfactant at 2 nm has a very small shift in the hydrodynamic diameter, most probably because of its neutral charge, which decreases the interaction with H_2O molecules and causes the hydrodynamic diameter to be lower than for the other surfactant molecules. TEM images of the surfactant stabilised **AuNP13**s (Figure 2.17) show monodisperse AuNP with sizes within the error of the citrate stabilised **AuNP13**s. This was expected as TEM measures electronically dense metals which appear as dark patches, hence the sizes should not differ from that of the citrate **AuNP13**.

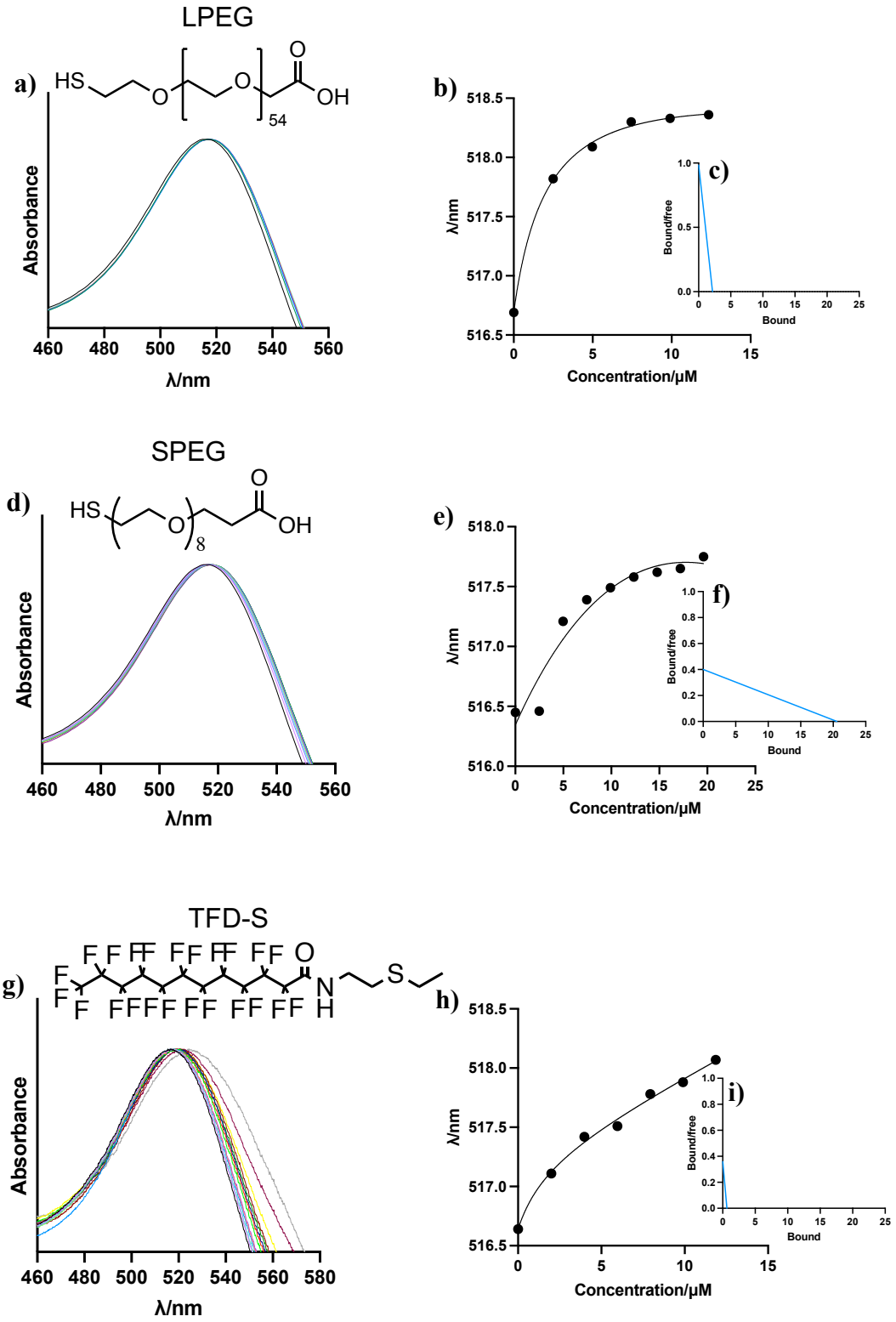


Figure 2.14. UV-vis absorbance spectra for the addition of ***a) LPEG****,* ***d) SPEG*** *and* ***g) TFD-S*** *to 2.6 nM* ***AuNP13****s. Binding curves with non-linear fit for the coating of* ***b) LPEG****,* ***e) SPEG*** *and* ***h) TFD-S*** *onto 2.6 nM* ***AuNP13****. Inlaid graphs show Scatchard plots of the bound/non-bound ratio of* ***c) LPEG****,* ***f) SPEG*** *and* ***i) TFD-S*** *surfactants, where the gradient equals the inverse of the dissociation constant. Concentration of the surfactant solutions were 1 mM in* H_2O *(****LPEG*** *and* ***SPEG****) and MeOH (****TFD-S****).*

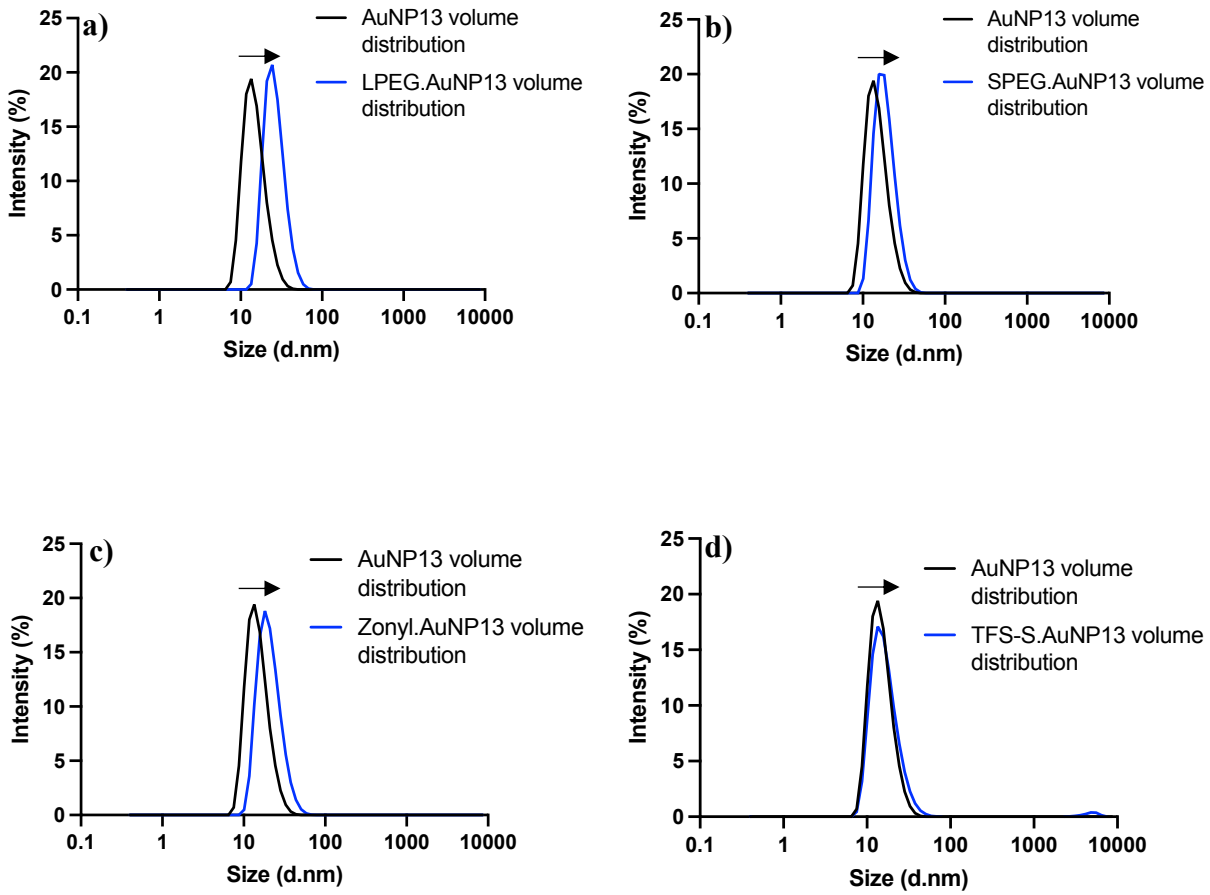


Figure 2.15. DLS volume distributions of ***a) LPEG.AuNP13****,* ***b) SPEG.AuNP13****,* ***c) Zonyl.AuNP13*** *and* ***d) TFD-S.AuNP13*** *samples compared with plain* ***AuNP13****s. Arrows show the change in size of the coating as the hydrodynamic diameter of the AuNPs changes.*

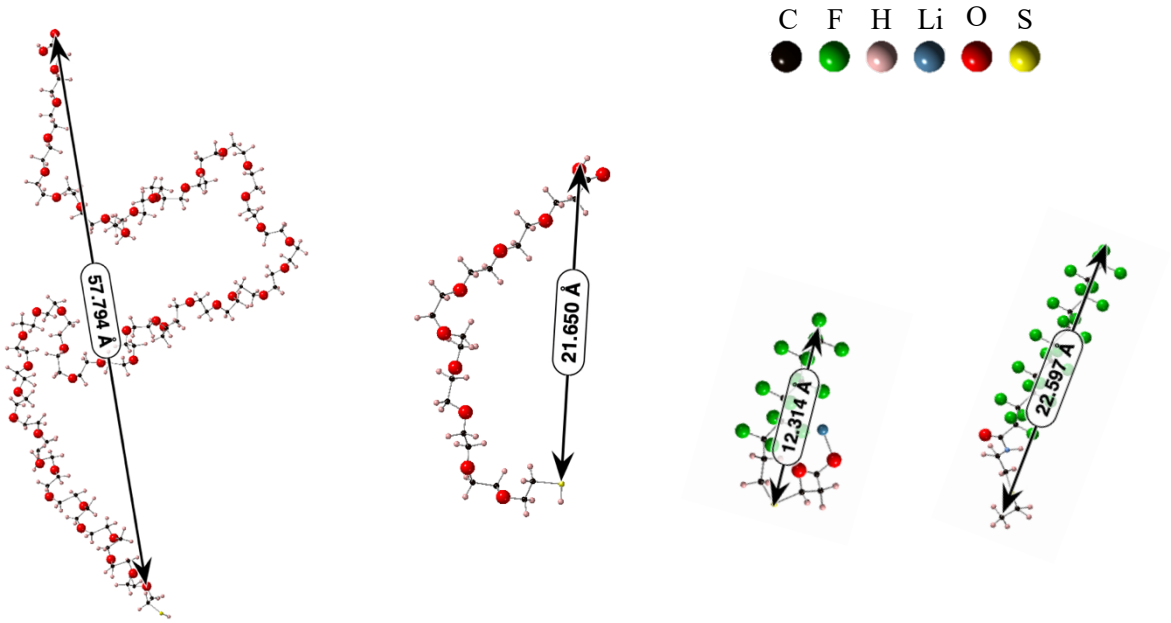


Figure 2.16. Structures of the surfactants ***a) LPEG, b) SPEG, c) Zonyl-FSA*** *and* ***d) TFD-S*** *relaxed and represented as ball and stick models. Images obtained using CrystalMaker, with elements colour-coded (top right).*

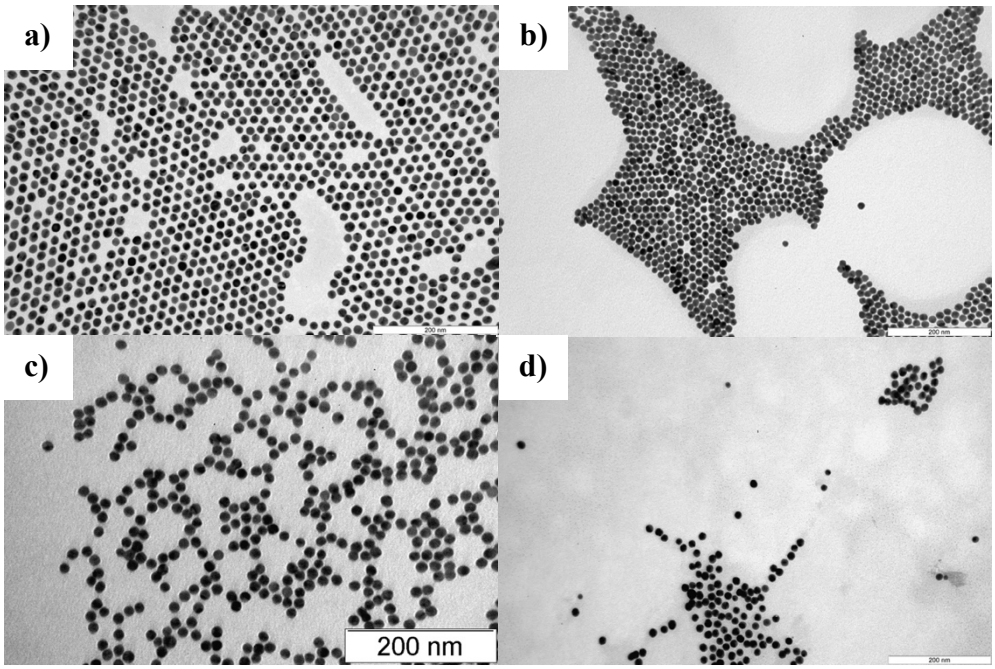


Figure 2.17. TEM images of ***a)*** *LPEG-,* ***b)*** *SPEG-* ***c)*** *Zonyl-FSA- and* ***d)*** *TFD-S- coated* ***AuNP13****s. Nanoparticle diameters were calculated from an average of 20 NPs and processed using ImageJ software. Scale bars = 200 nm. Sizes of the NPs were 15.5 ± 0.9 nm, 14.5 ± 1.0 nm, 15.4 nm ± 0.8 nm and 14.7 ± 1.4 nm for LPEG- SPEG-, Zonyl-FSA- and TFD-S- coated* ***AuNP13****s.*

2.6 Synthesis and characterisation of IrpqSS- and IrpqSH-coated AuNPs

Base was added for the addition of complexes to the surfactant-coated NPs. 2mM of hydrazine monohydrate in MeOH was added to 1mM of **IrpqSS** in MeOH before coating the AuNPs. 1 mM of NaOH in H_2O was added to **IrpqSH** in MeOH. It was observed that adding base improved the binding of the Ir(III) complexes to the nanoparticles, most probably by removing the hydrogen in the thiol group and stabilising the surface, promoting the formation of Au-S bonds. **AuNP**s aggregate in the presence of aqua regia, so the presence of a basic environment may stabilise the system. Coating of the iridium(III) complexes was determined by the binding curves (Figure 2.18) in the same manner as for the surfactants. The pH of the AuNPs after coating was measured to ensure that addition of the base would not affect the pH by a large amount, and it was seen that the pH of the NPs was not significantly affected, as the citrate **AuNP13**s had a pH of 5, and the final iridium(III)-coated NPs had a pH of 7 or less, so these NPs would be in the biological pH range.

When nonlinear regression was performed on these curve points where curve plateaus were present (Supplementary Figure 2.26, Supplementary Table 2.1), the dissociation constant and maximum specific binding enabled the binding constant calculation of 255167 M^{-1} for **IrpqSS** onto **LPEG.AuNP13**, 1198 M^{-1} for **IrpqSS** onto **TFD-S.AuNP13** and 1182 M^{-1} for **IrpqSH** onto **LPEG.AuNP13**. The optimal concentrations of **IrpqSS** to add were 20 μM, 6 μM, 16 μM and 38 μM to 3 nM of **LPEG.AuNP13**, **SPEG.AuNP13**, **Zonyl.AuNP13** and **TFD-S.AuNP13**. The optimal concentrations of **IrpqSH** to add were 20 μM, 10 μM, 20 μM and 4 μM to 3 nM of surfactant-coated NPs. **SPEG**, **Zonyl** and **TFD-S** for **IrpqSH** don't follow the standard binding curve appearance, therefore the optimal probe binding was determined by viewing the overlayed UV-vis absorbance curves (Supplementary Figure 2.24) and selecting a concentration at which the SPR peak had not broadened to cause aggregation. Iridium(III) complexes coated onto 3 nM surfactant-coated **AuNP13** and 2 nM surfactant-coated **AuNP25** gave the final NP concentrations of 1.7 nM and 1.1 nM for **AuNP13**s and **AuNP25**s respectively.

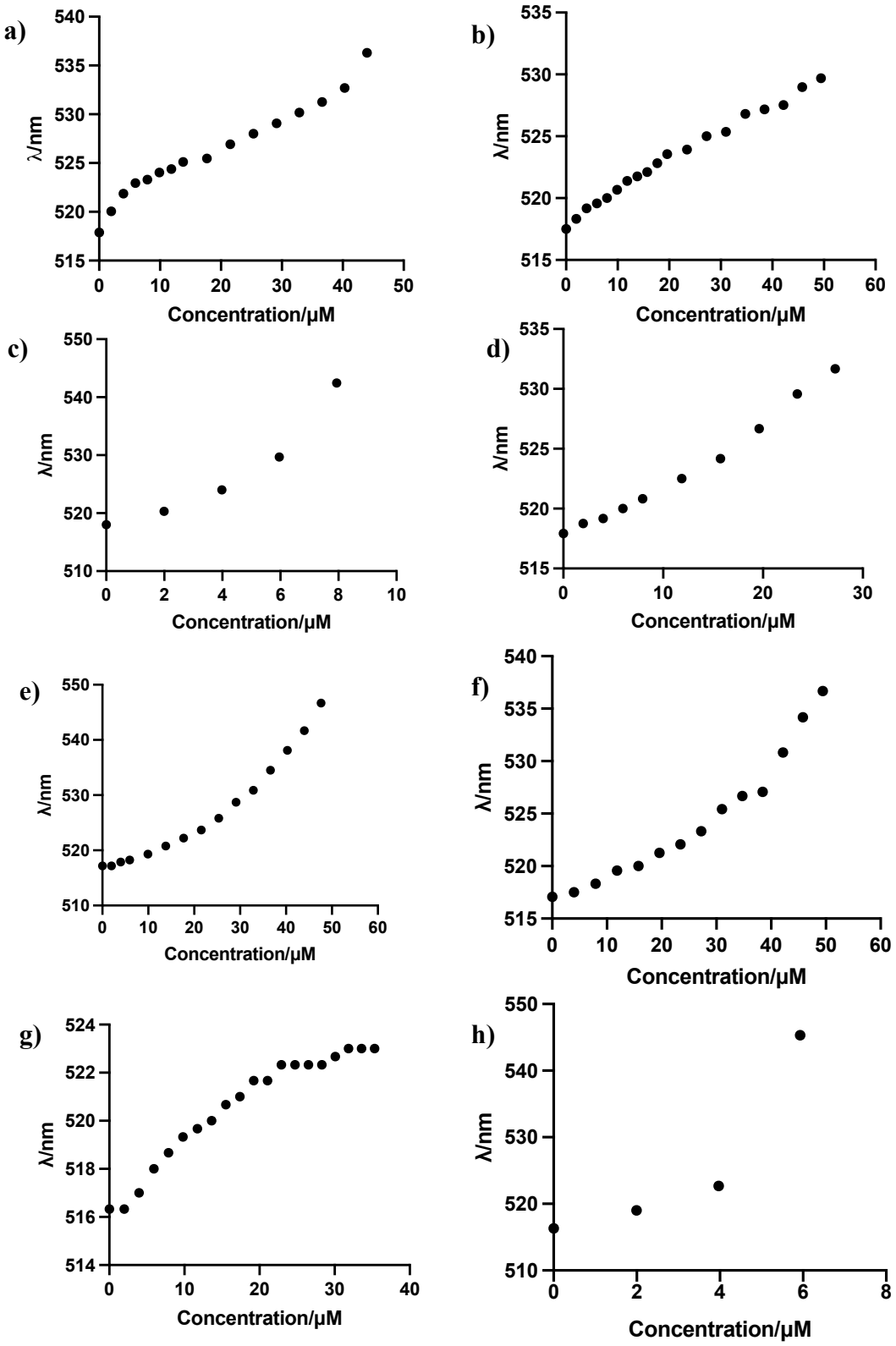


Figure 2.18. Binding curves of ***IrpqSS*** *onto 3 nM of* ***a) LPEG.AuNP13***, ***c) SPEG.AuNP13***, ***e) Zonyl.AuNP13*** *and* ***g) TFD-S.AuNP13*** *surfactants onto 3 nM of* ***AuNP13****. Binding curves of* ***IrpqSH*** *onto 3 nM of* ***b) LPEG.AuNP13***, ***d) SPEG.AuNP13***, ***f) Zonyl.AuNP13*** *and* ***h) TFD-S.AuNP13*** *surfactants onto 3 nM of* ***AuNP13****. Concentration of the iridium(III) complex solutions were 1 mM in MeOH.*

In DLS, a small quantity of large artifacts will scatter a lot more light (Chapter 1, Section 1.4.1), so this causes the PDI to be skewed even though TEM images show the monodispersity of the NPs. For example, in **IrpqSS.TFD-S.AuNP13** the volume and number distributions show a single peak and the expected size, however the intensity distribution shows an extra peak at <100 nm. As the size of an artefact increases, these larger objects scatter more light and the intensity of that scatter will increase, even though it is not present in the volume distribution. Thus, the PDI becomes affected (Table 2.6). However, **IrpqSS.TFD-S.AuNP13** can be considered as monodisperse due to the TEM images and UV-vis absorbance showing no aggregation in the NPs and good quality distribution of the NPs (Table 2.6, Figure 2.19, Figure 2.21). **AuNP25**s and larger NPs such as **AuNP50**s and **AuNP100**s (Supplementary Figure 2.23) show better PDI in DLS when coated compared to coated **AuNP13**s (Table 2.7, Table 2.8). The polydispersity index is better because size variation of coated NPs is reduced when the NPs are larger. The PDI increases as more compounds are added to the surface of the NPs. As modification of the NP surface occurs, it is not completely uniform throughout the whole sample, therefore the polydispersity increases, raising the PDI. DLS assumes that the NPs are spherical, however in solution, with the coating, this will not be exactly the case, and coating will also increase the hydrodynamic diameter due to interaction with the solvent. For **IrpqSS**, which is larger than **IrpqSH**, (Figure 2.20), the DLS values can be seen increasing slightly for corresponding NPs containing **IrpqSS** than for those containing **IrpqSH.** The reason for this can be attributed to the increased hydrodynamic diameter of the NPs with the larger **IrpqSS** complex, hence the increased numbers.

	Number distribution (nm)	Volume distribution (nm)	Intensity distribution (nm)	PDI	Z-Average (nm)
AuNP13	13 ± 3	16 ± 5	20 ± 6	0.092	19 ± 0.2
LPEG.AuNP13	22 ± 6	27 ± 8	33 ± 10	0.163	31 ± 0.3
SPEG.AuNP13	16 ± 4	19 ± 6	24 ± 7	0.129	22 ± 0.1
Zonyl.AuNP13	17 ± 5	21 ± 7	29 ± 10	0.154	25 ± 0.2
TFD-S.AuNP13	13 ± 4	17 ± 7	26 ± 11	0.246	23 ± 0.2
IrpqSS.LPEG.AuNP13	21 ± 6	26 ± 9	35 ± 12	0.212	33 ± 0.4
IrpqSH.LPEG.AuNP13	20 ± 5	25 ± 8	33 ± 11	0.117	29 ± 0.3
IrpqSS.SPEG.AuNP13	16 ± 4	19 ± 7	27 ± 9	0.208	25 ± 0.3
IrpqSH.SPEG.AuNP13	15 ± 4	19 ± 7	26 ± 9	0.125	23 ± 0.2
IrpqSS.Zonyl.AuNP13	20 ± 6	26 ± 12	45 ± 23	0.279	39 ± 0.6
IrpqSH.Zonyl.AuNP13	16 ± 4	20 ± 8	30 ± 12	0.167	26 ± 0.39
IrpqSS.TFD-S.AuNP13	17 ± 5	23 ± 10	38 ± 9	0.361	34 ± 0.014

*Table 2.6. DLS values of colloidal **AuNP13s** and **AuNP13**s coated with surfactants (**LPEG**, **SPEG**, **Zonyl** and **TFD-S**) and luminescent iridium(III) complexes (**IrpqSS** and **IrpqSH**).*

	Number distribution (nm)	Volume distribution (nm)	Intensity distribution (nm)	PDI	Z-average (nm)
AuNP25	18 ± 5	22 ± 7	29 ± 9	0.104	26 ± 0.2
IrpqSS.LPEG.AuNP25	27 ± 8	35 ± 13	50 ± 19	0.221	40 ± 0.6
IrpqSH.LPEG.AuNP25	25 ± 7	31 ± 10	40 ± 13	0.198	33 ± 0.2
IrpqSS.SPEG.AuNP25	21 ± 6	26 ± 10	37 ± 14	0.188	31 ± 0.3
IrpqSH.SPEG.AuNP25	22 ± 6	27 ± 8	34 ± 11	0.173	29 ± 0.3
IrpqSS.Zonyl.AuNP25	22 ± 6	28 ± 11	42 ± 17	0.225	36 ± 0.2
IrpqSH.Zonyl.AuNP25	22 ± 7	29 ± 11	43 ± 18	0.229	36 ± 0.3

*Table 2.7. DLS values of colloidal **AuNP25**s and **AuNP25**s coated with surfactants (**LPEG**, **SPEG** and **Zonyl**) and luminescent iridium(III) complexes (**IrpqSS** and **IrpqSH**).*

	Number distribution (nm)	Volume distribution (nm)	Intensity distribution (nm)	PDI	Z-average (nm)
AuNP50	36 ± 11	22 ± 7	47 ± 18	0.147	55 ± 0.6
AuNP100	94 ± 26	115 ± 34	121 ± 32	0.047	113 ± 0.9
Zonyl.AuNP100	105 ± 31	132 ± 40	142 ± 41	0.072	130 ± 1.1
IrpqSS.Zonyl.AuNP100	99 ± 27	121 ± 35	128 ± 33	0.057	119 ± 0.9

*Table 2.8. DLS sizes of colloidal **AuNP50**s and **AuNP100**s and **AuNP100** coated with **Zonyl-FSA** and **IrpqSS** complex.*

LPEG.AuNP13 display a UV-vis absorbance SPR shift of 517 nm, a 1 nm increase from **AuNP13**. The same shift is seen in **SPEG.AuNP13**. **Zonyl.AuNP13** displays a UV-vis SPR shift of 518 nm, a 2nm increase from **AuNP13**. **TFD-S.AuNP13** displays a UV-vis SPR shift of 521 nm, a 5nm increase from **AuNP13** (Table 2.9). Thus, the surface modification of the NPs at each step can be seen by UV-vis. The larger increases for the perfluorinated surfactants compared to the PEG surfactants may be due to lipophilicity of the compounds affecting the surface modification differently, or the difference in the position of the sulphur atoms between the PEG surfactants (thiols) and the perfluorinated surfactants (sulphides).

The importance of centrifuging the AuNPs before adding any surfactants was discovered to be very important in obtaining good sizes in DLS. DLS sizes of the final NPs that were made without centrifuging the AuNPs as the first step had very large sizes that were also confirmed with Nanoparticle Tracking Analysis (Figure 2.22). This indicated that possible aggregates/NP clusters were forming in solution, increasing the sizes of the NPs upon analysis by DLS and NTA, as the sizes obtained from this method were >100 nm in the volume distribution.

When the excess reagents were not removed before adding the surfactant and the iridium(III) complexes, a coating of 149 complexes per AuNP was seen for **IrpqSS.LPEG.AuNP13**, 47 complexes per AuNP for **IrpqSS.SPEG.AuNP13** and 97 complexes per AuNP for **IrpqSS.Zonyl.AuNP13** (Table 2.11). When compared to the coating for the AuNPs that were centrifuged before adding surfactant, the ICP-MS values obtained for the iridium(III) complex coating were 567 complexes for **IrpqSS.LPEG.AuNP13**, 173 complexes for **IrpqSS.SPEG.AuNP13**, 512 complexes for **IrpqSS.Zonyl.AuNP13**, 204 complexes for **IrpqSH.Zonyl.AuNP13** and 4511 complexes for **IrpqSS.TFD-S.AuNP13** (Table 2.11). The large coating number for **IrpqSS.TFD-S.AuNP13** indicates that there may be multiple layers of coating for **IrpqSS** on a **TFD-S.AuNP13** surface. Although the gold content was within a good calibration range, the iridium content was below the detection range in the system chosen for the improved coating method, hence these values are not reliable but are included here to show the importance of centrifuging as priority before modifying the AuNP surface. With the errors of **AuNP13** size by TEM image analysis taken into account (15.2 ± 1.8

nm), the range of complexes on each nanoparticle surface was found to be: 403 to 1744 complexes **IrpqSS.LPEG.AuNP13**, between 123 to 1889 complexes for **IrpqSS.SPEG.AuNP13**, between 364 to 2298 complexes for **IrpqSS.Zonyl.AuNP13**, 145 to 2814 complexes for **IrpqSH.Zonyl.AuNP13** and between 3210 and 6593 complexes for **IrpqSS.TFD-S.AuNP13**.

Purification of the final AuNPs was necessary to ensure that there was no free complex or surfactant in solution. There were three different methods attempted for purification of these AuNPs which will be discussed and outlined below. The first is purification using size exclusion chromatography. The second is purification using centrifugation, removal of supernatant and resuspension. The third is the purification using filter tubes, that expel excess water during centrifugation and allow resuspension of the NPs without the removal of supernatant using a pipette. Size exclusion chromatography with Sephadex was the most successful technique that was found for these AuNPs and has been shown to be successful for a variety of other AuNPs with luminescent inorganic complexes on their surfaces. Sephadex is a resin with pores that excludes compounds of a specific molecular weight, therefore the iridium(III) compounds that were unbound to the AuNPs during the coating method were able to be purified using Sephadex G-25, which has a size exclusion limit of Mr 5000. Purification by centrifugation of the AuNPs showed very weak luminescence in solution emission studies, indicating that the probe coating was very low. Filter tubes as the third purification method was similar to centrifugation because this technique removed a lot of the probe from the surface and resulted in low coating values. **Zonyl**-coated AuNPs, when attempted to be purified with this technique got stuck in the pores and excess supernatant could not be expelled. Hence, for AuNPs synthesised using the Vossmeyer and Ziegler methods, purification techniques using centrifugation were unsuccessful in creating a good loading of complex on the surface. For AuNPs synthesised using different seeding methods (Chapter 4, Section 4.2), purification with filter tubes was the acceptable method of purification, following previously studied protocols[51].

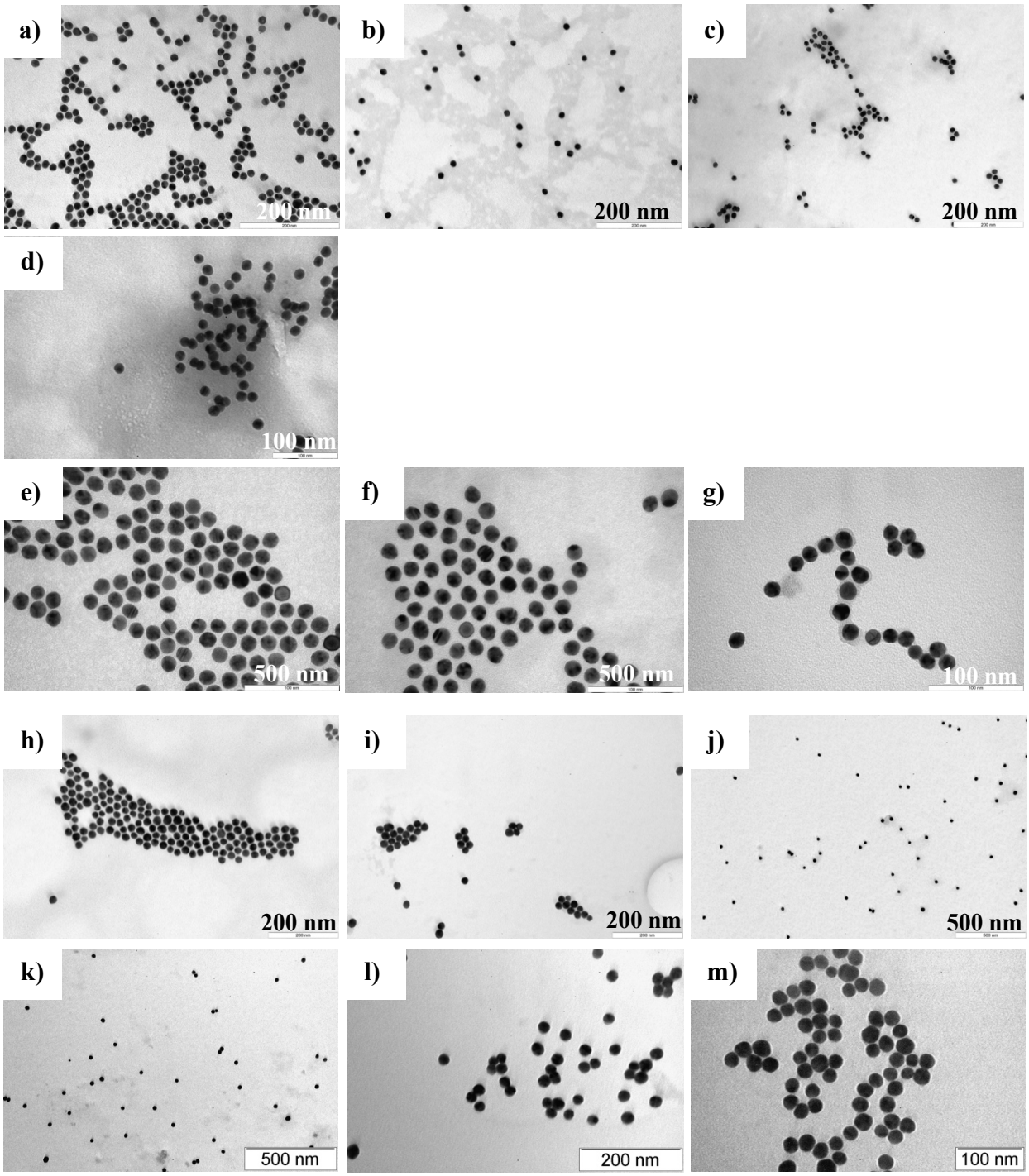


Figure 2.19. TEM images of ***a) IrpqSS.LPEG.AuNP13****,* ***b) IrpqSS.SPEG.AuNP13****,* ***c) IrpqSS.Zonyl.AuNP13****,* ***d) IrpqSS.TFD-S.AuNP13****,* ***e) IrpqSH.LPEG.AuNP13****,* ***f) IrpqSH.SPEG.AuNP13****,* ***g) IrpqSH.Zonyl.AuNP13****,* ***h) IrpqSS.LPEG.AuNP25****,* ***i) IrpqSS.SPEG.AuNP25****,* ***j) IrpqSS.Zonyl.AuNP25****,* ***k) IrpqSH.LPEG.AuNP25****,* ***l) IrpqSH.SPEG.AuNP25*** *and* ***m) IrpqSH.Zonyl.AuNP25****. Nanoparticle diameters were calculated from an average of 20 NPs and processed using ImageJ software. Scale bars = 200 nm (****a - j****), 500 nm* ***(k)****, 200 nm* ***(l)*** *and 100nm* ***(m)****. Sizes of NPs were* ***a)*** *15.8 ± 0.9 nm,* ***b)*** *15.7 ± 0.9 nm,* ***c)*** *14.7 ± 0.8 nm,* ***d)*** *15.3 ± 0.7 nm,* ***e)*** *16.3 ± 0.9 nm,* ***f)*** *16.0 ± 0.9 nm,* ***g)*** *16.6 ± 1.1 nm,* ***h)*** *23.2 ± 2.7 nm,* ***i)*** *23.2 ± 2.0 nm,* ***j)*** *23.6 ± 2.5 nm,* ***k)*** *23.3 ± 2.1 nm,* ***l)*** *23.2 ± 3.1 nm,* ***m)*** *24.3 ± 2.0 nm.*

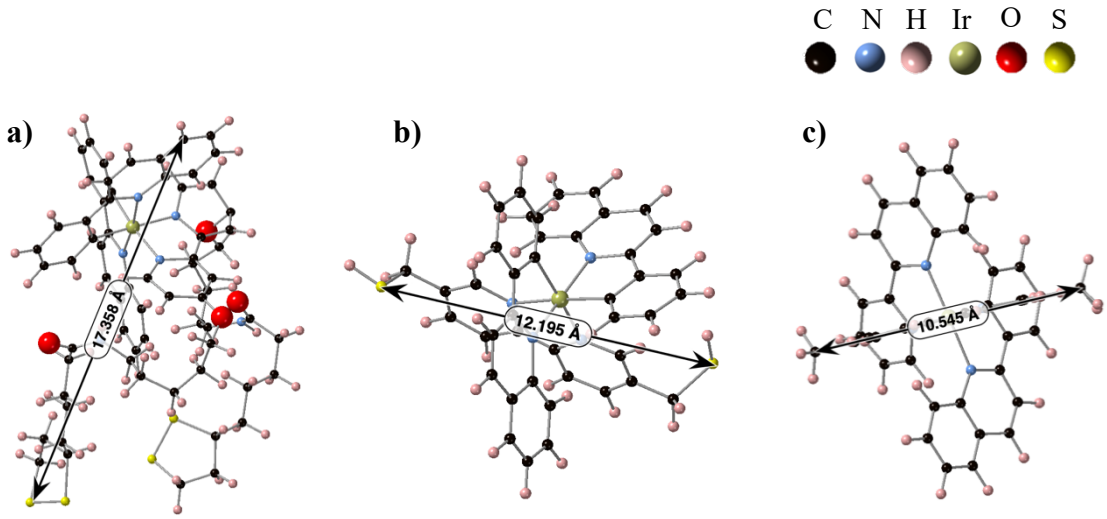


Figure 2.20. ***a) IrpqSS, b) IrpqSH and c) Irpqbpy*** *represented as a ball and stick models with arrows showing the approximate sizes. Images obtained using CrystalMaker, with elements colour-coded (top right).*

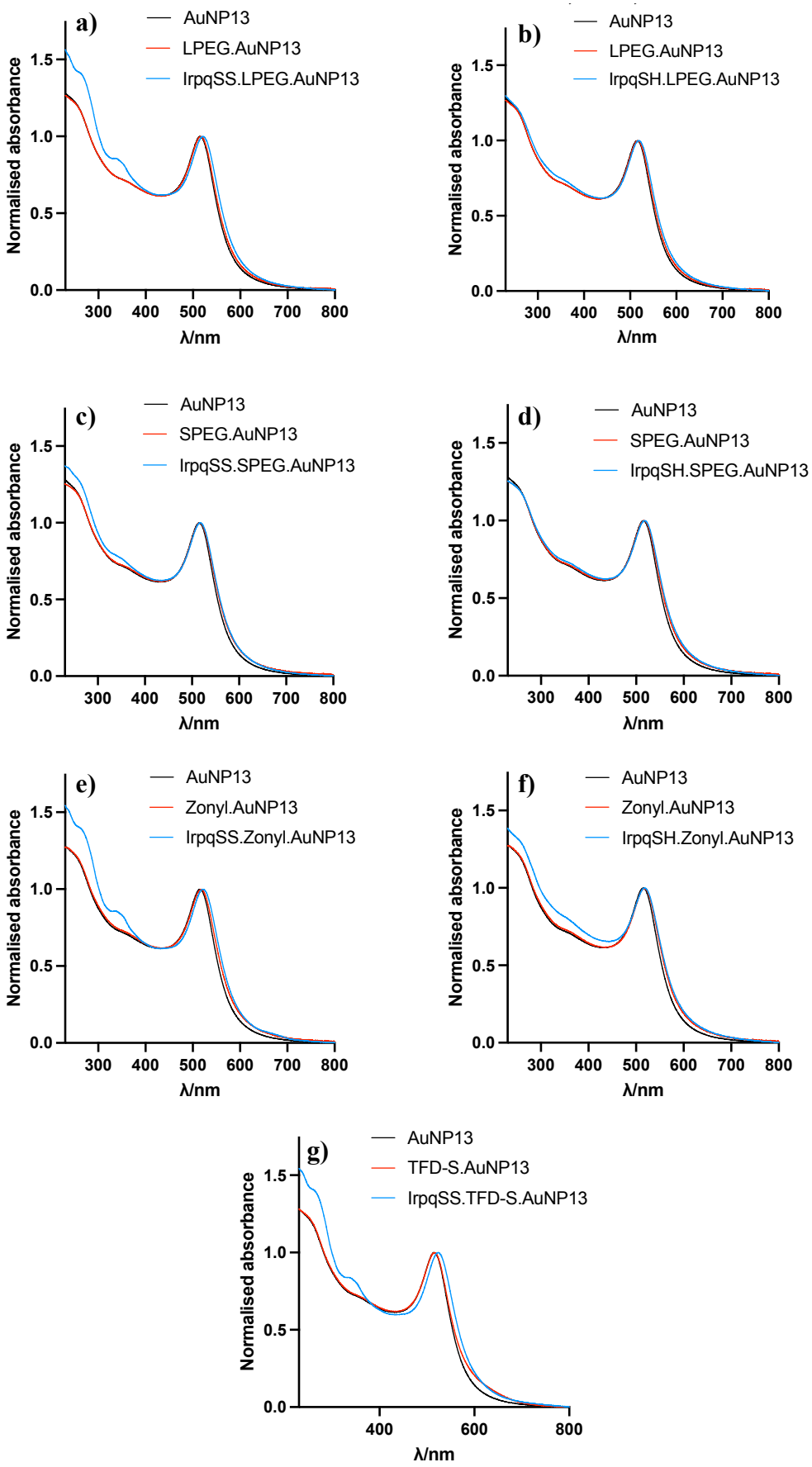


Figure 2.21. Normalized overlayed UV-vis absorbance spectra for the AuNPs. Citrate AuNPs (black), surfactant-coated AuNPs (red) and iridium-coated AuNPs (blue) for ***a) IrpqSS.LPEG.AuNP13****,* ***b) IrpqSH.LPEG.AuNP13****,* ***c) IrpqSS.SPEG.AuNP13****,* ***d) IrpqSH.SPEG.AuNP13****,* ***e) IrpqSS.Zonyl.AuNP13****,* ***f) IrpqSH.Zonyl.AuNP13*** *and* ***g) IrpqSS.TFD-S.AuNP13****.*

	λ_{max} / nm	Shift / nm		λ_{max} / nm	Shift / nm
AuNP13	516	0	**AuNP25**	519	0
LPEG.AuNP13	517	1	**LPEG.AuNP25**	521	2
SPEG.AuNP13	517	1	**SPEG.AuNP25**	521	2
Zonyl.AuNP13	518	2	**Zonyl.AuNP25**	521	2
TFD-S.AuNP13	521	5	**TFD-S.AuNP25**	-	-
IrpqSS.LPEG.AuNP13	522	6	**IrpqSS.LPEG.AuNP25**	524	5
IrpqSS.SPEG.AuNP13	518	2	**IrpqSS.SPEG.AuNP25**	521	2
IrpqSS.Zonyl.AuNP13	522	6	**IrpqSS.Zonyl.AuNP25**	522	3
IrpqSS.TFD-S.AuNP13	528	12	**IrpqSS.TFD-S.AuNP25**	-	-
IrpqSH.LPEG.AuNP13	520	4	**IrpqSH.LPEG.AuNP25**	523	4
IrpqSH.SPEG.AuNP13	520	4	**IrpqSH.SPEG.AuNP25**	521	2
IrpqSH.Zonyl.AuNP13	520	4	**IrpqSH.Zonyl.AuNP25**	522	3

Table 2.9. ***AuNP13*** *and* ***AuNP25*** *UV-vis absorbance SPR shifts after coating with surfactants and iridium(III) complexes, proving modification of the nanoparticle surface.*

	λ_{max} / nm	Shift / nm
AuNP100	559	0
Zonyl.AuNP100	560	1
IrpqSS.AuNP100	565	5

Table 2.10. ***AuNP100*** *UV-vis absorbance SPR shifts after coating with surfactants and iridium(III) complexes, proving modification of the nanoparticle surface.*

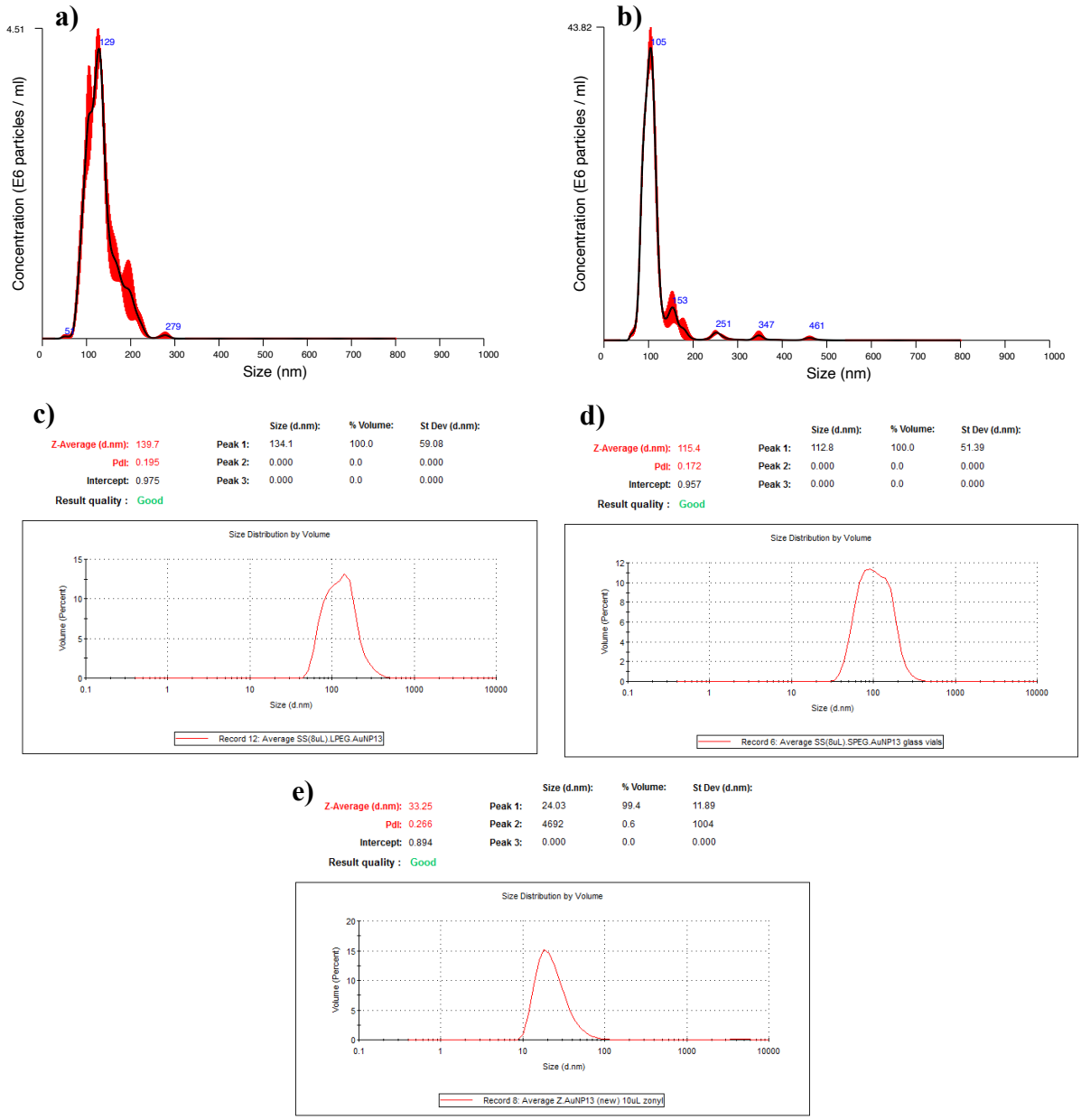


Figure 2.22. Nanoparticle Tracking Analysis (NTA) size distribution histograms of ***a) IrpqSS.LPEG.AuNP13*** *and* ***b) IrpqSS.SPEG.AuNP13****; DLS volume distributions of* ***c) IrpqSS.LPEG.AuNP13****,* ***d) IrpqSS.SPEG.AuNP13*** *and* ***e) IrpqSS.Zonyl.AuNP13*** *when the* ***AuNP13****s are not centrifuged before adding the surfactant.*

Sample	Average complex coating per NP (centrifugation before surfactant addition)	Average complex coating per NP (no centrifugation before surfactant addition)
IrpqSS.LPEG.AuNP13	567	149
IrpqSS.SPEG.AuNP13	173	47
IrpqSS.Zonyl.AuNP13	512	97
IrpqSH.Zonyl.AuNP13	204	-
IrpqSS.TFD-S.AuNP13	4511	-

Table 2.11. Approximate coating of luminescent Iridium(III) complexes for IrpqSS.LPEG.AuNP13, IrpqSS.SPEG.AuNP13, IrpqSS.Zonyl.AuNP13, IrpqSH.ZonylAuNP13 and IrpqSS.TFD-S.AuNP13, obtained by ICP-MS.

2.7 Photophysical characterisation of IrpqSS- and IrpqSH-coated AuNPs

In the emission spectra of the iridium(III)-coated AuNPs, λ_{em} is more red-shifted than free complex in H_2O (2% MeOH). This is because the emission of the free complexes in H_2O has a small quantity of methanol, but on the **AuNP**s, MeOH is removed during the purification process. Henceforth, the overall solvent of the final NPs is more polar than for the free iridium(III) complexes, so the red-shift is more pronounced and λ_{em} is at 610 nm (Figure 2.23) rather than < 600nm (Section 2.3). The ability to detect emission from these NPs shows great promise as an imaging agent, as the **AuNP** concentration at this point was at 1.7 nM for **AuNP13**s coated with **IrpqSS/IrpqSH** and **LPEG**, **SPEG** and **Zonyl** surfactant, with an absorbance of 0.6 (Supplementary Figure 2.27). The final **AuNP** concentration was 1.9 nM for **IrpqSS.TFD-S.AuNP13** and 1.1 nM for the **AuNP25** samples. **IrpqSH**-coated **AuNP**s

showed a weak luminescence emission spectrum with a scattering peak from the gold, confirming the weak emission expected due to the low QYs of the complex.

The luminescence lifetimes of the iridium(III) complexes are affected by interaction with the surfactants. For example, **LPEG** reduces the lifetime of **IrpqSS** slightly from 1410 ns to 1210 ns in solution (Table 2.12). On NPs, the lifetime decreases further to 1050 ns (Table 2.13). **SPEG** also reduces the lifetime of **IrpqSS** significantly to 490 ns in solution, but on the NPs, the lifetime is increased to 1100 ns**. Zonyl** reduces the lifetime of **IrpqSS** to 880 ns, and this is reduced further when on NPs to 680 ns. **Zonyl** also reduces the lifetime of **IrpqSH** to 400 ns, and this is further reduced to 350 ns when on NPs. Hence, the interaction of the complex with surfactants in solution and with the gold in the NP system affects the length of the lifetimes. The impact of the gold interaction with the iridium(III) complexes is seen further with **AuNP25**s. The luminescence lifetimes of the iridium(III)-coated **AuNP25**s differs from that of the iridium(III)-coated **AuNP13**s (Table 2.14), indicating that the gold is having an impact on the luminescence lifetime.

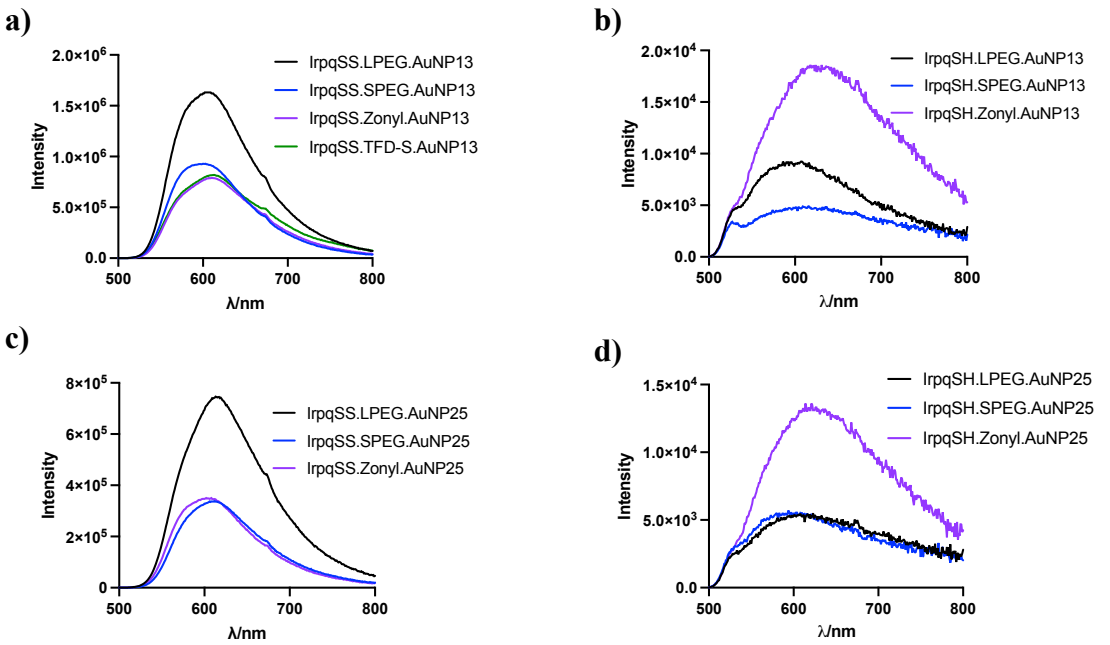


Figure 2.23. Emission spectra of ***a) AuNP13s*** *coated with* ***IrpqSS****,* ***b) AuNP13s*** *coated with* ***IrpqSH****,* ***c) AuNP25*** *coated with* ***IrpqSS*** *and* ***d) AuNP25s*** *coated with* ***IrpqSH*** *(H_2O, λ_{exc} = 440 nm, and a 530 nm filter).*

	IrpqSS						IrpqSH	
	+ LPEG		+ SPEG		+ Zonyl		+ Zonyl	
	%	τ / ns	%	τ / ns	%	τ / ns	%	τ / ns
Long component	45	**1210**	23	**490**	59	**880**	49	**400**

Table 2.12. ***IrpqSS*** *and* ***IrpqSH*** *(20 μM) + surfactants in H_2O. Concentration of surfactants was 10 μM.*

	IrpqSS.LPEG. AuNP13		IrpqSS.SPEG. AuNP13		IrpqSS.Zonyl. AuNP13		IrpqSS.TFD-S. AuNP13		IrpqSH.Zonyl. AuNP13	
	%	τ / ns	%	τ / ns	%	τ / ns	%	τ / ns	%	τ / ns
Long component	33	**1050**	52	**1100**	39	**680**	54	**880**	27	**350**

Table 2.13. Lifetimes of iridium(III)-coated ***AuNP13****s at a concentration of 9 nM in H_2O.*

	IrpqSS.LPEG. AuNP25		IrpqSS.SPEG. AuNP25		IrpqSS.Zonyl. AuNP25		IrpqSH.Zonyl. AuNP25	
	%	τ / ns	%	τ / ns	%	τ / ns	%	τ / ns
Long component	30	**910**	59	**1140**	67	**1020**	26	**430**

Table 2.14. Lifetimes of iridium(III)-coated ***AuNP25****s in H_2O.*

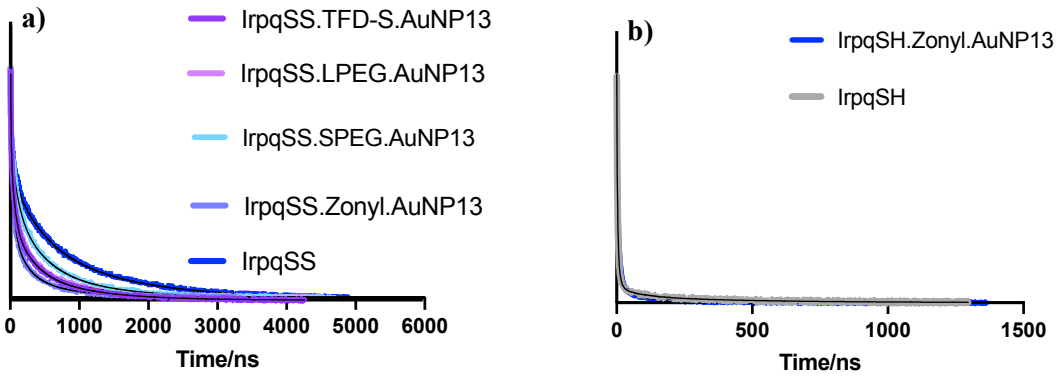


*Figure 2.24. Luminescence lifetime decay curves with lifetime fitting of 9 nM **IrpqSS**-coated AuNPs and free **IrpqSS** complex in H_2O **(a)** and **IrpqSH**-coated AuNPs and free **IrpqSH** complex in H_2O. **(b)**.*

Measurements of quantum yields of the iridium(III)-coated NPs were attempted using the same method as for the free iridium(III) complexes in solution, and water was used as the reference solvent. QYs were difficult to collect from the NPs due to a lack of strong signal. The standard protocol for QYs states that the absorbance value at λ_{exc} must be between 0.05 – 0.1. Assuming a coating of 1000 complexes per nanoparticle (as has been achieved previously for **AuNP13**s)[2] and using the extinction coefficient values of 2300 and 1300 for **IrpqSS** and **IrpqSH** respectively, the iridium(III) complex concentration would be 43 μM for **IrpqSS** and 77 μM for **IrpqSH** to obtain an iridium(III) complex absorbance value of 0.1 at 440 nm. This requires a concentration of 43 nM and 77 nM of **IrpqSS**-coated **AuNP13**s and **IrpqSH**-coated **AuNP13**s. This high nanoparticle concentration leads to the difficulties in measuring QY values of complexes on NP surfaces. As **IrpqSS.LPEG.AuNP13** gave the strongest signal of all the NPs, a QY was obtained of the NPs at 9 nM (Supplementary Figure 2.32), giving a value of 1%. This decrease in QY from 2% of free **IrpqSS** in H_2O can be attributed to the quenching from the gold, as the luminescence lifetimes for **IrpqSS.LPEG.AuNP13** also decrease compared to the free **IrpqSS** in H_2O.

2.8 Conclusions

Two nanoparticle sizes, **AuNP13** and **AuNP25**, along with three Ir(III) complexes with different auxiliary ligands were synthesised and characterised. The colloidal NPs were monodisperse, with PDI values of < 0.2 and TEM images showing a good quality size distribution. Long-chain **IrpqSS** and short-chain **IrpqSH** successfully conjugated onto **AuNP13**s and **AuNP25**s that were stabilised with **LPEG**, **SPEG** and **Zonyl-FSA** surfactants. **IrpqSS** was also successfully conjugated onto **AuNP13s** coated with **TFD-S** surfactant. All three complexes display an MLCT band in the visible spectrum, providing promising grounds for future studies in two-photon excitation using NIR light. It was shown that an increased solvent polarity increases luminescence lifetimes but decreases the quantum yield. However, in the same solvent system, the luminescence lifetime and luminescent intensity increases for deaerated solutions as expected, due to removal of molecular oxygen from the solvent. The long component in the lifetimes for **IrpqSS**, **IrpqSH** and **Irpqbpy** in H_2O (2% MeOH) were 1410 ns, 420 ns and 680 ns respectively, which is typical of similar probes in the same solvent, showing that these complexes present potential for use for future studies in luminescence lifetime imaging, as the lifetimes are longer than that of background autofluorescence in cells. The quantum yields of **IrpqSS**, **IrpqSH** and **Irpqbpy** in H_2O were 2%, 0.5% and 12% respectively.

The studies in this chapter show that monodisperse **AuNP**s functionalised with luminescent iridium(III) complexes can be made , and that can carry around 600 iridium(III) complexes on the surface. The **AuNP**s show emission at 610 nm at low concentrations of 1.7 nM, and with λ_{exc} = 440 nm being in the visible, it is very promising for using the NPs in this study for imaging in future cell studies. The **AuNP**s in this study also show that surface modification occurs upon addition of compounds to the surface, An SPR shift is seen for each modification step of the **AuNP** surface. Loading of the iridium(III) complexes on the **AuNP**s was carried out using ICP-MS, and a big difference was seen in the loading when the **AuNP**s were centrifuged before adding surfactant compared to when they were not, due to possible interference of excess reagents in the H_2O with the surfactants, which could then affect the binding of the iridium(III) complexes to the AuNPs. All the studies show that the **AuNP**s coated in this chapter

are suitable to be used for future cell studies, as they are luminescent at low concentrations, show long luminescence lifetimes and are monodisperse. They are also a suitable pH for use in cells. The most emissive nanoparticles chosen to be carried on to further studies were **IrpqSS.LPEG.AuNP13**, **IrpqSS.SPEG.AuNP13**, **IrpqSS.Zonyl.AuNP13**, **IrpqSH.Zonyl.AuNP13** and **IrpqSS.TFD-S.AuNP13.**

2.9 Further Studies

Future studies should investigate luminescent properties on the **AuNP50** and **AuNP100s** as well, as there may be different luminescent properties due to the gold interaction with the iridium(III) complexes, which could be studied in more depth. It would also be interesting to investigate the difference that **AuNP** size makes to cell studies. Investigation of deaerated quantum yields would also be important to obtain quantitative value, as the deaerated emission studies performed here were not done in an integrating sphere. Additional iridium(III) complex synthesis with varying cyclometalated and auxiliary ligands (Figure 2.1) could lead to further investigation of the differences between similar iridium(III) cyclometalated complexes such as the differences between **IrpqSS** and the 2-phenylpyridine version mentioned in this report[3]. Optimisation of the **TFD-S** synthesis will be necessary to use this surfactant in the future. A final yield of 1.5% was very low, however optimisation of the synthesis was unable to be finalised in the scope of this project and will be something important to be taken further in the future. EDC amide coupling was used at room temperature for the formation of **TFD-S**, however HBTU/DIPEA coupling has also been previously studied and shown to be effective for the formation of amides.[52, 53]

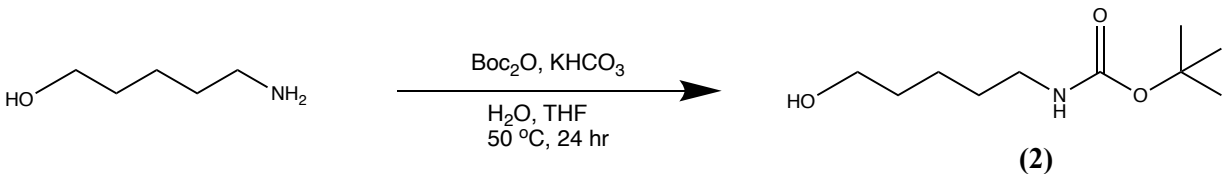
2.10 Experimental

All reagents were obtained from Sigma Aldrich, Thermo Fisher Scientific, Acros Organics or VWR and used as purchased, unless otherwise stated. NMR solvents were obtained from Goss Scientific. All reactions were carried out under nitrogen unless expressly stated. All organic compounds were characterised using NMR and mass spectrometry and all organometallic compounds characterised using NMR, mass spectrometry, infra-red spectroscopy and UV-vis absorbance spectroscopy. All nanoparticles were characterised by DLS, TEM and UV-vis. NMR spectra were collected on a Bruker AVIII400, AVIII300 or NEO400 spectrometer, and data acquisition and processing was performed by the TOPSPIN software. MestReNova software was used for analysis of the TOPSPIN data. UV-visible absorption spectra were collected on an Agilent Cary 5000 Cary 50 or Cary 60 spectrometer. Prism was used to plot and analyse data. Emission and excitation spectra of the organometallic complexes was collected on an Edinburgh Instruments FLSP920 spectrometer and a PTI Fluorescence spectrometer combined with FeliX for Windows software. Luminescence lifetimes and quantum yields were collected on the FLSP920 spectrometer, with the F900 software used for all processing of data. An integrating sphere was used for quantum yield measurements. Analysis of the data was performed using FAST software. A Horiba Fuorolog fluorospectrometer was used for the collection of deaerated lifetimes and deaerated emission spectra. DLS and Zeta potential measurements were collected on a Malvern Zetasizer Nano instrument. Nanoparticle Tracking Analysis was performed on a Nanosight NS300 instrument with the assistant of Menisha Manhota. TEM images were obtained using a Joel 1400 Bio Electron Microscope and Formvar Carbon support films from EMResolutions. The images were analysed by ImageJ software. Infra-red spectra were collected on a Varian 660-IR FT-IR spectrometer. ICP-MS measurements were run on a 7500cx ICPMS with an Agilent integrated auto-sampler at the Chemistry department at the University of Warwick. PlasmaCal calibration standards were obtained from QMX laboratories. Calibration curves were fitted to R^2 values of <0.998.

2.11 Six-step synthesis of bpySS ligand

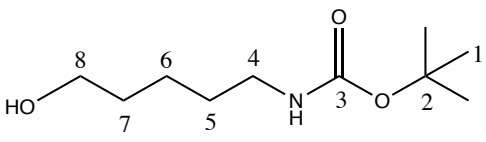
Synthesis methods obtained from previously used protocol[3]. NMR and mass spectroscopy matched previous results.

2.11.1 Synthesis of N-(Boc)-5-amino-1-pentanol *(2)*

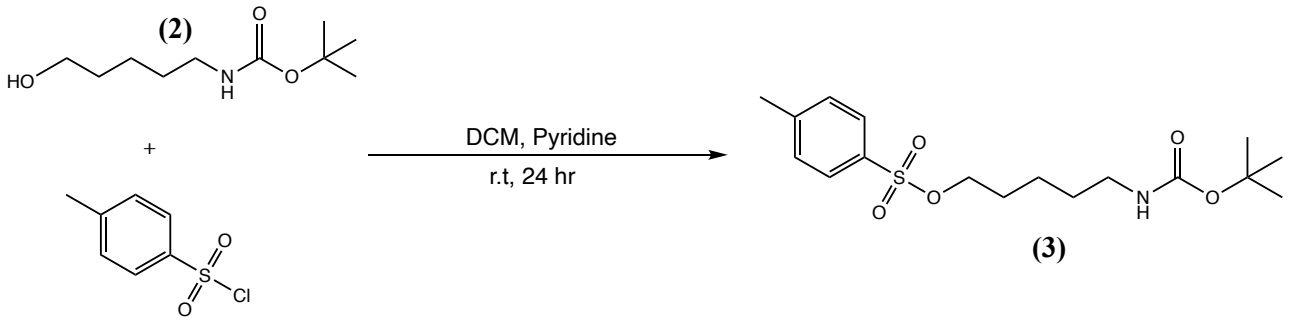


Scheme 2.3. Reaction scheme for the formation of N-(Boc)-5-amino-1-pentanol ***(2)****.*

Potassium bicarbonate (14.20 g, 141.0 mmol) and 5-amino-1-pentanol (5.22 g, 50.6 mmol) were suspended in H_2O (60 mL). The white suspension was cooled (0-10 ^{0}C), then di-tert-butyl dicarbonate (2 M in THF (25 mL), 50 mmol) was added slowly, with additional THF (25 mL). This was heated to 50 °C and stirred for 24 hrs. The organic phase of the biphasic mixture was separated and solvent partially removed in vacuo to form a white micro-suspension. H_2O:Et_2O (150 mL, 2:1) was added, and the organic phase separated. The aqueous phase was washed with Et_2O (50 mL) and the organic phase separated. Both organic phases were combined, dried with Na_2SO_4, and the solvent removed to give a yellow oil ***(2)*** (8.91 g, 43.9 mmol, 87%). δH (400 MHz; $CDCl_3$) 1.27 – 1.59 (6 H, m, H-5,6,7), 1.38 (9 H, s, H-1), 2.65 (1 H, s, O*H*), 3.05 (2 H, dt, *J* = 6.6, 6.7, H-4), 3.56 (2 H, dt, *J* = 4.1, 6.4, H-8), 4.75 (1 H, br s, N*H*); δC (101 MHz; $CDCl_3$) 23.0 (C-6), 28.5 (C1), 30.0 (C-7), 32.2 (C-5), 40.5 (C-4), 62.4 (C-8), 79.1 (C-2), 156.2 (C-3); MS $(ES)^+$ *m/z*: 226 $[M+Na]^+$.

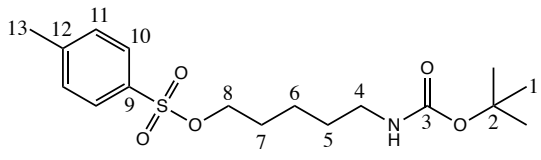


2.11.2 Synthesis of N-(Boc)-5-amino-1-tosylpentane *(3)*

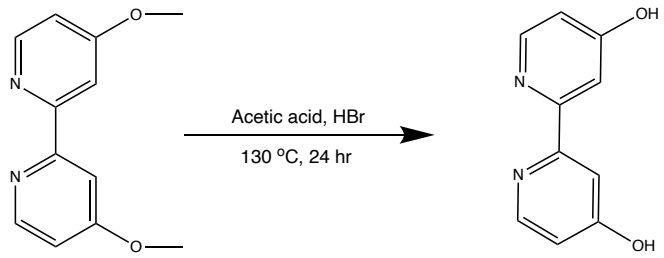


*Scheme 2.4. Reaction scheme for the formation of N-(Boc)-5-amino-1-tosylpentane **(3)**.*

(2) (6.94 g, 34.2 mmol) and para-toluenesulfonyl chloride (7.53 g, 39.5 mmol) in anhydrous CH_2Cl_2 (50 mL) was cooled (0-5 ^{0}C). Dry pyridine (11 mL, 136.5 mmol) was added slowly dropwise, maintaining the temperature of 0-5 ^{o}C. The mixture was warmed to room temperature and stirred for 24 hrs. The solvent was removed in vacuo till ~5 mL of a white suspension remained. H_2O:Et_2O (100 mL, 1:1) was added and subsequent washing of the organic phase with aqueous $NaHCO_3$ (50 mL) and brine (50 mL) and drying over Na_2SO_4 produced a yellow oil. The oil was triturated with hexane (50 mL), cooled (0-5 ^{o}C) for 48 hrs, and the resulting solid filtered and washed with cold hexane (3 x 30 mL) to give a white powder ***(3)*** (8.13 g, 22.8 mmol, 67%). δH (400 MHz; $CDCl_3$) 1.30-1.40 (4 H, m, H-6,7), 1.46 (9 H, s, H-1), 1.66 (2 H, tt, *J* = 7.4, 6.5, H-5), 2.45 (3 H, s, H-13), 3.06 (2 H, dt, *J* = 6.6, 6.7, H-4), 4.02 (2 H, t, *J* = 6.4, H-8), 4.48 (1 H, br s, N*H*), 7.35 (2 H, d, *J* = 8.2, H-10), 7.79 (2 H, d, *J* = 8.2, H-11); δC (101 MHz; $CDCl_3$) 21.8 (C-13), 22.8 (C-6), 28.5 (C-1), 28.6 (C-7), 29.6 (C-5), 40.4 (C-4), 70.5 (C-8), 79.3 (C-2), 128.0 (C-11), 130.0 (C-10), 133.2 (C-9), 144.89 (C-12), 156.1 (C-3); MS $(ES)^+$ *m/z*: 380 $[M+Na]^+$.



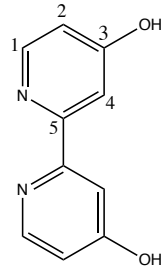
2.11.3 Synthesis of 4,4'-dihydroxy-2,2'-bipyridine *(4)*



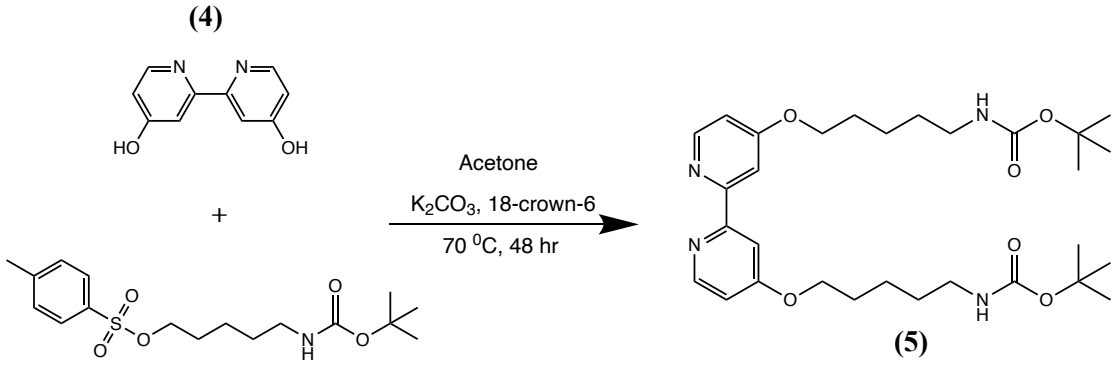
(4)

Scheme 2.5. Reaction scheme for the formation of 4,4'-dihydroxy-2,2'-bipyridine ***(4)****.*

4,4'-dimethoxy-2,2'-bipyridine (1.18 g, 5.5 mmol) was stirred in glacial acetic acid (150 mL). Hydrobromic acid (26 mL, 48%, 229.8 mmol) was added. The mixture was brought to reflux at 130 °C overnight; it was a clear brown colour. The mixture was allowed to cool, the solvent removed, the solid dissolved in water (30 mL) and neutralised with aqueous ammonia. The white precipitate was filtered under vacuum, washed with water and dried to give the product ***(4)*** (0.80 g, 4.2 mmol, 78%). δH (400 MHz; DMSO-d_6) 6.73 (2 H, d, J = 6.0, H-2), 7.48 (2 H, s, H-4), 8.23 (2 H, d, J = 6.0, H-1); δC (101 MHz; DMSO-d_6) 109.6 (C-2), 113.4 (C-4), 147.3 (C-1), 151.8 (C-3), 168.4 (C-5); MS $(ES)^+$ m/z: 189 $[M+H]^+$.

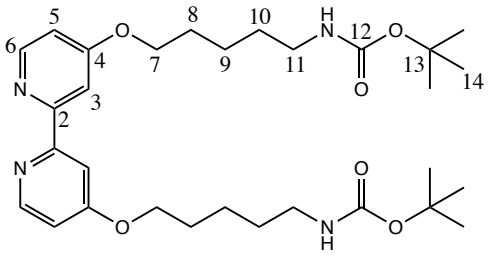


2.11.4 Synthesis of 4,4'-di-(N-(Boc)-5-amino-1-pentoxy)-2,2'-bipyridine *(5)*

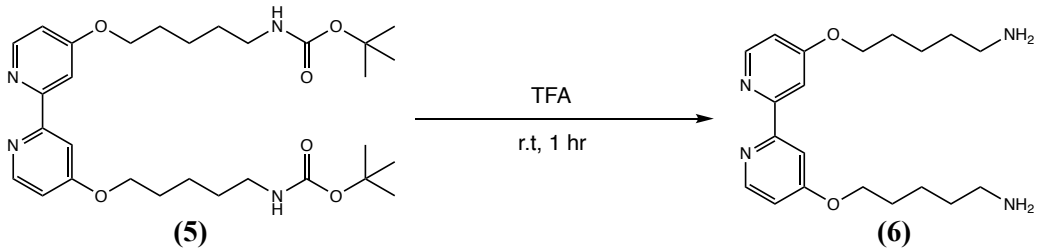


*Scheme 2.6. Reaction scheme for the formation of 4,4'-di-(N-(Boc)-5-amino-1-pentoxy)-2,2'-bipyridine **(5)**.*

Potassium carbonate (2.23 g, 16.1 mmol), ***(3)*** (5.67 g, 15.9 mmol), ***(4)*** (0.94 g, 5.0 mmol (obtained from PhD researcher Luke Watson)) and 18-crown-6 (catalytic) in acetone (210 mL) were stirred and brought to reflux at 70 ºC for 48 hrs, changing the colour from white to yellow. The yellow mixture was hot filtered, cooled to room temperature, and the filtrate was re-filtered to reveal a pale yellow solid. The solid was washed with water and dried, giving a final pale yellow solid ***(5)*** (2.67 g, 4.8 mmol, 96%). δH (300 MHz; $CDCl_3$) 1.43 (18 H, s, H-14), 1.48 – 1.60 (8 H, m, H-8,9), 1.83 (4 H, tt, *J* = 9.1, 8.9, H-10), 3.15 (4 H, dt, *J* = 8.5, 8.2, H-11), 4.12 (4 H, t, *J* = 6.3, H-7), 4.57 (2 H, br s, N*H*), 6.81 (2 H, dd, *J* = 5.6, 2.5, H-5), 7.93 (2 H, d, *J* = 2.5, H-3), 8.44 (2 H, d, *J* = 5.6, H-6); δC (101 MHz; $CDCl_3$) 23.4 (C-9), 28.6 (C-14), 28.8 (C-8), 29.9 (C-10), 40.6 (C-11), 67.9 (C-7), 79.3 (C-13), 106.8 (C-3), 111.5 (C-5), 150.3 (C-6), 156.1 (C-12), 158.0 (C-2), 166.2 (C-4); MS $(ES)^+$ *m/z*: 559 $[M+H]^+$.

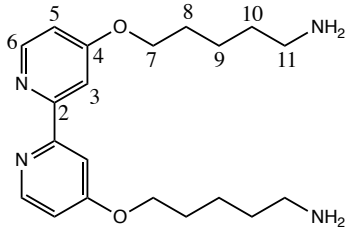


2.11.5 Synthesis of 4,4'-di-(5-amino-1-pentoxy)-2,2'-bipyridine *(6)*

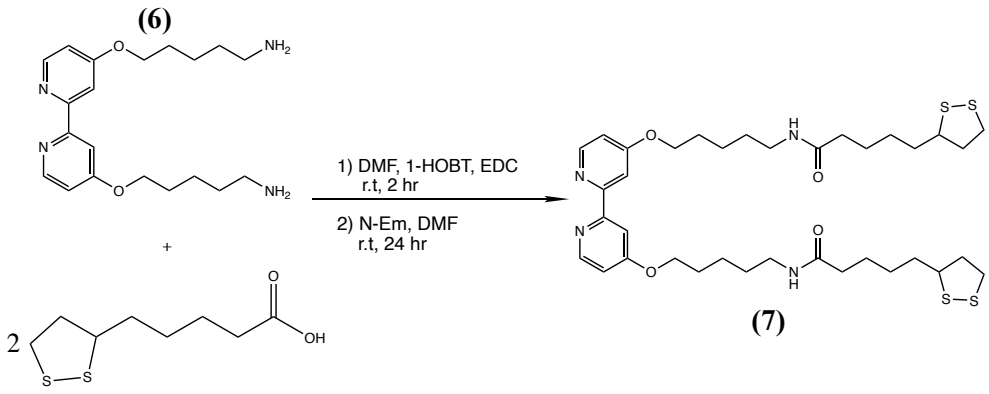


Scheme 2.7. Reaction scheme for the formation of 4,4'-di-(5-amino-1-pentoxy)-2,2'-bipyridine ***(6)****.*

(5) (0.33 g, 0.59 mmol) in TFA (15 mL) was stirred for 1 hour. The solvent was removed in vacuo. NaOH (1 M, 20 mL) was added and the product extracted with chloroform (20 mL). The aqueous phase was washed with chloroform (2 x 10 mL) and the organic phases combined and dried with Na_2SO_4 to give a pale yellow solid (0.17 g, 0.47 mmol, 80%). δH (400 MHz; CD_3OD) 1.42 – 1.65 (8 H, m, H-8,9), 1.85 (4 H, tt, *J* = 6.6, 6.7, H-10), 2.65 (4 H, t, *J* = 6.8, H-11), 4.17 (4 H, t, *J* = 6.4, H-7), 6.99 (2 H, dd, *J* = 5.8, 2.5, H-5), 7.79 (2 H, d, *J* = 2.5, H-3), 8.42 (2 H, d, *J* = 5.8, H-6); δC (101 MHz; CD_3OD) 24.4 (C-9), 29.8 (C-8), 33.5 (C-10), 42.4 (C-11), 69.4 (C-7), 109.0 (C-3), 112.1 (C-5), 151.4 (C-6), 158.7 (C-2), 168.0 (C-4); MS $(AP)^+$ *m/z*: 359 $[M+H]^+$.

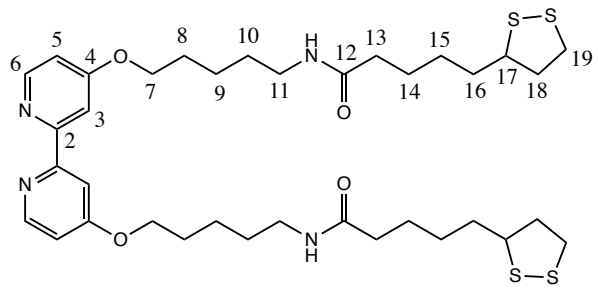


2.11.6 Synthesis of 4,4'-di-(5-lipoamido-1-pentoxy)-2,2'-bipyridine *(7)*

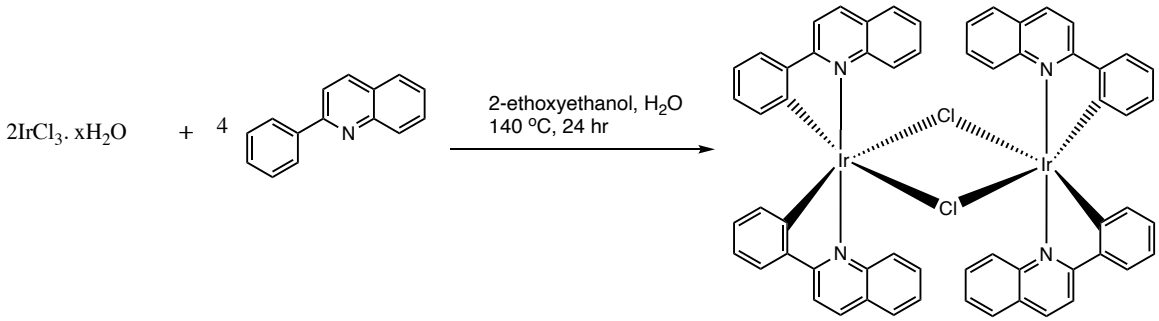


*Scheme 2.8. Reaction scheme for the formation of 4,4'-di-(5-lipoamido-1-pentoxy)-2,2'-bipyridine **(7)**.*

Lipoic acid (230.08 mg, 1.1 mmol) and 1-hydroxybenzotriazole hydrate (195.87 mg, 1.5 mmol) were cooled (0-5 ºC) in DMF (10 mL). 1-ethyl-3-(3-dimethylaminopropyl)carbodiimide (261.62 mg, 1.4 mmol) was added and stirred till fully dissolved (~ 1 hour), then warmed to room temperature and stirred for a further hour. N-ethyl morpholine (180.12 mg, 196 µL, 1.2 mmol) and ***(6)*** (170 mg, 0.47 mmol) in DMF (2 mL) were added and the mixture stirred overnight. The suspension was filtered and dried in air. The solid was washed in chloroform to give the final solid (180 mg, 0.25 mmol, 52%). δH (400 MHz; $CDCl_3$) 1.37 – 1.57 (12 H, m, H-8,9,15), 1.65 – 1.75 (8 H, m, H-14,16), 1.79 – 1.96 (6 H, m, H-10, H-18'), 2.17 (4 H, t, *J* = 7.3, H-13), 2.45 (2 H, dtd, *J* = 12.7, 6.5, 6.4, H-18), 3.03 – 3.21 (4 H, m, H-19), 3.29 (4 H, dt, *J* = 6.4, 6.6, H-11), 3.57 (2 H, tdd, *J* = 5.9, 8.3, 6.4, H-17), 4.13 (4 H, t, *J* = 6.3, H-7), 5.47 (2 H, s, N*H*), 6.82 (2 H, dd, *J* = 5.6, 2.5, H-5), 7.94 (2 H, d, *J* = 2.5, H-3), 8.45 (2 H, d, *J* = 5.6, H-6); δC (101 MHz; $CDCl_3$) 23.5 (C-9), 25.6 (C-14), 28.7 (C-15), 29.1 (C-8), 29.5 (C-10), 34.8 (C-16), 36.7 (C-13), 38.6 (C-19), 39.5 (C-11), 40.4 (C-18), 56.6 (C-17), 67.9 (C-7), 106.9 (C-3), 111.4 (C-5), 150.3 (C-6), 162.1 (C-2), 166.2 (C-4), 172.8 (C-12); MS $(ES)^+$ *m/z*: 735 $[M+H]^+$ (Supplementary Figure 2.11).

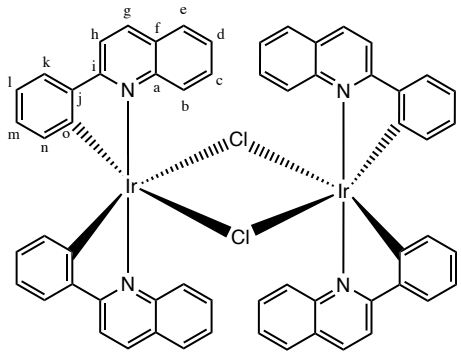


2.12 Synthesis of $[Ir(pq)_2Cl]_2$ dimer

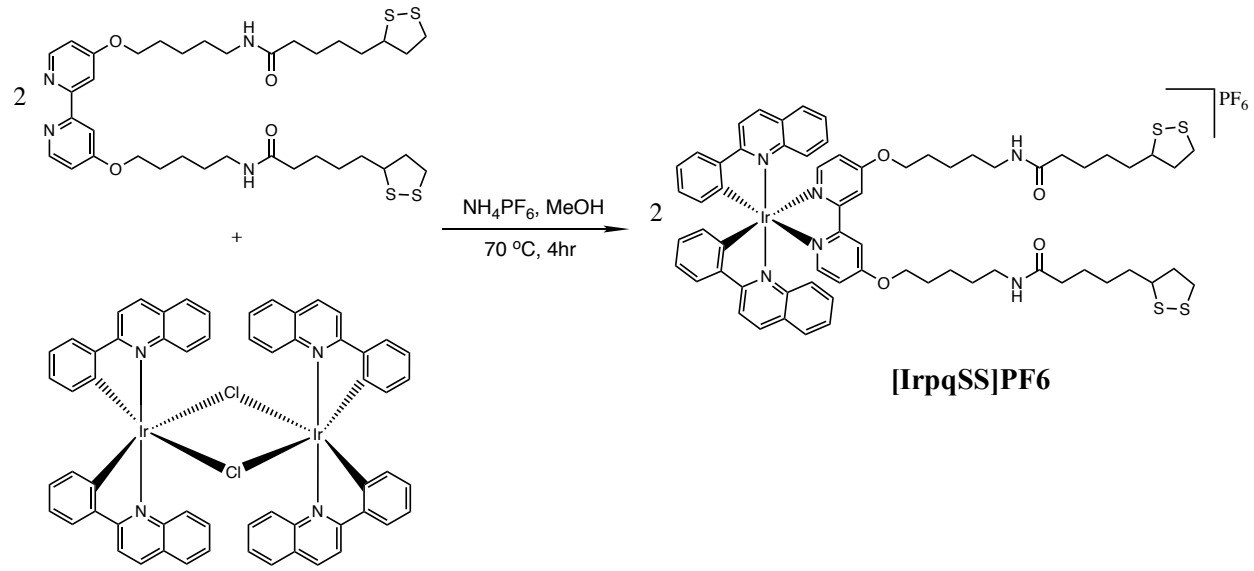


Scheme 2.9. Reaction scheme for the formation of ***$[Ir(pq)_2Cl]_2$*** *dimer.*

This synthesis was modified from published protocols[26,27]. $IrCl_3 \bullet xH_2O$ (389.13 mg, 1.3 mmol) and 2-phenylquinoline (515.61 mg, 2.5 mmol) were dissolved in 2-ethoxyethanol (30 mL) and H_2O (10 mL) and brought to reflux at 140 ^{0}C for 24 hrs. A colour change from dark brown to red-brown was observed. The mixture was cooled to room temperature, filtered and the residue washed with MeOH (60 mL) and acetone (60 mL). The filtrates were collected and the solvent removed in vacuo. The dark orange oily solid was dissolved in DCM (80 mL), washed with 0.1 M HCl (3 x 20 mL), dried with Mg_2SO_4 and had the solvent removed. The solid was re-dissolved in the minimum amount of DCM and hexane was added to induce precipitation. The solvents were removed in vacuo to reveal a dark orange solid (410 mg, 0.3 mmol, 50%). λ_{max} (MeCN) / nm (ε / $dm^3mol^{-1}cm^{-1}$), 259 (110100), 279 (68600), 323 (32900), 337 (30000) and 418 (6 100); δH (400 MHz; CD_2Cl_2) 7.50 – 7.59 (6 H, m, H-h,m,l), 7.63 (2 H, t, *J* = 7.5, H-d), 7.80 (2H, t, *J* = 7.7, H-c), 7.93 (2 H, d, *J* = 8.1, H-n), 7.97 (2 H, d, *J* = 8.6, H-k), 8.23 (2 H, d, *J* = 7.5, H-e), 8.23 (2 H, d, *J* = 7.7, H-b), 8.41 (2 H, d, *J* = 8.8, H-g); MS $(ES)^+$ *m/z*: 1238 $[M\text{-}Cl]^+$ (Supplementary Figure 2.9, Supplementary Figure 2.16).



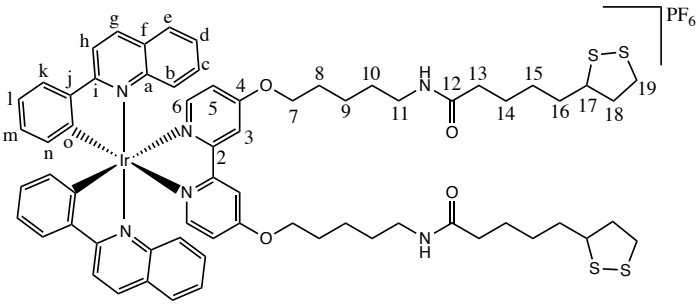
2.13 Synthesis of $[Ir(pq)_2bpySS]PF_6$ complex *[IrpqSS]PF6*



*Scheme 2.10. Reaction scheme for the formation of the **[IrpqSS]PF6** complex.*

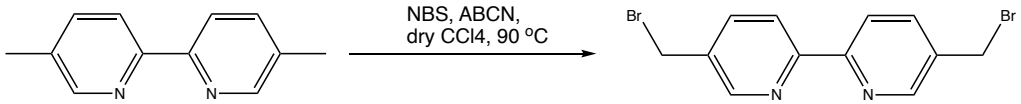
This synthesis was modified from published protocols[19,24]. $[Ir(pq)_2Cl]_2$ (49.59 mg, 0.04 mmol) and ***(7)*** (54.90 mg, 0.07 mmol) and ammonium hexafluorophosphate (12.28 mg, 0.08 mmol) in MeOH (10 mL) were brought to reflux at 70 ºC for 4 hrs. The mixture was cooled to room temperature, the solvent removed, the orange product dissolved in DCM (30 mL), filtered and the filtrate had the solvent removed in vacuo till ~5 mL remained. Hexane was added to induce precipitation, then all the solvent was removed to reveal an oily orange product (115 mg, 0.08 mmol, 104%). The product was purified using column chromatography (aluminium oxide, DCM/MeOH, 99:1) to yield the final product (53.3 mg, 0.04 μmol, 48%). ν_{max} / cm^{-1} 850 (PF_6 asymmetric stretch), 568 (symmetric stretch); δH (400 MHz; Acetone) 1.33 – 1.54 (16 H, m, H-9,10,15,16), 1.53 – 1.63 (6 H, m, H-13*,14), 1.77 (4 H, tt, *J* = 7.2, 6.6, H-8), 1.86 (2 H, dtd, *J* = 12.7, 6.3, 6.4, H-18*), 2.01-2.04 (4 H, H-13, masked by NMR solvent), 2.43 (2 H, dtd, *J* = 12.7, 6.3, 6.4, H-18), 3.00 – 3.22 (8 H, m, H-11,19), 3.55 (2 H, tdd, *J* = 6.1, 8.7, 6.2, H-17), 4.19 (4 H, t, *J* = 6.5, H-7), 6.54 (2 H, dd, *J* = 7.6, 0.8, H-n), 6.79 (2 H, td, *J* = 7.6, 7.4, 1.2, H-m), 7.07 – 7.12 (2 H, s, N***H***), 7.12 – 7.17 (2 H, m, H-l), 7.17 – 7.23 (4 H, m, H-5,d), 7.47 (2 H, ddd, *J* = 8.0, 7.0, 0.9, H-c), 7.52 (2 H, d, *J* = 8.8, H-e), 7.95 (2 H, dd, *J* = 8.1, 1.2, H-b), 8.02 (2 H, d, *J* = 2.5,

H-3), 8.05 (2 H, d, *J* = 6.5, H-6), 8.22 (2 H, dd, *J* = 8.0, 0.9, H-k), 8.47 – 8.56 (4 H, m, H-h,g); δC (101 MHz; Acetone) 23.8 (C-9), 26.3 (C-14), 28.9 (C-8), 29.3 – 30.9 (C-10,15, masked by NMR solvent), 35.5 (C-16), 36.6 (C-13), 39.2 (C-19), 39.3 (C-11), 41.0 (C-18), 57.4 (C-17), 70.5 (C-7), 111.8 (C-3), 115.4 (C-2), 118.8 (C-h,g), 123.6 (C-l), 126.0 (C-e), 127.7 (C-c), 128.3 (C-f), 128.9 (C-k), 130.3 (C-b), 131.4 (C-m), 131.9 (C-5,d), 135.4 (C-n), 141.1 (C-h,g), 147.1 (C-i), 148.6 (C-j), 149.8 (C-6), 152.8 (C-o), 158.3 (C-5,d), 168.3 (C-a), 171.4 (C-4), 205.9 (C-12); MS $(ES)^+$ *m/z*: 1335 $[M\text{-}PF_6]^+$(Supplementary Figure 2.12). NMR assignments confirmed by COSY, HSQC and HMBC.



2.14 Two-step synthesis of bpySH ligand

2.14.1 Synthesis of 5,5'-Bis(bromomethyl)-2,2'-bipyridine *(9)*

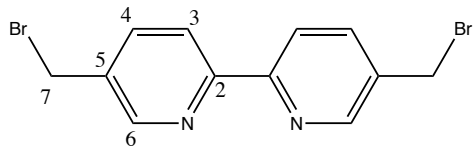


(8) **(9)**

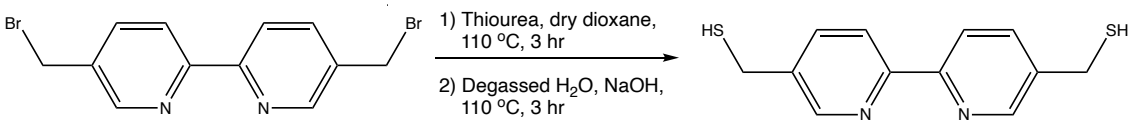
*Scheme 2.11. Reaction scheme for the formation of the bis-bromo ligand **(9)**.*

This synthesis method was obtained from published protocols[20]. 5,5'-Dimethyl-2,2'-bipyridyl (570.83 mg, 3.1 mmol), N-bromosuccinimide (2.90 g, 16.3 mmol) and 1,1'-azidobis(cyclohexanecarbonitrile) (79.93 mg, 0.3 mmol) were stirred together in dry CCl_4 (50 mL) and brought to reflux at 90 °C while monitoring by TLC (silica gel, DCM:MeOH, 1:1). A colour change from cloudy white to cloudy yellow observed. The reaction was hot filtered and the filtrate had the solvent removed in vacuo. The solid was dissolved in DCM (100 mL) and washed with sodium thiosulfate (23.72 g, 0.5M, 2 x 150 mL). The

aqueous phase was washed with DCM (2 x 50 mL) and the combined DCM fractions had the solvent removed to reveal a crude pale yellow solid (1.9 g). This was recrystallised from DCM to give a white solid (219.12 mg, 0.6 mmol, 21%). δH (300 MHz; $CDCl_3$) 4.54 (4 H, s, H-7), 7.86 (2 H, dd, *J* = 8.2, 2.4, H-4), 8.40 (2 H, dd, *J* = 8.2, 0.8, H-3), 8.68 (2 H, dd, *J* = 2.4, 0.8, H-6); δC (101 MHz; $CDCl_3$) 29.7 (C-7), 121.3 (C-3), 134.0 (C-5), 137.8 (C-4), 149.5 (C-6), 155.6 (C-2); MS $(ASAP)^+$ *m/z*: 343 $[M+H]^+$ (Supplementary Figure 2.13).



2.14.2 Synthesis of 5,5'-Bis(mercaptomethyl)-2,2'bipyridine *(10)*

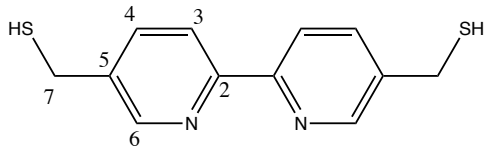


(9) **(10)**

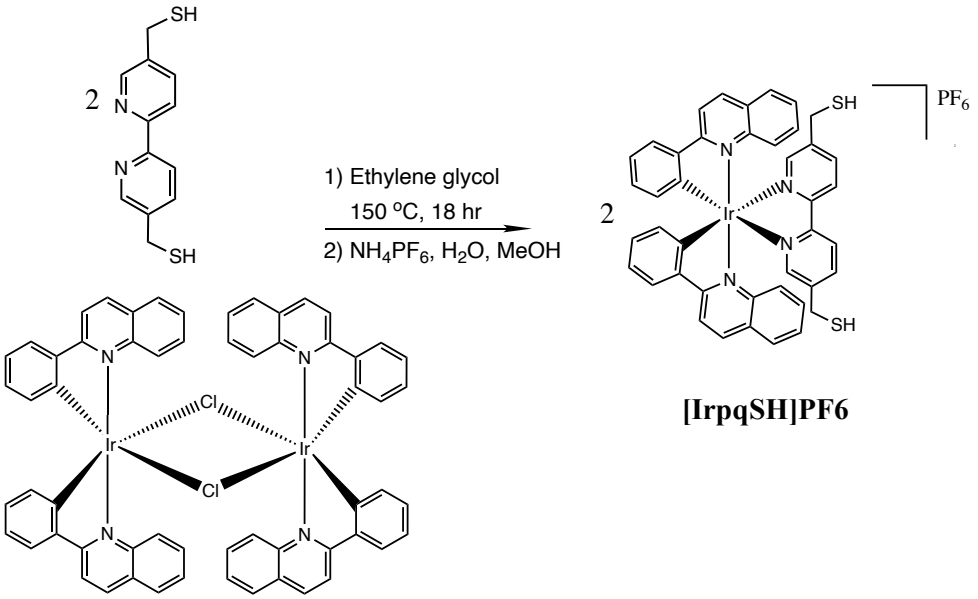
*Scheme 2.12. Reaction scheme for the formation of the **bpySH** ligand.*

This synthesis method was obtained from published protocols[28]. 5,5'-Bis(bromomethyl)-2,2'-bipyridine (105.70 mg, 0.3 mmol) and thiourea (65 mg, 0.9 mmol) were stirred in dry dioxane (15 mL) and brought to reflux at 110 °C for 3 hrs, during which there was a colour change from cloudy white to cloudy yellow. Degassed H_2O (5 mL) with NaOH (40 mg, 1.0 mmol) was added and the reflux continued for a further 3 hrs, during which the colour changed from pale yellow to clear yellow. The solvent was removed in vacuo to reveal a yellow material. Acidified degassed H_2O (12.5 mL, pH ~4) was added, and the aqueous phase extracted with DCM (5 x 20 mL). The organic phases were collected and the solvent removed in vacuo to give a yellow solid (51.4 mg, 0.2 mmol, 67%). δH (300 MHz;

$CDCl_3$) 3.81 (4 H, s, H-7), 7.80 (2 H, dd, *J* = 8.2, 2.4, H-4), 8.35 (2 H, d, *J* = 8.2, H-3), 8.61 (2 H, d, *J* = 2.4, H-6); MS $(ASAP)^+$ *m/z*: 249 $[M+H]^+$ (Supplementary Figure 2.13).



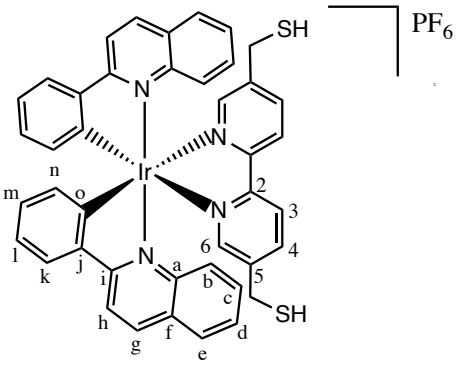
2.15 Synthesis of [Ir(pq)$_2$bpySH]PF6 complex *[IrpqSH]PF6*



*Scheme 2.13. Reaction scheme for the formation of the **[IrpqSH]PF6** complex.*

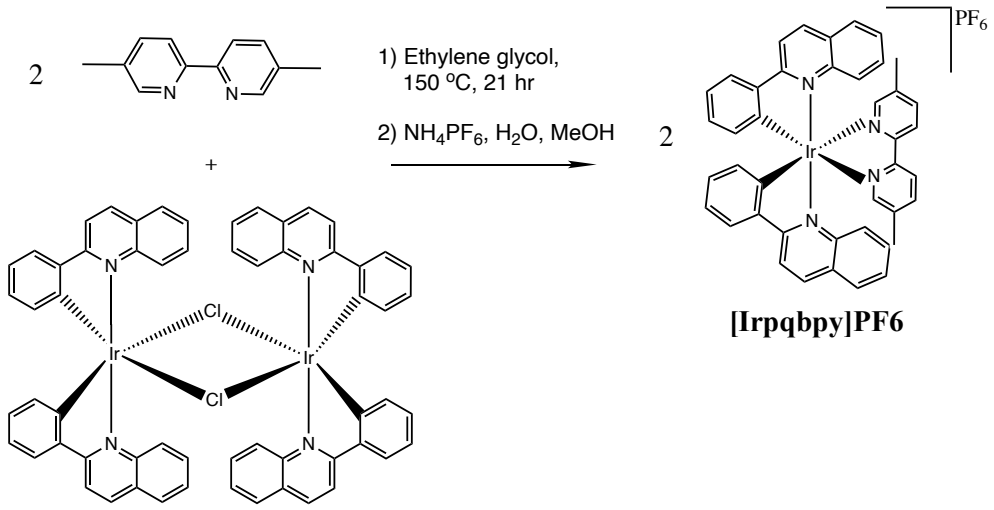
This synthesis was modified from published protocols[19,24]. $[Ir(pq)_2Cl]_2$ (92.15 mg, 0.07 mmol) and 5,5'-bis(mercaptomethyl)-2,2'bipyridine (51.4 mg, 0.21 mmol) were stirred together in ethylene glycol (6.5 mL) and brought to reflux at 150 °C for 18 hrs. H_2O (20 mL) and concentrated NH_4PF_6 in MeOH was added till the orange precipitate stopped forming. This was cooled (0 -5 °C), filtered and washed with H_2O. The orange-yellow product was washed with chloroform and dried (32.81 mg, 0.03 μmol, 23%). ν_{max} / cm^{-1} 828 (PF_6 asymmetric stretch), 559 (symmetric stretch); δH (400 MHz; Acetone) 2.29 (1 H, t, *J* = 8.4, S***H***), 3.75 (2 H, qd, *J* = 14.4, 8.5, **CH_2**), 6.56 (1 H, d, *J* = 7.8, H-n), 6.81 (1 H, ddd, *J* = 7.5,

7.4, 1.3, H-m), 7.09 (1 H, ddd, *J* = 8.7, 6.9, 1.6, H-c), 7.17 (1 H, ddd, *J* = 7.5, 6.9, 1.2, H-l), 7.36 – 7.49



(2 H, m, H-b,d), 7.87 (1 H, dd, *J* = 8.0, 1.4 , H-e), 8.00 (1 H, d, *J* = 2.1, H-4), 8.20 – 8.26 (2 H, m, H-k,3), 8.36 (1H, d, *J* = 2.1, H-6), 8.45 – 8.53 (2 H, m, H-h,g); MS $(ES)^+$ *m/z*: 849 $[M\text{-}PF_6]^+$ (Supplementary Figure 2.14). NMR assignments confirmed by COSY.

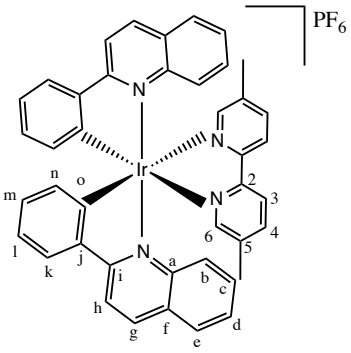
2.16 Synthesis of $[Ir(pq)_2bpy]PF6$ complex *[Irpqbpy]PF6*



*Scheme 2.14. Reaction scheme for the formation of the **[Irpqbpy]PF6** complex.*

5,5'-Dimethyl-2,2'-bipyridyl (24.97 mg, 0.14 mmol) and $[Ir(pq)_2Cl]_2$ (66.35 mg, 0.05 mmol) was stirred in ethylene glycol (6.5 mL) and brought to reflux at 150 °C for 21 hrs. H_2O (20 mL) and concentrated NH_4PF_6 in MeOH were added till the orange precipitate stopped forming. This was cooled (0-5 °C), filtered and washed with H_2O. Purification by column chromatography (aluminium oxide, DCM/MeOH, 99:1) gave the final orange solid (32.81 mg, 0.033 μmol, 32%). ν_{max} / cm^{-1} 833 (PF_6

asymmetric stretch), 564 (symmetric stretch); δH (400 MHz; Acetone) 2.26 (3 H, s, C***H₃***), 6.57 (1 H, ddd, *J* = 7.7, 1.2, 0.5, H-n), 6.83 (1 H, ddd, *J* = 7.7, 7.2, 1.3, H-m), 7.08 – 7.21 (2 H, m, H-b,l), 7.40 – 7.49 (2 H, m, H-c,e), 7.85 – 7.95 (2 H, m, H-4,d), 8.10 (1 H, dd, *J* = 2.1, 0.7, H-6), 8.19 – 8.28 (2 H, m, H-3,k), 8.48 – 8.56 (2 H, m, H-g,h); MS $(ES)^+$ *m/z*: 785 $[M\text{-}PF_6]^+$ (Supplementary Figure 2.15). NMR assignments confirmed by COSY.



2.17 Dowex ion exchange to form IrpqSS, IrpqSH and Irpqbpy from the PF6- salts

Dowex 1x8 200-400 (Cl) in a nanoparticle column was washed with deionised H_2O and MeOH. **[IrpqSS]PF6**, **[IrpqSH]PF6** or **[Irpqbpy]PF6** solutions in MeOH were passed through the Dowex to obtain a methanol solution of iridium(III) complex in chloride form (**IrpqSS**, **IrpqSH** and **Irpqbpy**).

IrpqSS:

λ_{max} (MeOH) / nm (ε / $dm^3mol^{-1}cm^{-1}$), 260 (36100), 335 (15600), and 440 (3200); λ_{max} (H_2O) / nm (ε / $dm^3mol^{-1}cm^{-1}$), 260 (27000), 335 (11600), and 440 (2300).

IrpqSH:

λ_{max} (MeOH) / nm (ε / $dm^3mol^{-1}cm^{-1}$), 259 (16200), 280 (15900), 321 (10000), and 435 (1600); λ_{max} (H_2O) / nm (ε / $dm^3mol^{-1}cm^{-1}$), 257 (13300), 279 (13000), 317 (8000), and 430 (1300).

Irpqbpy:

λ_{max} (MeOH) / nm (ε / $dm^3mol^{-1}cm^{-1}$) 260 (32700), 280 (31100), 313 (16700), 334 (14200) and 438 (3100); λ_{max} (H_2O) / nm (ε / $dm^3mol^{-1}cm^{-1}$) 260 (31600), 280 (27900), 313 (15900), 334 (13200) and 438 (3000).

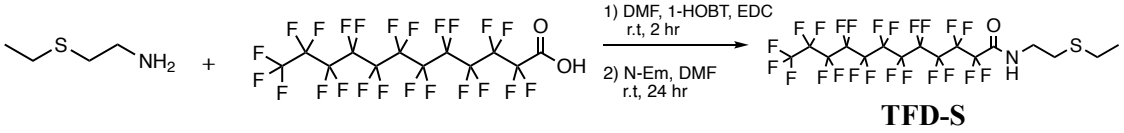
2.18 Gold nanoparticle synthesis *(AuNP13)*

The protocol for synthesis was obtained based on the method by Vossmeyer *et al.*[44] Trisodium citrate (60.6 mg, 0.23 mmol), Citric acid (13.3 mg, 0.07 mmol) and EDTA (1.3 mg, 0.004 mmol) were stirred and heated in MilliQ H_2O (100 mL) for 15 mins at 150 ºC. $HAuCl_4$ (8 mg, 0.02 mmol) was dissolved in MilliQ H_2O (25 mL) and heated to 100 ºC for 15 minutes. This was added quickly to the 100 mL citrate solution, causing a colour change from colourless to red pink. The reflux was continued for a further 30 mins in the dark, then the reaction was stirred and cooled to room temperature for 1 hr to make 125 mL of 1.5 ± 0.15 nM **AuNP13**s. λ_{max} (H_2O) = 517 nm (SPR), ζ-potential = -47.9 ± 9 mV, Diameter = 13 ± 0.31 nm (DLS number distribution), PDI = 0.092.

2.19 Gold nanoparticle synthesis *(AuNP25)*

The protocol for synthesis was obtained based on the published method by Ziegler *et al.*[54] Three stock solutions were made up. A) $HAuCl_4$ stock solution (5 mM): 49.25 mg (0.13 mmol) in filtered MilliQ H_2O (25 mL); B) Ascorbic acid stock solution (57 mM): 251mg (0.14 mmol) in filtered MilliQ H_2O (25 mL); C) Trisodium citrate stock solution (34 mM): 250 mg (0.85 mmol) in filtered MilliQ H_2O (25 mL). From these stock solutions, two seed solutions were made: Seed solution 1) $HAuCl_4$ stock solution (4 mL) and filtered MilliQ H_2O (16 mL); Seed solution 2) Ascorbic acid stock solution (1 mL), Trisodium citrate stock solution (0.5 mL) and filtered MilliQ H_2O (18.5 mL). **AuNP13**s (34 mL) had MilliQ H_2O (6 mL) added and were seeded with seed solutions 1) and 2) at room temperature using a peristaltic pump at a speed of 16.9. Then the NPs were brought to reflux for 30 mins at 150 ºC. They were stirred and cooled to room temperature for 1 hr to make 0.7 nM of **AuNP25**s. λ_{max} (H_2O) = 519 nm (SPR). Diameter 18 ± 5 nm (DLS number distribution), PDI = 0.104.

2.20 Synthesis of N-(2-(ethylthio)ethyl) tricosafluorododecanamide) surfactant *(TFD-S)*



*Scheme 2.15. Reaction scheme for the formation of **TFD-S** surfactant.*

Tricosafluorododecanoic acid (1001.02 mg, 1.63 mmol) and 1-hydroxybenzotriazole hydrate (326.44 mg, 2.42 mmol) were stirred in DMF (10 mL). The mixture was a cloudy white colour. The mixture was cooled on ice while under N_2, then 1-ethyl-3-(3-dimethylaminopropyl)carbodiimide (361.42 mg, 2.33 mmol) was added. The mixture was warmed and stirred for 1 hr under N_2. 2-(ethylthio)ethylamine (217 mg, 229 μL, 1.63 mmol) and N-ethyl morpholine (262 mg, 287.91 μL, 1.69 mmol) were added with DMF (10 mL), turning the cloudy white reaction mixture a yellow-orange colour. The mixture was stirred under N_2 overnight, then the solvent removed and the crude mixture purified using chromatography (aluminium oxide, DCM/MeOH, 9:1) followed by HPLC in a MeCN:H_2O mixture, to obtain the pure product (16.81 mg, 24 μmol, 1.5%). δH (400 MHz; CD_3OD) 1.27 (3H, t, *J* = 7.4, H-1), 2.60 (2H, q, J = 7.4, H-2), 2.75 – 2.67 (2H, m, H-3), 3.50 (2H, t, J = 7.1, H-4); δF (282 MHz; CD_3OD) -82.27, -118.03, -122.66, -123.60, -126.92 – -127.62; MS (ESI)$^-$ *m/z*: 700 $[M-H]^-$ (Supplementary

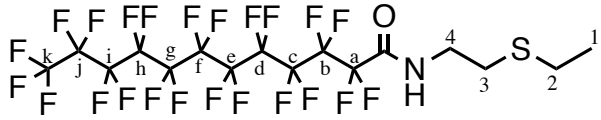


Figure 2.10, Supplementary Figure 2.17).

2.21 Coating of AuNP13 and AuNP25 with LPEG, SPEG, Zonyl-FSA and TFD-S surfactants

LPEG (Poly(ethylene glycol) 2-mercaptoethyl ether acetic acid, average M_n 2100) was obtained from sigma Aldrich, **SPEG** (α-Thio-ω-(propionic acid) octa(ethylene glycol)) was obtained from Iris

Biotech and **Zonyl-FSA** (Lithium 3-[2-(perfluoroalkyl)ethylthio]propionate,) was obtained from Sigma Aldrich. **TFD-S** (N-(2-(ethylthio)ethyl)-2,2,3,3,4,4,5,5,6,6,7,7,8,8,9,9,10,10,11,11,12,12,12-tricosafluorododecanamide) was synthesised from the experimental procedure described in "Synthesis of N-(2-(ethylthio)ethyl) tricosafluorododecanamide) surfactant *(TFD-S)*".

LPEG and **SPEG** surfactants were dissolved in H_2O to make a 1 mM solution. **Zonyl-FSA** (0.5 M, 25 wt.% Li carboxylate salt in water: isopropyl alcohol) was diluted in H_2O to make a 0.05 mM solution (0.05 M 2.5 wt.% Li carboxylate salt in water:isopropyl alcohol). TFD-S was dissolved in MeOH to make a 1 mM solution.

AuNP13 (3 x 2 mL, 1.5 nM) were centrifuged at 10 xg for 30 minutes at room temperature. The supernatant was removed and the NPs resuspended in MilliQ H_2O (3 x 1 mL) to make **AuNP13** (3 x 1 mL, 2.6 nM). **LPEG** (3 x 10 μL, 1mM) was added to **AuNP13** (3 x 1 mL, 2.6 nM). This was stirred for 20 minutes at room temperature. The NPs were centrifuged at 10 xg for 30 minutes at room temperature. The supernatant was removed and the NPs resuspended in MilliQ H_2O and combined to make 1 mL of 6 nM **LPEG.AuNP13**. This was diluted with MilliQ water in a 1:1 ratio to make 2 x 1 mL of 3 nM **LPEG.AuNP13**. This process was repeated with SPEG (30 μL, 1 mM) and TFD-S (10μL, 1 mM) to make 2 x 1 mL of 3 nM **SPEG.AuNP13** and **TFD-S.AuNP13**. The process was also repeated with Zonyl (10 μL, 0.05M), however the NPs were centrifuged twice after stirring for 20 minutes with Zonyl to obtain 2 x 1 mL of 3 nM **Zonyl.AuNP13**.

AuNP25 (2 x 2 mL, 0.7 nM) were centrifuged at 10 xg for 25 minutes at room temperature. The supernatant was removed and the NPs resuspended in MilliQ H_2O (2 x 1 mL) to make **AuNP25** (2 x 1 mL, 1.3 nM). **LPEG** (2 x 10 μL, 1mM) was added to **AuNP25** (2 x 1 mL, 1.3 nM). This was stirred for 20 minutes at room temperature. The NPs were centrifuged at 10 xg for 25 minutes at room temperature. The supernatant was removed and the NPs resuspended in MilliQ H_2O and combined to make 1 mL of 4 nM **LPEG.AuNP25**. This was diluted with MilliQ water in a 1:1 ratio to make 2 x 1 mL of 2 nM

LPEG.AuNP25. This process was repeated with SPEG (30 μL, 1 mM) and TFD-S (10μL, 1 mM) to make 2 x 1 mL of 2 nM **SPEG.AuNP25** and **TFD-S.AuNP25**. The process was also repeated with Zonyl (10 μL, 0.05M), however the NPs were centrifuged twice after stirring for 20 minutes with Zonyl.

2.22 Coating of LPEG.AuNP, SPEG.AuNP, Zonyl.AuNP and TFD-S.AuNP with IrpqSS and IrpqSH complexes

IrpqSS and **IrpqSH** were dissolved in MeOH to make a 1 mM solution. **IrpqSS** (20 μM) was added to **LPEG.AuNP13** (1 mL, 3 nM) while stirring for 20 minutes. The NPs were purified using a Sephadex G-25 column in deionised H_2O to produce 1.7 nM of **IrpqSS.LPEG.AuNP13**.

This method was repeated with **IrpqSH** (20 μM) while stirring for 20 minutes. Sephadex G-25 in deionised H_2O was used to purify the NPs to produce 1.7 nM of **IrpqSH.LPEG.AuNP13**.

This coating method for **IrpqSS** and **IrpqSH** was repeated with **SPEG.AuNP13**, **Zonyl.AuNP13**, **TFD-S.AuNP13**, **LPEG.AuNP25**, **SPEG.AuNP25** and **Zonyl.AuNP25** to produce 1.7 nM of iridium(III)-coated **AuNP13** as the final NP concentration and 0.9 nM of iridium(III)-coated **AuNP25** as the final NP concentration.

2.23 Preparing AuNPs for TEM imaging

NPs (5 μL), at a concentration of < 2nM were placed on EMResolution Formvar/Carbon film on Copper 200 mesh grids to be imaged using a Joel 1400 Bio Electron Microscope at the Centre for Electron Microscopy at the University of Birmingham.

2.24 Preparing samples for Quantum yield measurements

An FLSP920 spectrometer was fitted with an integrated sphere. The scatter of the required solvent was collected between 410 – 460 nm, using λ_{exc} = 440 nm, ensuring peak counts of <1 x 10^6. A filter of 475 nm was placed in the integrated sphere and emission between 500 – 800 nm, with λ_{exc} = 440 nm was collected of the solvent, at the same instrument settings. This process was repeated with a sample at which Abs_{440} = 0.1.

2.25 Preparing samples for ICP-MS analysis

Fresh aqua regia was made up from TraceSelect HNO_3 and HCl in a 1:3 ratio. The NP samples were digested in the aqua regia until the solution was clear. The solution was diluted with 4% HNO_3 solution (in ultrapure H_2O) to create a 5mL solution. This solution was diluted further to a 1:10, 1:20, 1:50 or 1:100 solution, as the experiment required. The solutions were transferred in 16.5mL polypropylene tubes to the School of Chemistry at the University of Warwick for ICP-MS analysis of gold and iridium content. Samples were run on a 7500cx ICPMS instrument with an Agilent integrated auto-sampler. PlasmaCal calibration standards were obtained from QMX laboratories. Calibration curves were fitted to R^2 values of <0.998 and the standard solutions of gold used were 0, 5, 10, 25, 50, 100, 250 and 500 and 1000 ppb.

2.26 References

1. N. J. Rogers, H. C. Jeffery, S. Claire, D. J. Lewis, G. Zikeli, N. J. Hodges, S. Egginton, G. B. Nash and Z. Pikramenou, *Nanomedicine*, 2017, **12**, 2725-2740.
2. S. M. King, S. Claire, R. I. Teixeira, A. N. Dosumu, A. J. Carrod, H. Dehghani, M. J. Hannon, A. D. Ward, R. Bicknell, S. W. Botchway, N. J. Hodges and Z. Pikramenou, *J. Am. Chem. Soc.*, 2018, **140**, 10242-10249.

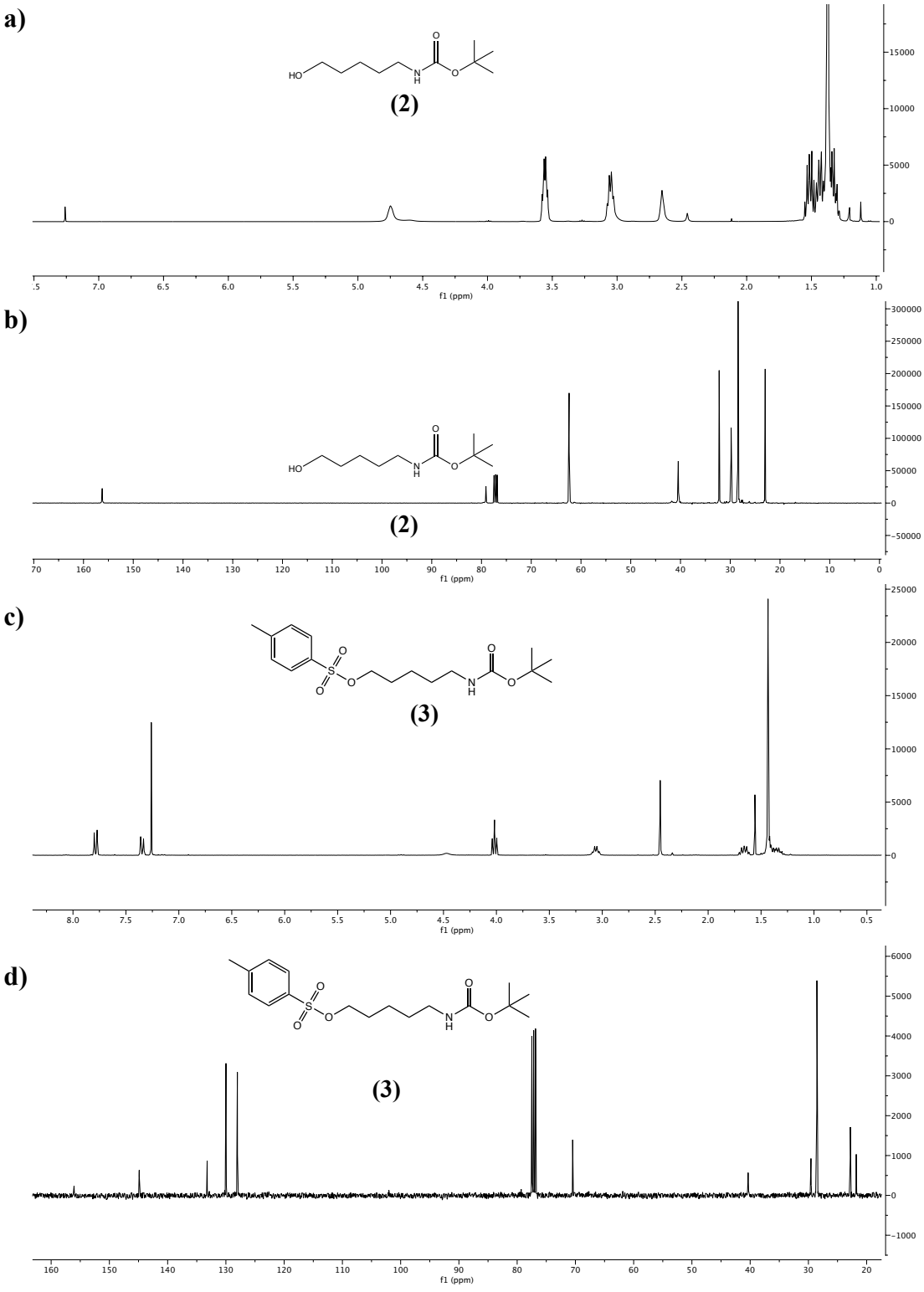
3. S. J. Adams, D. J. Lewis, J. A. Preece and Z. Pikramenou, *ACS Appl. Mater. Interfaces*, 2014, **6**, 11598-11608.
4. S. A. M. Osborne and Z. Pikramenou, *Faraday Discuss.*, 2015, **185**, 219-231.
5. A. N. Dosumu, S. Claire, L. S. Watson, P. M. Girio, S. A. M. Osborne, Z. Pikramenou and N. J. Hodges, *JACS Au*, 2021, **1**, 174-186.
6. J. R. Reimers, M. J. Ford, A. Halder, J. Ulstrup and N. S. Hush, *PNAS*, 2016, **113**, E1424-E1433.
7. Y. Xue, X. Li, H. Li and W. Zhang, *Nat. Commun.*, 2014, **5**, 4348.
8. M. S. Inkpen, Z. F. Liu, H. Li, L. M. Campos, J. B. Neaton and L. Venkataraman, *Nat. Chem.*, 2019, **11**, 351-358.
9. A. B. Tamayo, S. Garon, T. Sajoto, P. I. Djurovich, I. M. Tsyba, R. Bau and M. E. Thompson, *Inorg. Chem.*, 2005, **44**, 8723-8732.
10. A. F. Henwood and E. Zysman-Colman, *Chem. Commun.*, 2017, **53**, 807-826.
11. Y. Chen, L. Qiao, L. Ji and H. Chao, *Biomaterials*, 2014, **35**, 2-13.
12. C. Caporale and M. Massi, *Coord. Chem. Rev.*, 2018, **363**, 71-91.
13. Z. Yan, J. Wang, Y. Zhang, S. Zhang, J. Qiao and X. Zhang, *Chem. Commun.*, 2018, **54**, 9027-9030.
14. N. Yoshikawa, S. Yamazaki, N. Kato, N. Kanehisa, T. Inoue, E. Nakata and H. Takashima, *J. Mol. Struct.*, 2018, **1164**, 164-171.
15. P. A. Scattergood, A. M. Ranieri, L. Charalambou, A. Comia, D. A. W. Ross, C. R. Rice, S. J. O. Hardman, J.-L. Heully, I. M. Dixon, M. Massi, F. Alary and P. I. P. Elliott, *Inorg. Chem.*, 2020, **59**, 1785-1803.
16. K. K.-W. Lo, J. S.-W. Chan, L.-H. Lui and C.-K. Chung, *Organometallics*, 2004, **23**, 3108-3116.
17. B. Liu, L. Lystrom, S. L. Brown, E. K. Hobbie, S. Kilina and W. Sun, *Inorg. Chem.*, 2019, **58**, 5483-5493.
18. S. K. Sheet, B. Sen, K. Aguan and S. Khatua, *Dalton Trans*, 2018, **47**, 11477-11490.
19. C. Li, M. Yu, Y. Sun, Y. Wu, C. Huang and F. Li, *J. Am. Chem. Soc.*, 2011, **133**, 11231-11239.
20. M. Yu, Q. Zhao, L. Shi, F. Li, Z. Zhou, H. Yang, T. Yi and C. Huang, *Chem. Commun.*, 2008, DOI: 10.1039/B800939B, 2115-2117.
21. B. Wang, Y. Liang, H. Dong, T. Tan, B. Zhan, J. Cheng, K. K. W. Lo, Y. W. Lam and S. H. Cheng, *ChemBioChem*, 2012, **13**.
22. L. Murphy, A. Congreve, L.-O. Pålsson and J. A. G. Williams, *Chem. Commun.*, 2010, **46**, 8743-8745.
23. J. S. Nam, M.-G. Kang, J. Kang, S.-Y. Park, S. J. C. Lee, H.-T. Kim, J. K. Seo, O.-H. Kwon, M. H. Lim, H.-W. Rhee and T.-H. Kwon, *J. Am. Chem. Soc.*, 2016, **138**, 10968-10977.

24. K. Y. Zhang, H.-W. Liu, T. T.-H. Fong, X.-G. Chen and K. K.-W. Lo, *Inorg. Chem.*, 2010, **49**, 5432-5443.
25. J. Wang, J. Xue, Z. Yan, S. Zhang, J. Qiao and X. Zhang, *Angew. Chem. Int. Ed.*, 2017, **56**, 14928-14932.
26. K. Y. Zhang, Q. Yu, H. Wei, S. Liu, Q. Zhao and W. Huang, *Chem. Rev.*, 2018, **118**, 1770-1839.
27. C. Imberti, P. Zhang, H. Huang and P. J. Sadler, *Angew. Chem. Int. Ed.*, 2020, **59**, 61-73.
28. C. A. Juan, J. M. Pérez de la Lastra, F. J. Plou and E. Pérez-Lebeña, *Int. J. Mol. Sci.*, 2021, **22**.
29. P. Zhang, C. K. C. Chiu, H. Huang, Y. P. Y. Lam, A. Habtemariam, T. Malcomson, M. J. Paterson, G. J. Clarkson, P. B. O'Connor, H. Chao and P. J. Sadler, *Angew. Chem. Int. Ed.*, 2017, **56**, 14898-14902.
30. P. Zhang, H. Huang, S. Banerjee, G. J. Clarkson, C. Ge, C. Imberti and P. J. Sadler, *Angew. Chem. Int. Ed.*, 2019, **58**, 2350-2354.
31. A. Zamora, G. Vigueras, V. Rodríguez, M. D. Santana and J. Ruiz, *Coord. Chem. Rev.*, 2018, **360**, 34-76.
32. K. K.-S. Tso, K.-K. Leung, H.-W. Liu and K. K.-W. Lo, *Chem. Commun.*, 2016, **52**, 4557-4560.
33. Z. Feng, P. Tao, L. Zou, P. Gao, Y. Liu, X. Liu, H. Wang, S. Liu, Q. Dong, J. Li, B. Xu, W. Huang, W.-Y. Wong and Q. Zhao, *ACS Appl. Mater. Interfaces*, 2017, **9**, 28319-28330.
34. Q. Zhang, X. Lu, H. Wang, X. Tian, A. Wang, H. Zhou, J. Wu and Y. Tian, *Chem. Commun.*, 2018, **54**, 3771-3774.
35. E. Babu, J. Bhuvaneswari, P. Muthu Mareeswaran, P. Thanasekaran, H.-M. Lee and S. Rajagopal, *Coord. Chem. Rev.*, 2019, **380**, 519-549.
36. K. K.-W. Lo, *Acc. Chem. Res.*, 2015, **48**, 2985-2995.
37. A. Gilewska, B. Barszcz, J. Masternak, K. Kazimierczuk, J. Sitkowski, J. Wietrzyk and E. Turlej, *J. Biol. Inorg. Chem.*, 2019, **24**, 591-606.
38. P. Alam, C. Climent, G. Kaur, D. Casanova, A. Roy Choudhury, A. Gupta, P. Alemany and I. R. Laskar, *Cryst. Growth Des.*, 2016, **16**, 5738-5752.
39. U. S. Schubert, C. Eschbaumer and G. Hochwimmer, *Synthesis*, 1999, 779-782.
40. V. R. de Souza, A. M. da Costa Ferreira and H. E. Toma, *Dalton Trans*, 2003, 458-463.
41. Y. Zhou, W. Li, L. Yu, Y. Liu, X. Wang and M. Zhou, *Dalton Trans*, 2015, **44**, 1858-1865.
42. C. Climent, P. Alam, S. S. Pasha, G. Kaur, A. R. Choudhury, I. R. Laskar, P. Alemany and D. Casanova, *J. Mater. Chem. C.*, 2017, **5**, 7784-7798.
43. N. J. Rogers, S. Claire, R. M. Harris, S. Farabi, G. Zikeli, I. B. Styles, N. J. Hodges and Z. Pikramenou, *Chem. Commun.*, 2014, **50**, 617-619.
44. F. Schulz, T. Homolka, N. G. Bastús, V. Puntes, H. Weller and T. Vossmeyer, *Langmuir*, 2014, **30**, 10779-10784.

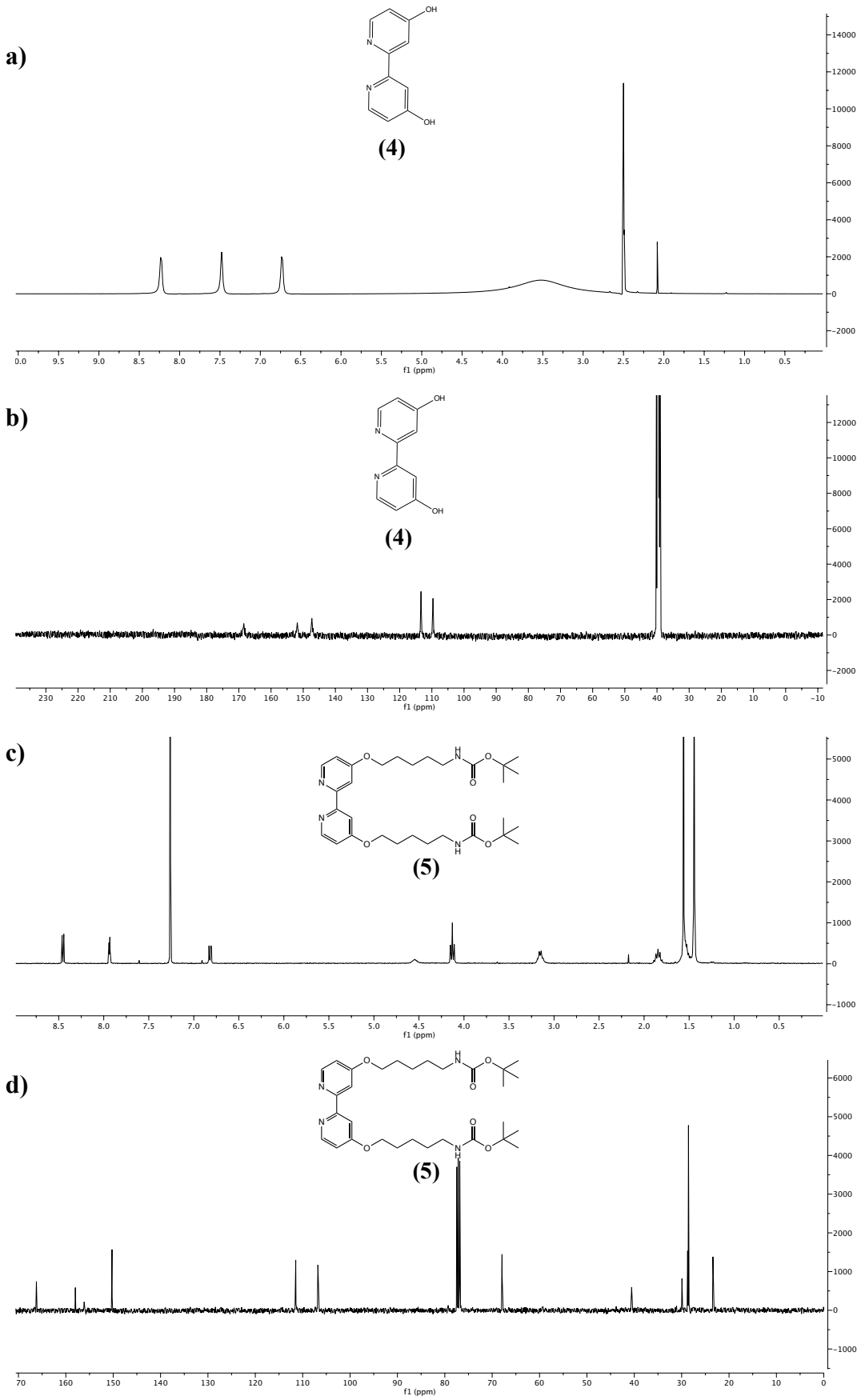
45. H. Tyagi, A. Kushwaha, A. Kumar and M. Aslam, *Nanoscale Res. Lett.*, 2016, **11**, 362.
46. X. Zhang, M. R. Servos and J. Liu, *J. Am. Chem. Soc.*, 2012, **134**, 7266-7269.
47. L. Malassis, R. Dreyfus, R. J. Murphy, L. A. Hough, B. Donnio and C. B. Murray, *RSC Adv.*, 2016, **6**, 33092-33100.
48. R. P. Carney, J. Y. Kim, H. Qian, R. Jin, H. Mehenni, F. Stellacci and O. M. Bakr, *Nat. Commun.*, 2011, **2**, 335.
49. J. Shang and X. Gao, *Chem. Soc. Rev.*, 2014, **43**, 7267-7278.
50. W. Haiss, N. T. K. Thanh, J. Aveyard and D. G. Fernig, *Anal. Chem.*, 2007, **79**, 4215-4221.
51. S. Kumar, J. Aaron and K. Sokolov, *Nat. Protoc.*, 2008, **3**, 314-314.
52. J. V. Gavette, J. M. McGrath, A. M. Spuches, A. L. Sargent and W. E. Allen, *J. Org. Chem.*, 2009, **74**, 3706-3710.
53. J. V. Gavette, A. L. Sargent and W. E. Allen, *J. Org. Chem.*, 2008, **73**, 3582-3584.
54. C. Ziegler and A. Eychmüller, *J. Phys. Chem. C.*, 2011, **115**, 4502-4506.

2.27 Appendix

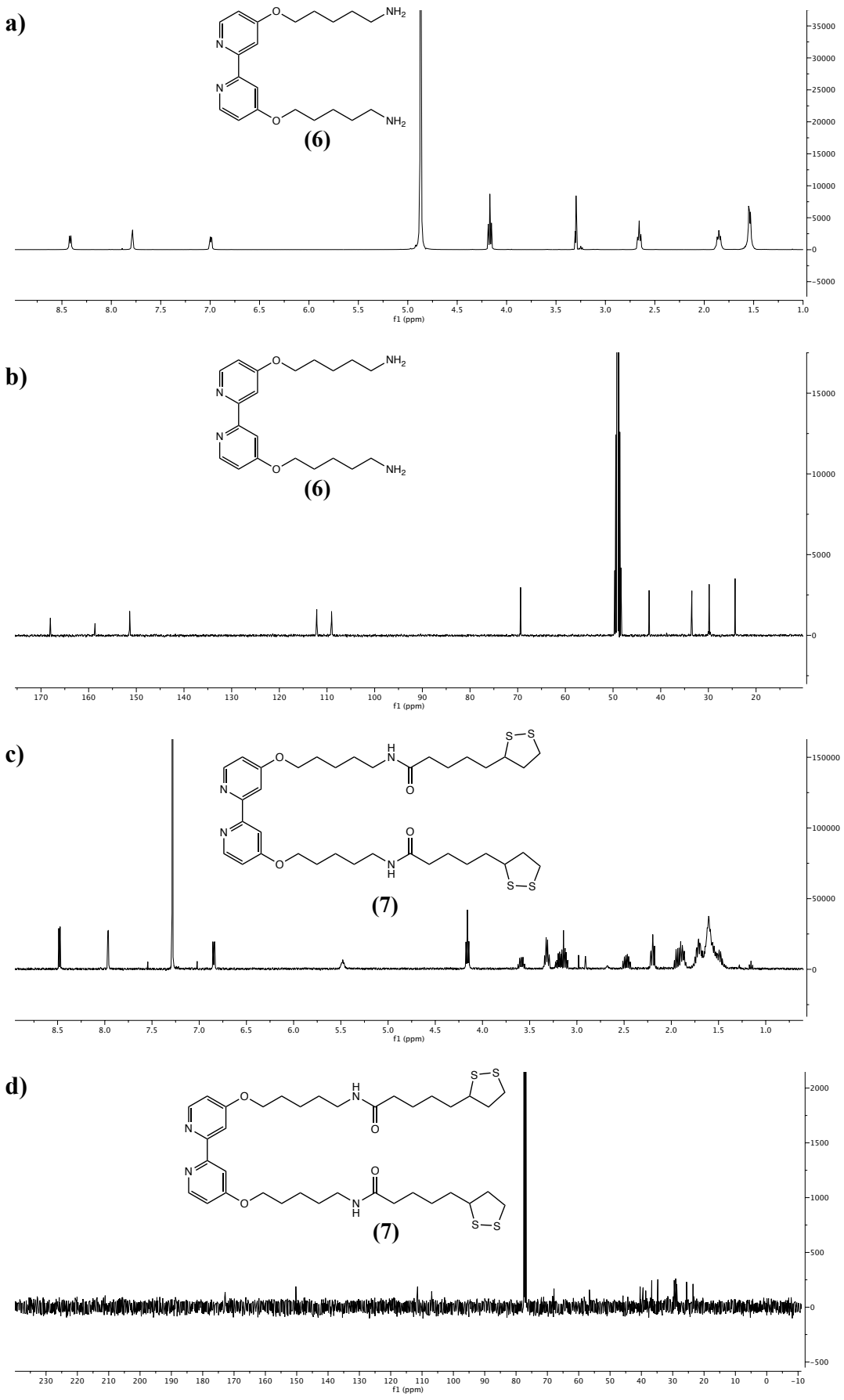
NMR



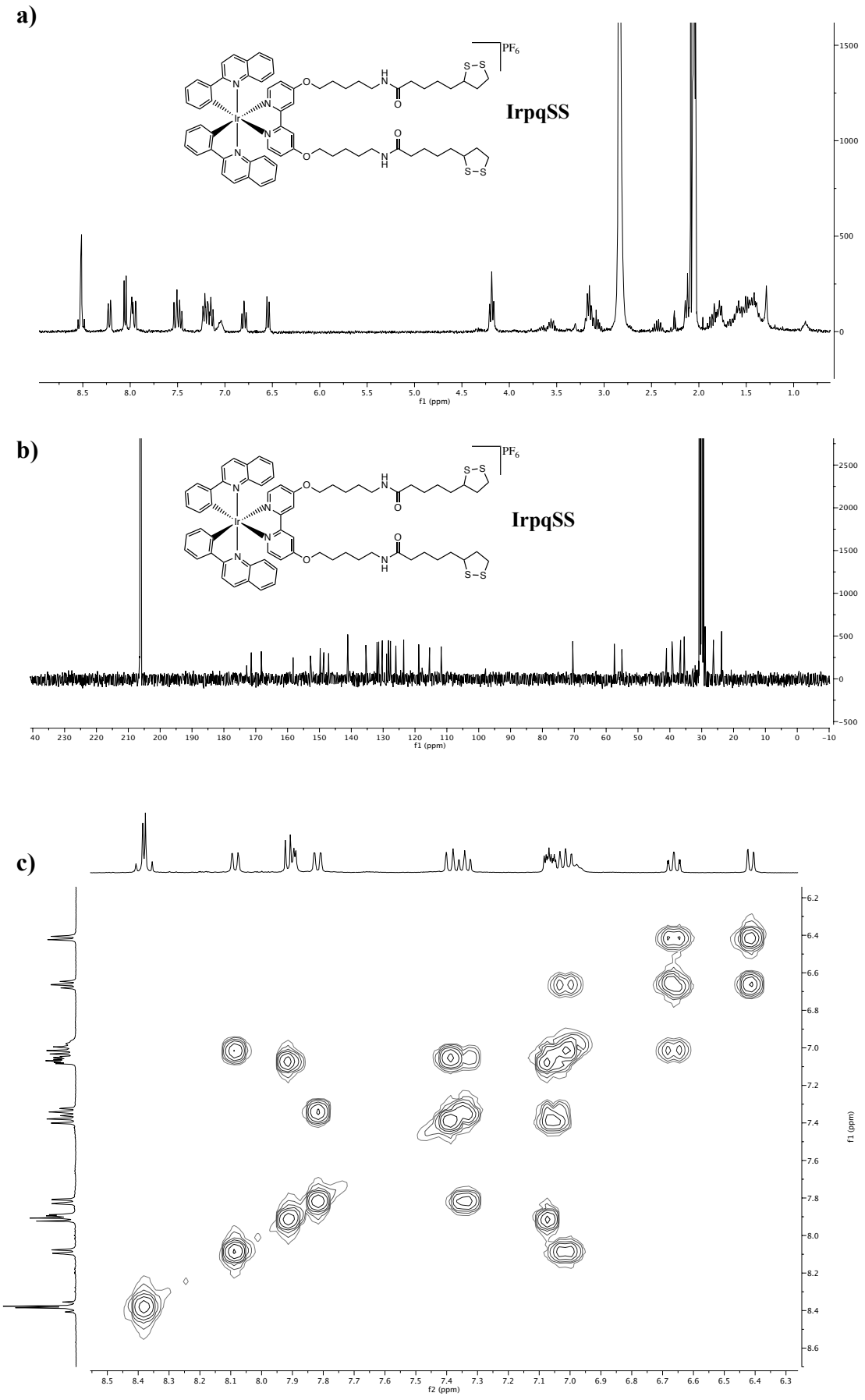
*Supplementary Figure 2.1. NMR spectra of ligands for **IrpqSS** synthesis: **a)** ^{1}H NMR of **(2)** in $CDCl_3$, **b)** ^{13}C NMR of **(2)** in $CDCl_3$, **c)** ^{1}H NMR of **(3)** in $CDCl_3$, **d)** ^{13}C NMR of **(3)** in $CDCl_3$.*



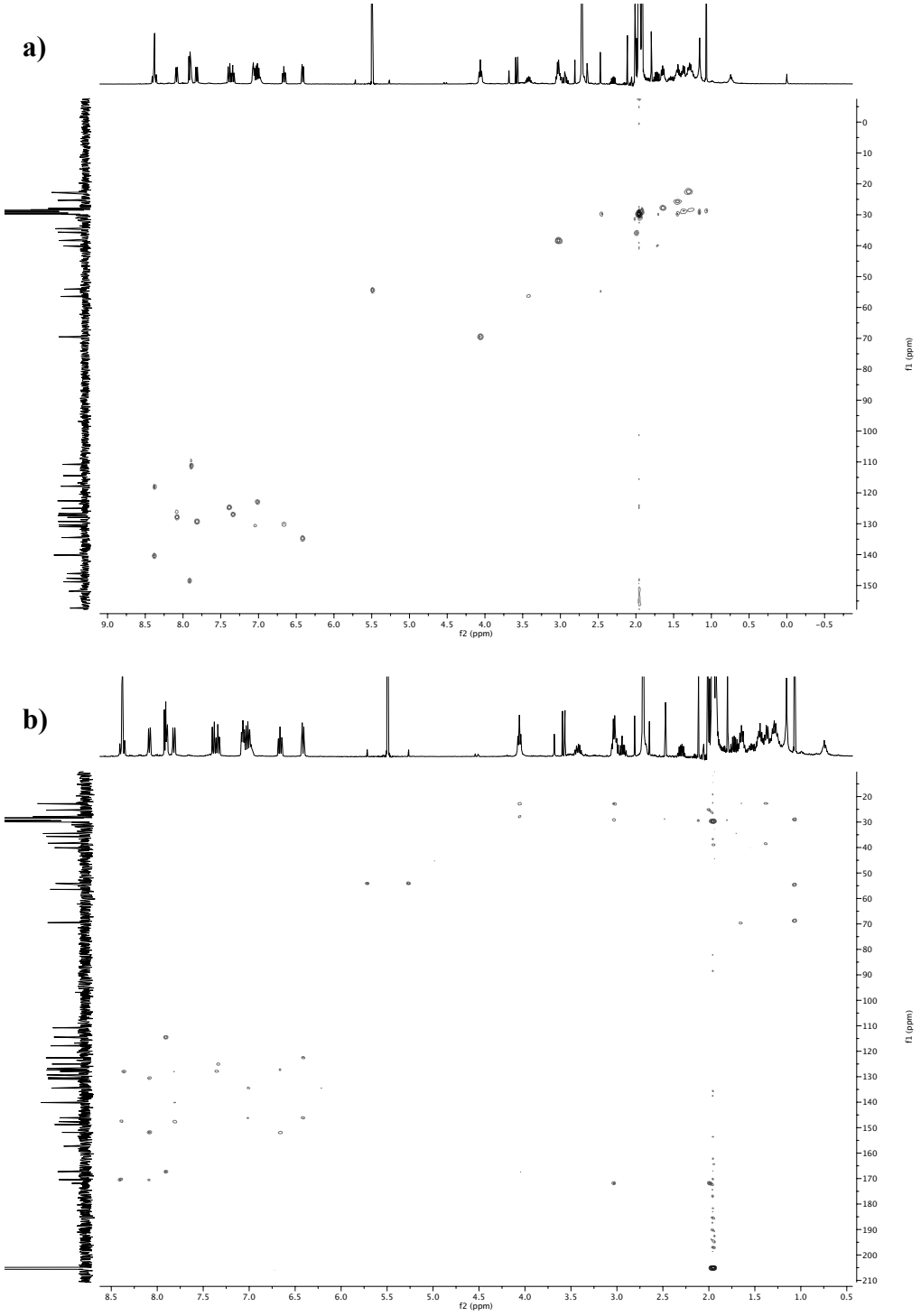
*Supplementary Figure 2.2. NMR spectra of ligands for **IrpqSS** synthesis: **a)** ^{1}H NMR of **(4)** in DMSO-d_6, **b)** ^{13}C NMR of **(4)** in DMSO-d_6, **c)** ^{1}H NMR of **(5)** in $CDCl_3$, **d)** ^{13}C NMR of **(5)** in $CDCl_3$.*



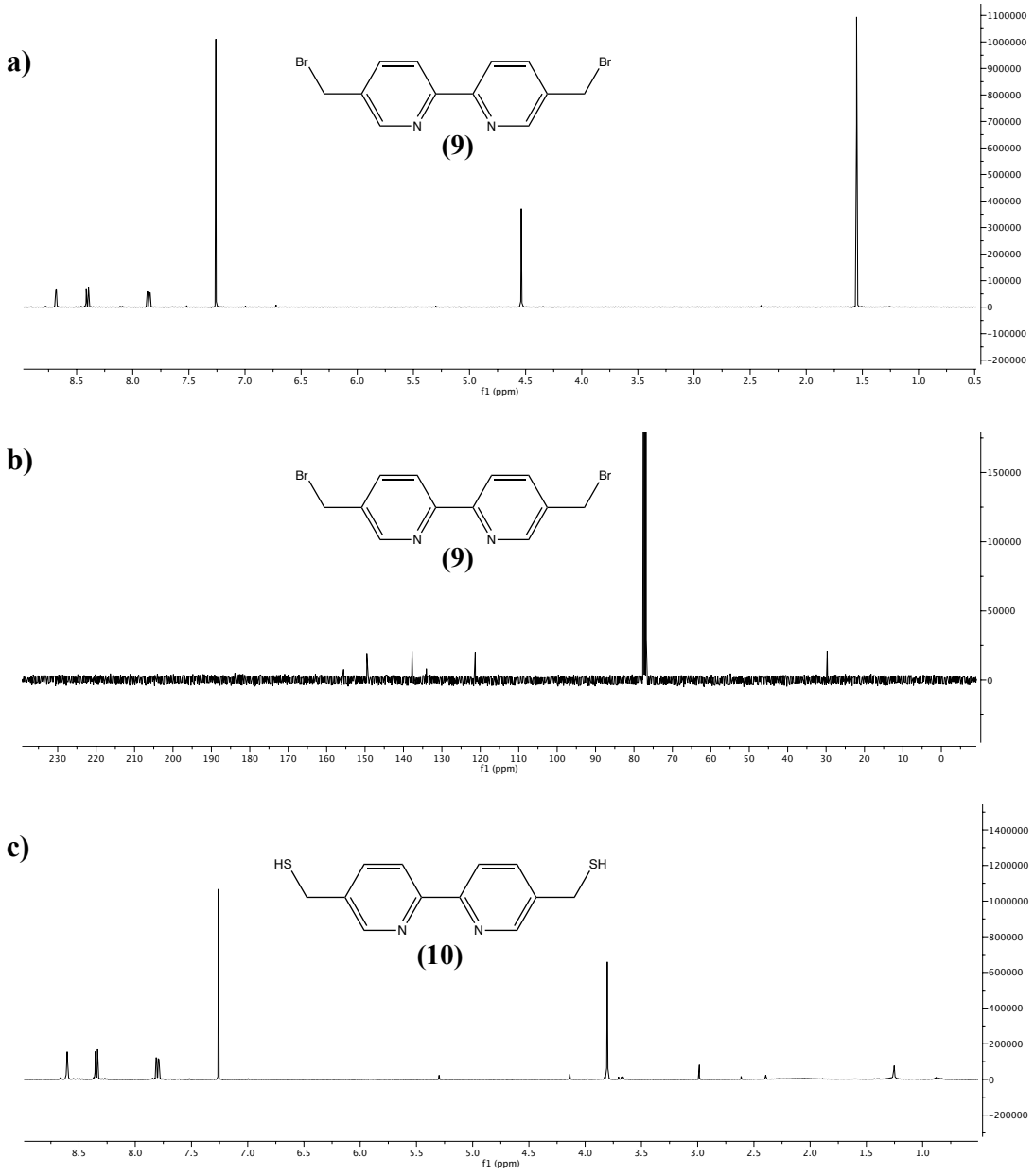
Supplementary Figure 2.3. NMR spectra of ligands for IrpqSS synthesis: ***a)*** *^{1}H NMR of* ***(6)*** *in CD_3OD,* ***b)*** *^{13}C NMR of* ***(6)*** *in CD_3OD,* ***c)*** *^{1}H NMR of* ***(7)*** *in $CDCl_3$,* ***d)*** *^{13}C NMR of* ***(7)*** *in $CDCl_3$.*



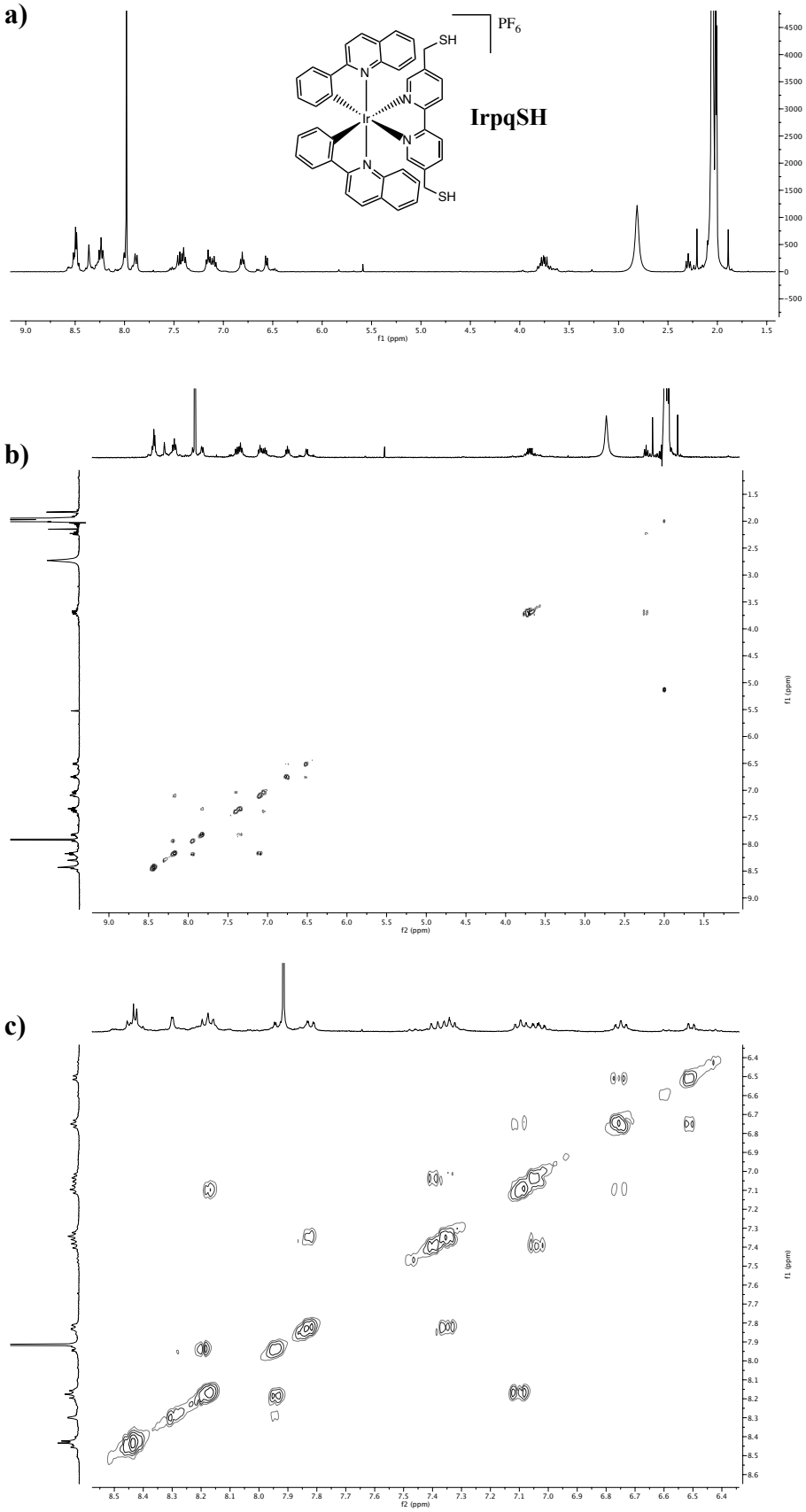
Supplementary Figure 2.4. NMR spectra: ***a)*** *^{1}H NMR and* ***b)*** *^{13}C NMR of* ***IrpqSS****, including* ***c)*** *2D COSY NMR. All spectra were collected in Acetone-d_6.*



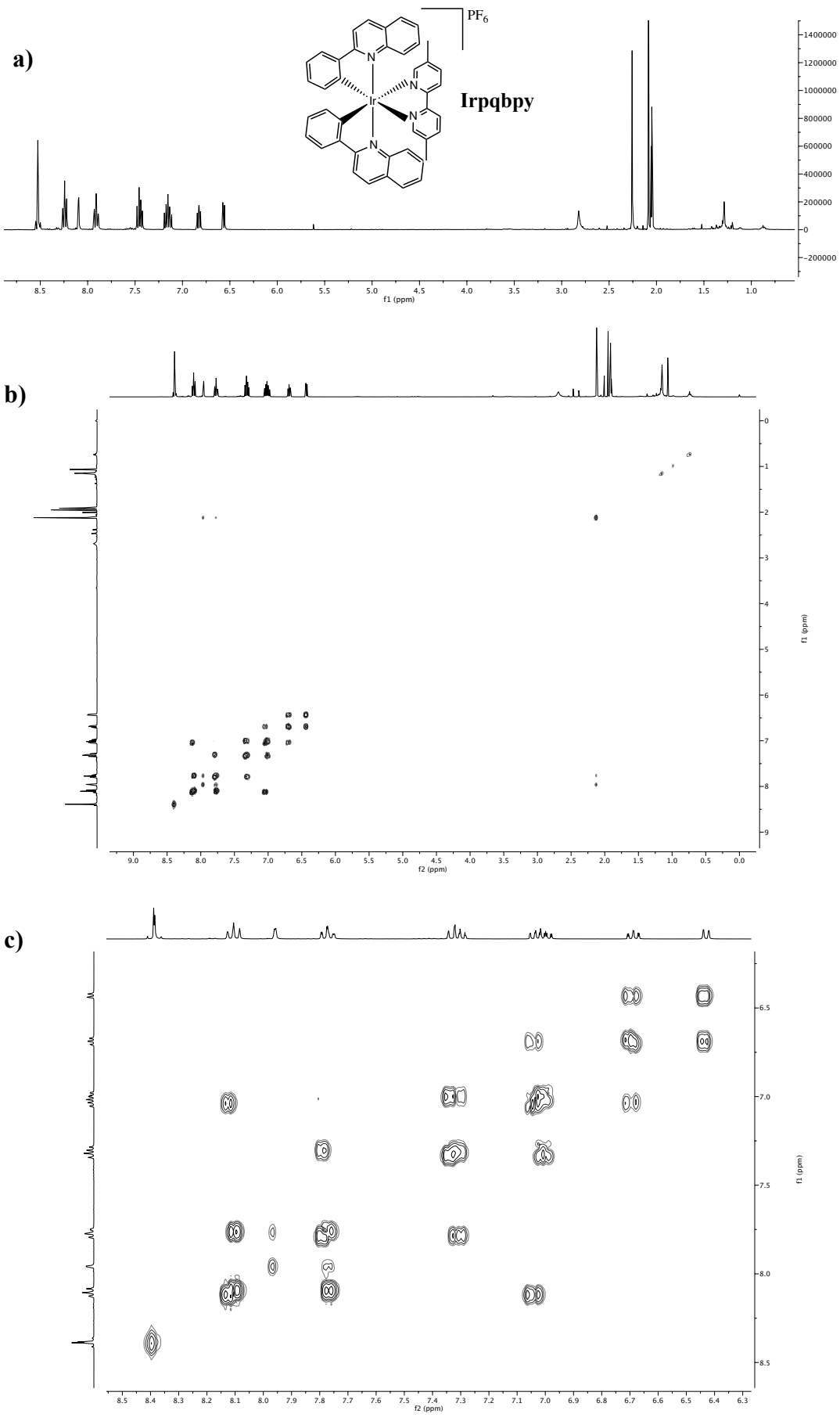
Supplementary Figure 2.5. 2D NMR spectra of ***IrpqSS****:* ***a)*** *HSQC and* ***b)*** *HMBC. All spectra were collected in Acetone-*d_6*.*



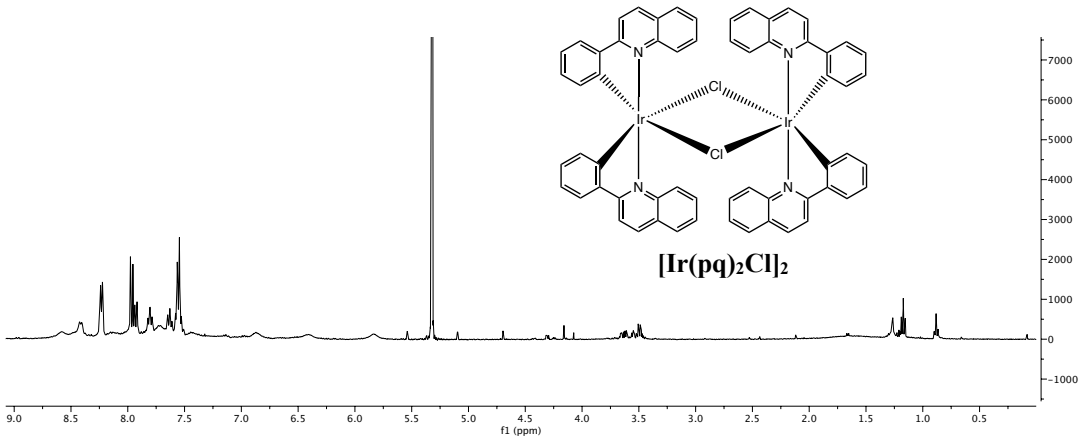
*Supplementary Figure 2.6. NMR spectra of ligands for **IrpqSH** synthesis: **a)** ^{1}H NMR of **(9)** in $CDCl_3$, **b)** ^{13}C NMR of **(9)** in $CDCl_3$, **c)** ^{1}H NMR of **(10)** in $CDCl_3$.*



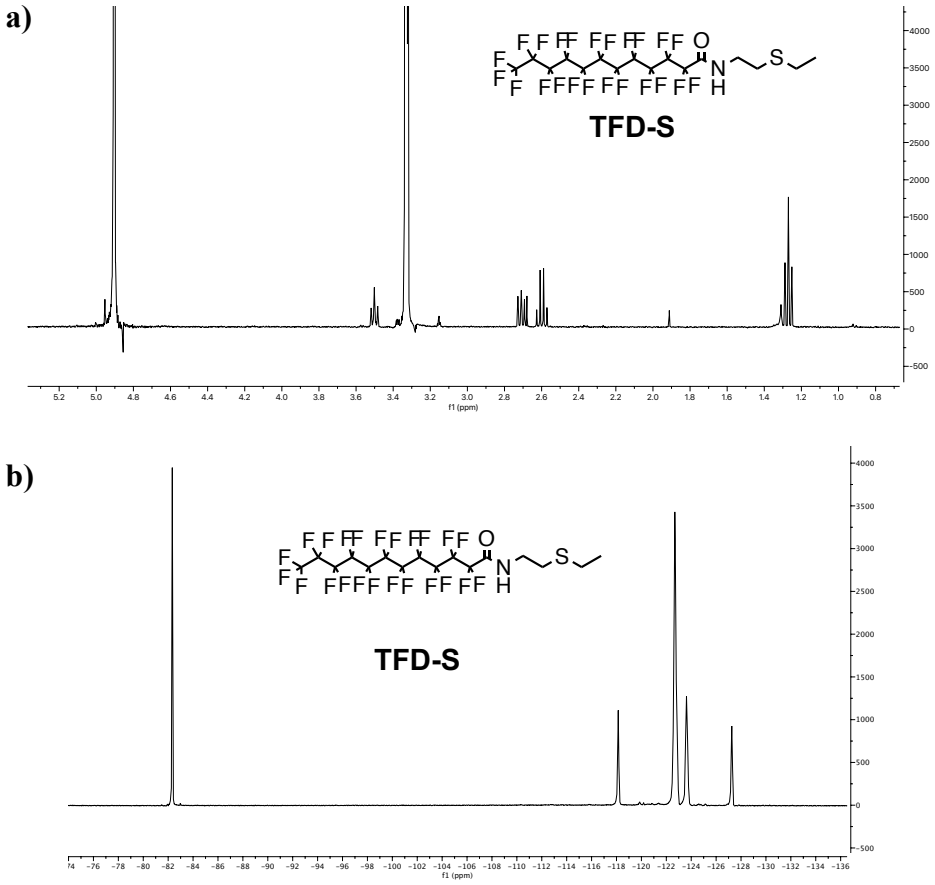
Supplementary Figure 2.7. NMR spectra: ***a)*** *^{1}H NMR and* ***b), c)*** *2D COSY NMR of* ***IrpqSH****. All spectra were collected in Acetone-d_6.*



Supplementary Figure 2.8. NMR spectra: ***a)*** *^{1}H NMR and* ***b), c)*** *2D COSY NMR of* ***Irpqbpy****. All spectra were collected in Acetone-d_6.*

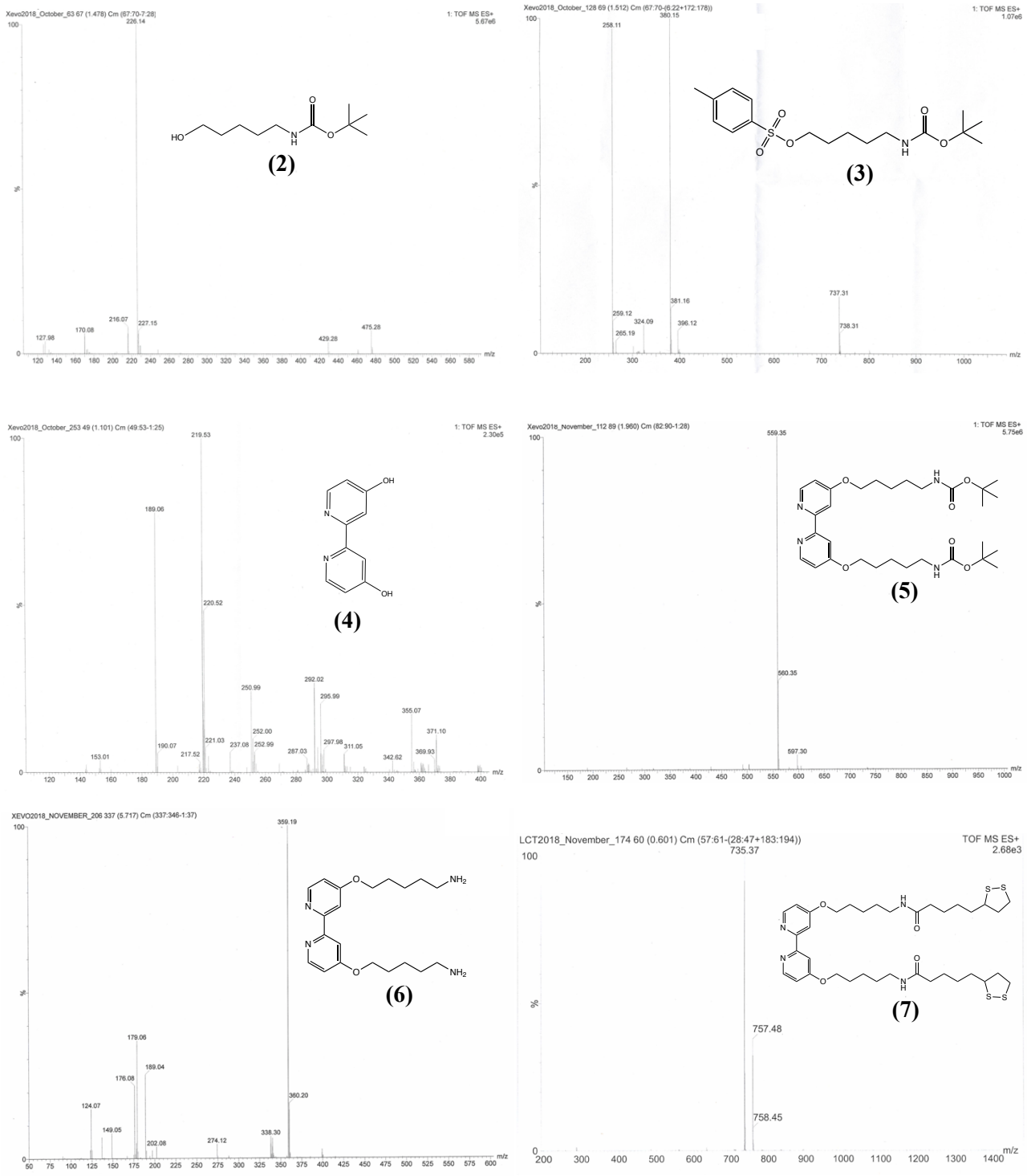


Supplementary Figure 2.9. ^{1}H NMR spectrum for ***[Ir(pq)$_2$Cl]$_2$*** *cyclometalated iridium(III) dimer in CD_2Cl_2.*

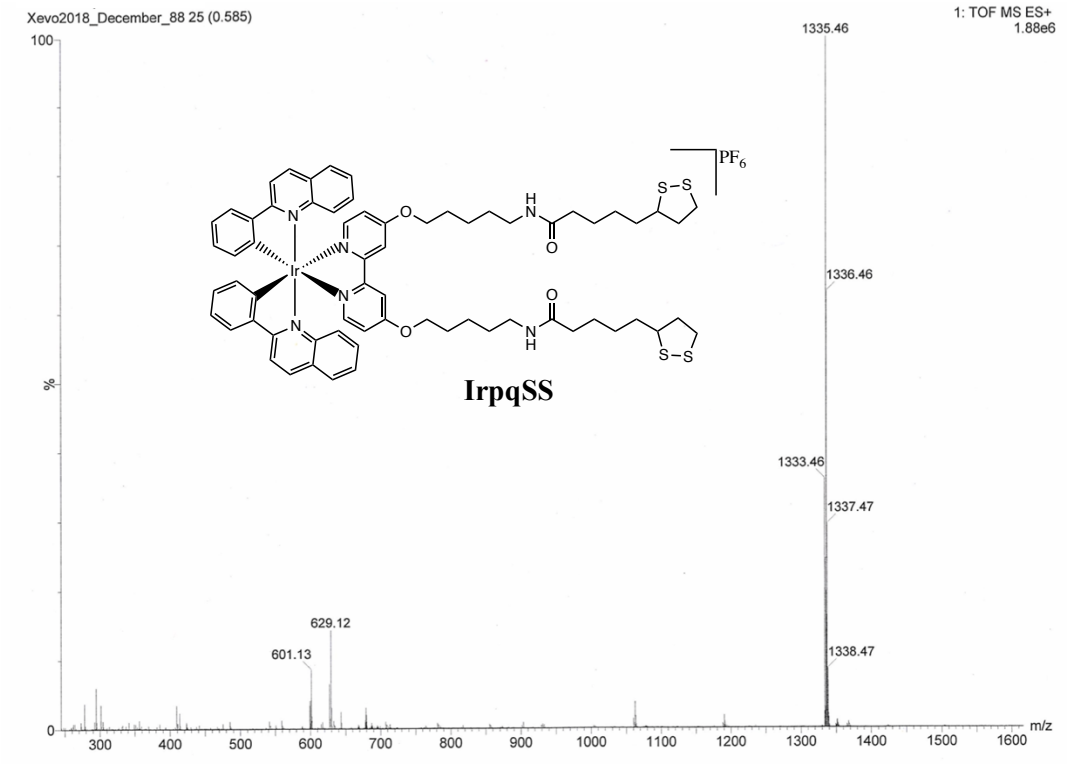


Supplementary Figure 2.10. NMR spectra of TFD-S in CD_3OD: ***a)*** *^{1}H NMR and* ***b)*** *^{19}F NMR spectra.*

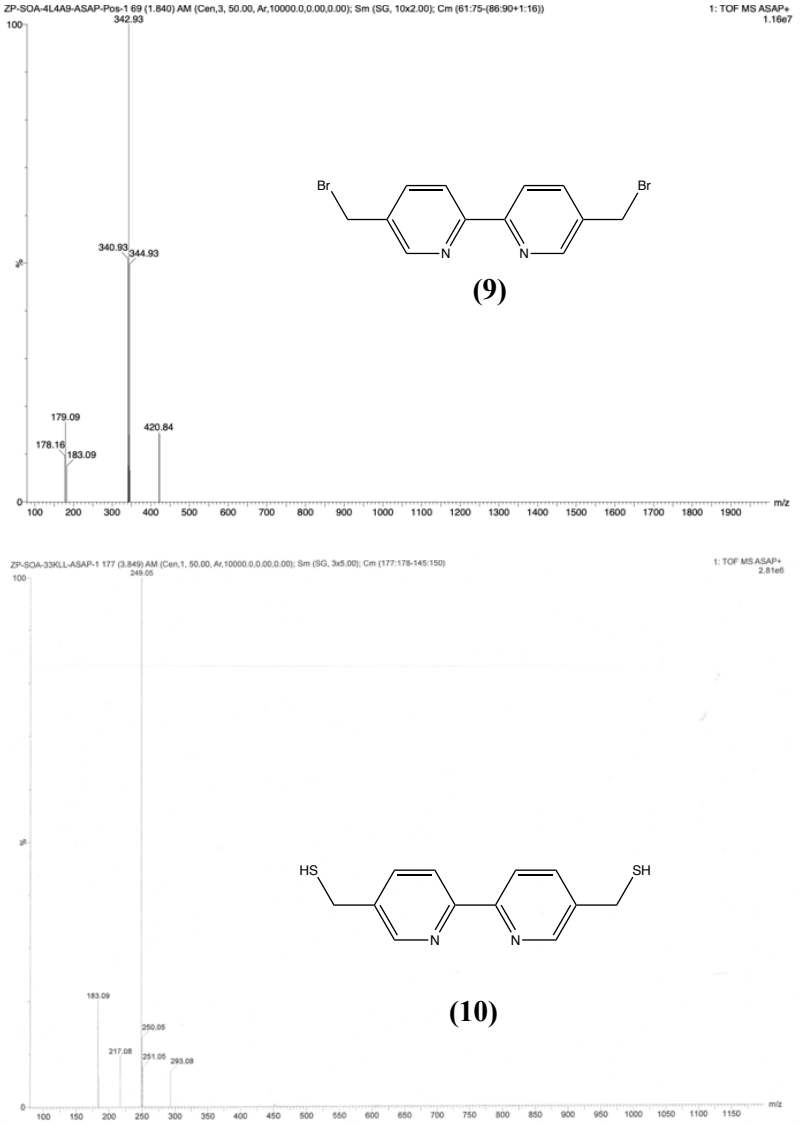
Mass Spectrometry



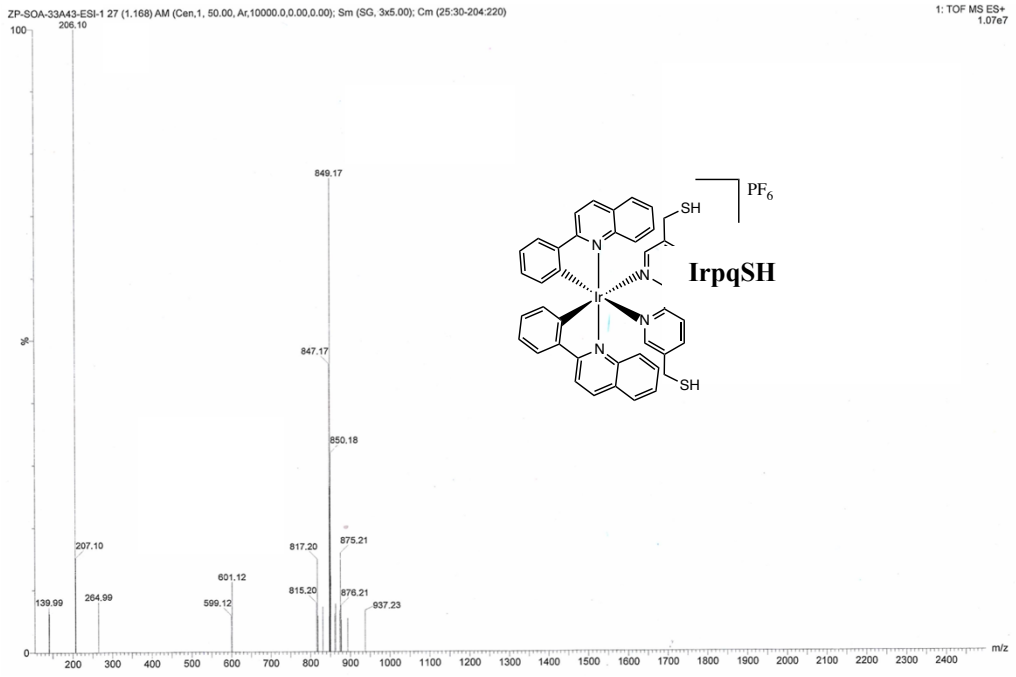
Supplementary Figure 2.11. Mass Spectra of ligands ***(1)*** *to* ***(7)****, used in the synthesis of* ***IrpqSS****.*



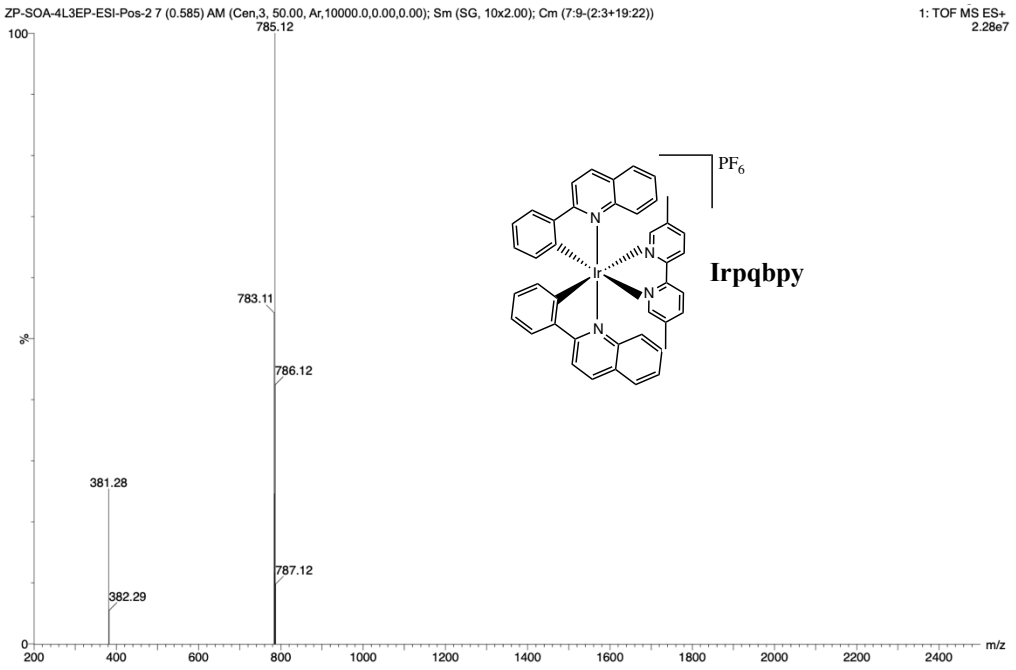
*Supplementary Figure 2.12. Mass spectrum of **IrpqSS** complex using TOF ES+ mass spectrometry.*



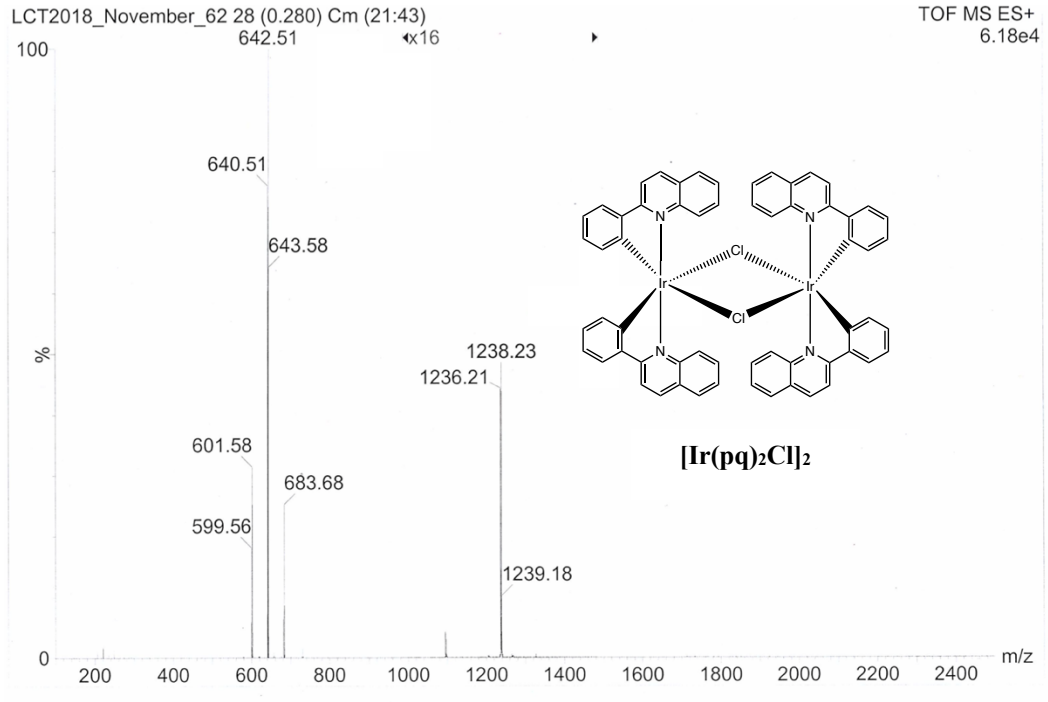
*Supplementary Figure 2.13. Mass spectra for the ligands used in **IrpqSH** complex synthesis.*



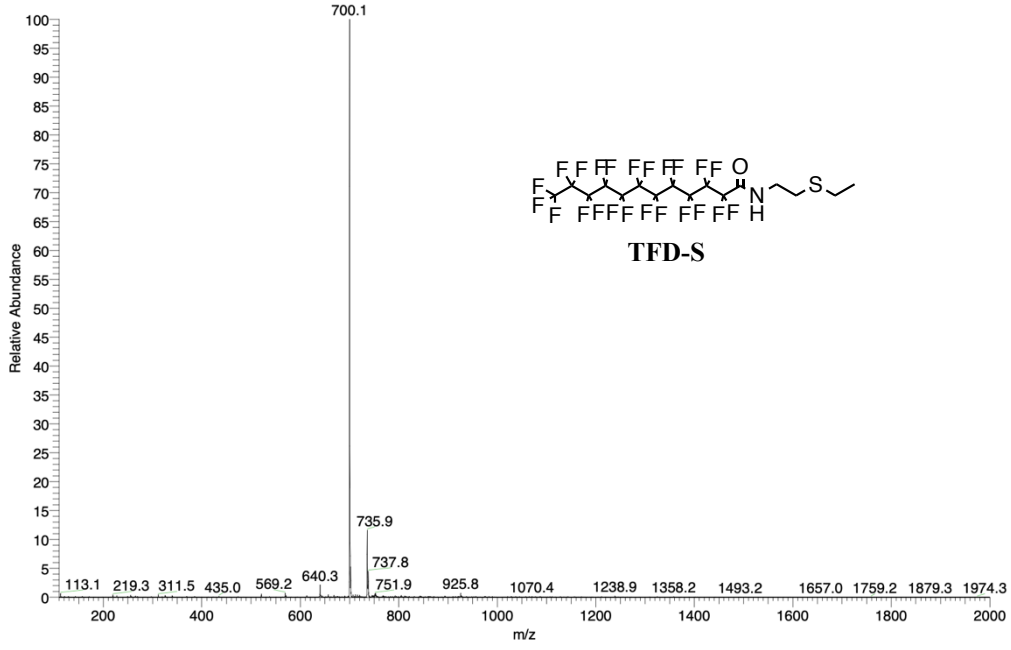
*Supplementary Figure 2.14. Mass spectrum for **IrpqSH** complex using TOF ES+ mass spectrometry.*



*Supplementary Figure 2.15. Mass spectrum for **Irpqbpy** complex using TOF ES+ mass spectrometry.*

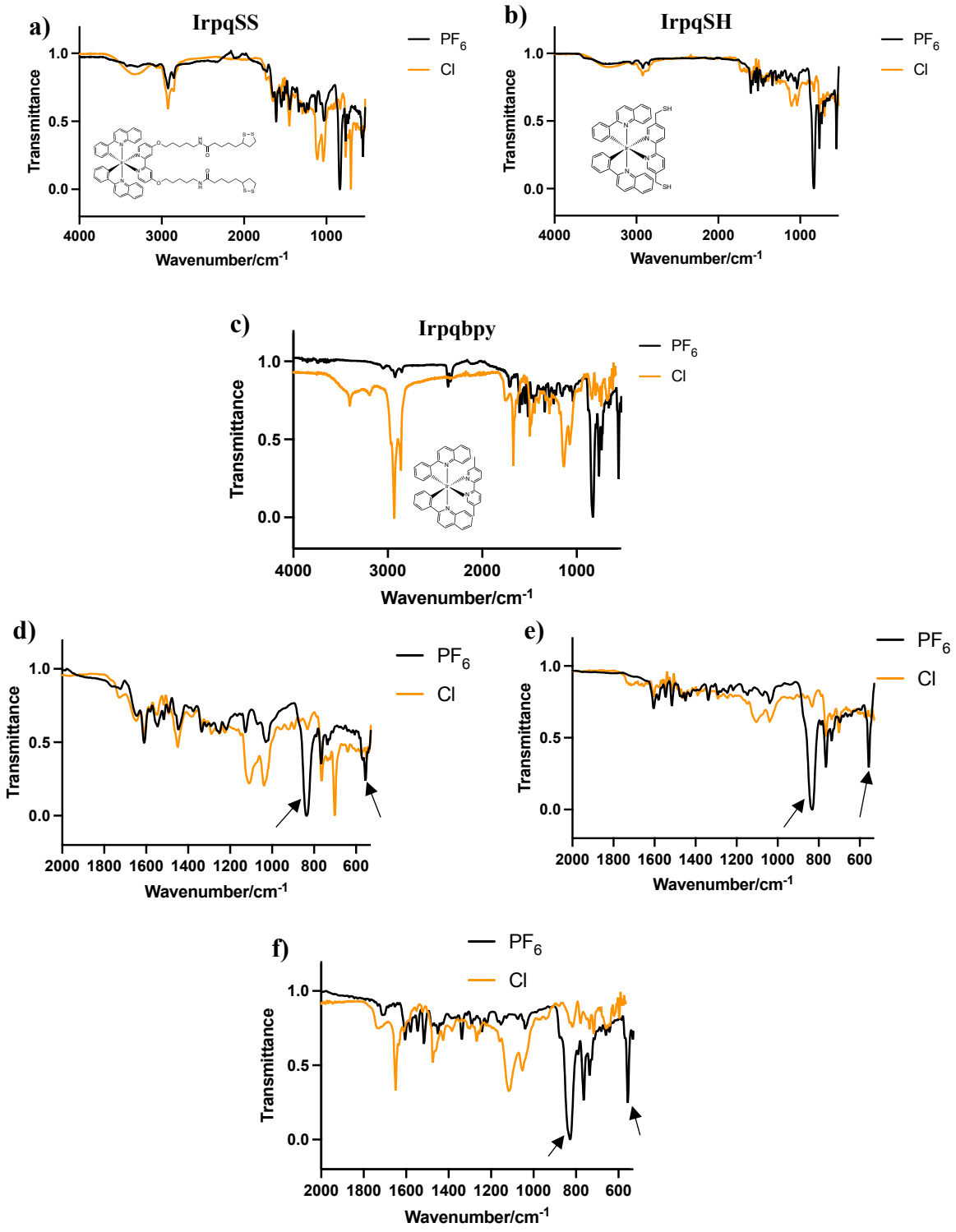


Supplementary Figure 2.16. Mass spectrum for ***[Ir(pq)$_2$Cl]$_2$*** *iridium cyclometalated dimer using TOF ES+ mass spectrometry.*



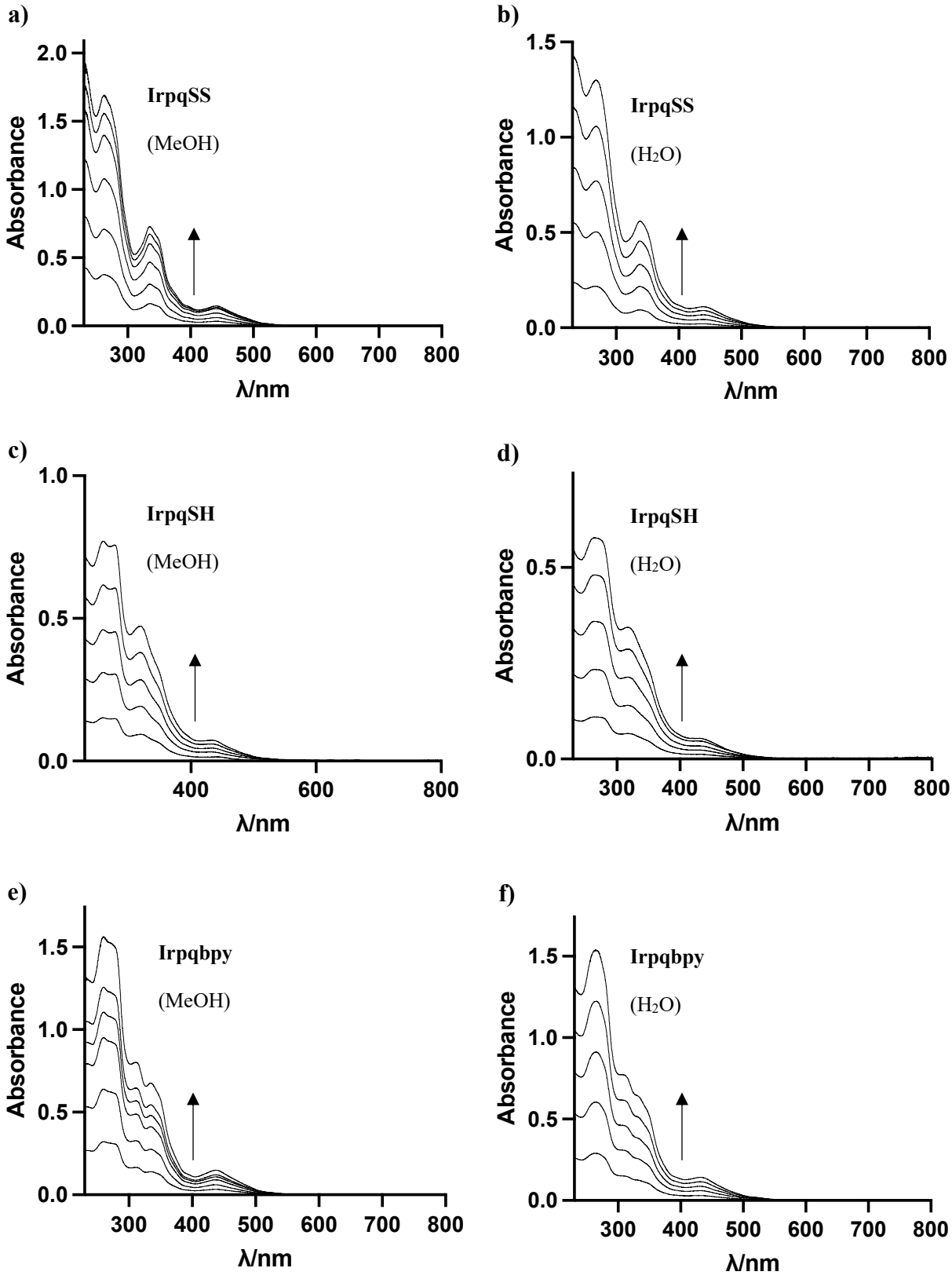
Supplementary Figure 2.17. Mass spectrum for the ***TFD-S*** *surfactant using ESI mass spectrometry.*

Infra-red spectroscopy

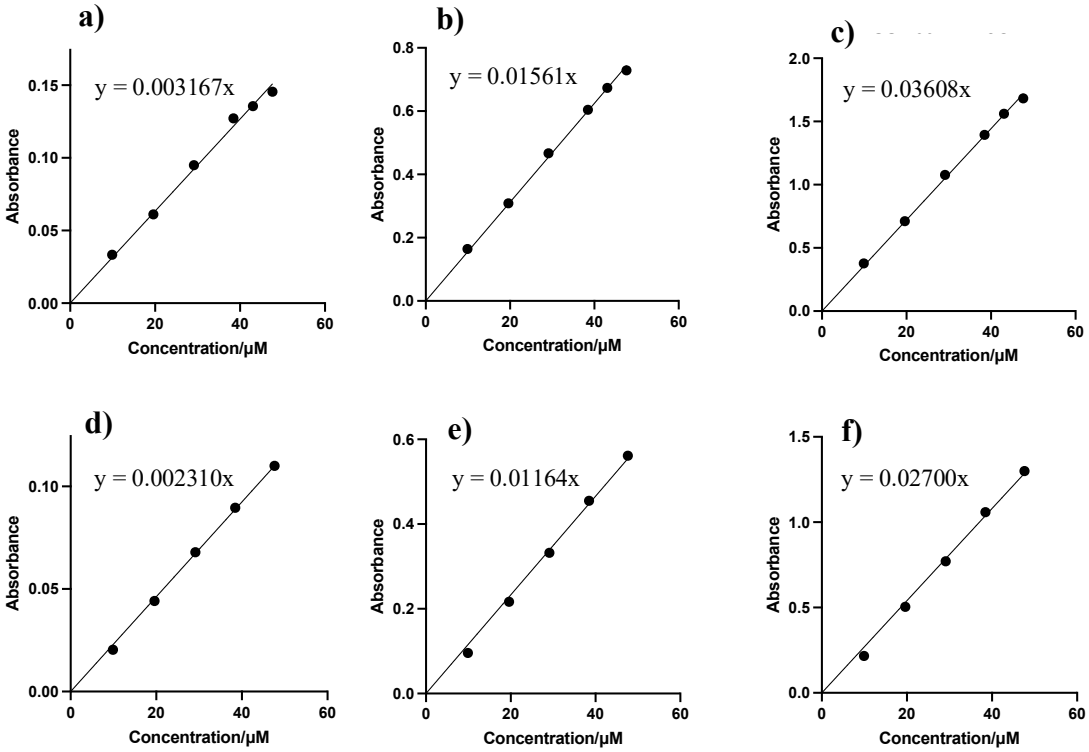


*Supplementary Figure 2.18. Infra-red spectra of **IrpqSS (a)**, **IrpqSH (b)** and **Irpqbpy (c)** with PF_6^- (black) and Cl^- (orange) counter ions. Zoomed-in infra-red spectra of **d) IrpqSS**, **e) IrpqSH** and **f) Irpqbpy**, showing the PF_6^- and Cl^- forms. Arrows point to the P-F vibrations of **IrpqSS** at 850 cm^{-1} (asymmetric) and 568 cm^{-1} (symmetric); in **IrpqSH** at 828 cm^{-1} (asymmetric) and 559 cm^{-1} (symmetric); and in **Irpqbpy** at 829 cm^{-1} (asymmetric) and 556 cm^{-1} (symmetric).*

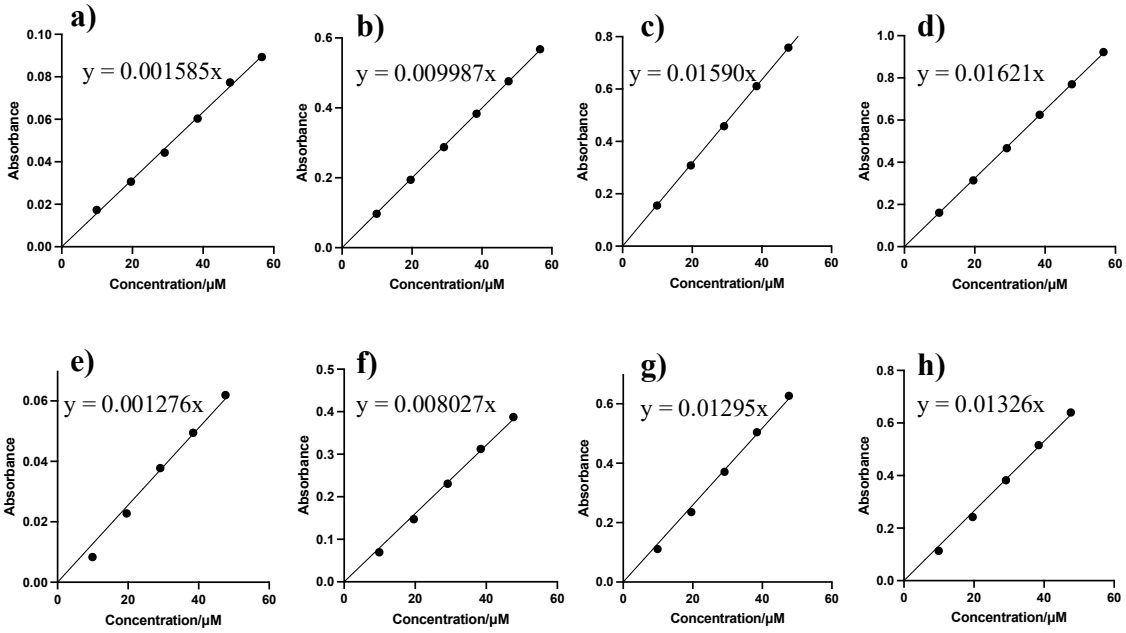
UV-vis absorbance



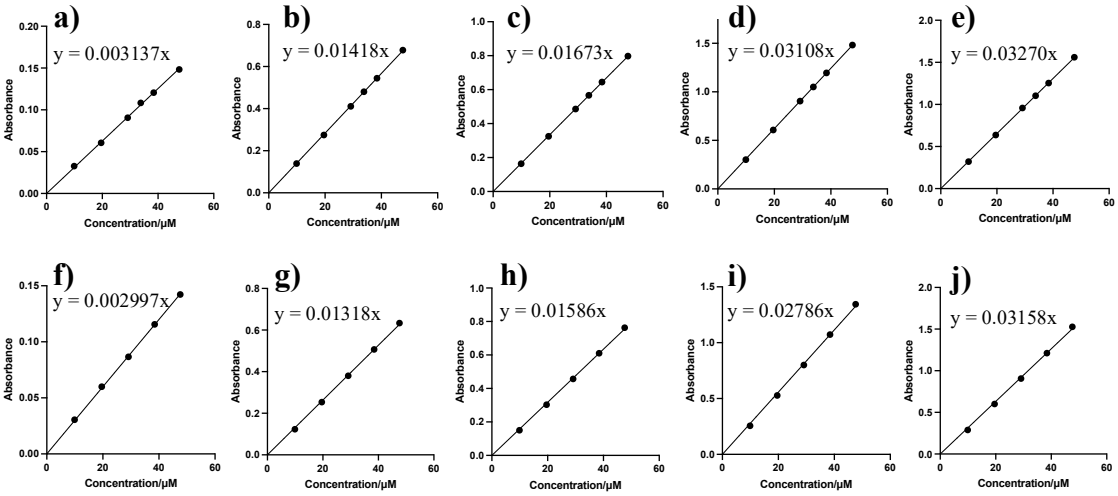
Supplementary Figure 2.19. UV-vis absorbance spectra of chloride salt-stabilized ***a) IrpqSS****,* ***c) IrpqSH*** *and* ***e) Irpqbpy*** *in MeOH, and of* ***b) IrpqSS****,* ***d) IrpqSH*** *and* ***f) Irpqbpy*** *in H_2O at concentrations from 9.9 μM to 47.6 μM. Arrows represent increasing absorbance with increasing concentration.*



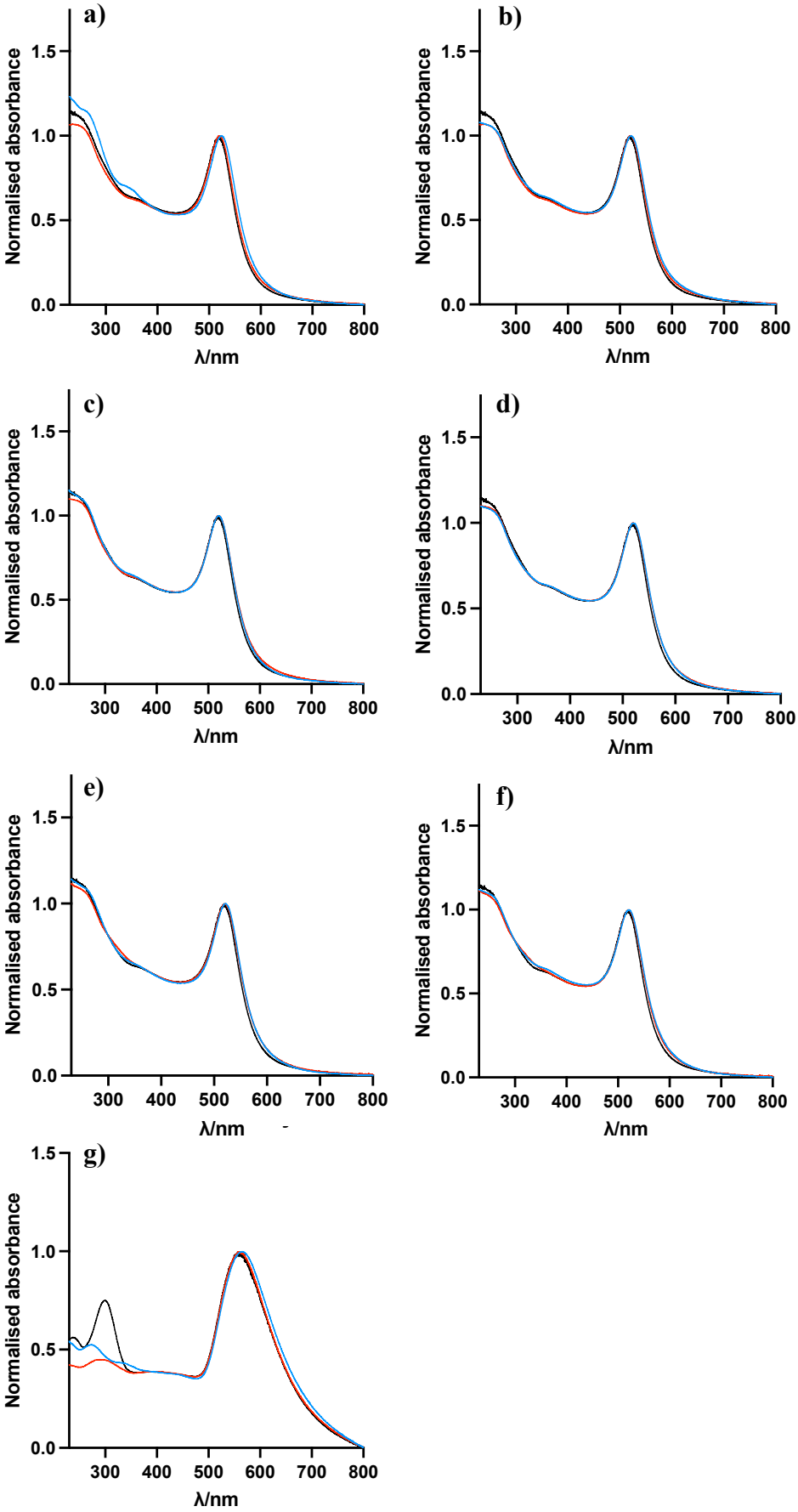
Supplementary Figure 2.20. Calibration curves showing Absorbance values vs. Concentration of solutions of ***IrpqSS*** *in MeOH at* ***a)*** *440nm,* ***b)*** *335nm and* ***c)*** *260nm, and in H_2O at* ***d)*** *440nm,* ***e)*** *335nm and* ***f)*** *260nm. Gradient of lines shows the extinction coefficient of the complex at that specific wavelength in $M^{-1}cm^{-1}$.*



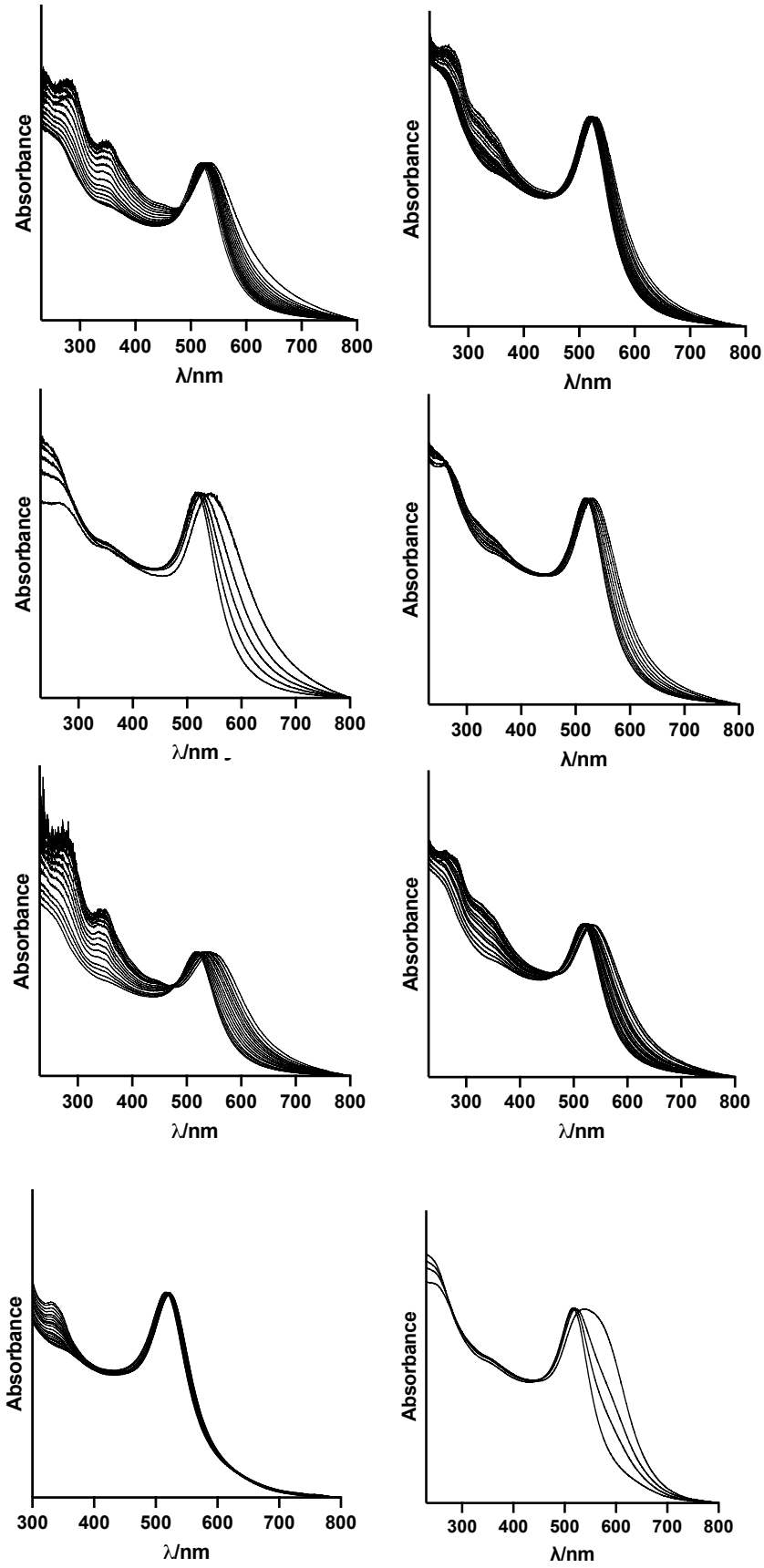
Supplementary Figure 2.21. Calibration curves showing Absorbance values vs. Concentration of solutions of ***IrpqSH*** *in MeOH at* ***a)*** *435nm,* ***b)*** *321nm,* ***c)*** *280nm and* ***d)*** *259nm, and in H_2O at* ***e)*** *430nm,* ***f)*** *317nm,* ***g)*** *279nm and* ***h)*** *257nm. Gradient of lines shows the extinction coefficient of the complex at that specific wavelength in $M^{-1}cm^{-1}$.*



Supplementary Figure 2.22. Calibration curves showing Absorbance values vs. Concentration of solutions of ***Irpqbpy*** *in MeOH at* ***a)*** *438nm,* ***b)*** *334nm,* ***c)*** *313nm,* ***d)*** *280nm and* ***e)*** *260nm, and in H_2O at* ***f)*** *433nm,* ***g)*** *334nm,* ***h)*** *313nm* ***i)*** *280nm and* ***j)*** *260nm. Gradient of lines shows the extinction coefficient of the complex at that specific wavelength in $M^{-1}cm^{-1}$.*

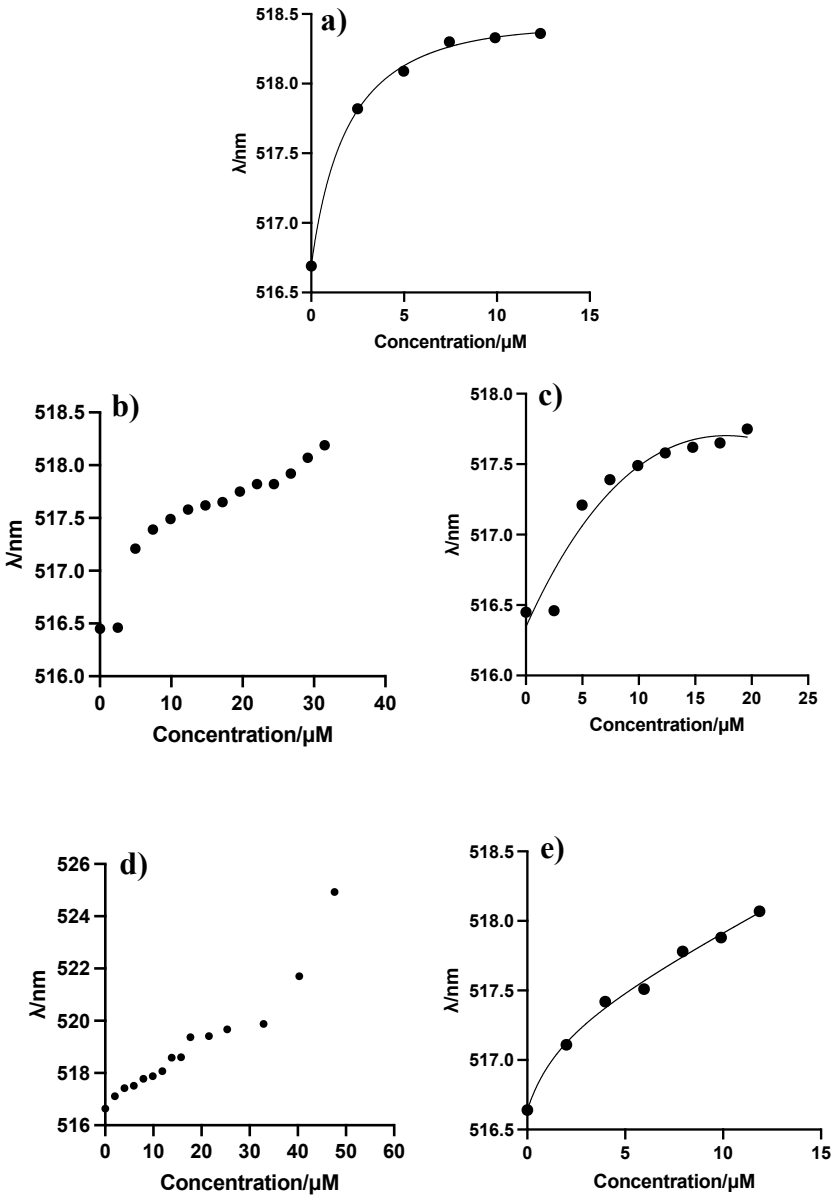


Supplementary Figure 2.23. Overlayed UV-vis absorbance spectra of citrate AuNPs (black), surfactant-coated AuNPs (red) and iridium(III) complex-coated AuNPs (blue) for ***a) IrpqSS.LPEG.AuNP25****, b) IrpqSH.LPEG.AuNP25, c) IrpqSS.SPEG.AuNP25, d) IrpqSH.SPEG.AuNP25, e) IrpqSS.Zonyl.AuNP25, f) IrpqSH.Zonyl.AuNP25* and *g) IrpqSS.Zonyl.AuNP100.*



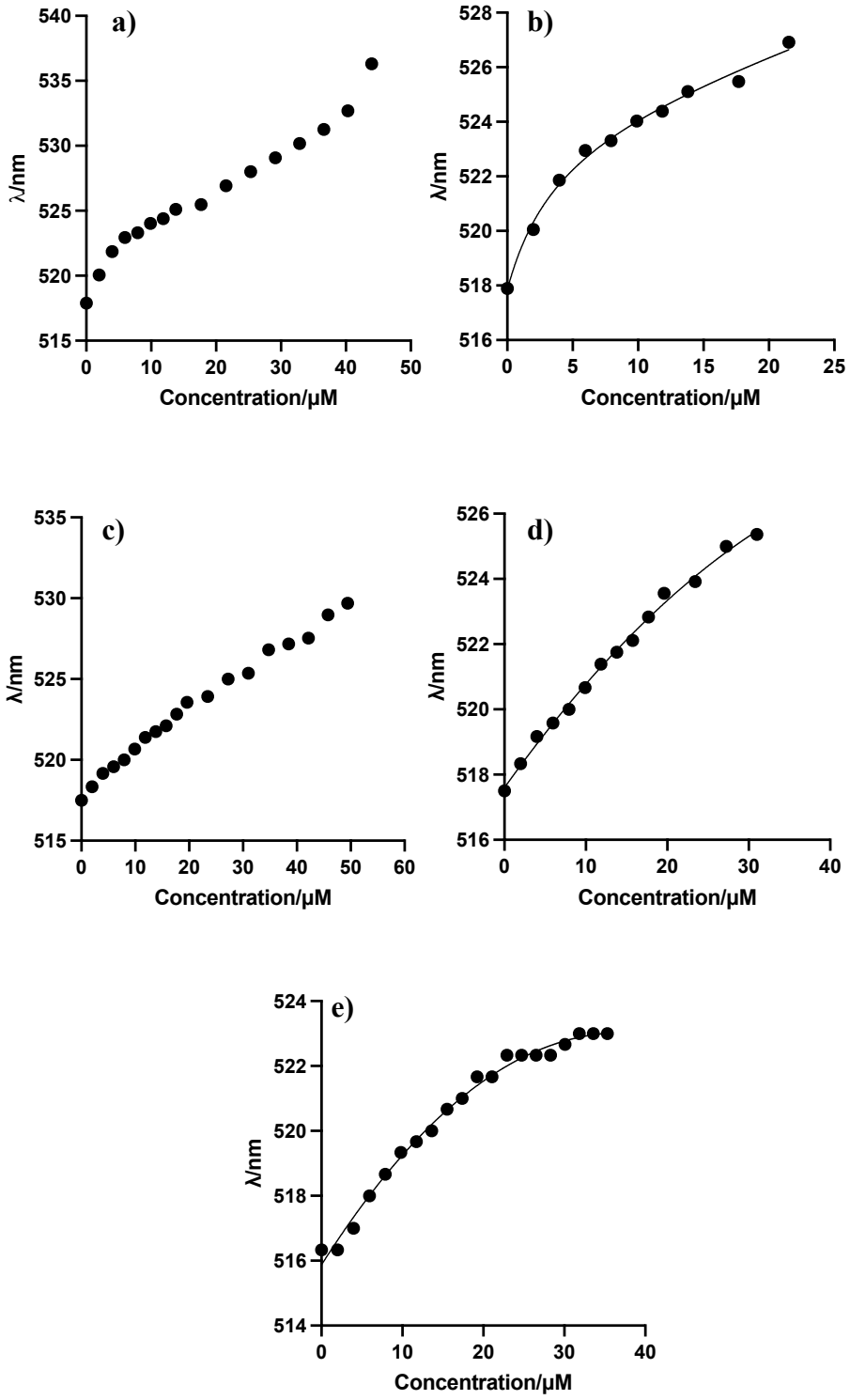
Supplementary Figure 2.24. UV-vis absorbance spectra showing the SPR shifts from ***IrpqSS*** *and* ***IrpqSH*** *complexes added to surfactant-coated* ***AuNP13s****.* ***IrpqSS*** *additions to* ***a) LPEG.AuNP13****,* ***b) SPEG.AuNP13****,* ***c) Zonyl.AuNP13*** *and* ***d) TFD-S.AuNP13****.* ***IrpqSH*** *additions to* ***e) LPEG.AuNP13, f) SPEG.AuNP13****,* ***g) Zonyl.AuNP13*** *and* ***h) TFD-S.AuNP13****.*

Binding curves for surfactant additions to AuNP13s



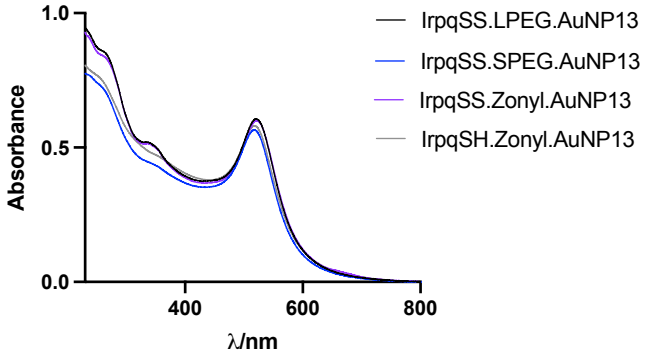
Supplementary Figure 2.25. Binding curves for surfactants addition to ***AuNP13****s.* ***a)*** *LPEG surfactant addition with non-linear fit to find the binding constant,* ***b)*** *SPEG surfactant addition,* ***c)*** *SPEG surfactant addition with a non-linear fit to find the binding constant,* ***d)*** *TFD-S surfactant addition,* ***e)*** *TFD-S surfactant addition with a non-linear fit to find the binding constant.*

Binding curves for iridium(III) complex additions to surfactant-coated AuNP13s



Supplementary Figure 2.26. Binding curves for iridium(III) complex addition to surfactant-coated AuNP13s. ***a) IrpqSS*** *complex addition to* ***LPEG.AuNP13****,* ***b) IrpqSS*** *complex addition to* ***LPEG.AuNP13*** *with a non-linear fit to find the binding constant,* ***c) IrpqSH*** *complex addition to* ***LPEG.AuNP13****,* ***d) IrpqSH*** *complex addition to* ***LPEG.AuNP13*** *with a non-linear fit to find the binding constant,* ***e) IrpqSS*** *complex addition to* ***TFD-S.AuNP13****.*

UV-vis absorbance spectra for coated AuNP13s



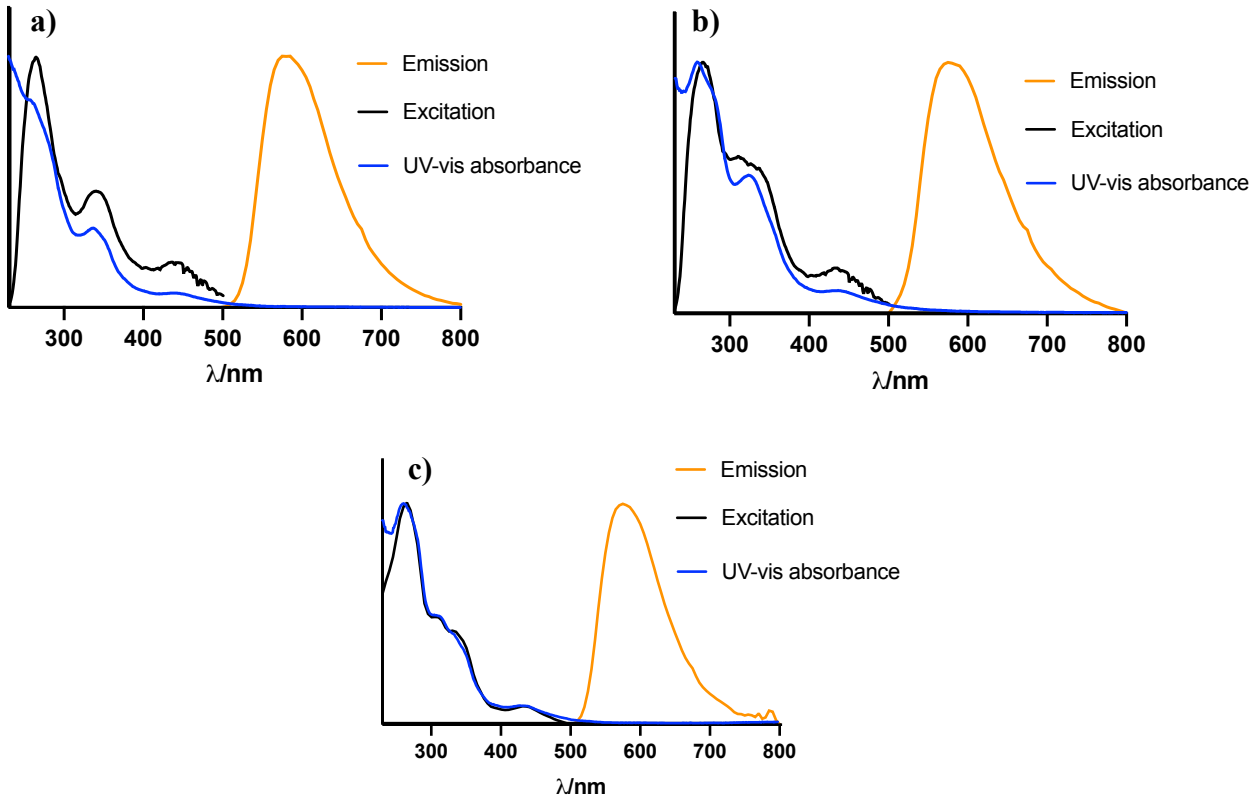
*Supplementary Figure 2.27. The UV-vis absorbance spectra for 1.7 nM **LPEG**, **SPEG** and **Zonyl**-coated AuNPs, and 1.9 nM of **TFD-S**-coated AuNPs. obtained from the ratio of absorbance of the citrate AuNPs (0.531). The absorbance peaks were at 0.6 for all AuNP13 samples except for the TFD-S-coated AuNPs, with an absorbance of 0.7.*

Binding constants for surfactants and iridium(III) complexes

	LPEG onto AuNP13	**SPEG onto AuNP13**	**TFD-S onto AuNP13**	**IrpqSS.LPEG. AuNP13**	**IrpqSS.TFD-S.AuNP13**	**IrpqSH.LPEG. AuNP13**
Bmax / nm	2.167	20.56	0.6486	6.462	3942	2283
Kd / M	2.203	51.34	1.809	3.919	835	845.7
Ka / M^{-1}	453926	19478	552792	255167	1198	1182

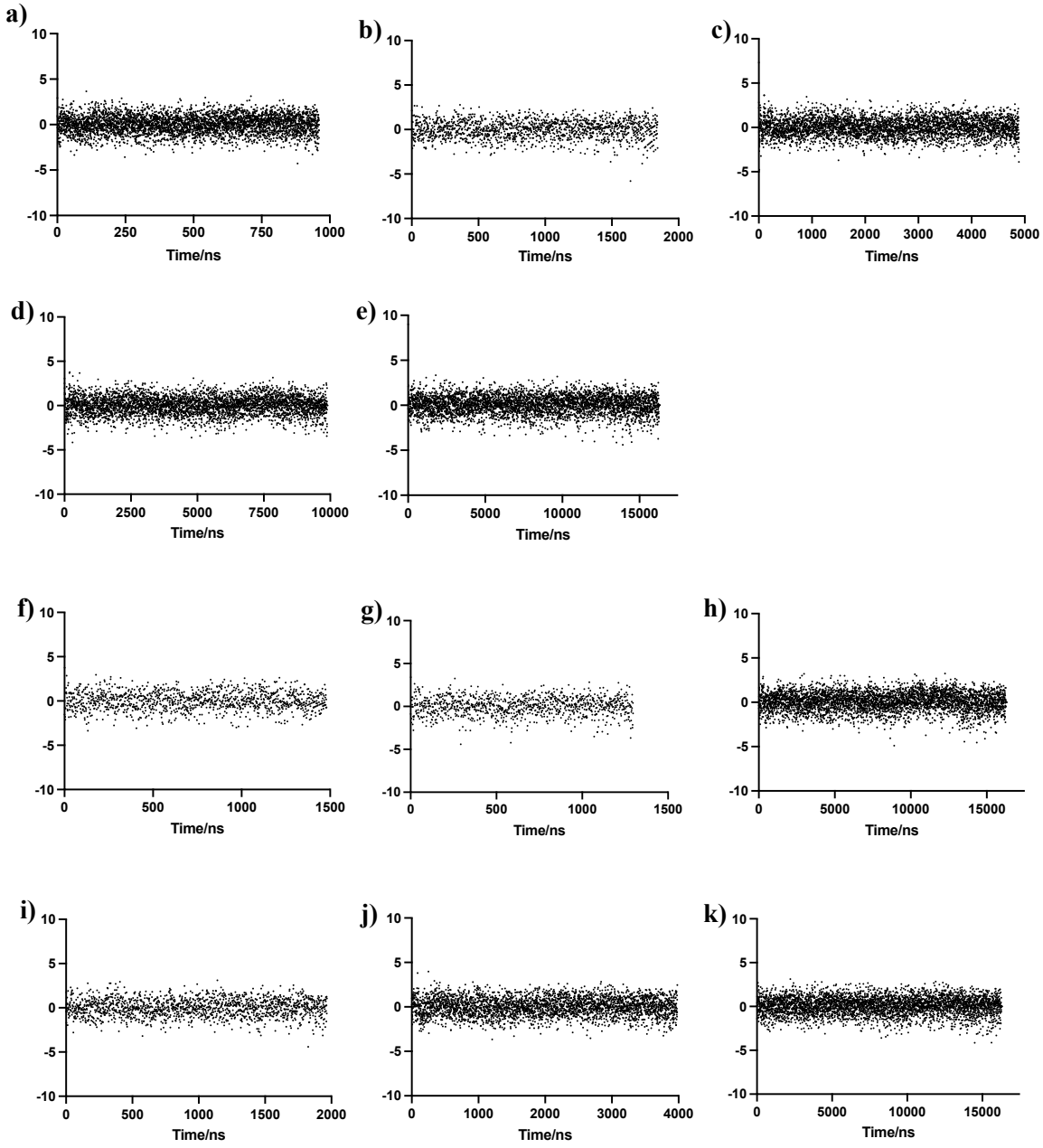
Supplementary Table 2.1. Binding constants for some AuNP13 coating of surfactants and iridium(III) complex. Bmax is maximum specific binding in nm. Kd is equilibrium dissociation constant in M. It is the concentration needed to achieve half maximum binding when the system is in equilibrium. Ka is binding constant in M^{-1}.

Emission

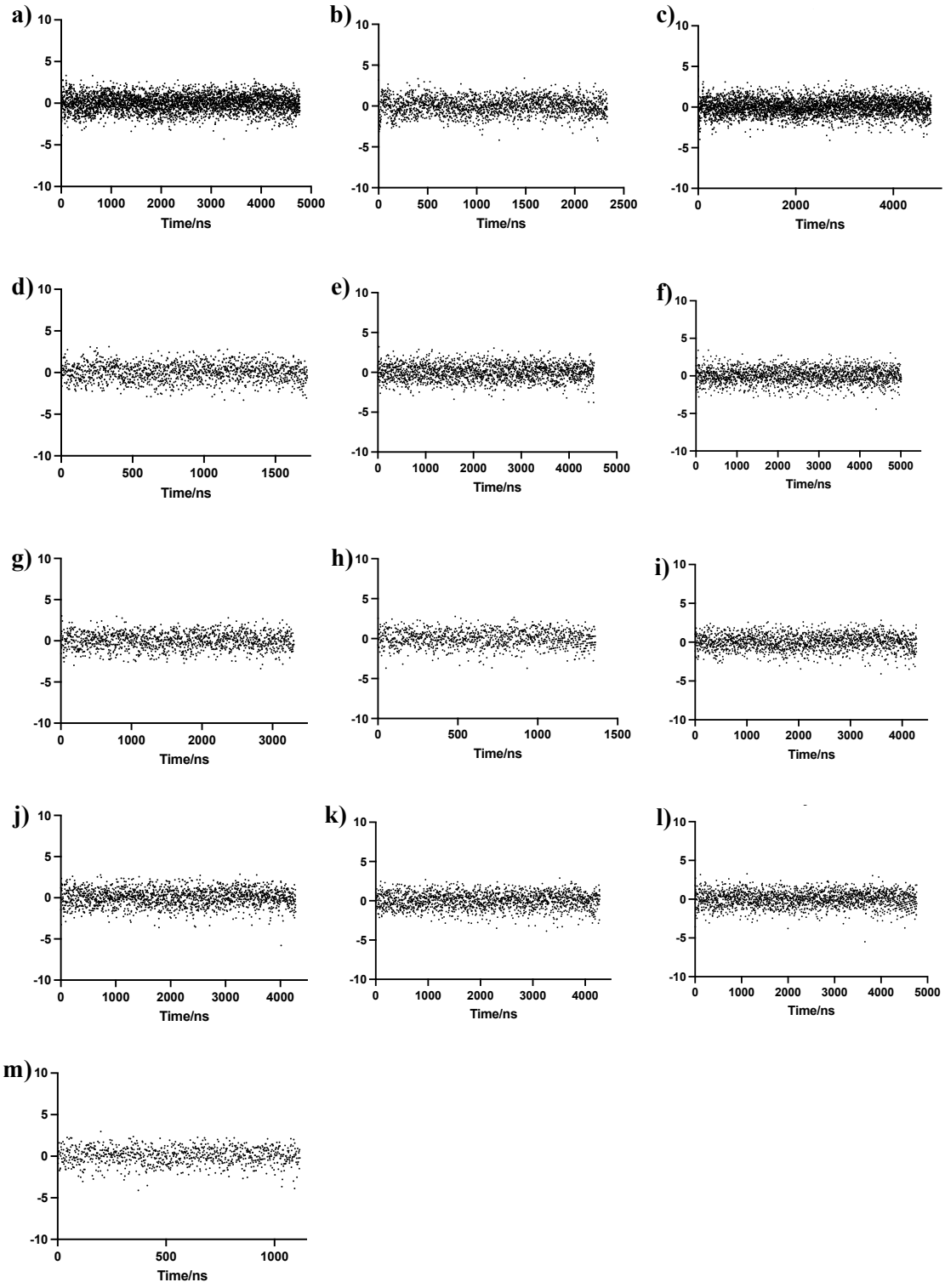


Supplementary Figure 2.28. Overlayed spectra of UV-vis absorbance (blue), excitation (black) and emission (orange) of ***a) IrpqSS****,* ***b) IrpqSH*** *and* ***c) Irpqbpy*** *in H_2O (2% MeOH) Concentration of the solutions used for collection of spectra was 20 μM. For emission spectra, $\lambda_{ex} = 440$nm.*

Luminescence Lifetimes

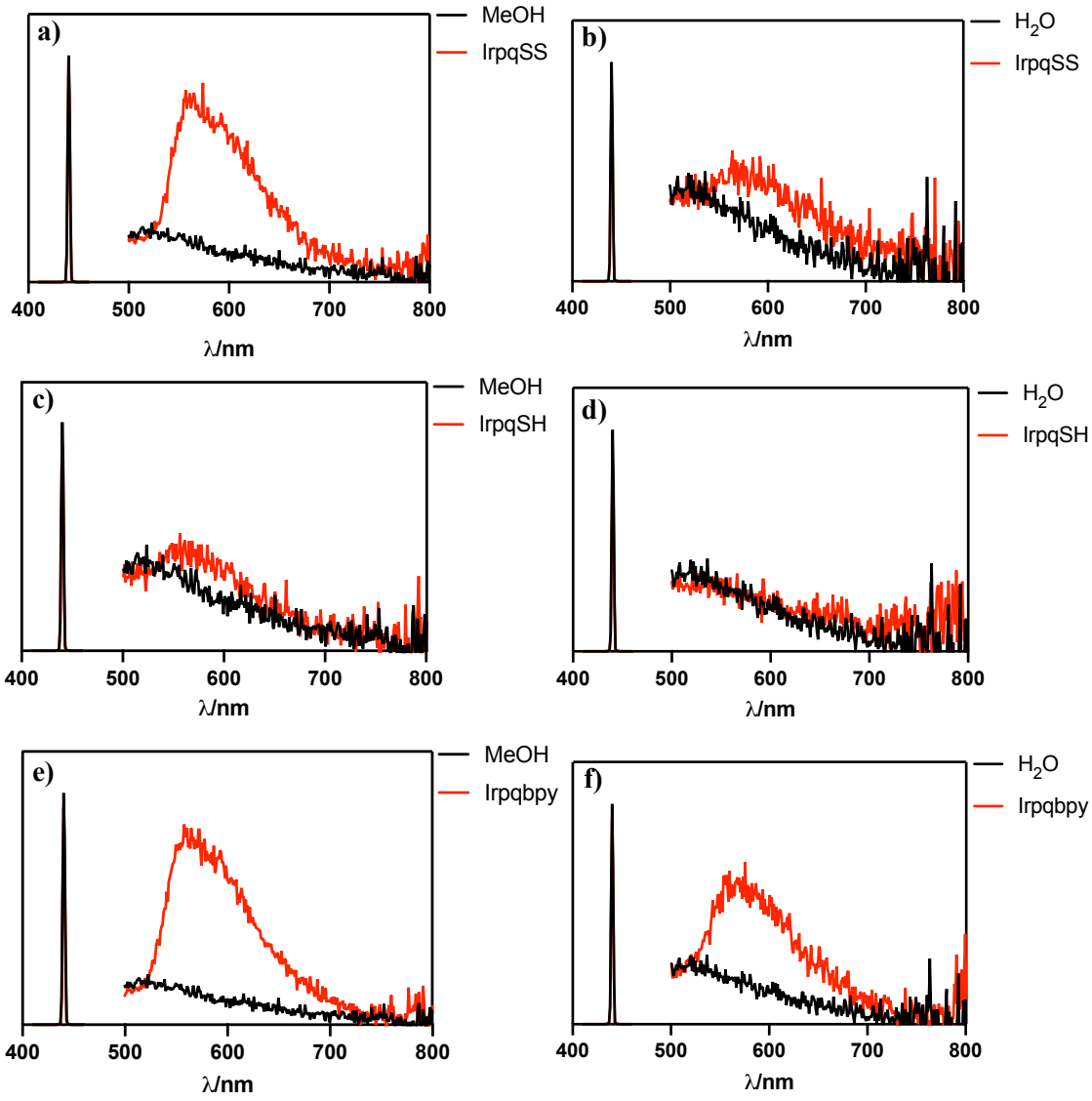


*Supplementary Figure 2.29. Luminescence lifetime residuals from the fittings in aerated MeCN, MeOH and H_2O (**a**, **b**, **c**) for **IrpqSS**, (**f**, **g**, **h**) for **IrpqSH** and (**i**, **j**, **k**) for **Irpqbpy**. Luminescence lifetime residuals from the fittings in deaerated MeCN and MeOH (**d**, **e**) for **IrpqSS**, in deaerated MeOH (**h**) for **IrpqSH** and (**k**) for **Irpqbpy**.*

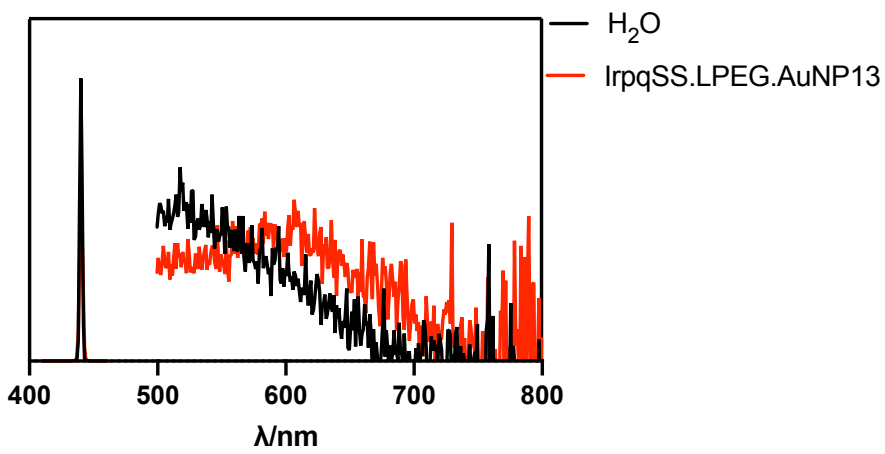


Supplementary Figure 2.30. Luminescence lifetime residuals from the fittings in H_2O for ***IrpqSS*** *+* ***LPEG (a)****, +* ***SPEG (b)****, and +* ***Zonyl (c)****, and for* ***IrpqSH*** *+* ***Zonyl (d)****.* ***IrpqSS.LPEG.AuNP13****,* ***IrpqSS.SPEG.AuNP13****,* ***IrpqSS.Zonyl.AuNP13****,* ***IrpqSH.Zonyl.AuNP13*** *and* ***IrpqSS.TFD.S.AuNP13*** *residuals at* ***e****,* ***f****,* ***g****,* ***h****, and* ***i*** *respectively.* ***IrpqSS.LPEG.AuNP25****,* ***IrpqSS.SPEG.AuNP25****,* ***IrpqSS.Zonyl.AuNP25*** *and* ***IrpqSH.Zonyl.AuNP25*** *residuals at* ***j****,* ***k****,* ***l****, and* ***m****.*

Quantum Yields



Supplementary Figure 2.31. Quantum yield luminescent spectra for the complexes in MeOH for ***a) IrpqSS****,* ***c) IrpqSH****,* ***e) Irpqbpy*** *and in H_2O for* ***b) IrpqSS****,* ***d) IrpqSH****,* ***f) Irpqbpy****. Quantum yield spectra were collected with λ_{ex} = 440 nm using an integrating sphere at concentrations of 31 μM, 63 μM and 32 μM in MeOH and 43 μM, 77 μM and 33 μM in H_2O for IrpqSS, IrpqSH and Irpqbpy respectively. The percentages of MeOH in the H_2O solutions were 4%, 8% and 3% for* ***IrpqSS****,* ***IrpqSH*** *and* ***Irpqbpy*** *respectively.*



Supplementary Figure 2.32. Quantum luminescence spectra for the calculation of ***IrpqSS.LPEG.AuNP13*** *QY at 9 nM in H_2O.*

ICP-MS calibrations and calculations

1) Calculate the ratio of iridium atoms to gold atoms. Ratio = Ir conc (ppb):Au conc (ppb)

2) Calculate the number of metal complexes by multiplying the ratio of Ir:Au by the number of atoms in 1 AuNP. For 15 nm AuNPs, the number of atoms is 1.04 x 10^5 atoms.

$$number\ of\ Ir\ complexes = number\ of\ atoms\ in\ 1\ AuNP\ x\ Ir{:}\ Au\ ratio$$

Chapter 3

3. Investigating the surfactant-dependent luminescence and localisation of iridium-coated nanoparticles

3.1 Introduction

Gold nanoparticles as a delivery vehicle for luminescent iridium(III) complexes have been widely used and the different iridium(III) complexes previously used will be will be discussed in this introduction, as iridium-coated nanoparticles are also used as imaging in this thesis. Coating of the nanoparticles with a surfactant is very important for stabilisation of the nanoparticles,[1] and localisation of the nanoparticles in cells due to the different characteristics of lipophilicity and solubility that is given by the surfactant on the surface of the AuNP, so the importance of two importance surfactant types, PEG and fluorinated surfactants will be discussed to explain and show why these types of surfactants were used in this thesis, in addition to possible localisation in the cells depending on the surfactant type. TEM images and the interpretation of TEM images will be outlined, as this was primarily used in this thesis for the identification of nanoparticle localisation in cells.

3.1.1 Iridium-coated nanoparticles for cell imaging

AuNPs coated with luminescent probes have been shown to be effective as vehicle delivery systems compared to free luminescent probes on their own in solution[2, 3]. This is because the AuNP can hold multiple complexes on the surface, enabling more efficient delivery of the luminescent probes. As a result of this, iridium(III) complexes with nanoparticles have been studied as luminescent complexes for cell imaging. For example, silica nanoparticles with iridium showed that the nanoparticles displayed photoluminescence.[4] In AuNPs, iridium(III) complexes with 2-phenylpyridine were also successful in imaging of cells (Figure 3.1)[5] and some were even found in the nucleus. Iridium(III) complexes have been attached to 3 nm AuNPs[6], 4 nm AuNPs[7], as well as 25 nm AuNPs (Figure 3.2) and 100 nm

AuNPs.[8] However, imaging of iridium-coated AuNPs has not been studied extensively[5, 8] in the same way that iridium(III) complexes on their own have been widely studied in cells (Chapter 2, Section 2.1.1). Hence there is a need for more development of iridium-coated AuNPs for imaging in cells. AuNPs coated with lanthanides[9] and ruthenium[10, 11] have been studied.

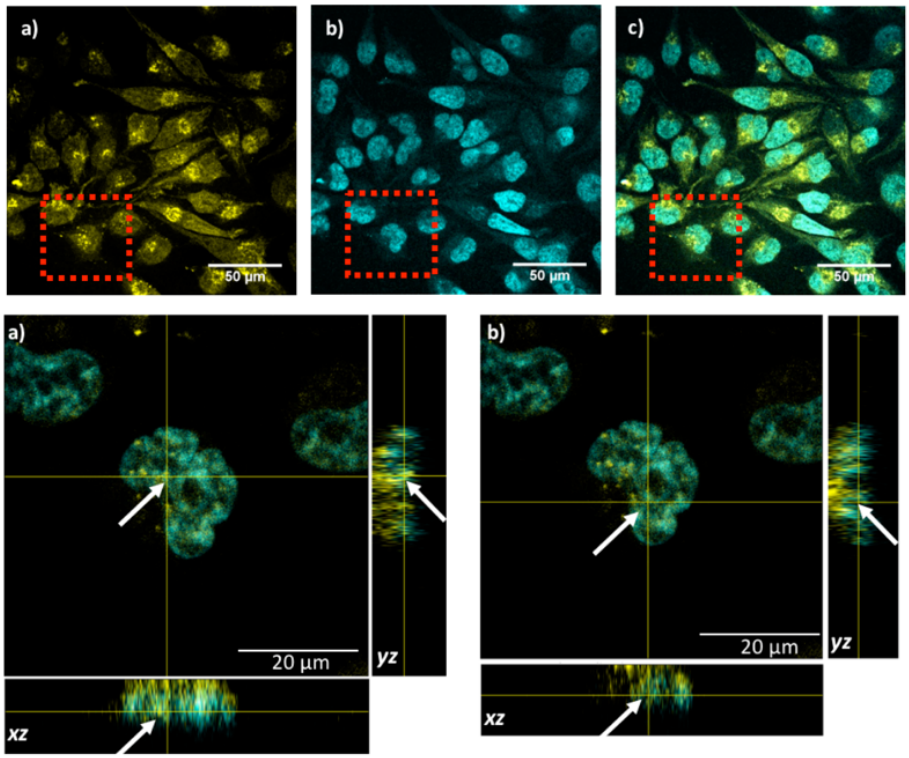


*Figure 3.1. Widefield confocal luminescence images of iridium-coated AuNP (**IrC6.AuNP25**). Top: 3 h incubation. **(a)** Image of iridium luminescence signal, **(b)** Image of Hoechst luminescence signal, **(c)** overlay of iridium and Hoechst luminescence images, 50 µm scale bar. Bottom: nanoparticle clusters at two locations **(a)** and **(b)** 20 µm scale bar. Image obtained from **S. M. King et al., J. Am. Chem. Soc., 2018, 140, 10242-10249**.*

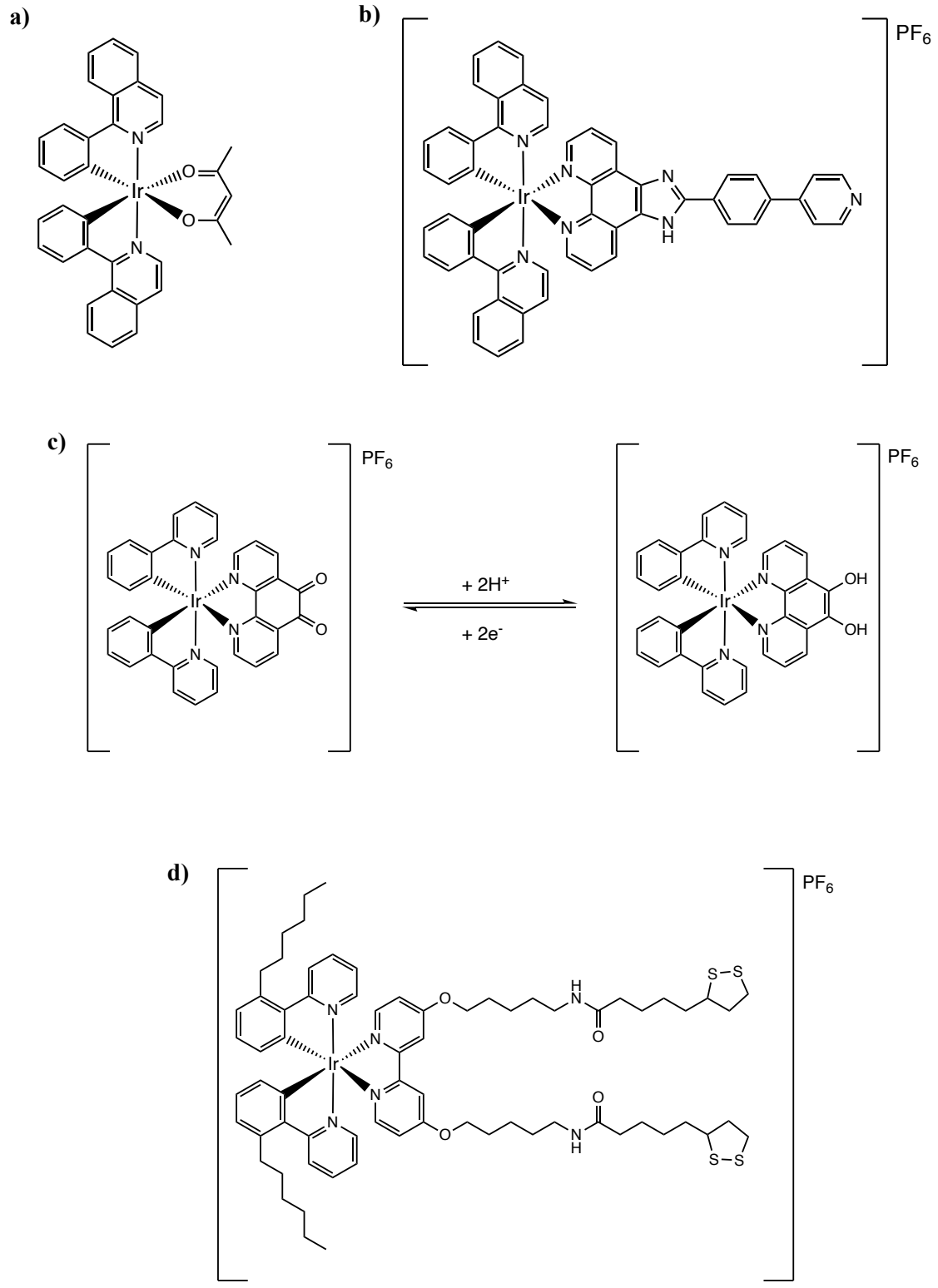


Figure 3.2. Iridium(III) complexes used for coating AuNPs. Images obtained from ***a) & b) F. Miomandre et al., J. Phys. Chem. C., 2013, 117, 12806-12814****, c) X. Miao et al., Sci. Rep., 2017, 7, 42740* *and* ***d) S. M. King et al., J. Am. Chem. Soc., 2018, 140, 10242-10249****.*

3.1.2 Effect of surfactants on nanoparticle stability, functionalisation, and uptake

As outlined in Section 3.1.1, luminescent AuNPs coated with metal complexes can be used for imaging in cells. Standard protocols require a surfactant to reduce the surface tension before the addition of the other complexes, and provide stability.[1, 12] 'Surfactants' used in the context of this thesis do not have the traditional definition of being amphiphilic compounds but instead are named 'surfactants' because they are used to coat the surface of NPs.[12] The uptake of the AuNPs in cells and the biological response to them can be affected by the nature of the surfactant, and a surfactant that is predominantly used is PEG (polyethylene glycol)[13, 14], however some are fluorinated surfactants.[10, 11] lipoic acid[15] and BPEI (branched polyethyleneimine).[16] Depending on the charge that a particular surfactant can give to a nanoparticle surface, the localisation and the speed of uptake can be affected. For example, a study in HEK (Human Epidermal Keratinocytes) cells was performed, where the uptake of 40 and 80 nm AuNPs with different coatings was investigated.[15] The different coatings were PEG, BPEI and lipoic acid. The investigation showed that BPEI-AuNPs showed greatest uptake in the cells with PEG-AuNPs showing the least uptake, although the PEG-AuNPs showed increased uptake at later timepoints, indicating a time dependent uptake. PEG is a neutral coating, lipoic acid is negatively charged and BPEI is positively charged, which caused possible increased interaction to the cell membrane. Positive nanoparticles (or those with a positively charged coating) would therefore be optimal for increased uptake in cells.[17, 18] In Sections 3.1.2.1 and 3.1.2.2, previous research on PEG AuNP coatings and fluorinated compound NP coatings will discussed, as they are the AuNP coatings used for this thesis. These sections on the different surfactants are included to show the difference in the depth of research between these two types of NP coating, and why more investigation is required for fluorinated NP coatings, which is not as common or deeply studied as PEG.

3.1.2.1 PEG nanoparticle coating

PEGylation (coating nanoparticle surfaces with PEG) is a commonly used method for improving the efficiency of delivery of moieties to target cells[19], and research surrounding this NP surfactant is quite extensive.[20] PEG-based surfactants are non-lipophilic and hydrophilic[21] and have been shown to increase the circulation time of AuNPs by prolonging aggregation and excretion from the body[22] by

forming a hydrophilic layer on the AuNP surface to protects it.[23] PEG coated nanoparticles have been shown to increase the half-life in blood[24], as evidence shows that PEG can prevent phagocytosis of the nanoparticles.[25, 26]

Previous research has outlined the many effects that PEG may have on the mechanical properties, nanoparticle stability, drug encapsulation/release, plasma protein adsorption, mucus penetration, selectivity of targeting, cell internalisation, circulation time in vivo and blood clearance effects of nanoparticles (Figure 3.3).[23] Although not all the effects of PEG will be explored here, this shows the wide field of research into PEGylation.

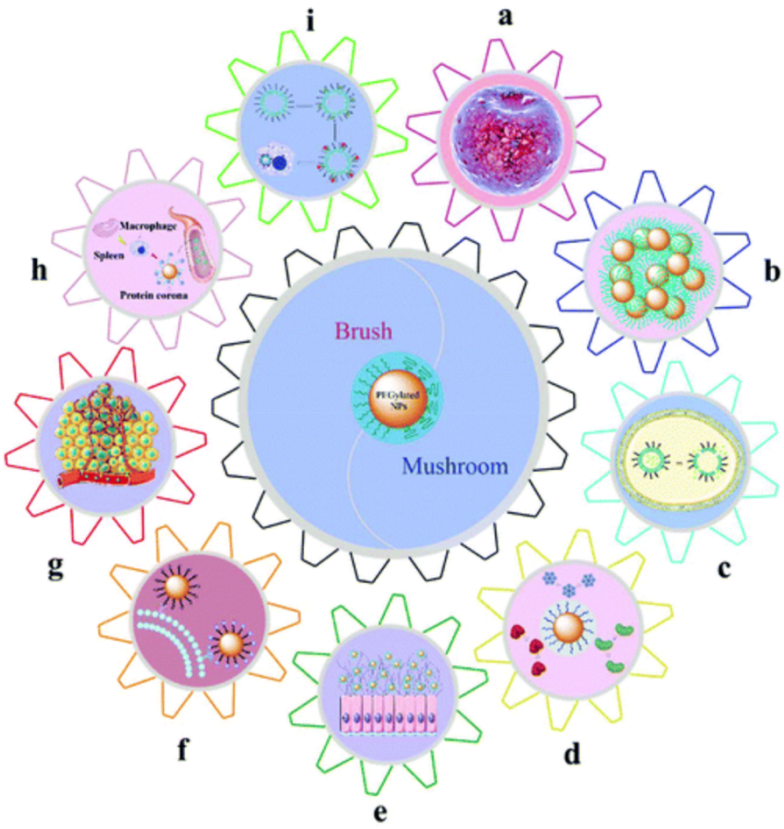


Figure 3.3. Image showing the effect of PEG on nanoparticles: ***a)*** *mechanical properties,* ***b)*** *nanoparticle stability,* ***c)*** *drug encapsulation/release,* ***d)*** *plasma protein adsorption,* ***e)*** *mucus penetration,* ***f)*** *selectivity of targeting,* ***g)*** *cell internalization,* ***h)*** *circulation time in vivo and* ***i)*** *blood clearance effects. Image obtained from* ***L. Shi et al., Nanoscale, 2021, 13, 10748-10764****.*

Nanoparticle colloidal stability through steric repulsion is evident in PEG-coated particles due to the distance between the two particles created by the chain length of the PEG.[23] Hence, longer PEG chains with higher molecular weights were found to increase steric repulsion and reduce aggregation of the particles.[27] Fast clearing of PEGylated nanoparticles in the body, commonly termed accelerated blood clearance (ABC), is a phenomenon that occurs due to anti-PEG IgM in the spleen.[28] This fast clearance limits the development of PEGylated nanoparticles, as even if efficient targeting and endocytosis is achieved in vivo, fast clearing of the nanoparticle limits their activation timescale, reducing their overall efficiency. Therefore, some alternatives to PEGylated nanoparticles are necessary, one of which are fluorinated surfactants (Section 3.1.2.2) used in this thesis. When NPs are used for targeting receptors, the PEG surfactant can be used to attach to the ligands used for targeting the receptors, as in the case of direct conjugation of antibodies to AuNPs.[29] Studies have shown that large molecular weight PEG molecules with increased chain flexibility get tangled with one another, reducing the effectivity of the receptor targeting.[19] Therefore a balance between nanoparticle stability and targeting efficiency needs to be considered when designing nanoparticles for a particular function.

PEG surfactants have been shown to improve stability of AuNPs at different pH[30] and in different media in vitro by modifying the density of the surfactant on the surface.[31] Interaction of the PEG-capped AuNPs with PBS, PBS/BSA and DCM was studied. Whereas citrate-stabilised AuNPs aggregated, the PEG-capped AuNPs remained stable in these media. A linear relationship was found between PEG coating and the stability of the AuNPs. An optimal coating of PEG was found to be ~1.13 chains /nm^2.[31] Cyclic PEG molecules for dispersion stability were studied in varying conditions such as freezing, freeze-drying and heating[32] (Figure 3.4) showing that physisorbed cyclic PEGs were better than thiolated PEGs in these conditions.

The interaction of PEG chains with proteins to form protein coronas could influence the uptake, circulation, degradation, elimination and stealth properties of PEGylated liposomes and nanoparticles in the blood.[23, 33, 34] PEG molecules with small molecular weights had more protein absorbed, with larger PEGs having greater anti-protein absorption due to the hydrophilic hydration layer formed around the

nanoparticle[35] (Figure 3.5, Figure 3.6).[36, 37] The surface charges of the AuNPs can change as well as the hydrophilic nature of the particles when PEGylated.[23, 38] In Figure 3.5, the density of the PEG was increased alongside the molecular weight of the PEG, and higher density of PEG coating alongside higher PEG molecular weight was the best for anti-protein absorption. In Figure 3.6[37] also, as the PEG density increased, the adsorbed protein quantity decreased. This reduced protein absorption brought about by higher molecular weight PEG (longer chain PEG) is what gives rise to the stealth effect, prolonging nanoparticle circulation time, reducing uptake, degradation and elimination[23].

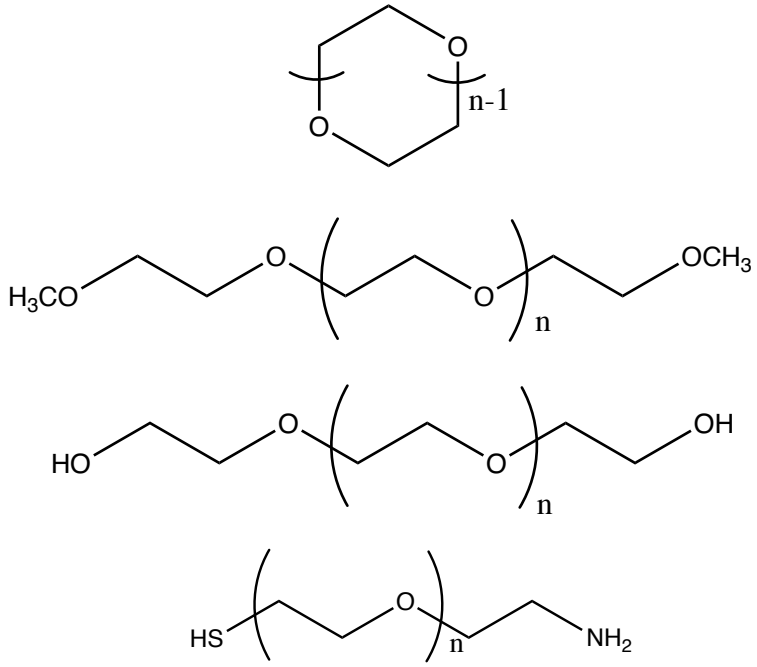


Figure 3.4. A variety of PEG surfactants previously studied for stabilizing AuNPs and performing stabilization studies in different environments. Structures obtained from ***Y. Wang et al., Nat. Commun., 2020, 11, 6089****,* ***J. A. Zamora-Just et al., J. Nanomater., 2019****, and* ***Y.-C. Huang et al., Biomed. Res. Int., 2014, 2014, 182353-182353****.*

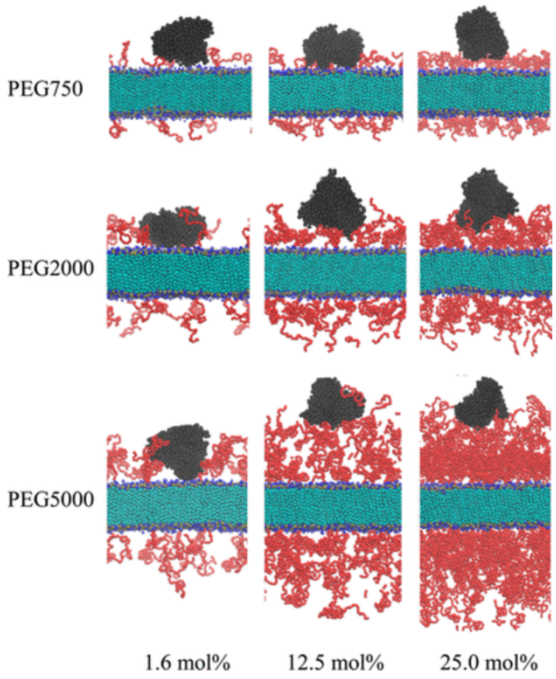


Figure 3.5. Image showing the effect of PEG chain length on protein adsorption of nanoparticles at different PEG coating densities. As PEG chain length and density increases, protein adsorption decreases. Image obtained from ***H. Lee and R. G. Larson, Biomacromolecules, 2016, 17, 1757-1765.***

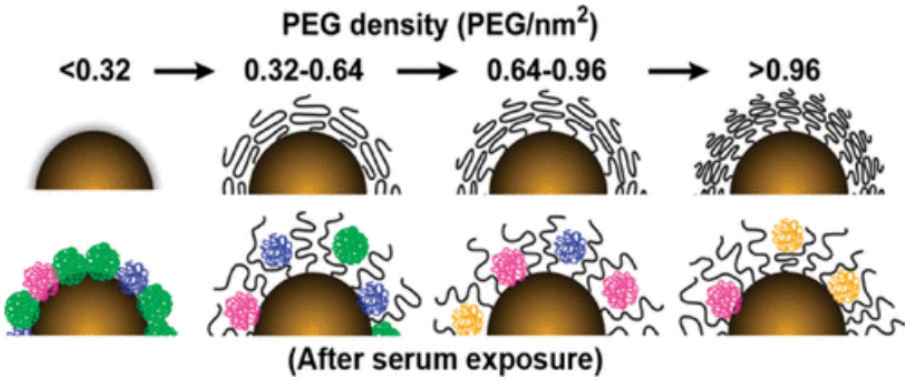


Figure 3.6. Image showing the effect of PEG density on protein adsorption of nanoparticles. Higher density of PEG causes less protein to be adsorbed and causes PEG conformation to change. Image obtained from ***C. D. Walkey et al., J. Am. Chem. Soc., 2012, 134, 2139-2147.***

Aside from PEG chain length and density of coating, the conformation of PEG at the nanoparticle surface plays a role in the adsorption of proteins. PEG has different conformations on a nanoparticle surface, namely mushroom (collapsed PEG chain conformation which takes up more AuNP surface area)[39], brush ('extended PEG chain conformation which takes up less AuNP surface area)[40] and dense brush conformations[41]. Higher density coatings of PEG would adopt the brush formation rather than the mushroom, to avoid steric hindrance caused by neighbouring PEG molecules. When the density is low, the PEG chains are collapsed in the mushroom formation[23]. For larger molecular weight PEG molecules, there is less space at the nanoparticle surface compared to a smaller molecular weight PEG, so the density at the surface of the nanoparticle is higher. Therefore, the larger PEG would adopt a brush formation more readily than a smaller PEG and be able to increase steric repulsion and reduce aggregation of the particles.[27] Therefore, by modifying PEG chain length and AuNP coating density, the protein corona can be modified and circulation time and uptake of the AuNPs can also be modified to suit a particular function.

3.1.2.2 Fluorinated compound nanoparticle coating

Fluorinated surfactants are more lipophilic than PEG due to the absence of oxygens in the chain. As seen in Section 3.1.2.1, extensive research has been performed with PEG to overcome the limitations and optimise its advantages. There is a need for other surfactants that may be able to improve immunogenicity of surfactant-coated nanoparticles in vivo[21]. Fluorinated surfactants are one of them. The limitation of fluorinated nanoparticle coating compared to the PEG coating is that they may be toxic to cells[42] and are more lipophilic. Another method aside may be forgo surfactants altogether, such as the method for adding DNA to AuNPs avoid the surfactant method and reduce toxicity.[43] However NPs without a coating are not as stable as with the coating. AuNP coating with fluorinated surfactants[10] have been shown to go into subcellular components such as autophagic vacuoles and lamella bodies. Majority of the studies with fluorinated surfactants have been conducted with silica nanoparticles, not gold nanoparticles. For example, (trifluoromethyl)-propanoic acid, a degradable fluorinated surfactant was used for silica nanoparticle synthesis and was able to control the particle size, shape and morphology.[44] Unlike with PEG, the current research with fluorinated nanoparticle coatings is not as

extensive with gold nanoparticles, so choosing fluorinated coatings to compare to PEG would provide an interesting novelty.

3.1.3 TEM characterisation of subcellular components for localisation studies

The methods of internalisation of gold nanoparticles into cells are: clathrin-mediated endocytosis, caveolin-mediated endocytosis, clathrin & caveolin independent endocytosis, phagocytosis and micropinocytosis.[45] Phagocytosis, clathrin- and caveolin-mediated internalisation are receptor dependent endocytosis methods, whereas passive uptake and micropinocytosis are receptor independent endocytosis methods. Upon cell internalisation, the nanoparticles are trafficked to different cell components. Localisation of AuNPs in cells can be identified using methods such as fractionation, Dark Field Microscopy, Scanning Near-Optical Microscopy, Surface-enhanced Raman spectroscopy and Transmission Electron Microscopy (TEM).[46] TEM is a technique that enables the cross-section of the cells to be seen, so that sub-cellular components are visible, as well as the nanoparticles inside them. As TEM (Chapter 1, Section 1.4.3) was used extensively in this thesis to identify the possible localisation of the nanoparticles used for the project, in this section, the sub-cellular components and their identification characteristics in TEM will be outlined. Cell uptake and sub-cellular localisation of nanoparticles is dependent on various factor such as charge, size, pH, lipophilicity, and even cell type.[45, 47, 48] The factors are so many that in the field of nanoparticle research, more understanding of these properties is still needed.[48, 49]

The nucleus of cells in TEM is the easiest structure to identify as it is the largest sub-cellular organelle with a defined membrane (Figure 3.7a)[50], responsible for storing the cell's DNA[51]. Mitochondria have an oval shaped structure with lines on the inside which are the inner membrane (Figure 3.7b)[52] and they are the site of cellular respiration[51]. The Golgi apparatus is curved in shape and has vesicles at the end to identify them (Figure 3.7c).[53] The Golgi apparatus modifies any proteins from the endoplasmic reticulum[51]. Lysosomes are a bit larger than the Golgi apparatus and have a circular structure (Figure 3.7d).[54] They contain digestive enzymes and have defined membranes to protect the acidic environment

inside them. They play a part in breaking down large molecules into smaller molecules, providing the rest of the cell with nutrients from large proteins[51].

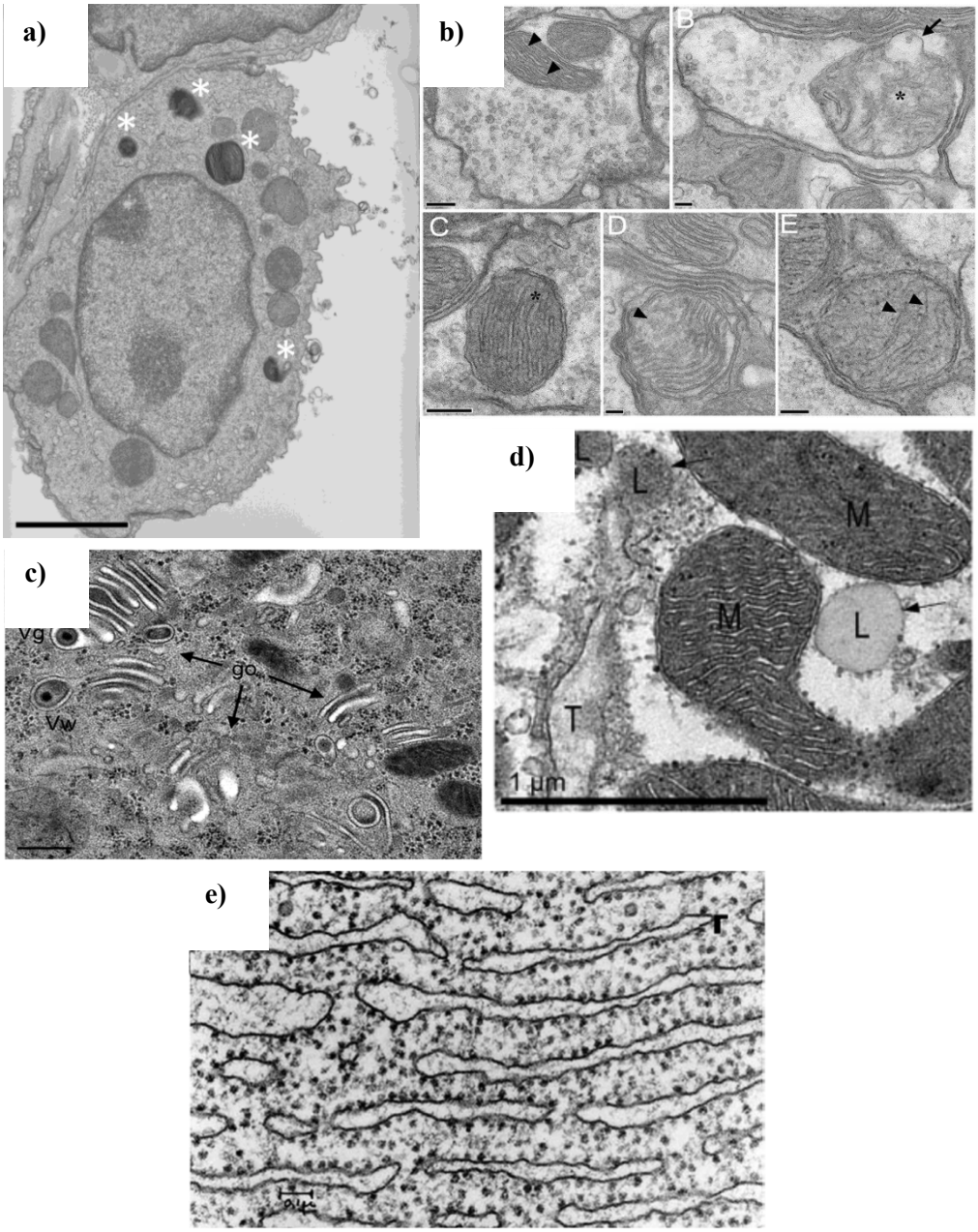


Figure 3.7. TEM images of sub-cellular organelles: ***a)*** *Nucleus (2.5 µm scale bar),* ***b)*** *Mitochondria,* ***c)*** *Golgi apparatus (500 nm scale bar),* ***d)*** *Lysosomes (1 µm scale bar) and* ***e)*** *Rough endoplasmic reticulum. Nucleus images were obtained from* ***K. Osanai, J. Mol. Sci., 2018, 19****. Mitochondria images were obtained from* ***S. Poddighe et al., PLOS ONE, 2013, 8, e73156****. Golgi apparatus images were obtained from* ***P. Wild et al., Viruses, 2015, 7, 52-71****. Lysosome images were obtained from* ***D. Aston et al., Sci. Rep., 2017, 7, 40620****. Rough endoplasmic reticulum images were obtained from* ***G. Chaldakov et al., Acta Biol. Marisiensis, 2021, 4, 31-43****.*

The rough and smooth endoplasmic reticulum – seen as a network of tubes (Figure 3.7e, Figure 3.8a)[55, 56]– can be differentiated because the rough endoplasmic reticulum is related to the ribosomes, which appear as black dots in TEM close to the structures. The rough endoplasmic reticulum is involved with the manufacture of proteins and shares part of its membrane with the nucleus. The smooth endoplasmic reticulum produces lipids[51]. The ribosomes close to the rough endoplasmic reticulum can be found in the cytoplasm and are responsible for synthesising proteins[51]. Endosomes are characterised by weak or non -existent membranes and can be more clearly seen when AuNPs or other materials are localised inside to identify them (Figure 3.8b).[57] They deliver material from the cell surface to the lysosomes for degradation or recycling within the cell via the Golgi network. Vesicles are small structures, circular in shape and similar to endosomes, transport materials between organelles. Vacuoles are identified by a smooth internal pattern due to the water filling them (Figure 3.8c).[58] They assist in removing waste products for exocytosis and in also assist in endocytosis[51]. Autophagic vacuoles include autophagosomes, amphisomes and autolysosomes. They are characterised by double layer membranes and have some characteristics of vacuoles, with the smooth internal structure (Figure 3.8d)[59] and a smaller darker component indicating the fusing of organelles that form the autophagic vacuoles. Autophagic vacuoles are involved in the degradation process of protein and organelles that are long-lived and need to be removed. Autophagosomes form when a membraned phagophore engulf portions of the cytoplasm and the membranes fuse, forming a closed structure that assists in the autophagy process. Amphisomes form upon fusion of endosomes with autophagosomes and they are an intermediate organelle that is produced before the eventual fusion with lysosomes that produce autophagosomes. Lamella bodies have rough structures with multiple circular inner membranes (Figure 3.7a, Figure 3.8e)[50, 60], found in lung cells and some skin cells.[61, 62]

Detection of sub-cellular organelles (semi-automatic) from TEM by software[63] was proposed in 2015 to lighten the load of TEM experts as sub-cellular organelle detection by experts requires a lot of expertise and training, such as sample preparation and sample sectioning, interpretation and analysis of images. Therefore, although TEM is a good technique for visualisation of the nanoparticles in sub-

cellular organelles, it requires a lot of expertise, and therefore localisation seen in TEM is best confirmed by a secondary technique.

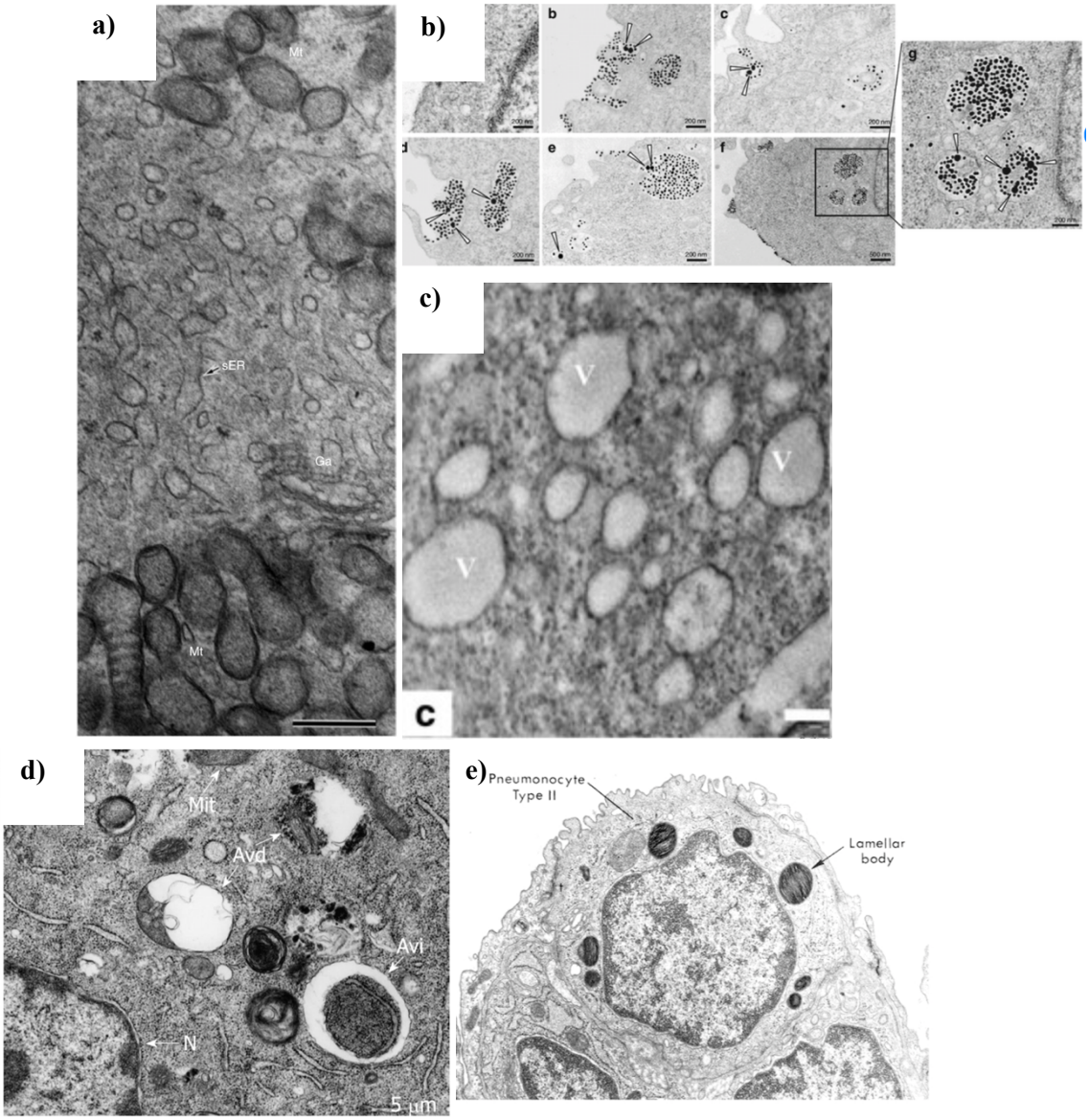


Figure 3.8. TEM images of sub-cellular organelles: ***a)*** *Smooth endoplasmic reticulum (0.5 µm scale bar),* ***b)*** *Endosomes (200 nm scale bar (bottom right: 500 nm scale bar)),* ***c)*** *Vacuoles (0.5 µm scale bar),* ***d)*** *Autophagic vacuoles and* ***e)*** *Lamella bodies. Smooth endoplasmic reticulum images were obtained from* ***T. Kaneko et al., Reproduction (Cambridge, England), 2004, 126, 817-826****. Endosome images were obtained from* ***Y. Wei et al., Nat. Commun., 2019, 10****. Vacuole images were obtained from* ***M. Thakur et al., J. Nanobiotechnology, 2014, 12, 42****. Autophagic vacuole images were obtained from* ***J. M. Esteve et al., J. Biol. Chem., 2011, 2, 232-238****. Lamella body images were obtained from* ***A. Laniece, 2018****.*

3.1.4 Chapter Summary

As outlined in Chapter 2, Sections 2.2 – 2.6, **IrpqSS**- and **IrpqSH**- coated AuNPs were synthesised and characterised. **Irpqbpy** was also synthesised as a control complex to be used alone in cells. The photophysical studies indicated that the AuNPs were luminescent and would be suitable imaging agents for cells, especially **IrpqSS.LPEG.AuNP13**, **IrpqSS.SPEG.AuNP13**, **IrpqSS.Zonyl.AuNP13**, **IrpqSS.TFD-S.AuNP13** and **IrpqSH.Zonyl.AuNP13**, which all showed the greatest luminescence in H_2O, and are the ones used in this chapter. This chapter will outline the results of the effect of surfactants on cellular uptake and imaging capabilities in cells. Different surfactants have been shown to affect the uptake of AuNPs in cells. This chapter will show the effect of different types of surfactants – perfluorinated surfactants and polyethylene glycol (PEG) surfactants on imaging and the NP localisation in cells, and whether different iridium(III) complexes affect localisation of the NPs when the same surfactant remains the same. The different surfactants compared will be **LPEG** (Poly(ethylene glycol) 2-mercaptoethyl ether acetic acid, average M_n 2100), **SPEG** (α-Thio-ω-(propionic acid) octa(ethylene glycol)), **Zonyl-FSA** (Lithium 3-[2-(perfluoroalkyl)ethylthio]propionate,) and **TFD-S** (N-(2-(ethylthio)ethyl)-2,2,3,3,4,4,5,5,6,6,7,7,8,8,9,9,10,10,11,11,12,12,12-tricosafluorododecanamide).

3.2 Uptake of coated AuNPs and Irpqbpy in A549 cells

To confirm that the AuNPs chosen for this chapter could be visualised in cells under a confocal microscope, initial imaging studies in A549 cells (Figure 3.9, Figure 3.10, Figure 3.11) were undertaken to ensure that the AuNPs and **Irpqbpy** could be seen in cells before optimisation in the pancreatic cancer cell lines. The reason for this is that A549 cells (human lung carcinoma epithelial cells) are a common cell line used for many studies. In Chapter 4, Section 4.4, the selection of the pancreatic cancer cell lines used in this project (MiaPaca-2 and CFPAC-1) will be outlined in more depth. **IrpqSS.Zonyl.AuNP13**, **IrpqSS.LPEG.AuNP13** and **Irpqbpy** were chosen for the initial A549 cell studies because the nanoparticles had different surfactants, and **Irpqbpy** is the control complex without

the sulphur groups. Hoechst chemical dye was used to stain the cell nucleus for the images, giving a blue colour under a confocal microscope.

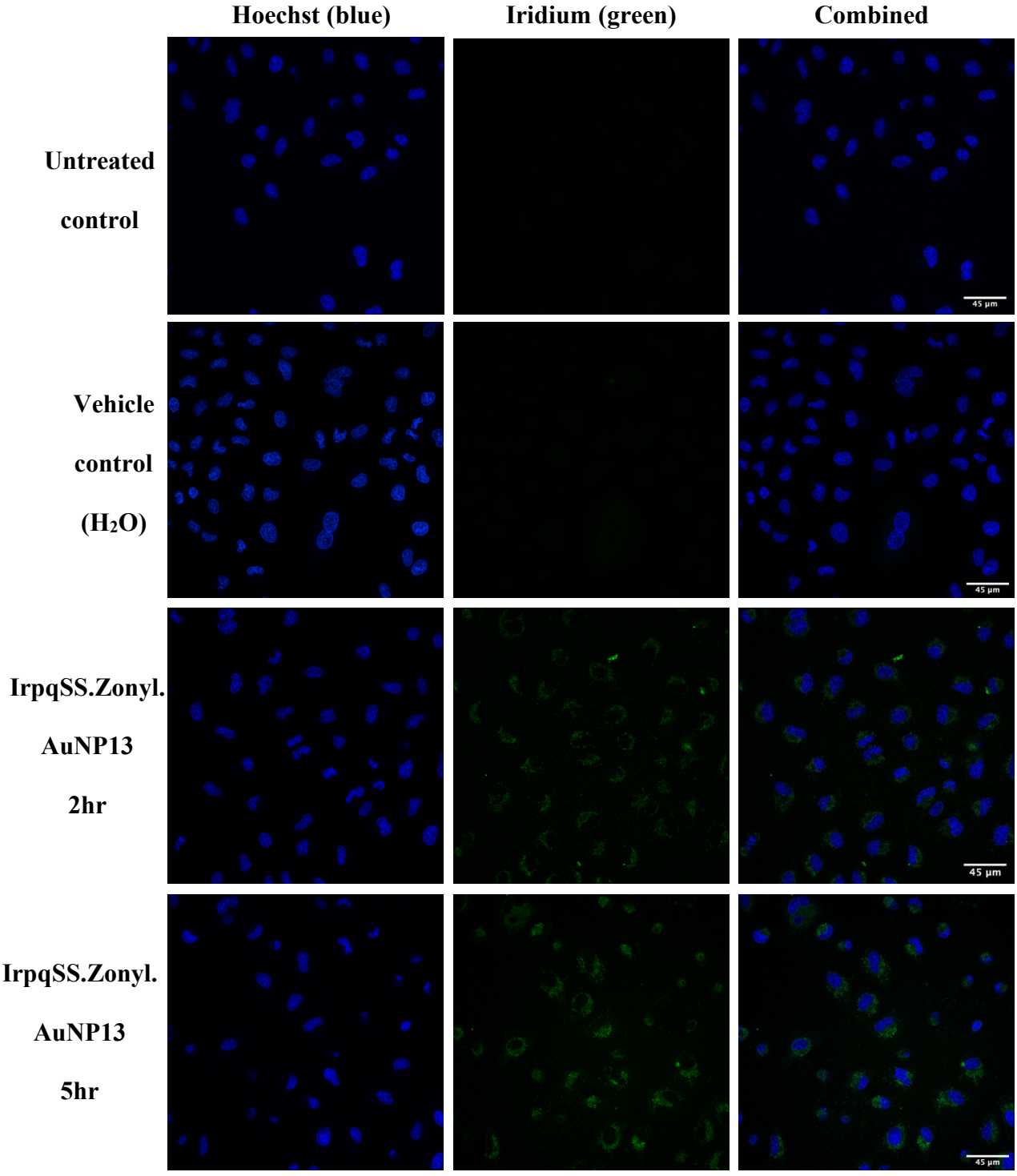


*Figure 3.9. Confocal live cell images in A549 cells for **IrpqSS.Zonyl.AuNP13** at 2.2 nM for 2 and 5 hrs. Images were collected on a Leica SP8 upright microscope using a 40x ceramic water dipping objective lens. Hoechst (blue) settings: λ_{exc} = 402, λ_{em} = 419 – 472 nm; Iridium(green): λ_{exc} = 458 nm, λ_{em} = 550 – 750 nm.*

LPEG, is a hydrophilic, non-lipophilic surfactant, whereas **Zonyl** is a perfluorinated, hydrophobic, lipophilic surfactant. Uptake in cells for PEG-coated AuNPs has been studied before (Section 3.1.2.1). **IrpqSS.Zonyl.AuNP13** at 2.2 nM showed an even spread over the cytoplasm (Figure 3.9), whereas **IrpqSS.LPEG.AuNP13** at 2.6 nM had a scattering pattern, with points of bright luminescence (Figure 3.10). This provided initial indication that **Zonyl** and **LPEG** supported internalisation in different sub-cellular compartments, possibly due to differences in lipophilicity.

Irpqbpy at 5 μM and 10 μM showed a strong signal in the cells (Figure 3.11), remaining firmly in the cytoplasm. The coated NP samples remained firmly within the cytoplasm without going into the nucleus. The concentrations used for the initial study did not seem to cause damage to the cells by visual observation under confocal. Once luminescence from A549 cells incubated with the coated NPs had been confirmed, studies with pancreatic cancer cells commenced.

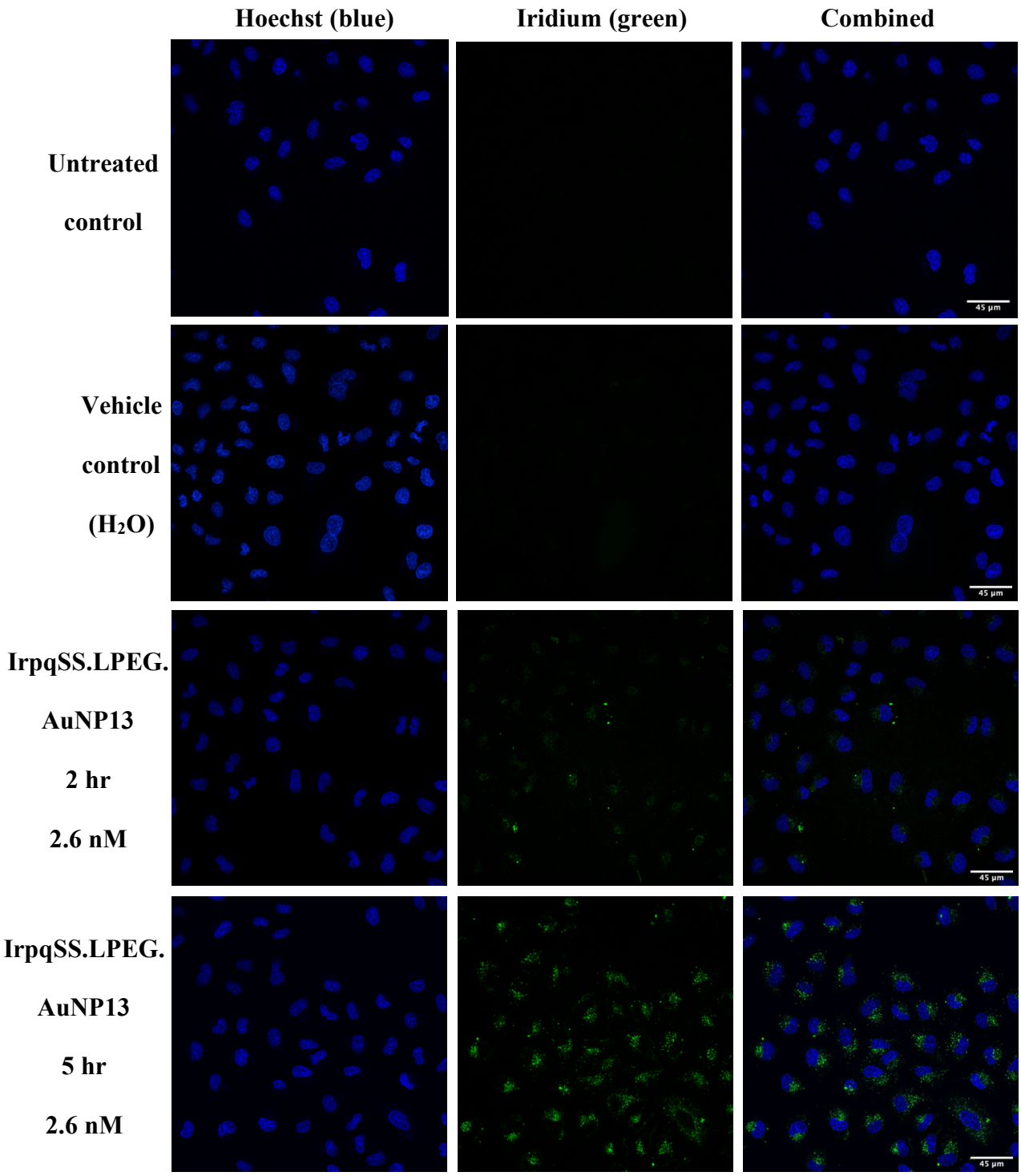


*Figure 3.10. Confocal live cell images in A549 cells for **IrpqSS.LPEG.AuNP13** at 2.6 nM for 2 and 5 hrs. Images were collected on a Leica SP8 upright microscope using a 40x ceramic water dipping objective lens. Hoechst (blue) settings: λ_{exc} = 402, λ_{em} = 419 – 472 nm; Iridium(green): λ_{exc} = 458 nm, λ_{em} = 550 – 750 nm.*

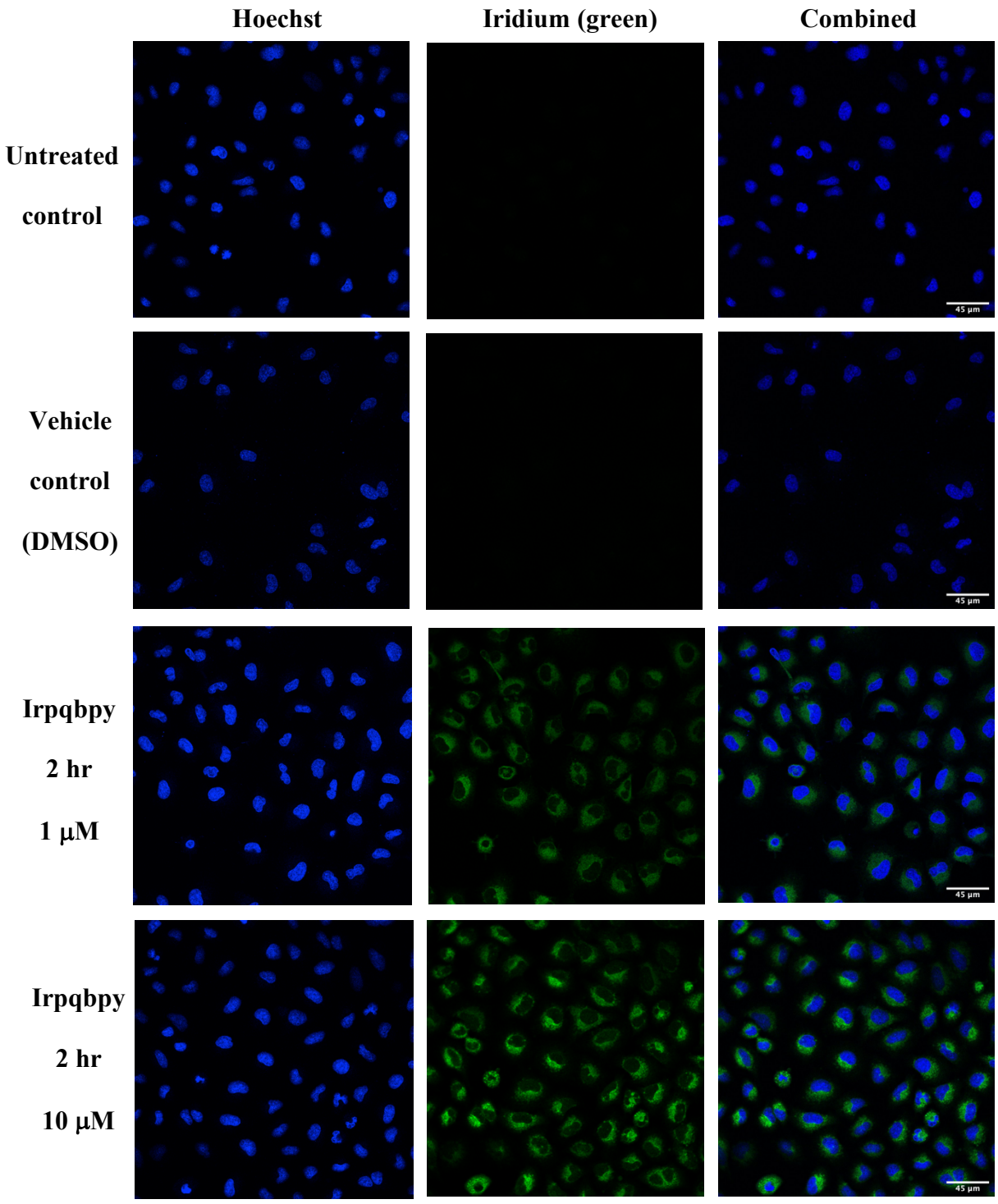


*Figure 3.11. Confocal live cell images in A549 cells for **Irpqbpy** at 1 μM and 10 μM for 2 hrs. Images were collected on a Leica SP8 upright microscope using a 40x ceramic water dipping objective lens. Hoechst (blue) settings: λ_{exc} = 402, λ_{em} = 419 – 472 nm; Iridium(green): λ_{exc} = 458 nm, λ_{em} = 550 – 750 nm.*

3.3 Cell survival assays in MiaPaca-2 and CFPAC-1 cells

MTT (3-(4, 5-dimethylthiazolyl-2)-2, 5-diphenyltetrazolium bromide) assays were performed across the two pancreatic cancer cell lines with **IrpqSS.LPEG.AuNP13**, **IrpqSS.SPEG.AuNP13**, **IrpqSS.Zonyl.AuNP13**, **IrpqSH.Zonyl.AuNP13** and **Irpqbpy** (Figure 3.12). MTT assays are colorimetric assays that asses the metabolic activity of cells, indicating the viability of the cells. The maximum concentration of the NPs used in the MTT assays was 1.2 nM because a 10% dilution from the stock 12 nM AuNPs in H_2O was used to make the 1.2 nM DMEM (Dulbecco's Modified Eagle Medium) concentration, with 10% H_2O. The maximum concentration of **Irpqbpy** used in the assays was 10 μM. The stock **Irpqbpy** concentration was 1 mM in H_2O (10% DMSO), so the final concentration of H_2O in the assays was 1% in DMEM. The concentrations determined as optimal to use for both the MiaPaca-2 and CFPAC-1 cells was 0.6 nM for the NPs and 0.63 μM for **Irpqbpy** for effective comparison between the two cell lines. 0.6 nM did not show a statistically significant decrease in % cell viability compared to the untreated cells for 3 out of 4 NP sample incubations in CFPAC-1 cells and 2 out of 4 NP sample incubations in MiaPaca-2 cells. Hence 0.6 nM was determined as a concentration that would provide overall low toxicity for all AuNP incubations while being at a high enough concentration to be imaged on a confocal microscope. **Irpqbpy** at concentrations of > 2.5 μM in MiaPaca-2 cells was just as toxic as 1% Triton. As studies in this chapter will outline, MiaPaca-2 cells showed greater internalisation than CFPAC-1 when incubated with the same concentration of treatment samples, so from this, due to more complexes of **Irpqbpy** being internalised in MiaPaca-2 compared to CFPAC-1, this led to greater toxicity in that cell line at low concentrations.

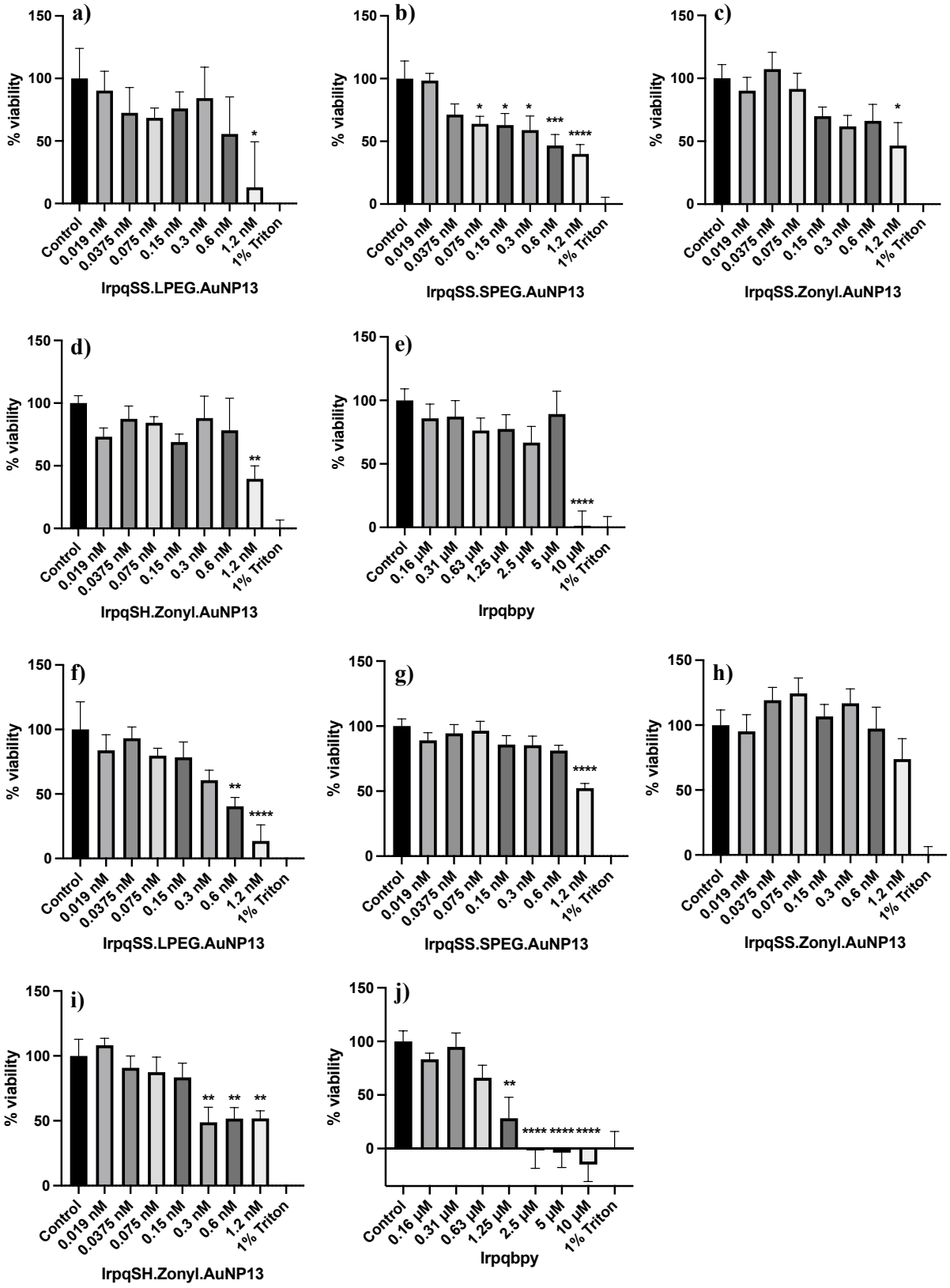


Figure 3.12. MTT assays of the iridium-coated AuNPs and ***Irpqbpy*** *in CFPAC-1* ***(a – e)*** *and MiaPaca-2* ***(f - j)****. The mean of two experiments carried out in quintuplicates with untreated (control) cells and 1% Triton positive controls. Samples were normalized to the 1% Triton signal. A maximum AuNP concentration of 1.2 nM and a maximum* ***Irpqbpy*** *concentration of 10 µM was used. P-value upper limits obtained from ANOVA analysis were represented by * = 0.0332, ** = 0.0021, *** = 0.002 and **** = 0.0001.*

Previous studies with ruthenium-coated NPs and different iridium-coated NPs than the ones in this project have shown that **AuNP13** concentrations up to 0.9 nM are not toxic to A549 cells.[10] From the MTT assays of the MiaPaca-2 and CFPAC-1 cell lines, a concentration of 0.9 nM for most of the samples is toxic to the cells (Figure 3.12). In the confocal studies with the A549 cells (Section 3.2), it was noticed that the concentration of Hoechst that could be added (up to 20 μM) and the concentration of NPs that could be added (up to 2.6 nM) was much higher than for the MiaPaca-2 and CFPAC-1 cell lines (20 nM for Hoechst and 0.6 nM for the AuNPs). In addition, up to 10 μM of **Irpqbpy** could be incubated with the A549 cells, but a concentration of 10 μM was toxic to both pancreatic cancer cell lines. This indicates that A549 cells are a more robust cell line compared to the pancreatic cancer cell lines, and MiaPaca-2 and CFPAC-1 are more sensitive to the concentration of Hoechst, NPs and iridium(III) complexes that they are incubated with, as there was no visual toxicity in the A549 cells at NP concentrations of 2.2 nM and 2.6 nM, and **Irpqbpy** concentrations of 5 and 10 μM.

3.4 Uptake and localisation of coated AuNPs and Irpqbpy in pancreatic cancer cells

3.4.1 Confocal luminescence of nanoparticles in MiaPaca-2 and CFPAC-1 cell lines

The confocal images showed that all NPs incubated with the cells exhibited fluorescence at an incubation concentration of 0.6 nM. The fluorescence of the iridium-coated nanoparticles in MiaPaca-2 and CFPAC-1 cells had different visual fluorescence patterns between the different cell lines (Figure 3.13, Figure 3.15, Supplementary Figure 3.8, Supplementary Figure 3.9), which is seen more clearly in the enlarged images (Figure 3.14, Figure 3.16), where the NPs in the MiaPaca-2 cell line seem to be spread all over the cytoplasm, without localised bright spots. In CFPAC-1, the **LPEG** and **SPEG**-coated **AuNP**s have localised spots of bright emission, whereas the **Zonyl**-coated NPs seem to be spread all over the cytoplasm. The difference in patterns could be due to the different surfactants on the AuNPs, and different localisation in the cub-cellular compartments for each cell line due to the different nature of the cells.

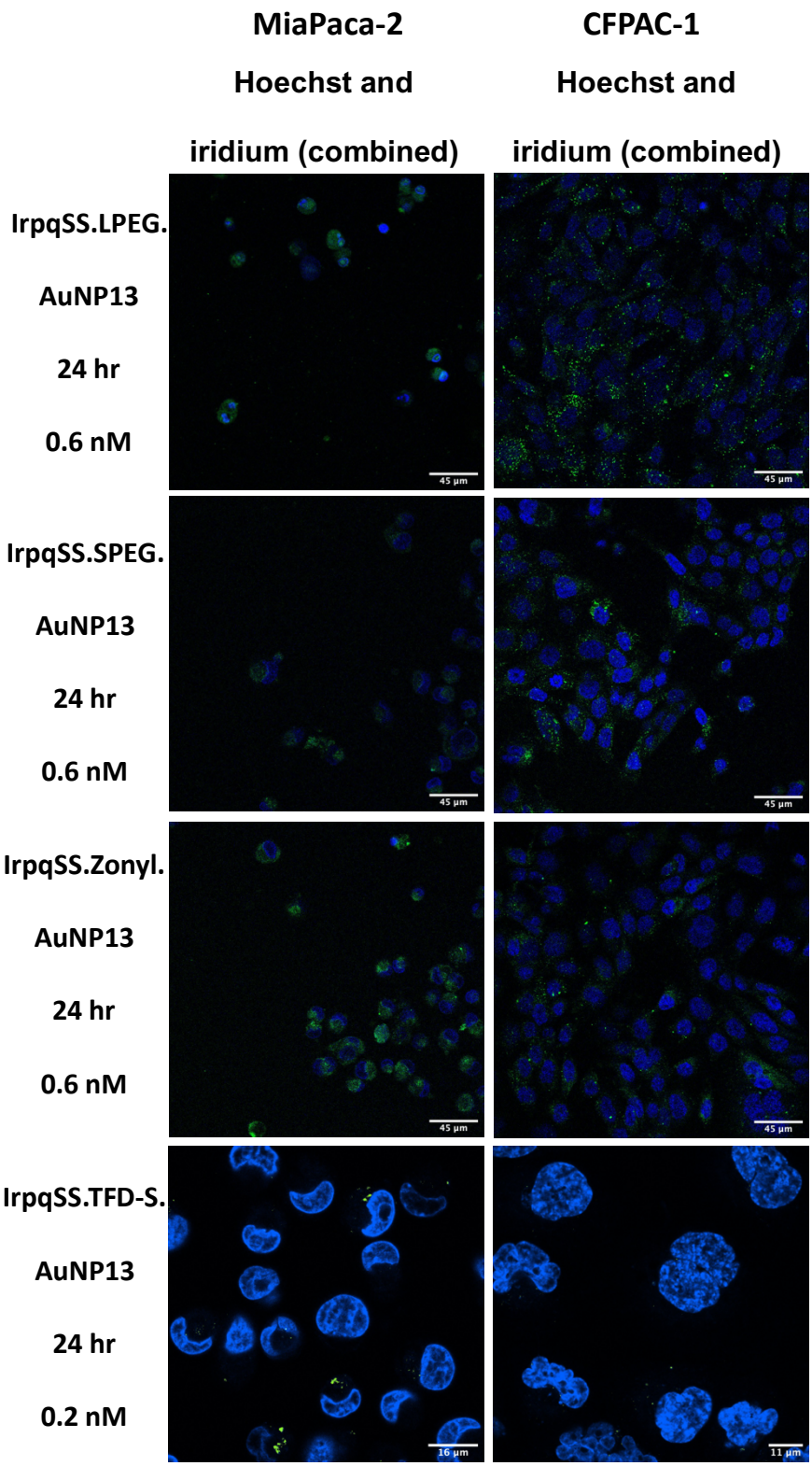


Figure 3.13. Confocal live cell images in MiaPaca-2 and CFPAC-1 cell lines of ***IrpqSS.LPEG.AuNP13****,* ***IrpqSS.SPEG.AuNP13****,* ***IrpqSS.Zonyl.AuNP13*** *at 0.6 nM for 24 hr collected on a Leica sp8 upright microscope using a 40x ceramic water dipping objective lens. Hoechst (blue) settings:* λ_{exc} *= 402,* λ_{em} *= 419 – 472 nm; Iridium(green):* λ_{exc} *= 458 nm,* λ_{em} *= 550 – 750 nm. Live cell images of* ***IrpqSS.TFD-S.AuNP13*** *at 0.2 nM for 24 hr collected on a Zeiss LSM900 inverted microscope using a 63x oil immersion objective lens. Hoechst (blue) settings:* λ_{exc} *= 402,* λ_{em} *= 450 - 495 nm; Iridium(green):* λ_{exc} *= 488 nm,* λ_{em} *= 500 – 700 nm.*

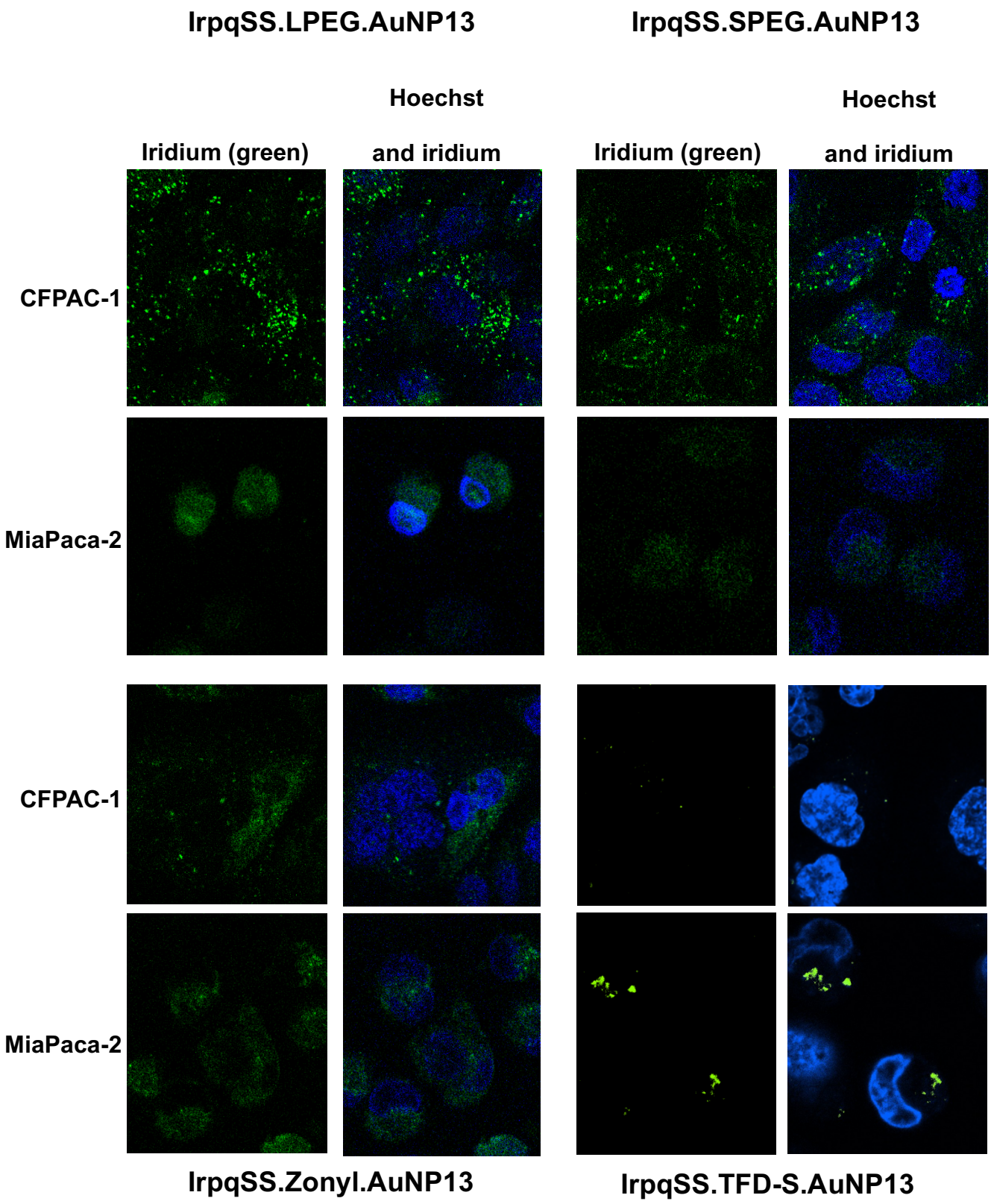


Figure 3.14. Enlarged confocal images of ***IrpqSS.LPEG.AuNP13****,* ***IrpqSS.SPEG.AuNP13****,* ***IrpqSS.Zonyl.AuNP13*** *and* ***IrpqSS.TFD-S.AuNP13*** *in MiaPaca-2 and CFPAC-1 at 0.6 nM for 24 hr.* ***IrpqSS.TFD-S.AuNP13*** *images were collected at 0.2 nM for 24 hr.*

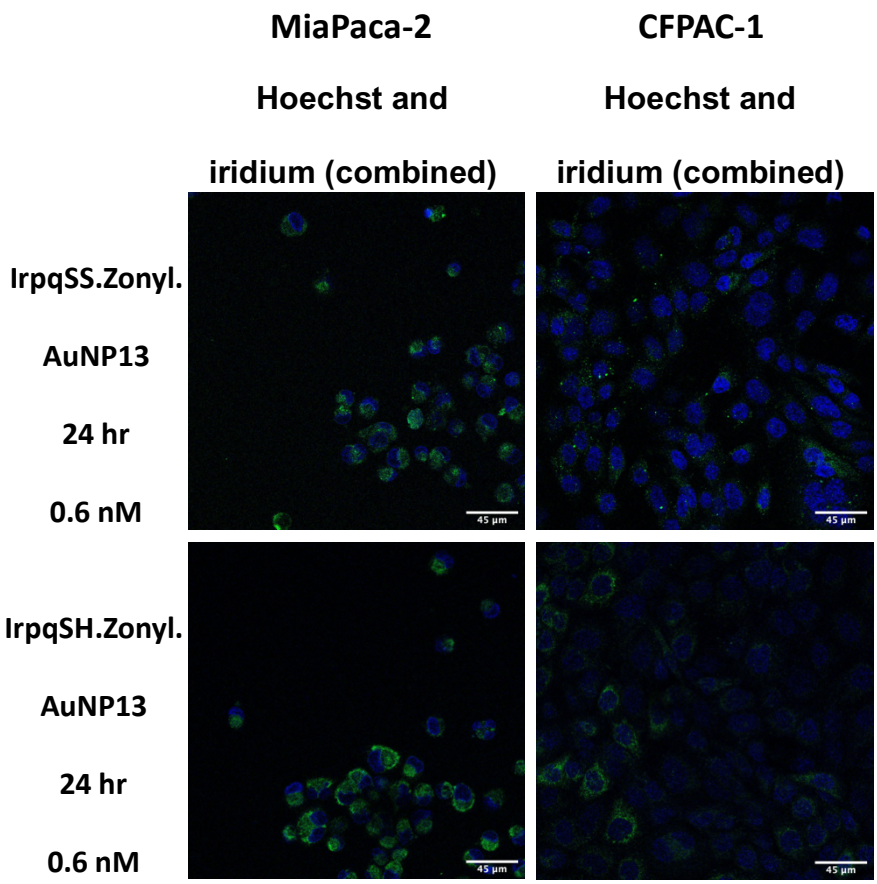


Figure 3.15. Confocal images of MiaPaca-2 and CFPAC-1 cell lines with 0.6 nM of ***IrpqSS.Zonyl.AuNP13*** *and* ***IrpqSH.Zonyl.AuNP13*** *for 24 hr collected on a Leica sp8 upright microscope using a 40x ceramic water dipping objective lens. Hoechst (blue) settings:* λ_{exc} *= 402,* λ_{em} *= 419 – 472 nm; Iridium(green):* λ_{exc} *= 458 nm,* λ_{em} *= 550 – 750 nm.*

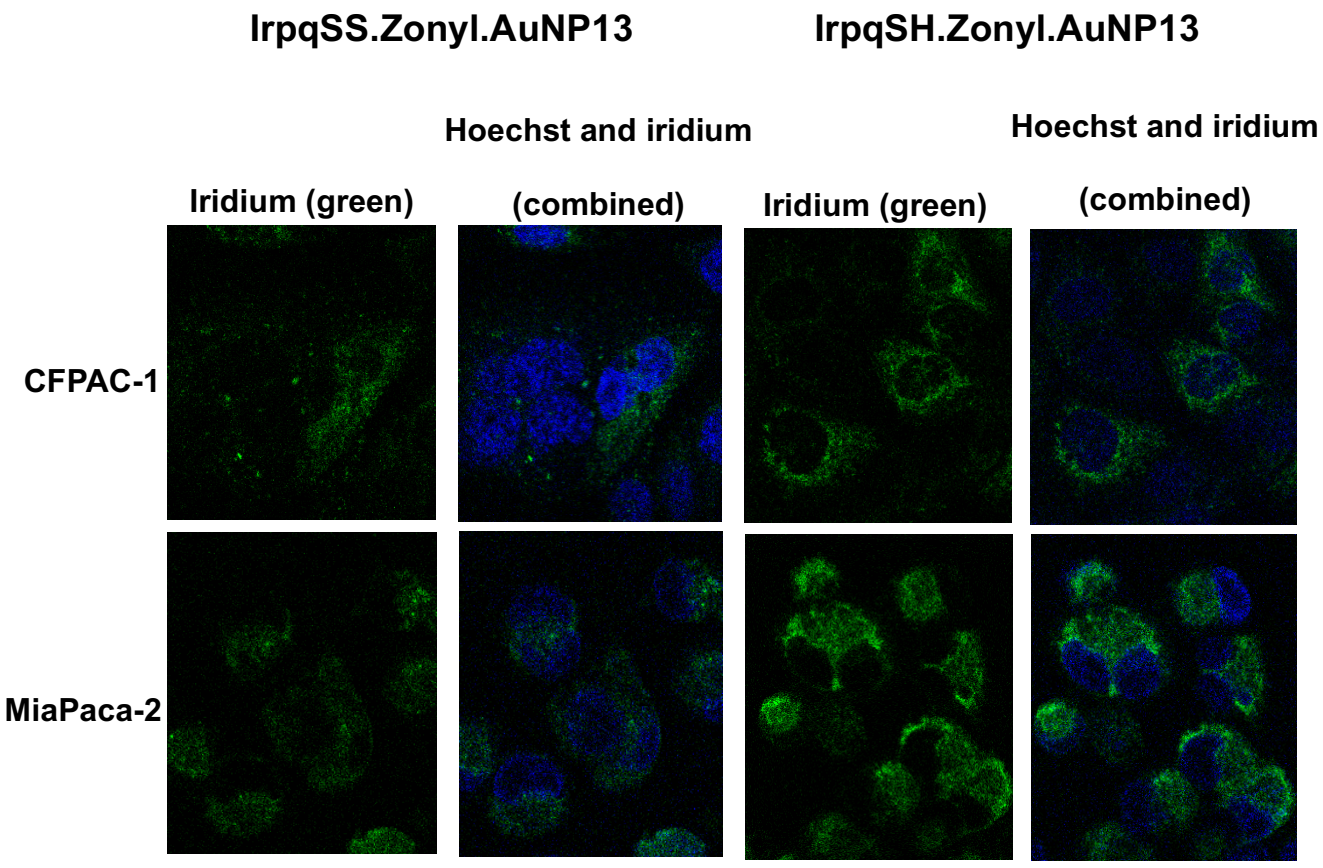


*Figure 3.16. Enlarged confocal images of **IrpqSS.Zonyl.AuNP13** and **IrpqSH.Zonyl.AuNP13**,in MiaPaca-2 and CFPAC-1 at 0.6 nM for 24 hr.*

The in-depth biological comparison of nanoparticle uptake between the two different cell lines will not be discussed in this thesis as the biological differences between the cell lines are beyond the scope of this project.

All the confocal images were captured on a Leica sp8 inverted microscope, with the exception of **IrpqSS.TFD-S.AuNP13**, which had images captured on a Zeiss LSM900 microscope, at a concentration of 0.2 nM, compared to the rest of the NPs at 0.6 nM. The Zeiss LSM900 microscope had a laser excitation wavelength of 488 nm, which is not at the peak of the MLCT excitation curve for the **IrpqSS** complex at 440 nm. Hence, less light from the laser could be absorbed compared to the other samples, and the resulting images are not as bright, and the luminescence pattern in the cells could not be visually seen. Therefore, the confocal image brightness cannot be compared to the other NPs,

however the images are included here to show that luminescence is seen in the cells at a **IrpqSS.TFD-S.AuNP13** concentration of 0.2 nM. This nanoparticle requires further optimisation (Section 3.6) as the stock AuNP solution was 2 nM, so a 10% dilution for the NP incubation in cells gave 0.2 nM final AuNP concentration. Therefore, the low concentrations used for these studies mean that the confocal results for this NP sample are inconclusive, although some quite interesting findings were observed in the ICP-MS uptake studies which will be discussed (Section 3.4.4). **Irpqbpy** confocal images in both cell lines (Figure 3.17, Figure 3.18) showed a spread over the whole cytoplasm as well without entering the nucleus and a very bright signal in both cell lines.

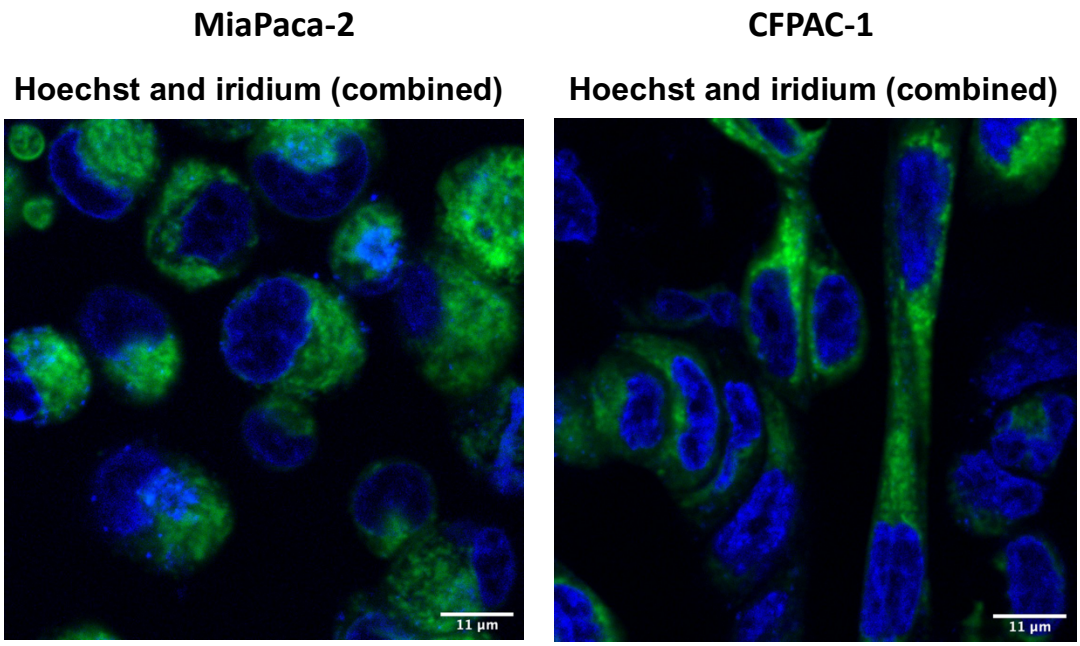


*Figure 3.17. Confocal live cell images in MiaPaca-2 and CFPAC-1 cell lines of **Irpqbpy** at 0.75 µM for 18 hr collected on a Zeiss LSM900 inverted microscope using a 63x oil immersion objective lens. Hoechst (blue) settings: λ_{exc} = 402, λ_{em} = 450 - 495 nm; Iridium(green): λ_{exc} = 488 nm, λ_{em} = 500 – 700 nm.*

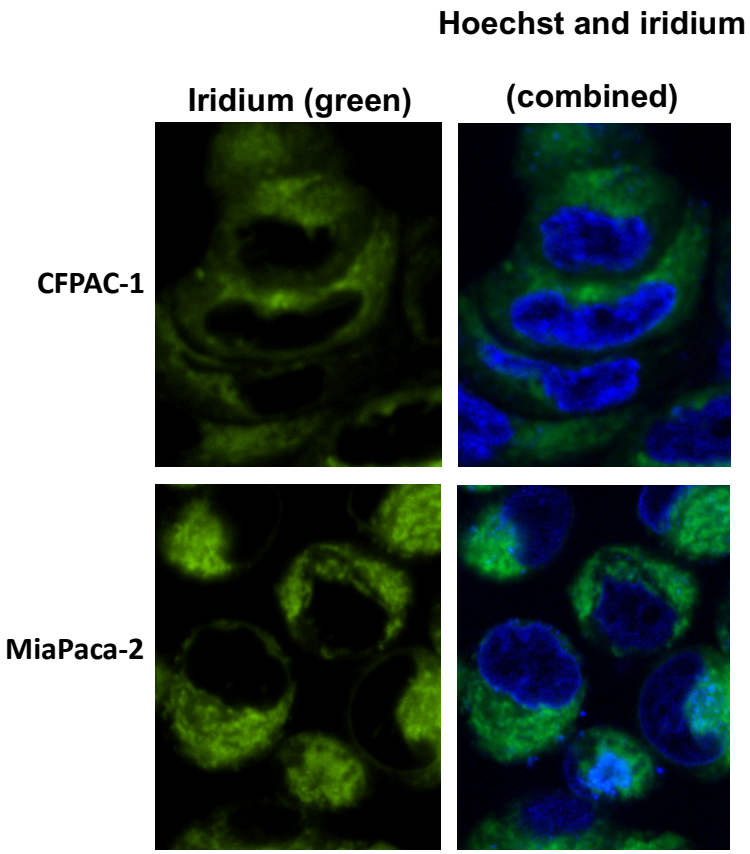


*Figure 3.18. Enlarged confocal images of **Irpqbpy** in MiaPaca-2 and CFPAC-1 at 0.75 μM for 18 hr. Images show the localization of the iridium(III) complex in the cells.*

3.4.2 Quantification of confocal luminescence

To quantify the confocal luminescence, the bright spots for the iridium-coated nanoparticle emission in the confocal images were measured over an average of 5 cells (Figure 3.19) in order to compare the luminescence between NPs with the same iridium(III) complex and different surfactants, and also the same surfactant but different iridium(III) complex.

3.4.2.1 MiaPaca-2 vs. CFPAC-1: cell line comparison

Between MiaPaca-2 and CFPAC-1, all NPs except for **IrpqSS.SPEG.AuNP13** showed a statistically significant difference in luminescence between the two cell lines (Figure 3.19a), with the MiaPaca-2 cells having a brighter luminescence from the nanoparticles that they were incubated with compared with CFPAC-1. This is most likely because the uptake of NPs in the MiaPaca-2 cell line is greater than that of CFPAC-1. Whether this is the case will be seen in Section 3.4.4.1, where the quantification of NP uptake will be discussed. Therefore, considering confocal luminescence imaging only (without yet quantifying NP uptake), the NPs studied in this chapter show brighter luminescence imaging in MiaPaca-2 cells compared to CFPAC-1, when incubated with 0.6 nM of NPs.

Irpqbpy luminescence in the confocal images had no statistically significant difference between MiaPaca-2 and CFPAC-1 (Figure 3.19b) indicating that **Irpqbpy** luminescence imaging is similar in these two cell lines at an incubation concentration of 0.75 μM. This is most likely because the uptake of the complex is similar in both cell lines. Whether this is the case will be seen in Section 3.4.3, where the flow cytometry will be discussed.

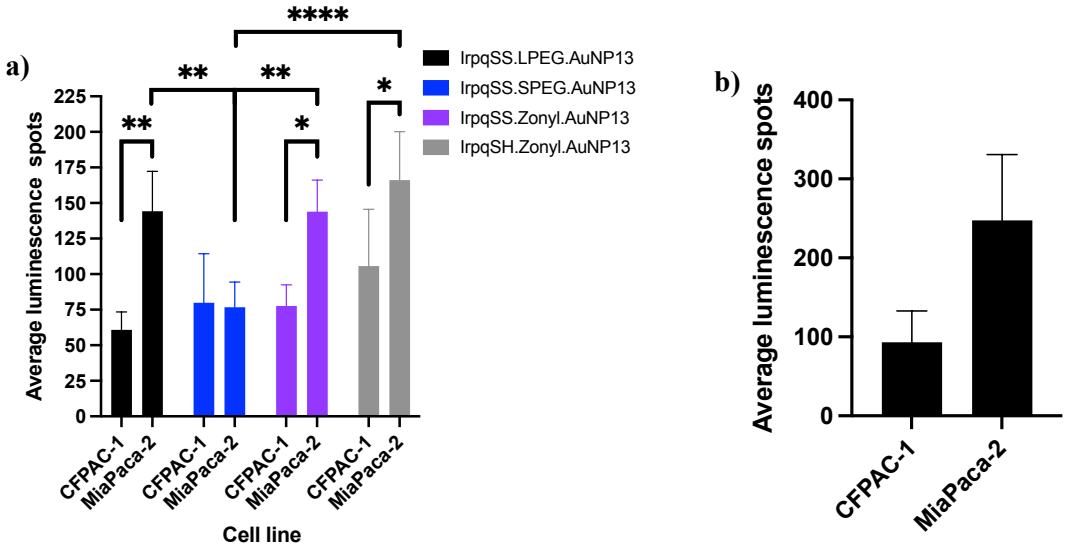


*Figure 3.19. Quantification of luminescence spots in cells obtained from confocal images, with an average of five cells measured for each sample for **a)** NP incubation and **b) Irpqbpy** incubation. Results were analyzed using ANOVA to determine statistical significance, and p-values obtained were represented by * = 0.0332, ** = 0.0021, *** = 0.002 and **** = 0.0001.*

3.4.2.2 CFPAC-1: nanoparticle comparison

Within the CFPAC-1 cell line, there are two factors to compare. The luminescence of the **IrpqSS**-coated NPs with the different surfactants (**LPEG**, **SPEG** and **Zonyl**), and the luminescence of the **Zonyl**-NPs with the different iridium(III) complexes (**IrpqSS and IrpqSH**):

The **IrpqSS.LPEG.AuNP13**, **IrpqSS.SPEG.AuNP13** and **IrpqSS.Zonyl.AuNP13** nanoparticle incubation in CFPAC-1 cells did not show any statistically significant difference in luminescence between samples (Figure 3.19a), showing that the imaging capabilities of all NPs in CFPAC-1 were very similar, and that the type of surfactant (**LPEG/SPEG/Zonyl**) was not affecting the luminescence of the NPs in this cell line under confocal. This could be due to the uptake of the different NPs being very similar in CFPAC-1 regardless of the surfactant used, so variation in luminescence is not seen. Whether this is the case will be seen in Section 3.4.2.2, where the quantification of NP uptake will be discussed.

Nanoparticles **IrpqSS.Zonyl.AuNP13** and **IrpqSH.Zonyl.AuNP13** incubated in CFPAC-1 did not show any statistically significant difference in luminescence under confocal (Figure 3.19a), indicating similarities in emissive properties for both of the **IrpqSS**- and **IrpqSH**-coated nanoparticles when **Zonyl** is used as the surfactant. So, changing the Ir(III) complex on the surface of the Zonyl-coated NPs did not affect the luminescence. This was unexpected, because in Chapter 2, Section 2.7, the luminescence spectrum of **IrpqSH.Zonyl.AuNP13** was much lower than **IrpqSS.Zonyl.AuNP13,** due to the lower quantum yield of the **IrpqSH** complex compared to **IrpqSS**. Therefore, the similar luminescence under confocal in both cell lines required further investigation (Sections 3.4.4.2 and 3.4.6), where the quantification of NP uptake and further luminescence studies will be discussed. The uptake of **IrpqSH.Zonyl.AuNP13** could be much greater than that of **IrpqSS.Zonyl.AuNP13**, causing the luminescence under confocal to be similar. However, if the uptake is similar, another factor is causing the enhanced luminescence of **IrpqSH.Zonyl.AuNP13**.

Hence, when comparing confocal imaging alone (without yet quantifying NP uptake), the brightness of luminescence imaging in CFPAC-1 cells follows the trends:

IrpqSS.LPEG.AuNP13 ≈ IrpqSS.SPEG.AuNP13 ≈ IrpqSS.Zonyl.AuNP13

and **IrpqSS.Zonyl.AuNP13 ≈ IrpqSH.Zonyl.AuNP13**, where '≈' is used for those NPs with similar luminescence in the cells.

Therefore, for the CFPAC-1 cell line, none of the nanoparticles studied in this chapter is statistically better than any other for luminescence imaging of CFPAC-1 cells when incubated with 0.6 nM of NPs, regardless of which Ir(III) complex or surfactant is on the nanoparticle surface.

3.4.2.3 MiaPaca-2: nanoparticle comparison

For the MiaPaca-2 cell line, there were also two factors to compare. The luminescence of the **IrpqSS**-coated NPs with the different surfactants (**LPEG**, **SPEG** and **Zonyl**), and the luminescence of the **Zonyl**-NPs with the different iridium(III) complexes (**IrpqSS and IrpqSH**):

There was no statistically significant difference in luminescence between **IrpqSS.LPEG.AuNP13** and **IrpqSS.Zonyl.AuNP13** when incubated in the MiaPaca-2 cells (Figure 3.19a), indicating similarities in imaging capabilities for these two NPs. **IrpqSS.SPEG.AuNP13** showed a statistically significant decrease in luminescence values compared with **IrpqSS.LPEG.AuNP13** and **IrpqSS.Zonyl.AuNP13**, showing that the **IrpqSS.SPEG.AuNP13** sample has the weakest luminescence imaging capability in MiaPaca-2 cells. This could be due to the uptake of **IrpqSS.SPEG.AuNP13** being less than that of **IrpqSS.LPEG.AuNP13** and **IrpqSS.Zonyl.AuNP13**. Whether this is the case will be seen in Section 3.4.4.3, where the quantification of NP uptake will be discussed.

IrpqSS.Zonyl.AuNP13 and **IrpqSH.Zonyl.AuNP13** nanoparticle incubation in MiaPaca-2 cells did not show any statistically significant difference in luminescence within the same cell line under confocal (Figure 3.19a), indicating similarities in the luminescence imaging capabilities of the **IrpqSS**- and

IrpqSH-coated NPs in this cell line, when the surfactant (**Zonyl**) was kept the same. Similar to the CFPAC-1 cell line, this was unexpected as **IrpqSH.Zonyl.AuNP13** luminescence was expected to be lower than **IrpqSS.Zonyl.AuNP13** due to their lower weaker luminescence. If this similar luminescence is due to the higher uptake of **IrpqSH.Zonyl.AuNP13**, this will be discussed in Section 3.4.4.3.

Hence, when comparing confocal imaging alone (without yet quantifying NP uptake), the brightness of luminescence imaging in MiaPaca-2 cells follows the trend:

IrpqSS.LPEG.AuNP13 ≈ **IrpqSS.Zonyl.AuNP13** > **IrpqSS.SPEG.AuNP13**,

and **IrpqSS.Zonyl.AuNP13** ≈ **IrpqSH.Zonyl.AuNP13**, where '≈' is used for those NPs with similar luminescence in the cells and '>' is used for those with greater luminescence.

Therefore, for the MiaPaca-2 cell line, the NPs studied in this chapter show statistically similar luminescence image brightness, with the exception of **IrpqSS.SPEG.AuNP13**, which had statistically significantly lower luminescence brightness than the other nanoparticles and hence this nanoparticles is the weakest for luminescence imaging of MiaPaca-2 cells when incubated at a concentration of 0.6 nM.

3.4.3 Flow cytometry of nanoparticles in MiaPaca-2 and CFPAC-1 cell lines

Flow cytometry studies performed on both cell lines after NP incubation concentrations of 0.6 nM (Table 3.1, Figure 3.20, Supplementary Figure 3.10, Supplementary Figure 3.11) showed that MiaPaca-2 cells have stronger luminescence when incubated with the NPs compared to CFPAC-1 cells. CFPAC-1 luminescence as measured by flow cytometry had less than 10,000 counts for every type of nanoparticle incubated, whereas MiaPaca-2 luminescence had more than 3,000 counts and up to 31,000 counts depending on which nanoparticle was incubated in the cells (Table 3.1). Therefore, the flow cytometry results confirmed what was indicated by the confocal images, that the luminescence of

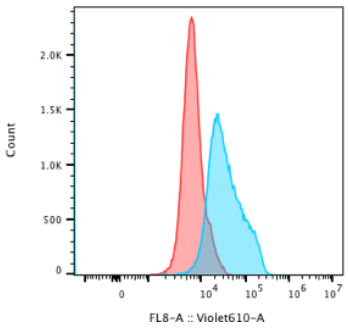
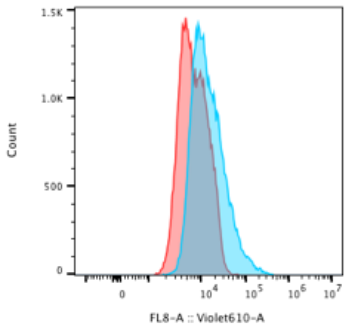
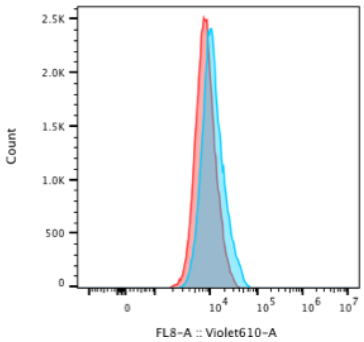
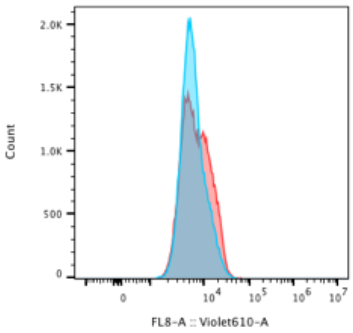
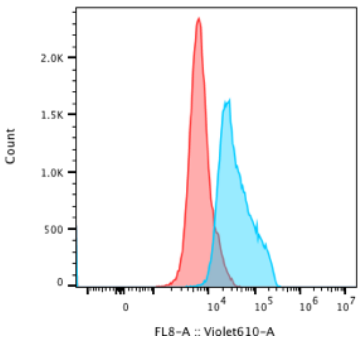
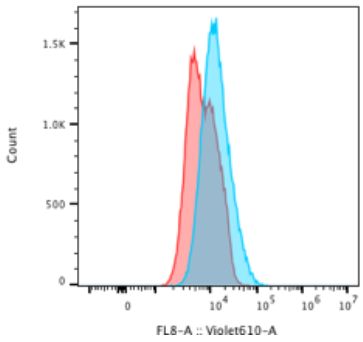
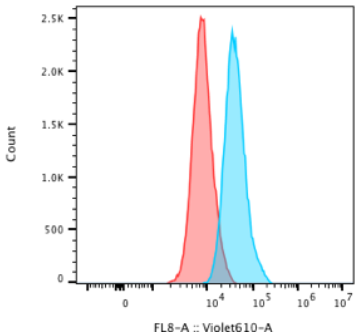
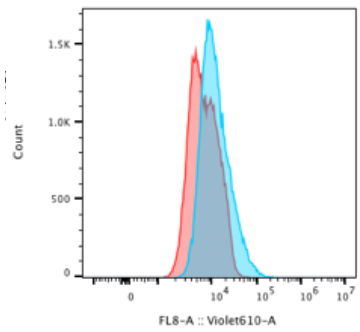
iridium-coated NPs in MiaPaca-2 cells is stronger than in CFPAC-1, therefore MiaPaca-2 is the better cell line for luminescence imaging.

Cell line	IrpqSS.LPEG. AuNP13	IrpqSS.SPEG. AuNP13	IrpqSS.Zonyl. AuNP13	IrpqSH.Zonyl. AuNP13
MiaPaca-2	13,859	3,065	24,632	30,567
CFPAC-1	7,150	-	6,062	5,045

Table 3.1. Average fluorescence intensity of the flow cytometry histograms of the AuNP uptakes in MiaPaca-2 and CFPAC-1, where the background fluorescence signal is zeroed.

Figure 3.20. Flow cytometry histograms of the different AuNP uptakes in MiaPaca-2 and CFPAC-1 cell lines, using the Violet610 channel (emission range: 590 – 630 nm) with a 405 nm laser. Cells were incubated with 0.6 nM of NPs for 24 hr. The red histogram shows the luminescence from the untreated cells and the blue histogram shows the luminescence from the treated cells.

Key: Treated cells Untreated cells

	MiaPaca-2	CFPAC-1
IrpqSS.LPEG.AuNP13 24hr 0.6 nM		
IrpqSS.SPEG.AuNP13 24hr 0.6 nM		
IrpqSS.Zonyl.AuNP13 24hr 0.6 nM		
IrpqSH.Zonyl.AuNP13 24hr 0.6 nM		

When comparing flow cytometry luminescence averages, the following trend is seen for CFPAC-1: **IrpqSS.LPEG.AuNP13** > **IrpqSS.Zonyl.AuNP13** > **IrpqSS.SPEG.AuNP13**, and **IrpqSS.Zonyl.AuNP13** > **IrpqSH.Zonyl.AuNP13**, where '>' is used for those NPs with greater luminescence. In MiaPaca-2, the following trend was seen: **IrpqSS.Zonyl.AuNP13** > **IrpqSS.LPEG.AuNP13** > **IrpqSS.SPEG.AuNP13**, and **IrpqSH.Zonyl.AuNP13** > **IrpqSS.Zonyl.AuNP13**, where '>' is used for those NPs with greater luminescence.

Flow cytometry was also performed with **Irpqbpy** at a concentration of 0.75 μM which also showed increased luminescence in MiaPaca-2 of over 1 million counts compared to CFPAC-1 which had less than 570,000 counts (Table 3.2, Figure 3.21). This was different result from the confocal luminescence studies which showed that the brightness of the cells was the same in both cell lines (Section 3.4.2.1). Although there was no statistically significant difference on confocal luminescence for **Irpqbpy** between MiaPaca-2 and CFPAC-1, the average fluorescence was higher for MiaPaca-2 (Figure 3.19b). Therefore, because flow cytometry has high fluorescence sensitivity, and allows analysis of a larger population of cells than confocal microscopy,[64] it was able to pick up the brighter luminescence of the MiaPaca-2 cells better than confocal imaging.

Cell line	**Irpqbpy**
MiaPaca-2	1,059407
CFPAC-1	567,522

*Table 3.2. Average fluorescence intensity of the flow cytometry histograms of the **Irpqbpy** uptakes in MiaPaca-2 and CFPAC-1, where the background fluorescence signal was zeroed.*

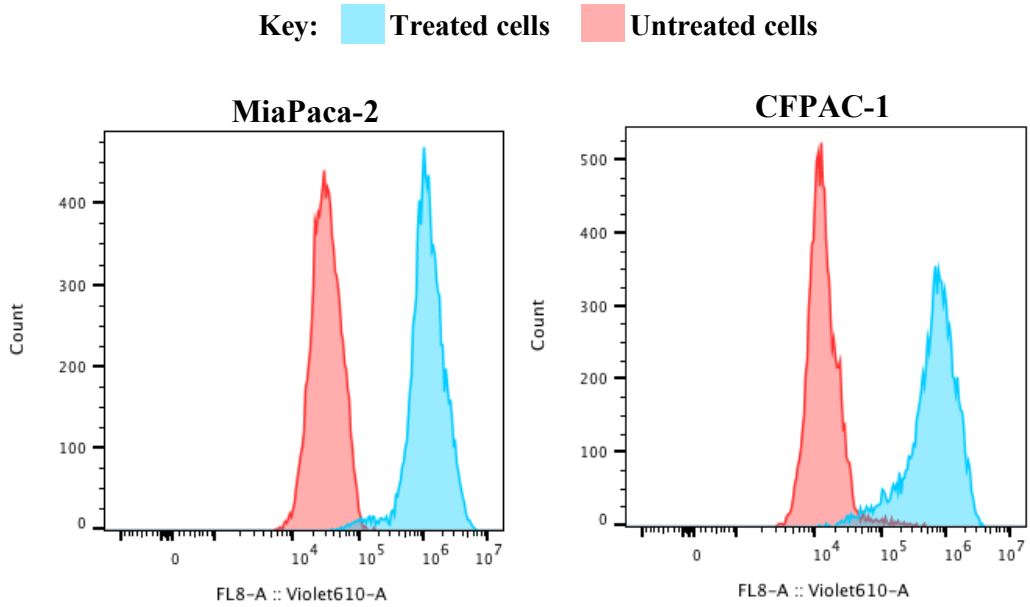


*Figure 3.21. Flow cytometry histograms of **Irpqbpy** uptake in MiaPaca-2 and CFPAC-1 cell lines, using the Violet610 channel (emission range: 590 – 630 nm) with a 405 nm laser. Cells were incubated with 0.75 μM of **Irpqbpy** for 18 hr. The red histogram shows the luminescence from the untreated cells and the blue histogram shows the luminescence from the treated cells.*

3.4.4 Quantification of nanoparticle uptake using ICP-MS

3.4.4.1 MiaPaca-2 vs. CFPAC-1: cell line comparison

Confocal imaging and flow cytometry showed the greater capability of the MiaPaca-2 cells for fluorescence imaging; however, fluorescence imaging could not show the quantity of nanoparticles in the cell and whether the uptake was greater. ICP-MS was required to confirm NP uptake from the gold content present in the cells. ICP-MS gold content values of some of the cells studied in this chapter were below the detection range of the ICP-MS instrument in the systems chosen. More cells would need to be analysed per nanoparticle sample to increase the gold content (Supplementary Figure 3.13, Section 3.6). However, because values were obtained and the error was for all the samples, these ICP-MS values are included here to give context for tor the confocal images and flow cytometry results.

ICP-MS confirmed that the uptake of the NPs in the MiaPaca-2 cells was statistically greater than the CFPAC-1 cells (Table 3.3, Figure 3.22), with the exception of **IrpqSS.Zonyl.AuNP13** and **IrpqSH.Zonyl.AuNP13**. However, the averages of the ICP-MS uptake for **IrpqSS.Zonyl.AuNP13** and **IrpqSH.Zonyl.AuNP13** was still higher in MiaPaca-2. Between the CFPAC-1 and MiaPaca-2 cell lines, **IrpqSS.LPEG.AuNP13** showed an 4518% increase in uptake, **IrpqSS.SPEG.AuNP13** showed a 341% increase, **IrpqSS.Zonyl.AuNP13** showed a 73% increase, **IrpqSS.TFD-S.AuNP13** showed a 65% increase and **IrpqSH.Zonyl.AuNP13** showed a 133% increase. Therefore, the increased luminescence in MiaPaca-2 cells seen in the confocal images and flow cytometry is due to better uptake of NPs in MiaPaca-2 compared to CFPAC-1.

Cell line	**Sample**	**Average NPs per cell**
CFPAC-1	**IrpqSS.LPEG.AuNP13**	630
	IrpqSS.SPEG.AuNP13	2,570
	IrpqSS.Zonyl.AuNP13	2,430
	IrpqSS.TFD-S.AuNP13	15,214
	IrpqSH.Zonyl.AuNP13	2085
MiaPaca-2	**IrpqSS.LPEG.AuNP13**	29,092
	IrpqSS.SPEG.AuNP13	11,324
	IrpqSS.Zonyl.AuNP13	4,202
	IrpqSS.TFD-S.AuNP13	25,060
	IrpqSH.Zonyl.AuNP13	4,850

*Table 3.3. Average ICP-MS values of the different uptakes of the AuNP samples, using an average AuNP size of 15 nm for the calculations. Cells were incubated with 0.6 nM of AuNPs for 24 hr, with the exception of **IrpqSS.TFD-S.AuNP13**, that had a concentration of 0.4 nM.*

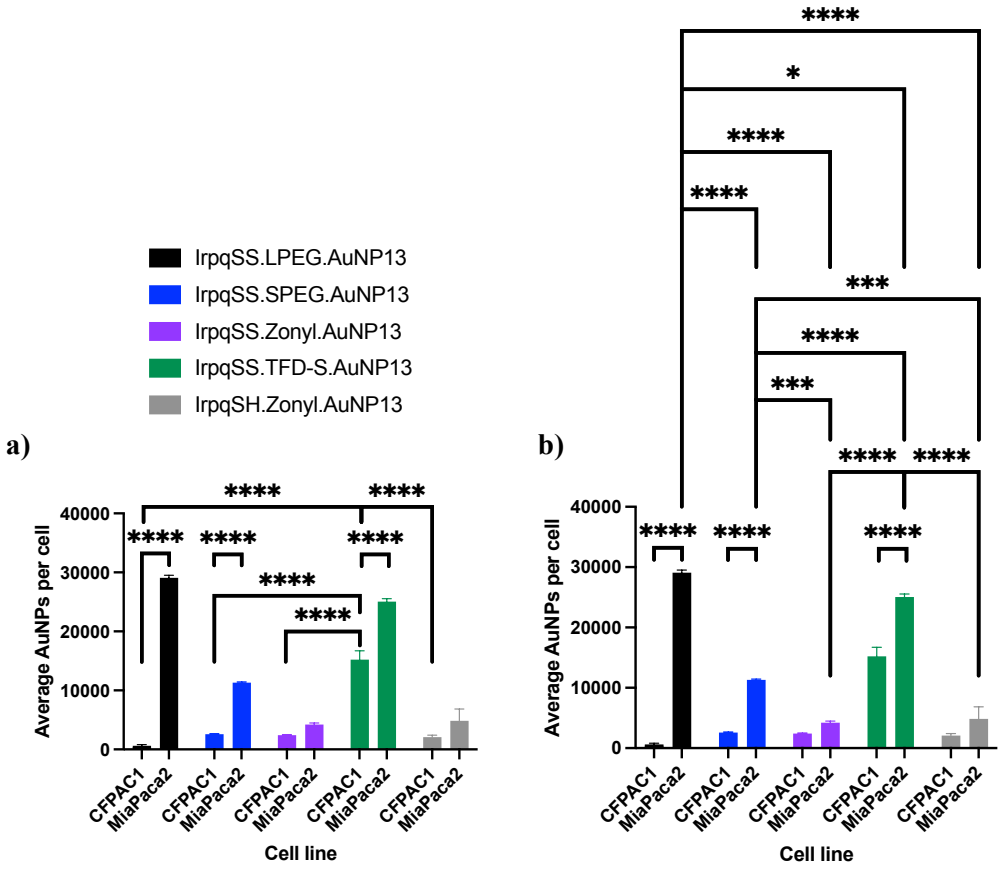


*Figure 3.22. Average AuNP uptake per cell obtained from ICP-MS gold content for MiaPaca-2 and CFPAC-1. The difference in uptakes was analyzed using ANOVA to determine statistical significance, where **a)** shows the statistical significance between different NP samples in CFPAC-1 and **b)** shows the statistical significance between different NP samples in MiaPaca-2. The p-values obtained were represented by * = 0.0332, ** = 0.0021, *** = 0.002 and **** = 0.0001.*

3.4.4.2 CFPAC-1: nanoparticle comparison

The greatest uptake in the CFPAC-1 cells was the **IrpqSS.TFD-S.AuNP13** sample, with 15,214 AuNPs per cell (Table 3.3). **IrpqSS.LPEG.AuNP13**, **IrpqSS.SPEG.AuNP13**, and **IrpqSS.Zonyl.AuNP13** did not show statistically significant difference in uptake between samples (Figure 3.22a), however these three AuNP samples all showed statistically significant decrease in uptake compared to **IrpqSS.TFD-S.AuNP13**, (at **IrpqSS.TFD-S.AuNP13** incubation concentration of 0.4 nM), showing that **TFD-S** nanoparticle coating is the best for uptake in CFPAC-1 cells.

The high uptake of **IrpqSS.TFD-S.AuNP13** could be due to the lipophilic hydrophobic nature of the surfactant because of its fluorine atoms. Hydrophobic NPs have been shown to directly penetrate the cell membrane rather than adsorb onto the cell membrane.[65] Because of the amide group on **TFD-S**, positive ions can form, similar to BPEI-coated AuNPs, which were shown to have increased uptake into cells due to the positive charge of the coating from the amine groups[15]. Because cell membranes are negatively charged,[66] positively charged NPs are easily attracted to the cell membrane.[48] **LPEG** and **SPEG** are hydrophilic and negative, **Zonyl** is lipophilic, hydrophobic and negative, **TFD-S** is lipophilic, hydrophobic and positive.

The **Zonyl-**coated AuNPs had statistically similar uptake, with **IrpqSS.Zonyl.AuNP13** at a value of 2,430 and **IrpqSH.Zonyl.AuNP13** at a value of 2,085 in CFPAC-1. Therefore, the coating with **IrpqSS** and **IrpqSH** did not affect the uptake when the **Zonyl** surfactant was kept the same. Therefore, the similar luminescence between **IrpqSS.Zonyl.AuNP13** and **IrpqSH.Zonyl.AuNP13** mentioned in Section 3.4.2.2 in CFPAC-1 is not due to the increased uptake of **IrpqSH.Zonyl.AuNP13** compared to **IrpqSS.Zonyl.AuNP13**. Since **IrpqSH.Zonyl.AuNP13** is a less fluorescent NP than **IrpqSS.Zonyl.AuNP13**, and the uptake by ICP-MS was similar between the NPs, another reason must be responsible for the increased luminescence seen in the confocal images for **IrpqSH.Zonyl.AuNP13** (Section 3.4.2.2).

Hence, when comparing nanoparticle uptake, the trend for CFPAC-1 is as follows:
IrpqSS.TFD-S.AuNP13 > **IrpqSS.LPEG.AuNP13** ≈ **IrpqSS.SPEG.AuNP13** ≈ **IrpqSS.Zonyl.AuNP13**,
and **IrpqSS.Zonyl.AuNP13** ≈ **IrpqSH.Zonyl.AuNP13**, where '≈' is used for those NPs with similar uptake in the cells and '>' is used for those with greater uptake.

Therefore, the trend for uptake in in CFPAC-1 cells matches the trend for the confocal luminescence (Section 3.4.2.2), showing that the similar luminescence imaging capability of the **LPEG**-, **SPEG** and

Zonyl-coated NPs is due to similar uptake. The trend for uptake also does not contradict that seen for flow cytometry (Section 3.4.3). Since the NP uptake was the same for all NPs as seen by ICP-MS, any trends in the flow cytometry data were due to the iridium(III) complex coating of the NPs (Chapter 2, Section 2.6). So **LPEG**-coated NPs had the highest iridium(III) complex coating and **SPEG**-coated NPs had the lowest iridium(III) coating out of those compared, confirming the higher luminescence and lowest luminescence seen in flow cytometry for SPEG- and SPEG- coated NP respectively. Taking the error of the **AuNP13** sizes into account (15.2 ± 1.8 nm), AuNP uptake values in CFPAC-1 were between 410 and 843 particles for **IrpqSS.LPEG.AuNP13**, between 1,759 and 3,613 particles for **IrpqSS.SPEG.AuNP13**, between 1,664 and 3,418 particles for **IrpqSS.Zonyl.AuNP13**, between 10,407 and 21,378 particles for **IrpqSS.TFD-S.AuNP13** and between 1,428 and 2,933 particles for **IrpqSH.Zonyl.AuNP13**.

3.4.4.3 MiaPaca-2: nanoparticle comparison

The greatest uptake in the MiaPaca-2 cells was **IrpqSS.LPEG.AuNP13** (Table 3.3), with 29,092 AuNPs per cell, however the **IrpqSS.TFD-S.AuNP13** sample had a similar uptake of 25,060 AuNPs per cell which was a statistically significant decrease (p value = 0.0312) in uptake. This was followed by **IrpqSS.SPEG.AuNP13**, then **IrpqSS.Zonyl.AuNP13** with the lowest uptake. All four **IrpqSS**-coated AuNPs in MiaPaca-2 showed statistically significant uptake compared to each other (Figure 3.22b). This showed that the different NP coatings play an important role in the uptake for the MiaPaca-2 cell line.

From these results, **IrpqSS.TFD-S.AuNP13** has very good uptake, because the ICP-MS cell uptake studies were performed with a nanoparticle concentration of 0.4 nM for **IrpqSS.TFD-S.AuNP13**, whereas the concentration was 0.6 nM for the rest of the samples (same as for CFPAC-1). It can be predicted that due to a concentration dependent uptake in cells[67], **IrpqSS.TFD-S.AuNP13** concentrations of 0.6 nM would show even greater uptake in both cell lines than the 0.4 nM concentrations used. Hence, **IrpqSS.TFD-S.AuNP13** is one of the best AuNP samples for cell uptake

out of these studied, however further study is needed to confirm this at an incubation concentration of 0.6 nM (Section 3.6). **IrpqSS.TFD-S.AuNP13** was also the best NP for uptake in the CFPAC-1 cells, so these ICP-MS studies show the potential of **TFD-S** as a good nanoparticle coating for increased uptake in cells.

The **Zonyl-**coated AuNPs within the MiaPaca-2 cell line did not show statistically significant difference in uptake, indicating that **IrpqSS** and **IrpqSH** does not affect uptake. As with CFPAC-1, since **IrpqSH.Zonyl.AuNP13** is a less fluorescent NP than **IrpqSS.Zonyl.AuNP13**, and the uptake by ICP-MS is similar between the NPs, there must be a different reason for the increased luminescence seen for **IrpqSH.Zonyl.AuNP13** (Section 3.4.2.3).

Hence, when comparing nanoparticle uptake, the trend for MiaPaca-2 is as follows:
IrpqSS.LPEG.AuNP13 > **IrpqSS.TFD-S.AuNP13** > **IrpqSS.SPEG.AuNP13** > **IrpqSS.Zonyl.AuNP13**,
and **IrpqSS.Zonyl.AuNP13** ≈ **IrpqSH.Zonyl.AuNP13**, where '≈' is used for those NPs with similar uptake in the cells and '>' is used for those with greater uptake.

Therefore, the trend for uptake in MiaPaca-2 cells does not match the trend for the confocal luminescence (Section 3.4.2.3) or flow cytometry (Section 3.4.3). In confocal imaging, **IrpqSS.LPEG.AuNP13** and **IrpqSS.Zonyl.AuNP13** had similar imaging capabilities, with **IrpqSS.SPEG.AuNP13** having the lowest imaging capability; in flow cytometry, So the NP imaging capabilities and luminescence of the cells does not depend on uptake for the MiaPaca-2 cell line. Taking the error of the **AuNP13** sizes into account (15.2 ± 1.8 nm), **AuNP** uptake values in MiaPaca-2 were between 15,052 and 30,917 particles for **IrpqSS.LPEG.AuNP13**, between 7,745 and 15,909 particles for **IrpqSS.SPEG.AuNP13**, between 2,880 and 5,916 particles for **IrpqSS.Zonyl.AuNP13**, between 17,150 and 35,228 particles for **IrpqSS.TFD-S.AuNP13** and between 3,322 and 6,823 particles for **IrpqSH.Zonyl.AuNP13**.

3.4.5 Localisation of nanoparticles in TEM images

TEM images were collected to give an indication of NP localisation in cells (Section 3.1.3) and possible methods of uptake. Due to the expertise required for TEM of cells as it a complicated technique for sub-cellular identification, strong conclusions about localisation is only possible with a secondary technique like fractionation (Section 3.6). Therefore, within the scope of the project, localisation will be referred to as possible localisation: MiaPaca-2 cells were incubated with all five NP samples investigated in this chapter for TEM image comparison of uptake in this cell line. TEM images were also collected in CFPAC-1, however only for one NP sample, as a comparison. This was done due to TEM cell sample preparation being a time consuming and expensive technique, and as MiaPaca-2 cell had the best uptake, they would give better images in TEM as they would have greater nanoparticle visibility.

From the TEM images in the MiaPaca-2 cells, **IrpqSS.LPEG.AuNP13** localises all over the cell, including the nucleus, and was not found in any specific sub-cellular compartments (Figure 3.23). This confirms the confocal images showing that MiaPaca-2 cells incubated with **IrpqSS.LPEG.AuNP13** display luminescence from all over the cell including the nucleus (Figure 3.13, Figure 3.14). Through TEM, particles can also be seen near the cell membrane, however membrane ruffling around areas of cell uptake was not seen. As previously studied TEM images have shown membrane ruffling and defined subcellular compartments when NPs are taken up by endocytosis[57], the lack of membrane ruffling and lack of NPs seen in sub-cellular components points to passive uptake of these NPs into these cells[68].

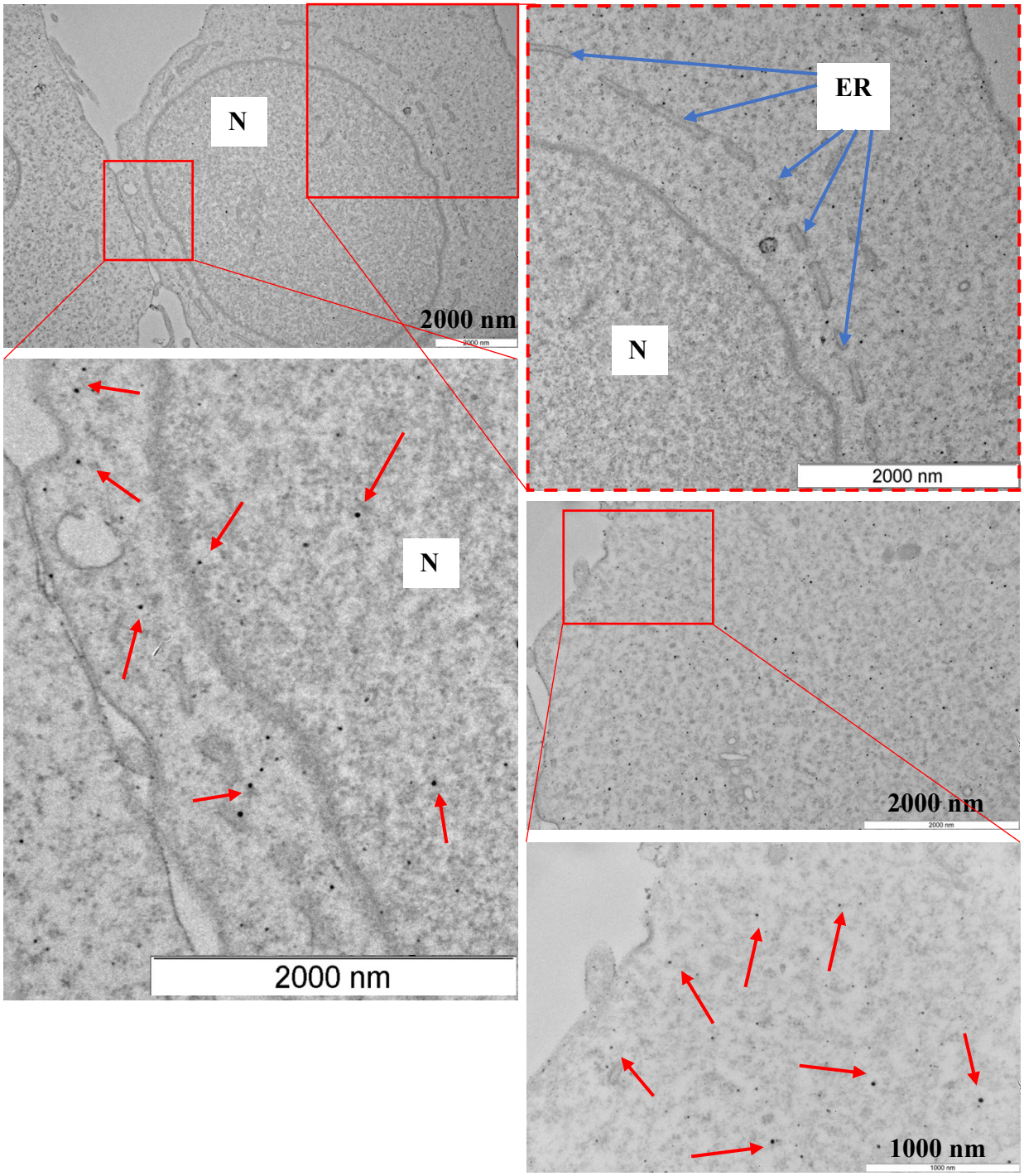


*Figure 3.23. TEM images showing the localization of **IrpqSS.LPEG.AuNP13** in the MiaPaca-2 cells, where 100,000 cells were incubated with 0.6 nM of NPs. Red arrows show the location of the NPs, red boxes show the enlarged images of the cells, **ER** shows the endoplasmic reticulum and **N** shows the nucleus.*

IrpqSS.SPEG.AuNP13 in MiaPaca-2 cells were seen in multiple sub-cellular compartments such as possible lysosomes, autophagic vacuoles and mitochondria (Figure 3.24). Particles were also seen in the nucleus, however they was not as evenly spread in the nucleus as for **IrpqSS.LPEG.AuNP13**. This shows that the difference in the sizes of the **LPEG** surfactant (average M_n 2100) and the **SPEG** surfactant (Mr 458.56) cause different cellular uptake. This is most likely due to lipophilicity differences, however conclusions about exact sub-cellular component localisation for comparing between the two PEG sizes cannot be finalised without fractionation or colocalization of luminescence from confocal (Section 3.6). Although there was a difference in localisation in the cells between the two PEGs, the multiple sub-cellular uptake for **IrpqSS.SPEG.AuNP13** would lead to the spread in luminescence seen all over the cytoplasm seen in the confocal images. These findings indicate what has already been studied (Section 3.1.2.1), where larger PEG surfactants increase circulation time of AuNPs[23]. As autophagic vacuoles and lysosomes are responsible for breaking down components in the cell, **LPEG** could be delaying the uptake of the AuNPs into these compartments, whereas with particles containing **SPEG**, the AuNPs are not as protected.

For **IrpqSS.Zonyl.AuNP13** in MiaPaca-2 cells, the particles were located in possible lamella bodies and autophagic vacuoles (Figure 3.25), matching studies performed previously with ruthenium-coated **Zonyl.AuNP13**s which also localised in lamella bodies and autophagic vacuoles[10].

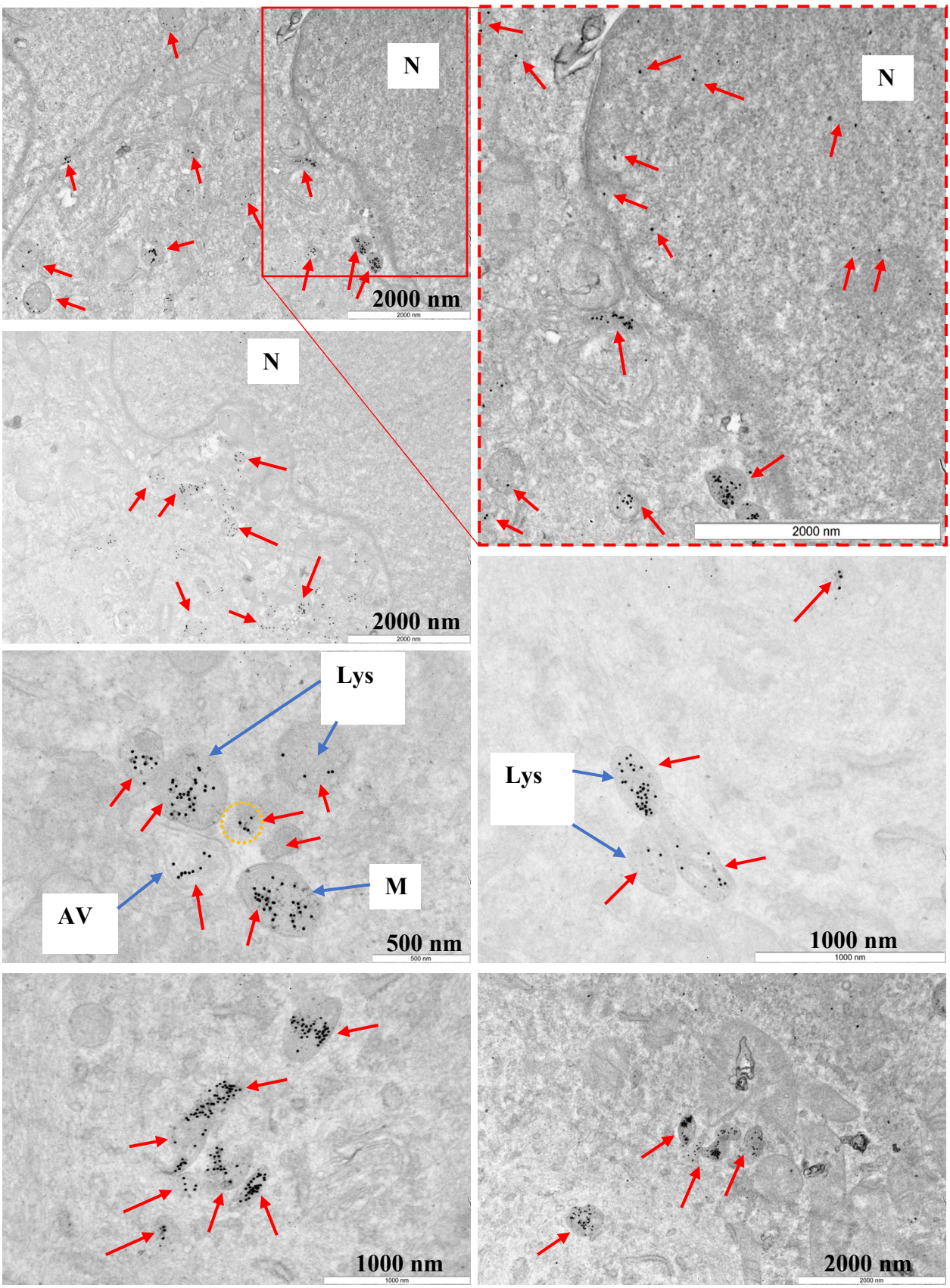


*Figure 3.24. TEM images showing the localization of **IrpqSS.SPEG.AuNP13** in the MiaPaca-2 cells, where 100,000 cells were incubated with 0.6 nM of NPs. Red arrows show the location of the NPs, red boxes show the enlarged images of the cells, yellow dotted circles show poorly defined endosomal membranes, **Lys** shows the lysosomes, **AV** shows autophagic vacuoles, **M** shows mitochondria and **N** shows the nucleus.*

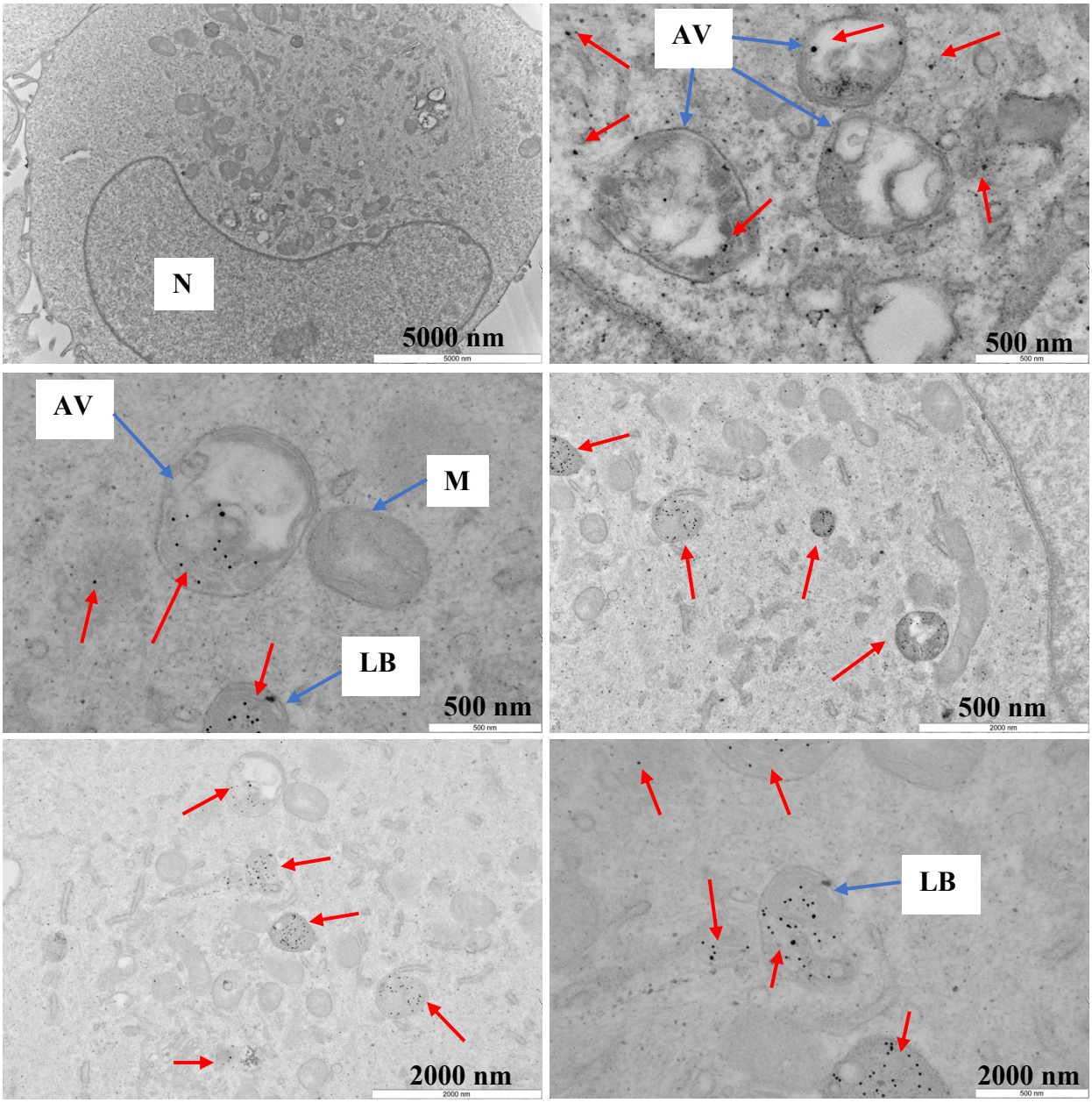


*Figure 3.25. TEM images showing the localization of **IrpqSS.Zonyl.AuNP13** in the MiaPaca-2 cells, where 100,000 cells were incubated with 0.6 nM of NPs. Red arrows show the location of the NPs, **LB** shows lamella bodies, **AV** shows the autophagic vacuoles, **M** shows mitochondria and **N** shows the nucleus.*

Few particles were seen in TEM for **IrpqSS.TFD-S.AuNP13** in MiaPaca-2 cells (Figure 3.26) due to the low incubation concentration (> 7x dilution compared to a 0.6 nM incubation concentration of the other NPs, see Sections 3.4.1 and 3.6). Of the particles that could be seen, most were located on the cell

membrane. The lack of nanoparticles in defined sub-cellular components pointed to passive uptake[57], a possible reason why **IrpqSS.TFD-S.AuNP13** had the second highest uptake after **IrpqSS.LPEG.AuNP13**, which also did not localise in specific sub-cellular components. Hydrophobic nanoparticles have also been shown to go into cells by simple diffusion,[48] and positive nanoparticles have greater attraction to the cell membrane[17, 18]. As **TFD-S** is both hydrophobic and can be positively charged due to the amide groups, this surfactant has positive qualities for cell internalisation and these effects are seen in the TEM images.

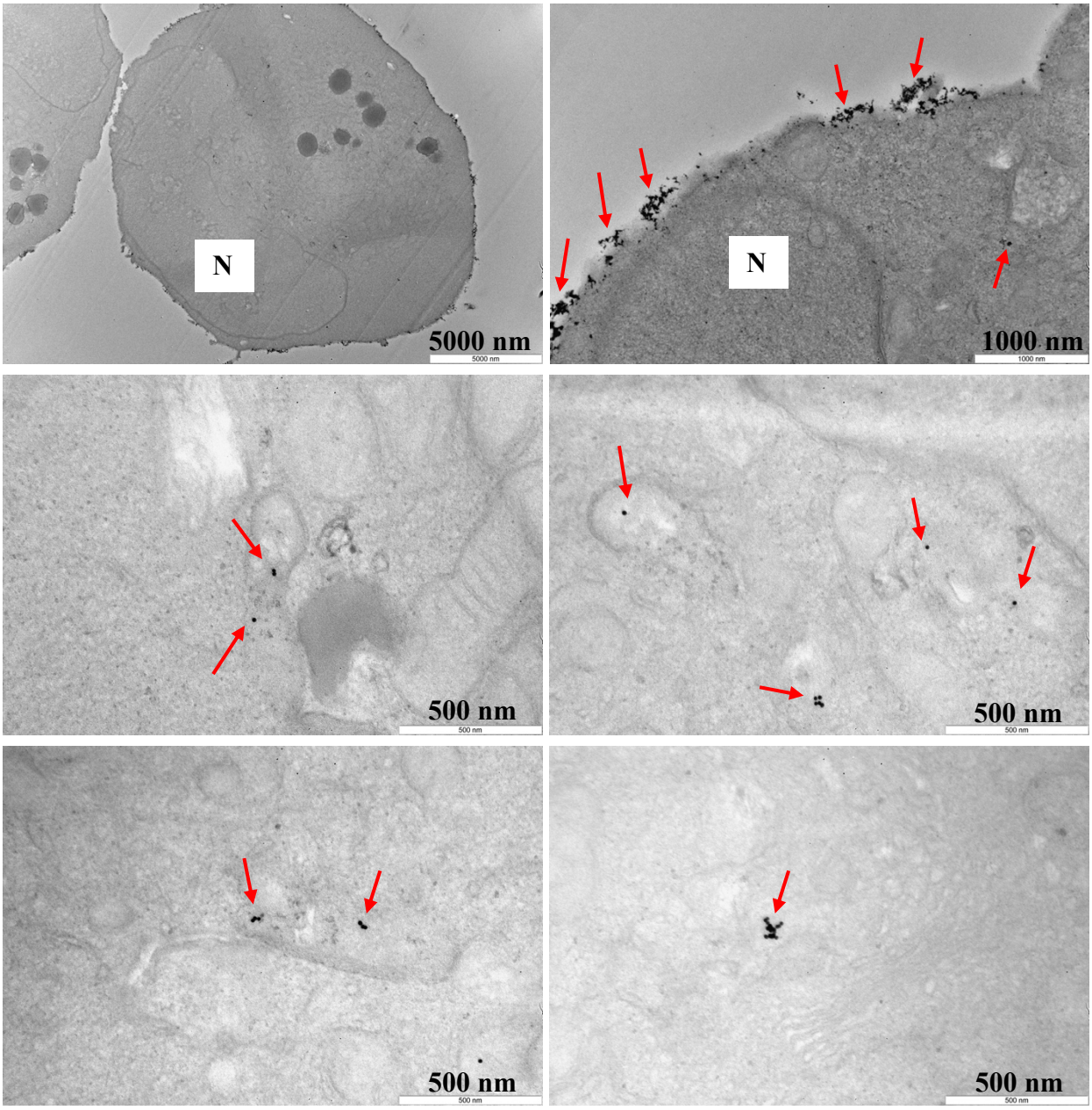


*Figure 3.26. TEM images showing the localization of **IrpqSS.TFD-S.AuNP13** in the MiaPaca-2 cells, where 100,000 cells were incubated with 0.08 nM of NPs. Red arrows show the location of the NPs, and **N** shows the nucleus.*

IrpqSH.Zonyl.AuNP13 were seen in possible mitochondria, lysosomes and lamella bodies (Figure 3.27). The iridium(III) complex may be affecting the localisation as these sub-cellular components are possibly different from those of **IrpqSS.Zonyl.AuNP13**, however a conclusion cannot be made without further studies (Section 3.6),

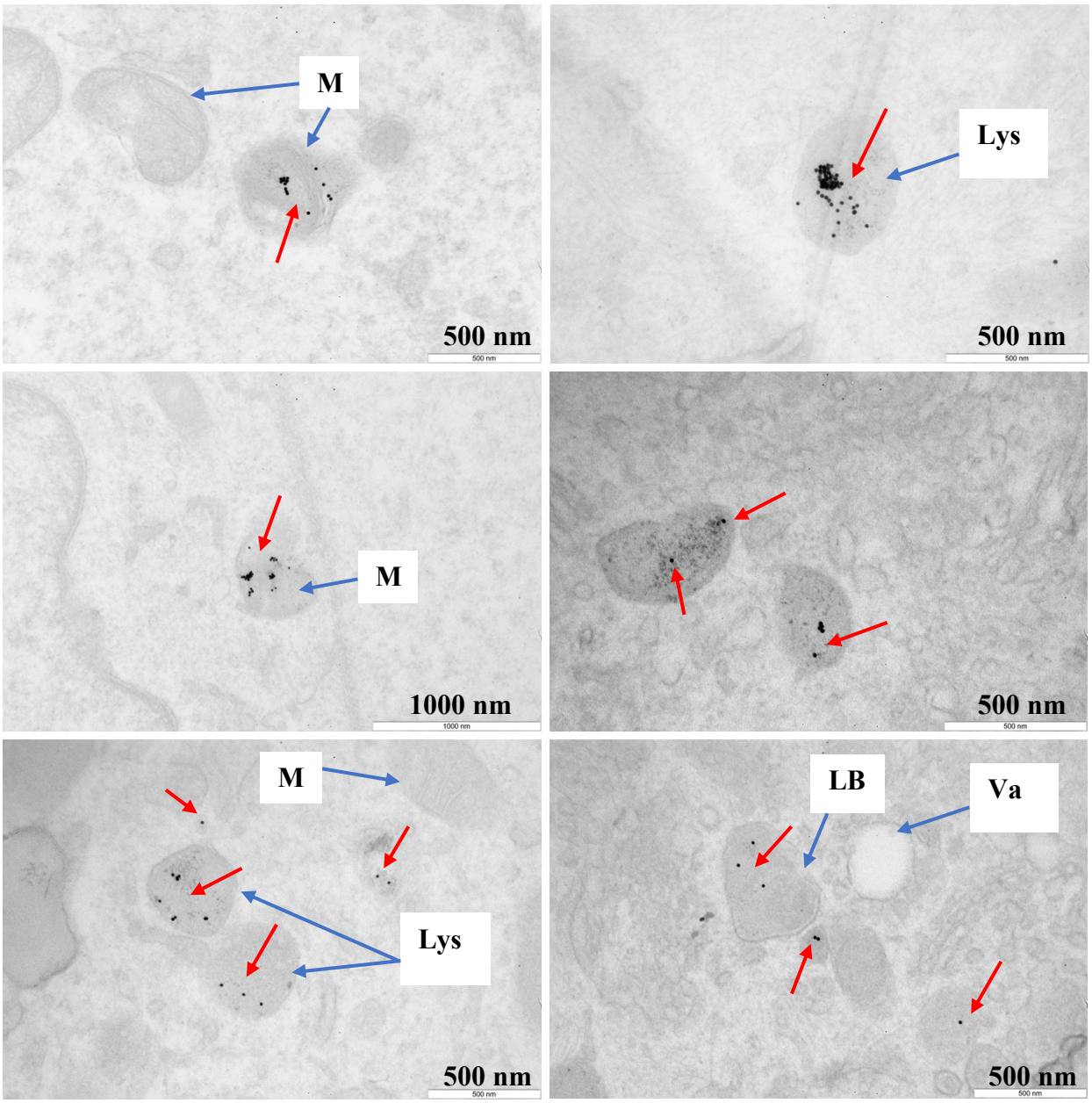


*Figure 3.27. TEM images showing the localization of **IrpqSH.Zonyl.AuNP13** in the MiaPaca-2 cells, where 100,000 cells were incubated with 0.6 nM of NPs. Red arrows show the location of the NPs, **LB** shows lamella bodies, **Va** shows vacuoles, **M** shows mitochondria and **Lys** shows lysosomes.*

IrpqSS.SPEG.AuNP13 in CFPAC-1 cells (Figure 3.28) were just seen in possibly lysosomes. Therefore, these NPs go into different organelles compared to MiaPaca-2. This would explain the difference in scattering pattern seen in the confocal images of CFPAC-1 compared to the spread of luminescence seen in MiaPaca-2 (Figure 3.14).

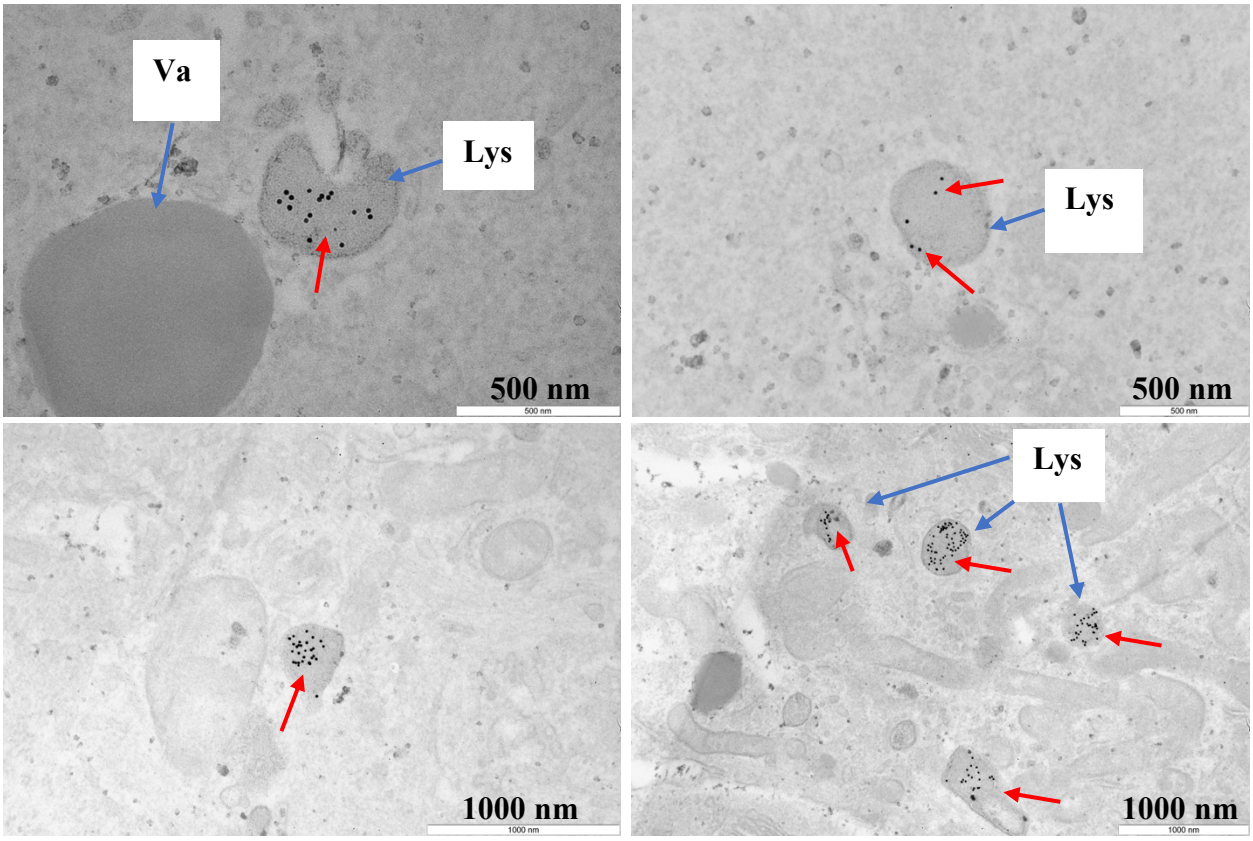


*Figure 3.28. TEM images showing the localization of **IrpqSS.SPEG.AuNP13** in the CFPAC-1 cells, where 100,000 cells were incubated with 0.6 nM of NPs. Red arrows show the location of the NPs, **Va** shows the vacuole and **Lys** shows the lysosomes.*

Therefore, TEM shows the difference in localisation between the NPs coated with different PEG sizes and different fluorinated surfactants. Surfactant type does affect localisation. **LPEG** and **TFD-S** did not promote the localisation into any specific sub-cellular organelles, and this seems to be linked to higher uptake and passive diffusion as both had good uptake in the cells. **SPEG** and **Zonyl** promoted localisation into sub-cellular components.

3.4.6 Gold nanoparticle interaction with cell media

The confocal images of the **IrpqSH.Zonyl.AuNP13** sample were unexpected due to the low quantum yield of **IrpqSH** compared to **IrpqSS**, and the weaker emission of **IrpqSH.Zonyl.AuNP13** compared to **IrpqSS.Zonyl.AuNP13**. The emission profile with **IrpqSS.Zonyl.AuNP13** showed a maximum emission peak intensity that was higher than **IrpqSH.Zonyl.AuNP13** by a power of 10^2 (Chapter 2, Section 2.7). The photophysical studies of the AuNPs were performed in H_2O, however in cell imaging, many components can interact with the AuNPs and hinder/enhance their emission, including solvent interaction, proteins, amino acids, salts, etc. ICP-MS uptake studies showed that **IrpqSH.Zonyl.AuNP13** had similar uptake to **IrpqSS.Zonyl.AuNP13**, therefore increased uptake of the less luminescent NP was not the reason for the unexpectedly bright luminescence. In this section, the possible factors that could be causing enhanced emission of **IrpqSH.Zonyl.AuNP13** will be discussed.

The first hypothesis for this enhanced effect was that the Ir(III) complexes on the AuNP surface could be interacting with the DMEM, as DMEM was used as the medium for the live cell confocal imaging. As discussed in Chapter 2, Section 2.3, iridium(III) cyclometalated complexes have an increased quantum yield in less polar solvents such as MeCN/MeOH compared to H_2O[69]. Hence, more hydrophobic environments generate greater luminescence from the complexes. In proteins such as Bovine Serum Albumin (BSA) which is one of the components of Fetal Bovine Serum (FBS) in supplemented DMEM, hydrophobic pockets are presen;[70] therefore the luminescence of AuNPs in H_2O and phenol red-free DMEM that had been supplemented with FBS (10%), Penicillin-Streptomycin (1%) and Eagle's Minimal Essential Medium (MEM) non-essential amino acids (1%) (Figure 3.29) was measured. The area under the curve for each emission spectrum was measured to determine the luminescence (Table 3.4). The concentration of each type of AuNPs in the two environments was kept the same and the settings on the spectrophotometer was also kept the same between the two environments of each sample. The concentration of the NPs could be found out from the diameter of the NPs from TEM images and the absorbance in the UV-vis (Supplementary Figure 3.1,

Supplementary Figure 3.2). The same pipettes were used within the same AuNP samples for H_2O and DMEM to minimise error.

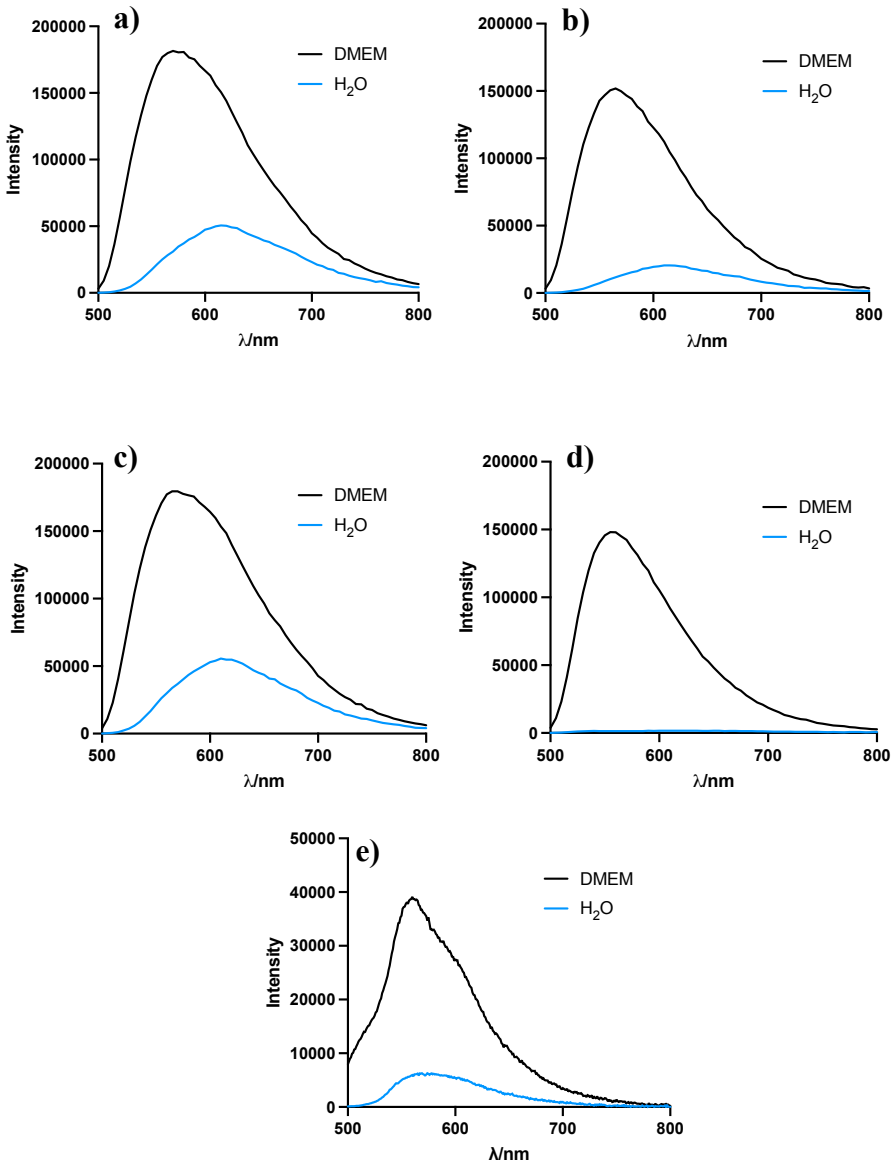


Figure 3.29. Luminescence emission spectra of the NPs suspended in H_2O (blue) and DMEM – 10% H_2O (black) for ***a)*** *1.2 nM of* ***IrpqSS.LPEG.AuNP13****,* ***b)*** *1.2 nM of* ***IrpqSS.SPEG.AuNP13****,* ***c)*** *0.8 nM of* ***IrpqSS.Zonyl.AuNP13****,* ***d)*** *0.7 nM of* ***IrpqSH.Zonyl.AuNP13*** *and* ***e)*** *7 μM of* ***Irpqbpy****. λ_{exc} = 440 nm. Filters used were the 530 nm filter for the NPs and the 475 nm filter for* ***Irpqbpy****. Emission was collected between 500 – 800 nm.*

From Table 3.4, **IrpqSS.LPEG.AuNP13** showed a 253% increase in luminescence intensity at 1.2 nM between H_2O and DMEM. **IrpqSS.SPEG.AuNP13** showed a 568% increase in luminescence intensity at 1.2 nM between H_2O and DMEM. The percentage increase of the luminescence intensity between H_2O and DMEM for **IrpqSS.Zonyl.AuNP13** at 8 nM was 226%. **IrpqSH.Zonyl.AuNP13** showed a 4626% increase in luminescence intensity between H_2O and DMEM. Lastly, **Irpqbpy** showed a 505% increase in luminescence intensity between H_2O and DMEM. **IrpqSH.Zonyl.AuNP13** was influenced the most by the interaction with DMEM compared to **IrpqSS.Zonyl.AuNP13**.

	Area under curve				
	IrpqSS.LPEG. AuNP13	**IrpqSS.SPEG. AuNP13**	**IrpqSS.Zonyl. AuNP13**	**IrpqSH.Zonyl. AuNP13**	**Irpqbpy**
H_2O	7,076,579	2,791,548	7,586,869	354,382	669,259
DMEM	24,990,440	18,648,484	24,725,808	16,747,893	4,047,443

*Table 3.4. Area under curve of the emission spectra for the AuNP solutions in DMEM and H_2O of **IrpqSS.LPEG.AuNP13, IrpqSS.SPEG.AuNP13**, **IrpqSS.Zonyl.AuNP13** and **IrpqSH.Zonyl.AuNP13** at 1.2 nM, 1.2 nM, 0.8 nM and 0.7 nM respectively. Stock AuNP solutions of 12 nM, 8 nM and 7 nM were diluted by 10% to achieve the final solutions in H_2O and phenol red-free DMEM.*

This experiment was also repeated with FBS-free DMEM and unsupplemented DMEM, and an increased luminescence between H_2O and DMEM was still seen. The emission spectrum of unsupplemented DMEM alone without nanoparticles displayed an emission profile when excited at 440 nm, with an emission band at 545 nm. This indicated that the proteins in DMEM were not responsible for this enhanced emission, as the unsupplemented DMEM showed the same effect as the supplemented DMEM. In addition, fixed confocal images were also collected, eliminating the presence of DMEM (Supplementary Figure 3.3, Supplementary Figure 3.4, Supplementary Figure 3.5, Supplementary

Figure 3.6, Supplementary Figure 3.7). During the process of fixing, the cells were washed and the DMEM was replaced by PBS. The images obtained showed the brightest emission visibly of **IrpqSS.Zonyl.AuNP13** and **IrpqSH.Zonyl.AuNP13**, further indicating that it was not the DMEM itself that was leading to the enhanced emission, but components within the cell.

The second hypothesis for this enhanced effect was that another component was interacting with the Ir(III) complexes on the AuNP surface. The DMEM used was from Thermofisher scientific (11880 - DMEM, low glucose, pyruvate, no glutamine, no phenol red). It contained 14 amino acids, including the three aromatic amino acids tyrosine, phenylalanine and tryptophan, which can form a hydrophobic environment in DMEM due to the interaction between the aromatic rings. Also present in DMEM were 8 vitamins – folic acid, niacinamide, pyridoxine hydrochloride, riboflavin and thiamine hydrochloride were the 5 aromatic ones. Out of these listed, only riboflavin has an excitation wavelength of around 450 nm and emits at around 550 nm[71]. Flavins are present in cells at concentrations of amol/cell, and so the presence of these could be what is leading to increased luminescence in vitro of the **IrpqSH.Zonyl.AuNP13**s in cells and the fluorescence spectra in supplemented and unsupplemented DMEM. However, if the riboflavin only was responsible for the increased luminescence in cells, this effect would happen for all the AuNP samples, not just **IrpqSH.Zonyl.AuNP13**. It is important to note that **IrpqSH.Zonyl.AuNP13** was the only NP studied in this chapter with the **IrpqSH** complex. It may be that the quenching from H_2O was much greater for **IrpqSH** than for **IrpqSS**, as **IrpqSH** shows a much higher increase in luminescence in these hydrophobic environments compared to **IrpqSS**, most probably due to the hydrogen bonds formed in polar environments that increase quenching[72, 73].

These results show that even though an iridium(III) complex or iridium-coated AuNP may be a poor emitter in H_2O or other polar solvents, biological studies such as these cell media interactions are essential to conclude on the imaging capability, as the environment of in vitro study differs from the typical environment required when using a spectrophotometer with a cuvette and H_2O as the solvent. Hence, when engineering iridium(III) complexes for imaging agents in future studies, it would be

necessary for these cell media studies to be undertaken before any final conclusion is formed about the imaging ability of the complexes/AuNPs.

3.4.7 Photophysical studies of AuNPs in cells

To investigate the luminescence lifetimes of the different AuNP samples in the cells, both pancreatic cancer cell lines were incubated with the AuNPs and the **Irpqbpy** complex for 24 hr, and the cells in suspension in PBS were measured on a fluorospectrometer. Longer lifetimes were seen in the MiaPaca-2 cells compared to the CFPAC-1 cells for each AuNP sample (Figure 3.30, Table 3.5, Table 3.6). This shows that the AuNPs localise in different subcellular components, indicating different methods of uptake due to different methods of uptake and translocation, as shown in the confocal images and TEM images. The decay curves were fitted with exponential tail fitting (Supplementary Figure 3.12).

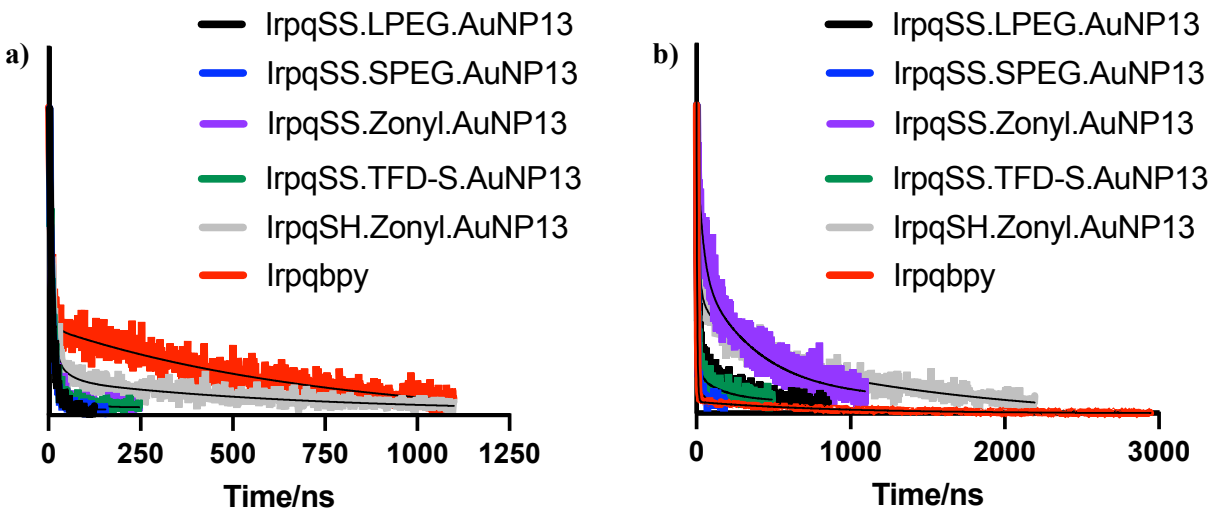


*Figure 3.30. Luminescence lifetime decay curves in cells with fittings in **a)** CFPAC1 and **b)** MiaPaca2, when cells were incubated with 0. 75 μM of **Irpqbpy** and 1.2 nM of AuNPs, with the exception of **IrpqSS.TFD-S.AuNP13**, which had a concentration of 0.4 nM.*

	IrpqSS.LPEG. AuNP13		IrpqSS.SPEG. AuNP13		IrpqSS.Zonyl. AuNP13		IrpqSH.Zonyl. AuNP13		IrpqSS.TFD-S. AuNP13		Irpqbpy	
	%	τ/ns	%	τ/ns	%	τ/ns	%	τ/ns	%	τ/ns	%	τ/ns
Long component	43	**20**	30	**10**	60	**170**	87	**660**	32	**50**	97	**730**

*Table 3.5. Lifetime in CFPAC-1 cells incubated with 0.75 μM of **Irpqbpy** and 1.2 nM of coated NPs with the exception of **IrpqSS.TFD-S.AuNP13** that had a concentration of 0.4 nM. The lifetime decay curves were fitted with a χ^2 of <1.2.*

	IrpqSS.LPEG. AuNP13		IrpqSS.SPEG. AuNP13		IrpqSS.Zonyl. AuNP13		IrpqSH.Zonyl. AuNP13		IrpqSS.TFD-S. AuNP13		Irpqbpy	
	%	τ/ns	%	τ/ns	%	τ/ns	%	τ/ns	%	τ/ns	%	τ/ns
Long component	81	**270**	41	**50**	90	400	91	**760**	69	**190**	84	**890**

*Table 3.6. Lifetime in MiaPaca-2 cells incubated with 0.75 μM of **Irpqbpy**, 1.2 nM of AuNPs with the exception of **IrpqSS.TFD-S.AuNP13** that had a concentration of 0.4 nM. The lifetime decay curves were fitted with a χ^2 of <1.2.*

3.5 Conclusions

In conclusion, confocal images and flow cytometry showed that MiaPaca-2 cells had brighter luminescence and greater uptake than CFPAC-1 when incubated with iridium-coated NPs. For CFPAC-1, there was no statistically significant difference in imaging brightness between **IrpqSS.LPEG.AuNP13**, **IrpqSS.SPEG.AuNP13** and **IrpqSS.Zonyl.AuNP13**, showing that the type of surfactant did not affect the imaging of the NPs in CFPAC-1. The **TFD-S** surfactant enabled the best NP uptake into the cells, and the type of iridium(III) complex (**IrpqSS**/**IrpqSH**) did not affect the luminescence or uptake of the NPs when the surfactant (**Zonyl**) was kept the same. In MiaPaca-2, **IrpqSS.LPEG.AuNP13** and **IrpqSS.Zonyl.AuNP13** showed significant increase in imaging brightness compared to **IrpqSS.SPEG.AuNP13**, and **LPEG** enabled the best NP uptake into cells. Therefore in MiaPaca-1, **IrpqSS.LPEG.AuNP13** was the best sample overall for both imaging and uptake. The type of iridium(III) complex (**IrpqSS**/**IrpqSH**) did not affect the luminescence or uptake of the NPs when the surfactant (**Zonyl**) was kept the same. **IrpqSH.Zonyl.AuNP13** luminescence was brighter than expected in both cell lines, despite the lower quantum yield of **IrpqSH** in H_2O compared to **IrpqSS**. This is most likely due to the interaction of **IrpqSH** with cell components that could enhance the emission.

When keeping the iridium(III) complex **IrpqSS** the same for the samples and varying the surfactant, the TEM images for the MiaPaca-2 cells showed that both PEG-coated AuNPs go into the nucleus, while the perfluorinated surfactants remain within the cytoplasm. **LPEG**-coated NPs did not localise in any specific sub-cellular compartments, whereas **SPEG**-coated NPs was able to do so. **TFD-S**-coated NPs did not localise in any specific sub-cellular compartments, whereas the **Zonyl**-coated NPs did. **LPEG** and **TFD-S**-coated NPs in MiaPaca-2 seem to be taken up by passive uptake as there is no evidence of membrane folding for endocytosis in the TEM images. As **LPEG** and **TFD-S**-coated NPs had the greatest uptake in MiaPaca-2 cells, there may be a link between high NP uptake and passive uptake in MiaPaca-2 cells. Luminescence lifetimes of both cell lines incubated with the NPs are different for each sample, showing that the localisation of the samples is in different components.

3.6 Further Studies

The imaging capabilities of the **IrpqSS.TFD-S.AuNP13** sample when incubated at a concentration of 0.6 nM would be required to obtain thorough comparison between perfluorinated and **PEG**-based surfactants. **IrpqSH.LPEG.AuNP13**, **IrpqSH.SPEG.AuNP13 and IrpqSH.TFD-S.AuNP13** should be in cells under confocal, flow cytometry, as the other surfactants with **IrpqSH** could also promote good enhancement of NP luminescence in cells. Fractionation experiments to confirm localisation from the TEM images would be necessary, as although TEM can show localisation, organelle identification by TEM is prone to human errors and can vary greatly depending on image quality and contrast and some organelles could be incorrectly identified due to contrasting issues. Staining of TEM organelles for imaging would also provide a more thorough investigation into the localisation of the AuNP samples in the cells. Another further study would be of the impact of different AuNP sizes on uptake because different sizes of AuNPs could localise in different subcellular compartments. Thus, performing the studies in this chapter with the larger **AuNP25**s would be good for comparison. The biological aspects for the different methods of uptake between the different NPs will require further study to explain biologically why MiaPaca-2 has greater uptake, and the different mechanisms of uptake between the two cell lines, however this was beyond the scope of this project. Finally, ICP-MS studies with more cells would be essential for further work so that the gold content detected is above the detection range of the instrument.

3.7 Experimental

All chemicals and consumables were obtained from Sigma Aldrich, Thermo Fisher Scientific and Greiner Bio One Ltd, unless otherwise stated. AuNP samples were synthesised and coated with **IrpqSS** or **IrpqSH** as outlined in Chapter 2, Sections 2.2 – 2.6). UV-visible absorption spectra were collected on an Agilent Cary 5000 Cary 50 or Cary 60 spectrometer. Prism was used to plot and analyse data.

3.7.1 Cell Culture

MiaPaca-2 and CFPAC-1 pancreatic cancer cells were cultured in vented cap T-75 flasks at 37 ^{o}C in 5% CO_2. The cell monolayer was grown in Dulbecco's modified Eagle medium (DMEM), supplemented with 10% fetal bovine serum (FBS), 1% Penicillin-Streptomycin (100X) and 1% of Eagle's Minimal Essential Medium (MEM) Non-Essential Amino Acid. The cells were sub-cultured when at high cell confluency, using TryplE Express enzyme (10 mins) to detach the cells. Much of this was performed with the assistance of Garret Rochford.

3.7.2 MTT assays

MiaPaca-2 and CFPAC-1 cells were counted using a Haemocytometer and seeded at a density of 5000 cells per well onto 96-well plates. The cells were adhered to the plates overnight at 37 ^{o}C in 5% CO_2. The treatment samples were added at different dilutions to the wells in repeats and incubated for 24 hr at 37 ^{o}C in 5% CO_2. A positive 1% Triton control in PBS was also added to the cells for the 24 hr incubations. All cell media was removed and the NPs in each well were incubated with 3-(4,5-dimethylthiazol-2-yl)-2,5-diphenyl tetrazolium bromide (5 mg/10 mL) in phenol red-free DMEM with 10% PBS. The cells were incubated at 37 ^{o}C in 5% CO_2 for 3-4 hrs, then the media was completely removed, DMSO was added to each well and the absorbances of the plates at 590 nm was measured using a Tecan Infinite 200 Pro plate reader. Samples were normalized to the 1% Triton signal.

3.7.3 Confocal Microscopy Imaging

A549, MiaPaca-2 and CFPAC-1 cells were counted using a Haemocytometer and seeded at a density of 100,000 cells onto 35 mm CELLview dishes with a 10 mm glass insert, or 35 mm cell culture dishes without glass inserts. The cells were adhered to the dish overnight at 37 ^{o}C in 5% CO_2. The treatment samples were added to the dish to obtain the final desired concentration, and the cells were incubated for the desired timescale at 37 ^{o}C in 5% CO_2. DMEM without phenol-red was used to incubate the cells. Cells were stained for at least 15 minutes with Hoechst 33342, at a final concentration of 20 μM for A549 and 20 nM for MiaPaca-2 and CFPAC-1. For live cell imaging, the cells were imaged without

washing, however for fixed cell imaging, the cells were washed twice with PBS and fixed with paraformaldehyde (4% in PBS) for 20 minutes. The paraformaldehyde was washed twice with PBS and the cells imaged in PBS. Confocal images and z-stacks were collected on a Leica SP8 upright microscope using a 40x ceramic water dipping objective lens, and also on a Zeiss LSM900 inverted confocal microscope with Airyscan using a 63x oil immersion objective lens. Images were acquired using fluorescence, reflectance and transmission mode. For the fluorescence channels on the Leica SP8 upright microscope, the settings used were: Hoechst (blue): λ_{exc} = 405 nm, λ_{em} = 419 – 472 nm, treatment sample luminescence (green): λ_{exc} = 458 nm, λ_{em} = 550 – 750 nm. For the fluorescence channels on the Zeiss LSM900 inverted confocal microscope, the settings used were: Hoechst (blue): λ_{exc} = 405 nm, λ_{em} = 400 – 495 nm, treatment sample luminescence (green): λ_{exc} = 488 nm, λ_{em} = 500 – 700 nm. All the images were processed with ImageJ.

3.7.4 Transmission Electron Microscopy

Cells were counted using a Haemocytometer and seeded at a density of 100,000 cells onto sterilised 13 mm glass coverslips that were placed in wells of six-well plates. The cells were adhered to the slips overnight at 37 ºC in 5% CO_2. The AuNPs were added to the cells at the required concentration and incubated for 24 hr at 37 ºC in 5% CO_2. The cells were rinsed twice with PBS and fixed with glutaraldehyde (2.5% in 0.1 M PBS) for 24 hr at 4 ºC. Samples were processed at the Centre for Electron Microscopy at the University of Birmingham. Ultrathin sections of the cells were cut and loaded onto Formvar Carbon support films. Images were acquired using a Joel 1400 Bio Electron Microscope and the images were analysed by ImageJ software. All this was done with the assistance of Theresa Morris.

3.7.5 Flow Cytometry

Cells were counted using a Haemocytometer and seeded at a density of 100,000 cells per well in six-well plates. The cells were adhered overnight at 37 ºC in 5% CO_2. The cells were incubated with the desired concentration of AuNPs in phenol red-free DMEM for 24hr at 37 ºC in 5% CO_2. The cells were washed twice with PBS, then detached with TryplE Express enzyme. The cells were centrifuged for 5

mins at 1500g to produce cell pellets that were resuspended in 200 μL of PBS (1% FBS). The samples were run on a Beckman Coulter CytoFLEX Flow Cytometer using the Violet610 channel, with a 405 nm laser and an emission detection range of 590 – 630 nm.

3.7.6 Inductively Coupled Plasma Mass Spectrometry (ICP-MS)

MiaPaca-2 and CFPAC-1 cells were counted using a Haemocytometer and seeded at a density of 2 x 10^6 cells per well in a six-well plate. The cells were adhered overnight at 37 ºC in 5% CO_2. The cells were incubated with the desired concentration of AuNPs in phenol red-free DMEM for the required timescale at 37 ºC in 5% CO_2. The cells were washed twice with PBS, then detached with TryplE Express enzyme. The cells were centrifuged for 5 mins at 1500g to produce cell pellets that were resuspended in PBS (1mL). The cells were counted again using a Haemocytometer. The cells in PBS were digested overnight in ultrapure HNO_3 while being stirred and heated. Then the digested samples were diluted with 4% HNO_3 in ultrapure H_2O to a final volume of 5 mL. ICP-MS measurements in duplicates of the gold content in the cell samples were run on a 7500cx ICPMS instrument with an Agilent integrated auto-sampler at the Chemistry department at the University of Warwick. PlasmaCal calibration standards were obtained from QMX laboratories. Calibration curves were fitted to R^2 values of <0.998 and the standard solutions of gold used were 0, 5, 10, 25, 50, 100, 250 and 500 ppb.

3.7.7 Incubation of cells for luminescence lifetime measurements

Cells were counted using a Haemocytometer and seeded at a density of 1 x 10^6 cells per well in six-well plates. The cells were adhered overnight at 37 ºC in 5% CO_2. The cells were incubated with the desired concentration of AuNPs or **Irpqbpy** in phenol red-free DMEM for 24 hr at 37 ºC in 5% CO_2. The cells were washed twice with PBS, then detached with TryplE Express enzyme. The cells were centrifuged for 5 mins at 1500g to produce cell pellets that were resuspended in 1 mL of PBS. The samples were run on an Edinburgh Instruments FLSP920 spectrometer and a PTI Fluorescence spectrometer combined with FeliX for Windows software. Luminescence lifetimes and quantum yields were collected on the FLSP920 spectrometer, with the F900 software used for all processing of data.

3.8 References

1. J. U. Menon, S. Kona, A. S. Wadajkar, F. Desai, A. Vadla and K. T. Nguyen, *J. Biomed. Mater. Res.*, 2012, **100A**, 1998-2005.
2. V. Chandrakala, V. Aruna and G. Angajala, *Emergent Mater.*, 2022, **5**, 1593-1615.
3. D. Chenthamara, S. Subramaniam, S. G. Ramakrishnan, S. Krishnaswamy, M. M. Essa, F.-H. Lin and M. W. Qoronfleh, *Biomater. Res.*, 2019, **23**, 20.
4. M. Cheng, L. Zhou, J. Ma, J. Mu, C. Yi and M.-J. Li, *Mater. Sci. Eng. C.*, 2019, **104**, 109972.
5. S. M. King, S. Claire, R. I. Teixeira, A. N. Dosumu, A. J. Carrod, H. Dehghani, M. J. Hannon, A. D. Ward, R. Bicknell, S. W. Botchway, N. J. Hodges and Z. Pikramenou, *J. Am. Chem. Soc.*, 2018, **140**, 10242-10249.
6. F. Miomandre, S. Stancheva, J.-F. Audibert, A. Brosseau, R. B. Pansu, M. Lepeltier and C. R. Mayer, *J. Phys. Chem. C.*, 2013, **117**, 12806-12814.
7. X. Miao, C.-N. Ko, K. Vellaisamy, Z. Li, G. Yang, C.-H. Leung and D.-L. Ma, *Sci. Rep.*, 2017, **7**, 42740.
8. N. J. Rogers, H. C. Jeffery, S. Claire, D. J. Lewis, G. Zikeli, N. J. Hodges, S. Egginton, G. B. Nash and Z. Pikramenou, *Nanomedicine*, 2017, **12**, 2725-2740.
9. D. J. Lewis and Z. Pikramenou, *Coord. Chem. Rev.*, 2014, **273-274**, 213-225.
10. A. N. Dosumu, S. Claire, L. S. Watson, P. M. Girio, S. A. M. Osborne, Z. Pikramenou and N. J. Hodges, *JACS Au*, 2021, **1**, 174-186.
11. S. A. M. Osborne and Z. Pikramenou, *Faraday Discuss.*, 2015, **185**, 219-231.
12. R. Suárez-López, V. F. Puntes, N. G. Bastús, C. Hervés and C. Jaime, *Sci. Rep.*, 2022, **12**, 13926.
13. M. Uz, V. Bulmus and S. Alsoy Altinkaya, *Langmuir*, 2016, **32**, 5997-6009.
14. R. Stiufiuc, I. Cristian, R. Nicoara, G. Stiufiuc, A. Florea, M. Achim and M. Lucaciu, *J. Nanomater.*, 2013, **2013**.
15. Y. Li and N. A. Monteiro-Riviere, *Nanomedicine*, 2016, **11**, 3185-3203.
16. M. Ortega-Muñoz, M. D. Giron-Gonzalez, R. Salto-Gonzalez, A. B. Jodar-Reyes, S. E. De Jesus, F. J. Lopez-Jaramillo, F. Hernandez-Mateo and F. Santoyo-Gonzalez, *Chem. Asian J.*, 2016, **11**, 3365-3375.
17. S. Salatin and A. Yari Khosroushahi, *J Cell Mol Med*, 2017, **21**, 1668-1686.
18. M. J. Mitchell, M. M. Billingsley, R. M. Haley, M. E. Wechsler, N. A. Peppas and R. Langer, *Nat. Rev. Drug Discov.*, 2021, **20**, 101-124.
19. J. S. Suk, Q. Xu, N. Kim, J. Hanes and L. M. Ensign, *Adv. Drug Del. Rev.*, 2016, **99**, 28-51.
20. S. Zalba, T. L. M. ten Hagen, C. Burgui and M. J. Garrido, *J. Control. Release*, 2022, **351**, 22-36.

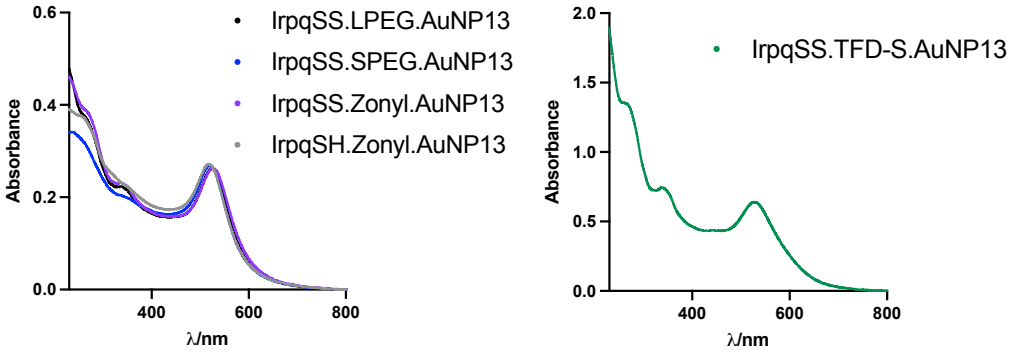
21. T. T. Hoang Thi, E. H. Pilkington, D. H. Nguyen, J. S. Lee, K. D. Park and N. P. Truong, *Polymers (Basel)*, 2020, **12**.
22. C. K. Elechalawar, M. N. Hossen, P. Shankarappa, C. J. Peer, W. D. Figg, J. D. Robertson, R. Bhattacharya and P. Mukherjee, *Int. J. Nanomedicine*, 2020, **15**, 991-1003.
23. L. Shi, J. Zhang, M. Zhao, S. Tang, X. Cheng, W. Zhang, W. Li, X. Liu, H. Peng and Q. Wang, *Nanoscale*, 2021, **13**, 10748-10764.
24. A. E. Nel, L. Mädler, D. Velegol, T. Xia, E. M. V. Hoek, P. Somasundaran, F. Klaessig, V. Castranova and M. Thompson, *Nat. Mater.*, 2009, **8**, 543-557.
25. M. A. Dobrovolskaia and S. E. McNeil, *Nat. Nanotechnol.*, 2007, **2**, 469-478.
26. A. Vonarbourg, C. Passirani, P. Saulnier and J.-P. Benoit, *Biomaterials*, 2006, **27**, 4356-4373.
27. Y. Jiang, T. P. Lodge and T. M. Reineke, *J. Am. Chem. Soc.*, 2018, **140**, 11101-11111.
28. M. M. El Sayed, H. Takata, T. Shimizu, Y. Kawaguchi, A. S. Abu Lila, N. E. Elsadek, E. Alaaeldin, Y. Ishima, H. Ando, A. Kamal, H. A. Sarhan and T. Ishida, *J. Control. Release*, 2020, **323**, 102-109.
29. S. Kumar, J. Aaron and K. Sokolov, *Nat. Protoc.*, 2008, **3**, 314-314.
30. J. A. Zamora-Justo, P. Abrica-Gonz·lez, G. R. V·zquez-MartÌnez, A. MuÒoz-Diosdado, J. A. Balderas-LÛpez and M. A. Ib·Òez-Hern·ndez, *J. Nanomater.*, 2019.
31. J. Manson, D. Kumar, B. J. Meenan and D. Dixon, *Gold Bull.*, 2011, **44**, 99-105.
32. Y. Wang, J. E. Q. Quinsaat, T. Ono, M. Maeki, M. Tokeshi, T. Isono, K. Tajima, T. Satoh, S.-i. Sato, Y. Miura and T. Yamamoto, *Nat. Commun.*, 2020, **11**, 6089.
33. J. B. Simonsen and R. Münter, *Angew. Chem. Int. Ed.*, 2020, DOI: 10.1002/anie.202004611, Accepted Author Manuscript.
34. R. Rampado, S. Crotti, P. Caliceti, S. Pucciarelli and M. Agostini, *Front. Bioeng. Biotechnol.*, 2020, **8**.
35. K. Abe, K. Higashi, K. Watabe, A. Kobayashi, W. Limwikrant, K. Yamamoto and K. Moribe, *Colloids Surf. Physicochem. Eng. Aspects*, 2015, **474**, 63-70.
36. H. Lee and R. G. Larson, *Biomacromolecules*, 2016, **17**, 1757-1765.
37. C. D. Walkey, J. B. Olsen, H. Guo, A. Emili and W. C. W. Chan, *J. Am. Chem. Soc.*, 2012, **134**, 2139-2147.
38. F. Jiao, J. Sang, Z. Liu, W. Liu and W. Liang, *Biophys. Chem.*, 2020, **266**, 106457.
39. C. Cruje and D. Chithrani, *Rev. Nanosci. Nanotechnol.*, 2014, **3**.
40. M. Li, S. Jiang, J. Simon, D. Paßlick, M.-L. Frey, M. Wagner, V. Mailänder, D. Crespy and K. Landfester, *Nano Lett.*, 2021, **21**, 1591-1598.
41. V. B. Damodaran, C. J. Fee, T. Ruckh and K. C. Popat, *Langmuir*, 2010, **26**, 7299-7306.
42. S. Rainieri, N. Conlledo, T. Langerholc, E. Madorran, M. Sala and A. Barranco, *Food Chem. Toxicol.*, 2017, **104**, 14-25.
43. X. Zhang, M. R. Servos and J. Liu, *J. Am. Chem. Soc.*, 2012, **134**, 7266-7269.

44. S. Nagappan, A. Mohan, A. M. Thomas, J.-M. Yoo, N. Eid, I. Chung, B. Ameduri and C.-S. Ha, *RSC Adv.*, 2021, **11**, 2194-2201.
45. R. Augustine, A. Hasan, R. Primavera, R. J. Wilson, A. S. Thakor and B. D. Kevadiya, *Mater. Today Commun.*, 2020, **25**, 101692.
46. M. D'Acunto, *Materials (Basel)*, 2018, **11**.
47. M. Wu, H. Guo, L. Liu, Y. Liu and L. Xie, *Int J Nanomedicine*, 2019, **14**, 4247-4259.
48. P. Sabourian, G. Yazdani, S. S. Ashraf, M. Frounchi, S. Mashayekhan, S. Kiani and A. Kakkar, *Int. J. Mol. Sci.*, 2020, **21**.
49. B. Yameen, W. I. Choi, C. Vilos, A. Swami, J. Shi and O. C. Farokhzad, *J. Control. Release*, 2014, **190**, 485-499.
50. K. Osanai, *Int. J. Mol. Sci.*, 2018, **19**.
51. Y. S. Khan and A. Farhana, *Histology, Cell*, StatPearls Publishing, 2022.
52. S. Poddighe, K. M. Bhat, M. D. Setzu, P. Solla, A. M. Angioy, R. Marotta, R. Ruffilli, F. Marrosu and A. Liscia, *PLoS One*, 2013, **8**, e73156.
53. P. Wild, S. Leisinger, A. Oliveira, E. Schraner, A. Kaech, M. Ackermann and K. Tobler, *Viruses*, 2015, **7**, 52-71.
54. D. Aston, R. A. Capel, K. L. Ford, H. C. Christian, G. R. Mirams, E. A. Rog-Zielinska, P. Kohl, A. Galione, R. A. B. Burton and D. A. Terrar, *Sci. Rep.*, 2017, **7**, 40620.
55. T. Kaneko, H. Iida, J. Bedford, S.-I. Oda and T. Mōri, *Reprod.*, 2004, **126**, 817-826.
56. G. Chaldakov, L. Aloe, A. Kádár, P. Ghenev, M. Fiore, R. Pancheva and P. Panayotov, *Acta Biol. Marisiensis*, 2021, **4**, 31-43.
57. Y. Wei, T. Tang and H. Pang, *Nat. Commun.*, 2019, **10**.
58. M. Thakur, H. Gupta, D. Singh, I. Ray Mohanty, U. Maheswari, G. Vangae and A. Joshi, *J. Nanobiotechnology*, 2014, **12**, 42.
59. J. M. Esteve and E. Knecht, *World J. Biol. Chem.*, 2011, **2**, 232-238.
60. A. Laniece, 2018.
61. R. Ridsdale, C.-L. Na, Y. Xu, K. D. Greis and T. Weaver, *PLoS One*, 2011, **6**, e16482-e16482.
62. A.-A. Raymond, A. G. de Peredo, A. Stella, A. Ishida-Yamamoto, D. Bouyssie, G. Serre, B. Monsarrat and M. Simon, *Mol. Cell. Proteomics*, 2008, **7**, 2151-2175.
63. T. Higaki, N. Kutsuna, K. Akita, M. Sato, F. Sawaki, M. Kobayashi, N. Nagata, K. Toyooka and S. Hasezawa, *Sci. Rep.*, 2015, **5**, 7794.
64. D. A. Basiji, W. E. Ortyn, L. Liang, V. Venkatachalam and P. Morrissey, *Clin. Lab. Med.*, 2007, **27**, 653-670, viii.
65. P. Foroozandeh and A. A. Aziz, *Nanoscale Res. Lett.*, 2018, **13**, 339.
66. Y. Ma, K. Poole, J. Goyette and K. Gaus, *Front. Immunol.*, 2017, **8**, 1513.

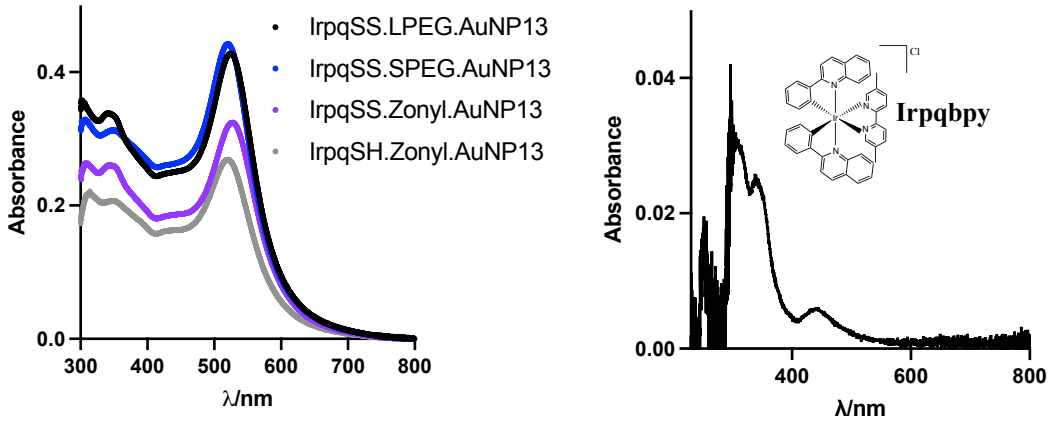
67. J. A. Coulter, S. Jain, K. T. Butterworth, L. E. Taggart, G. R. Dickson, S. J. McMahon, W. B. Hyland, M. F. Muir, C. Trainor, A. R. Hounsell, J. M. O'Sullivan, G. Schettino, F. J. Currell, D. G. Hirst and K. M. Prise, *Int. J. Nanomedicine*, 2012, **7**, 2673-2685.
68. M. Sousa de Almeida, E. Susnik, B. Drasler, P. Taladriz-Blanco, A. Petri-Fink and B. Rothen-Rutishauser, *Chem. Soc. Rev.*, 2021, **50**, 5397-5434.
69. K. K.-W. Lo, J. S.-W. Chan, L.-H. Lui and C.-K. Chung, *Organometallics*, 2004, **23**, 3108-3116.
70. M. Shahid and H. M. Chawla, *J. Lumin.*, 2017, **188**, 460-464.
71. A. Niazi, A. Yazdanipour, J. Ghasemi and A. Abbasi, *J. Chin. Chem. Soc.*, 2006, **53**.
72. M. M. H. Khalil, F. C. De Schryver, H. Keller and J. M. Lehn, *Supramol. Sci.*, 1995, **2**, 175-182.
73. L. A. H. van Bergen, M. Alonso, A. Palló, L. Nilsson, F. De Proft and J. Messens, *Sci. Rep.*, 2016, **6**, 30369.

3.9 Appendix

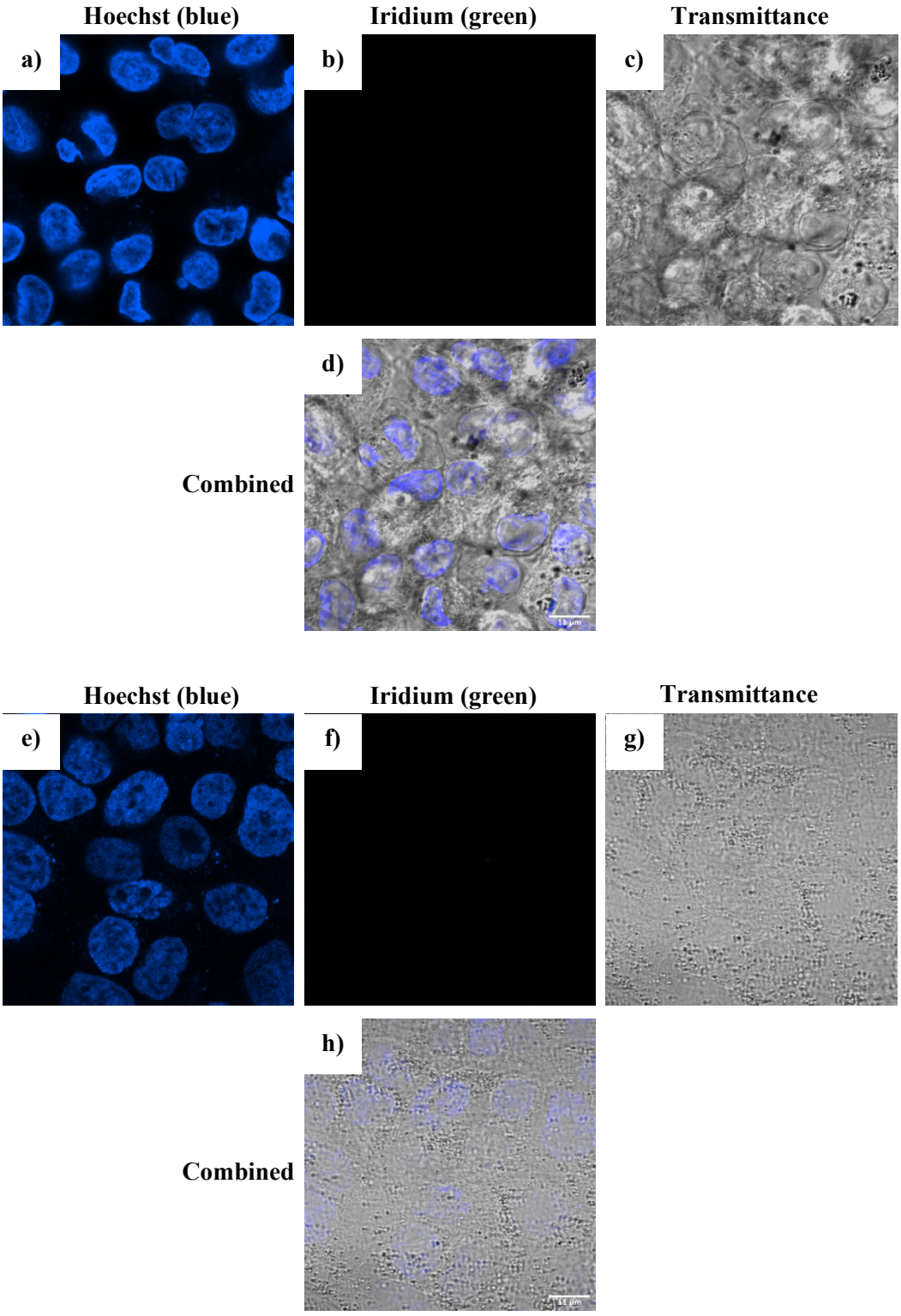
<u>UV-vis absorbance spectra</u>



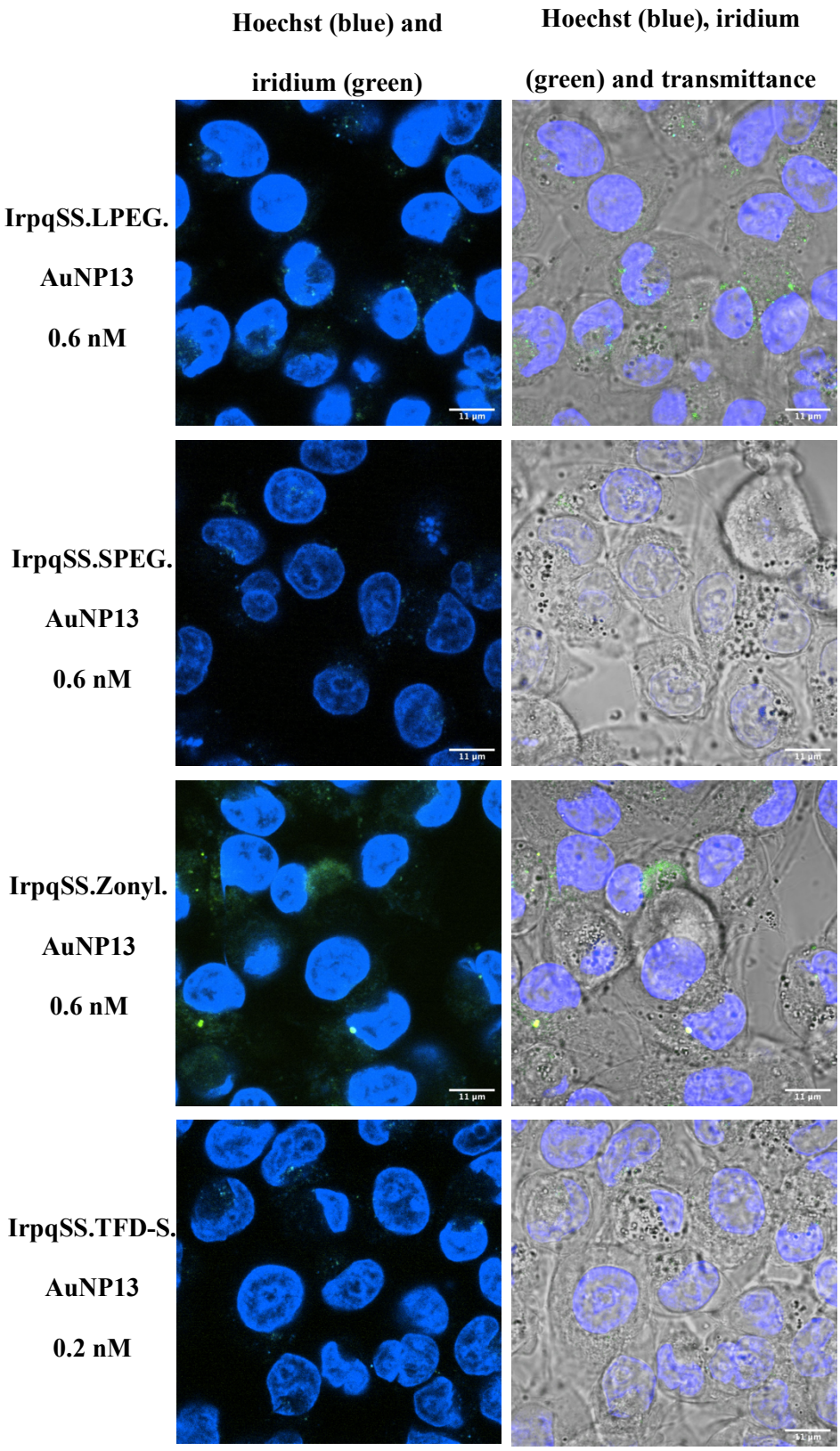
Supplementary Figure 3.1. UV-vis absorbance spectra of ***IrpqSS.LPEG.AuNP13****,* ***IrpqSS.SPEG.AuNP13****,* ***IrpqSS.Zonyl.AuNP13*** *and* ***IrpqSH.Zonyl.AuNP13*** *(left) at 7 nM (10% diluted) and* ***IrpqSS.TFD-S.AuNP13*** *(right) at 1.8 nM for quantitative studies such as Confocal, ICP-MS, flow cytometry and TEM.*



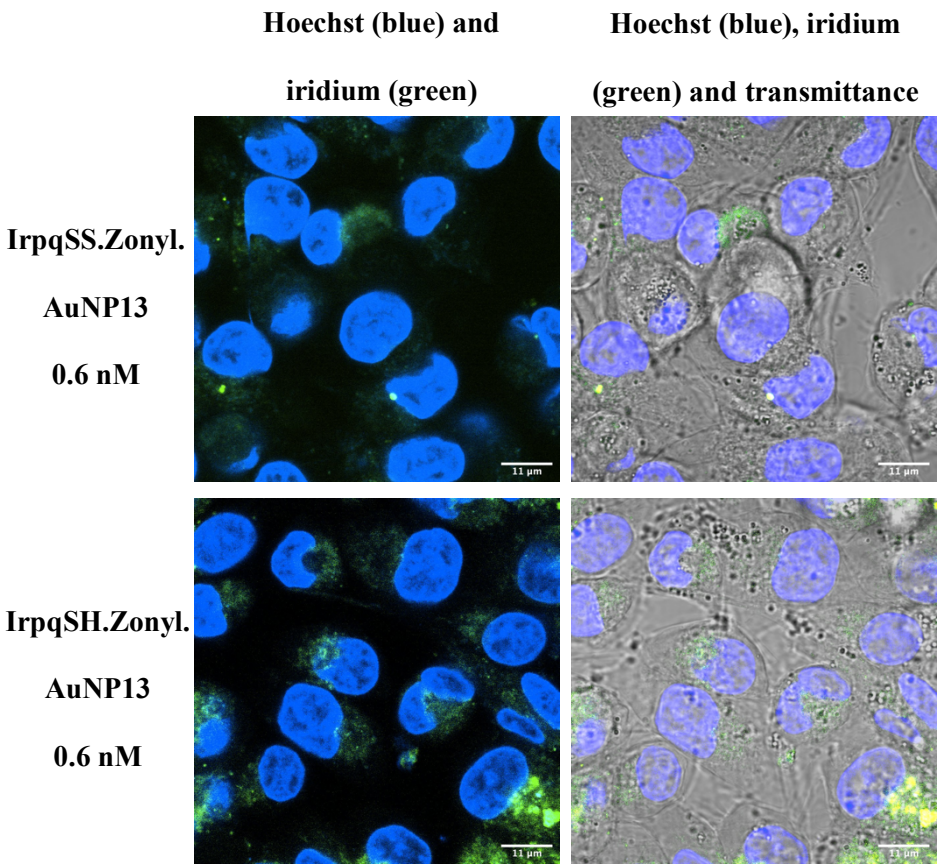
Supplementary Figure 3.2. UV-vis absorbance spectra of AuNPs in phenol red-free DMEM (left) and ***Irpqbpy*** *in phenol red-free DMEM (right), with DMEM as the baseline correction. From the citrate* ***AuNP13*** *solution with SPR Absorbance of 0.531 and size of 15 nm from TEM, the concentration of the NPs when 100 μL of the stock coated NPs was diluted in 900 μL of phenol red-free DMEM was be 1.2 nM, 1.2 nM, 0.8 nM and 0.7 nM for* ***IrpqSS.LPEG.AuNP13****,* ***IrpqSS.SPEG.AuNP13****,* ***IrpqSS.Zonyl.AuNP13*** *and* ***IrpqSH.Zonyl.AuNP13*** *respectively. The concentration of the* ***Irpqbpy*** *was 7 μM.*



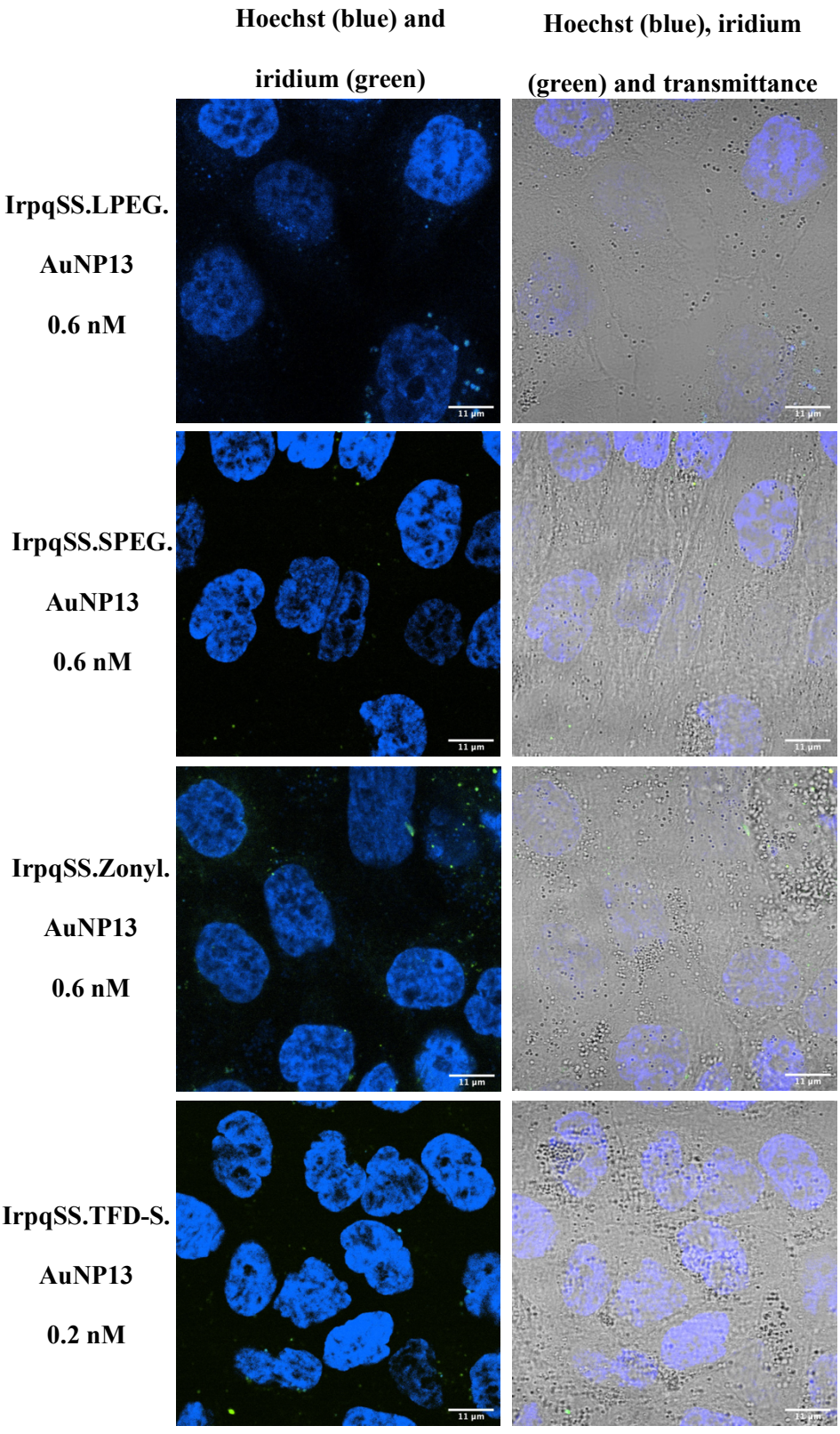
*Supplementary Figure 3.3. Confocal fixed cell images of untreated MiaPaca-2 (**a - d**) and CFPAC-1 (**e - h**) cells at 24 hr collected on a Zeiss LSM900 inverted microscope using a 63x oil immersion objective lens. Hoechst (blue) settings: λ_{exc} = 402, λ_{em} = 450 - 495 nm; Iridium(green): λ_{exc} = 488 nm, λ_{em} = 500 – 700 nm, transmittance: λ_{exc} = 488 nm, ESID (Electronically switchable illumination and detection module).*



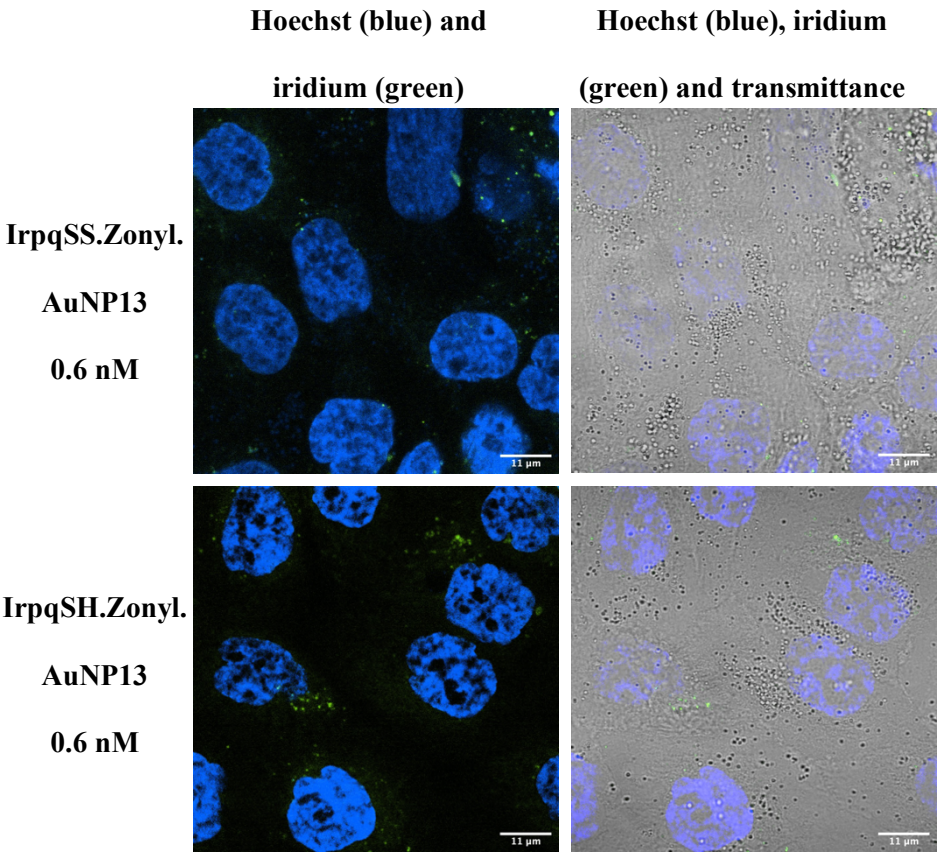
Supplementary Figure 3.4. Confocal fixed cell images in MiaPaca-2 cells of ***IrpqSS.LPEG.AuNP13*** *at 0.6 nM,* ***IrpqSS.SPEG.AuNP13*** *at 0.6 nM,* ***IrpqSS.Zonyl.AuNP13*** *at 0.6 nM and* ***IrpqSS.TFD-S.AuNP13*** *at 0.2 nM for 24 hr collected on a Zeiss LSM900 inverted microscope using a 63x oil immersion objective lens. Hoechst (blue) settings: λ_{exc} = 402, λ_{em} = 450 - 495 nm; Iridium(green): λ_{exc} = 488 nm, λ_{em} = 500 – 700 nm, transmittance: λ_{exc} = 488 nm, ESID (Electronically switchable illumination and detection module).*



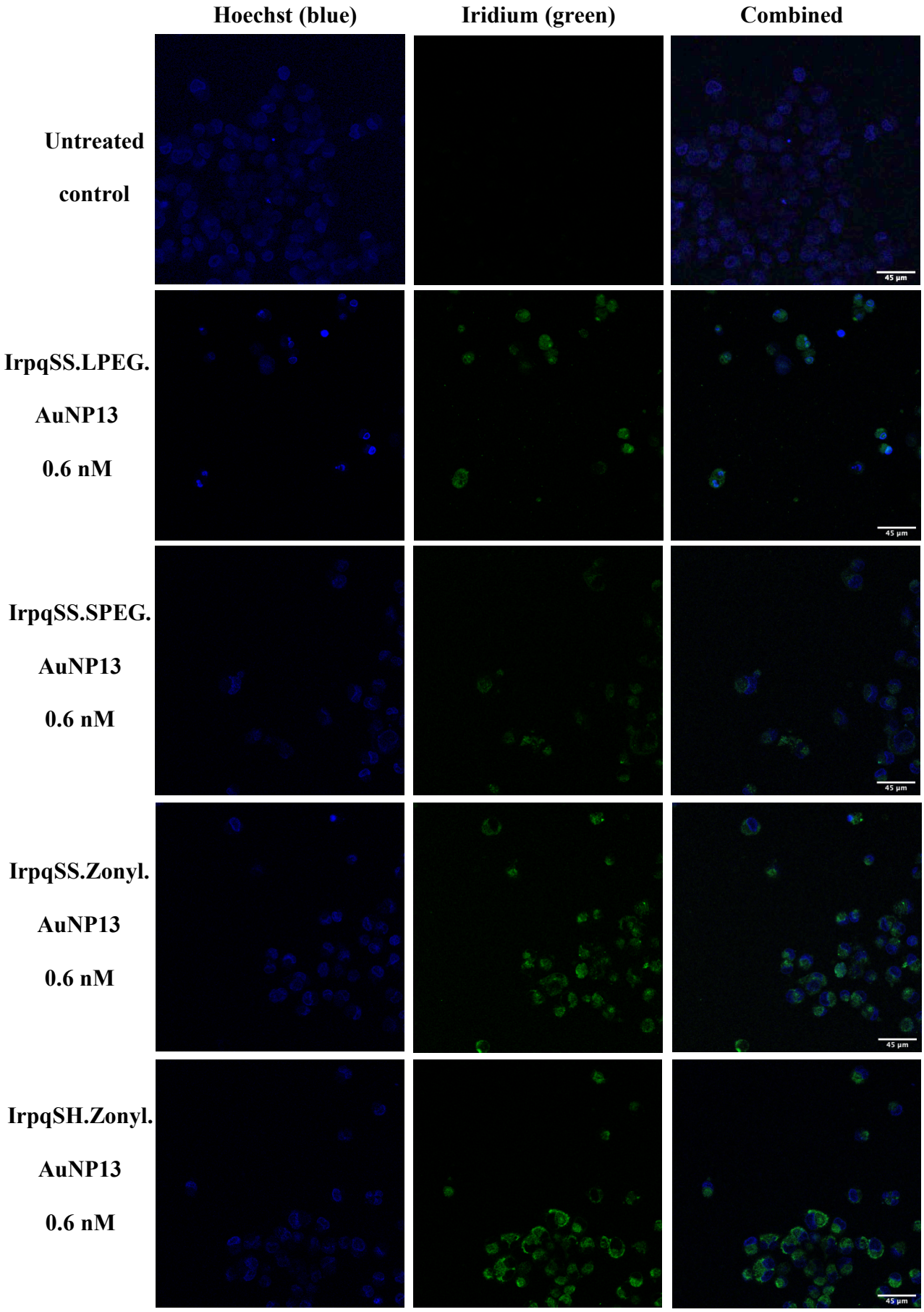
Supplementary Figure 3.5. Confocal fixed cell images in MiaPaca-2 cells of ***IrpqSS.Zonyl.AuNP13*** *at 0.6 nM and* ***IrpqSH.Zonyl.AuNP13*** *at 0.6 nM for 24 hr collected on a Zeiss LSM900 inverted microscope using a 63x oil immersion objective lens. Hoechst (blue) settings:* λ_{exc} *= 402,* λ_{em} *= 450 - 495 nm; Iridium(green):* λ_{exc} *= 488 nm,* λ_{em} *= 500 – 700 nm, transmittance:* λ_{exc} *= 488 nm, ESID (Electronically switchable illumination and detection module).*



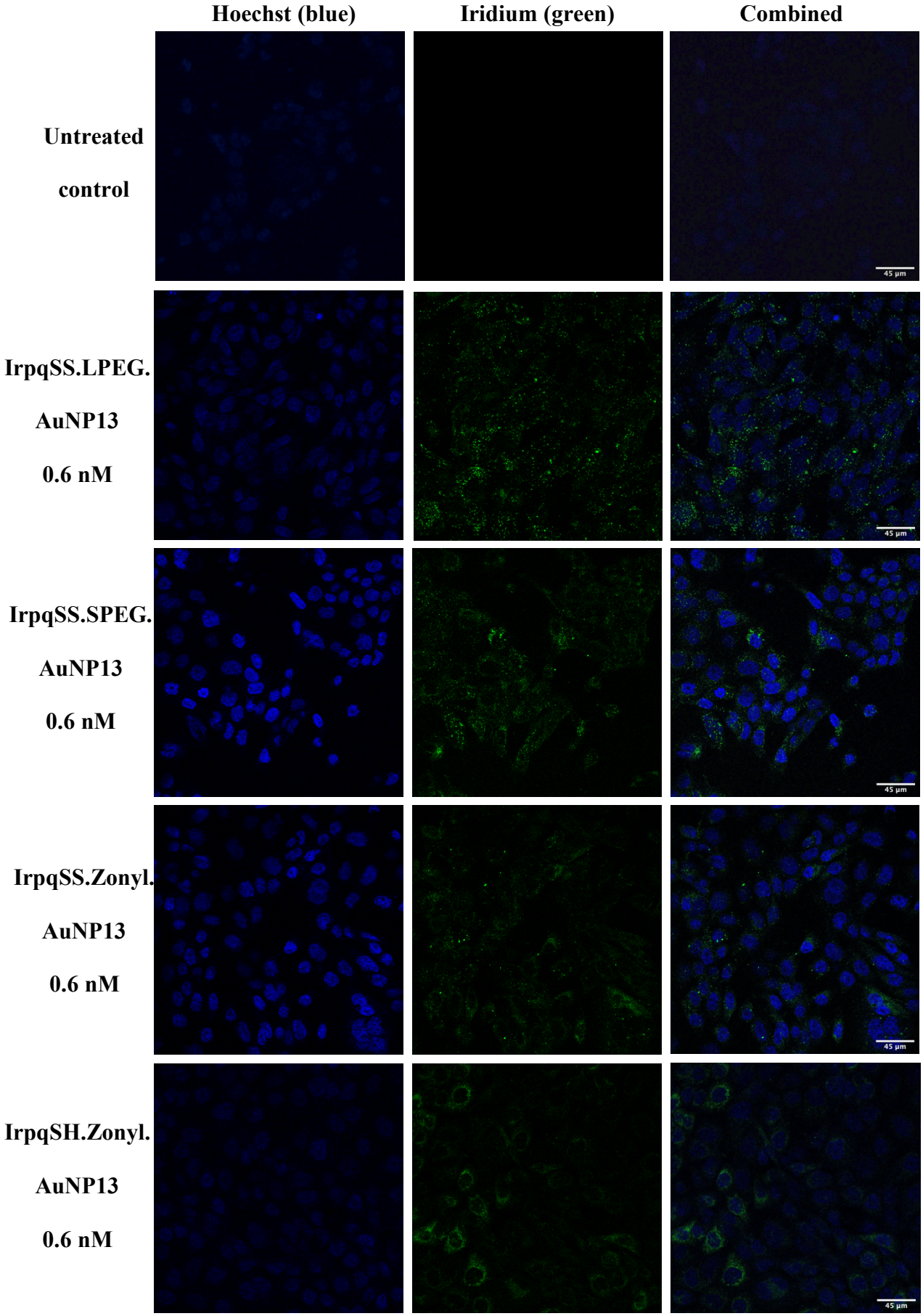
Supplementary Figure 3.6. Confocal fixed cell images in CFPAC-1 cells of ***IrpqSS.LPEG.AuNP13*** *at 0.6 nM,* ***IrpqSS.SPEG.AuNP13*** *at 0.6 nM,* ***IrpqSS.Zonyl.AuNP13*** *at 0.6 nM and* ***IrpqSS.TFD-S.AuNP13*** *at 0.2 nM for 24 hr collected on a Zeiss LSM900 inverted microscope using a 63x oil immersion objective lens. Hoechst (blue) settings:* λ_{exc} *= 402,* λ_{em} *= 450 - 495 nm; Iridium(green):* λ_{exc} *= 488 nm,* λ_{em} *= 500 – 700 nm, transmittance:* λ_{exc} *= 488 nm, ESID (Electronically switchable illumination and detection module).*



Supplementary Figure 3.7. Confocal fixed cell images in CFPAC-1 cells of ***IrpqSS.Zonyl.AuNP13*** *at 0.6 nM and* ***IrpqSH.Zonyl.AuNP13*** *at 0.6 nM for 24 hr collected on a Zeiss LSM900 inverted microscope using a 63x oil immersion objective lens. Hoechst (blue) settings:* λ_{exc} *= 402,* λ_{em} *= 450 - 495 nm; Iridium(green):* λ_{exc} *= 488 nm,* λ_{em} *= 500 – 700 nm, transmittance:* λ_{exc} *= 488 nm, ESID (Electronically switchable illumination and detection module).*

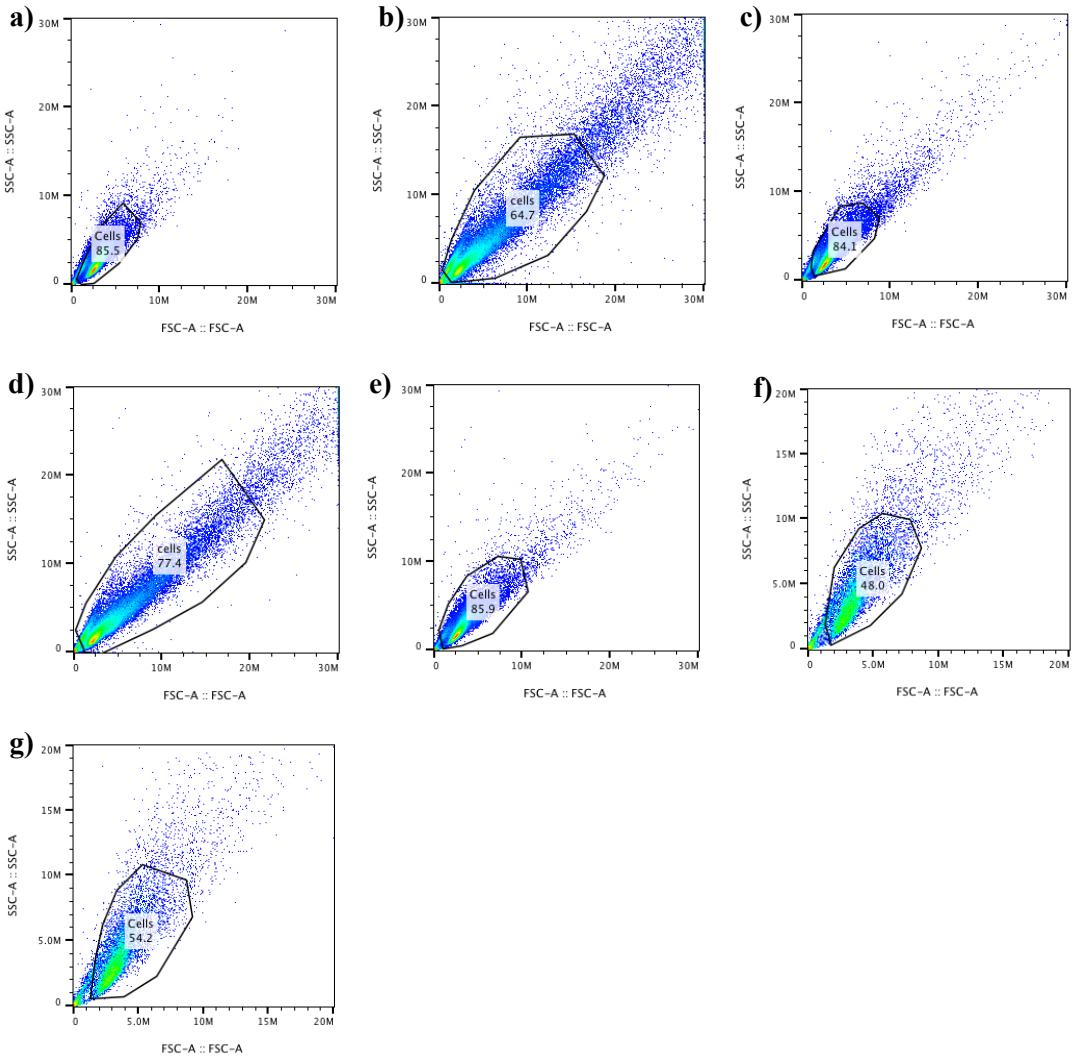


*Supplementary Figure 3.8. Confocal live cell images in MiaPaca-2 cells of **IrpqSS.LPEG.AuNP13**, **IrpqSS.SPEG.AuNP13**, **IrpqSS.Zonyl.AuNP13** and **IrpqSH.Zonyl.AuNP13** at 0.6 nM for 24 hr collected on a Leica sp8 upright microscope using a 40x ceramic water dipping objective lens. Hoechst (blue) settings: λ_{exc} = 402, λ_{em} = 419 – 472 nm; Iridium(green): λ_{exc} = 458 nm, λ_{em} = 550 – 750 nm. Scale bars = 45 µm.*

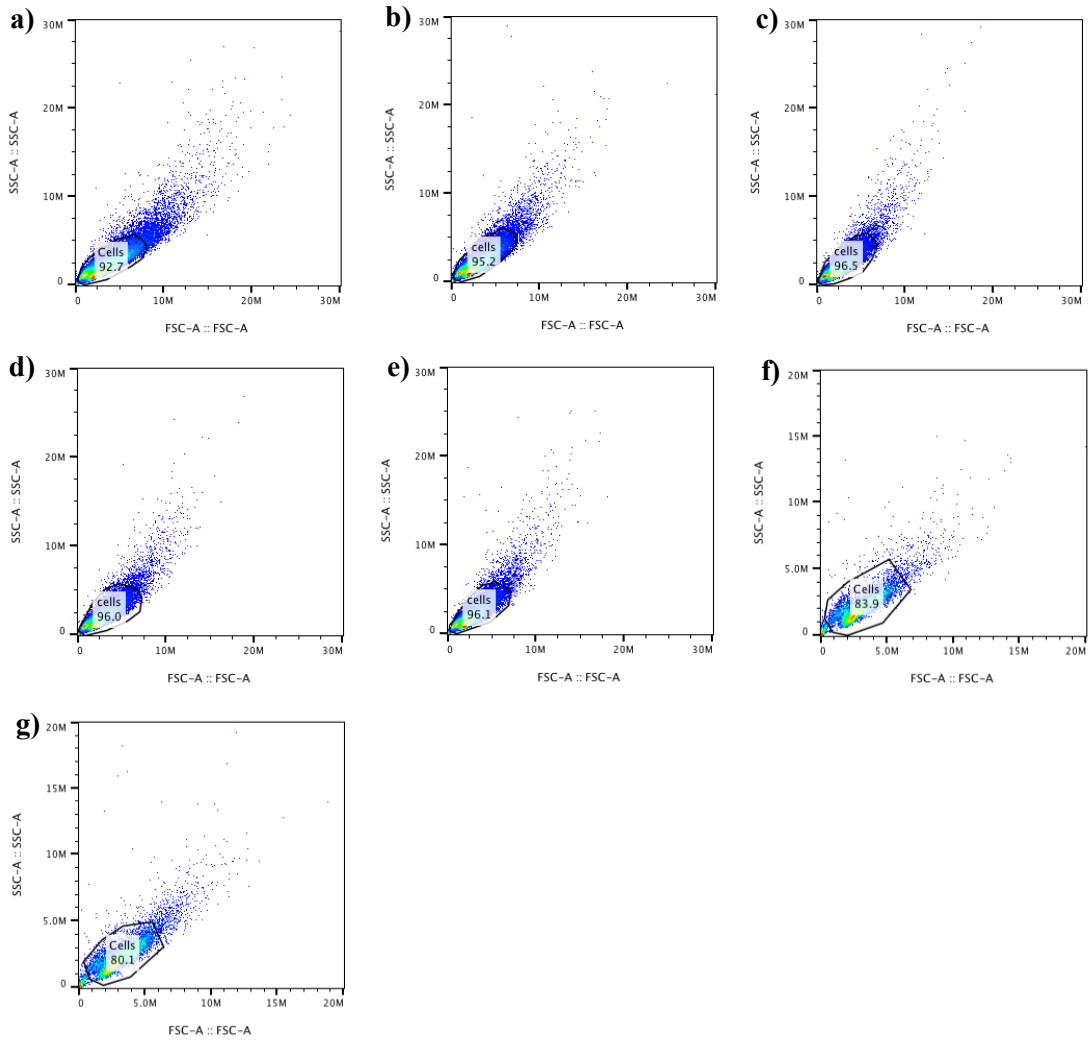


Supplementary Figure 3.9. Confocal live cell images in CFPAC-1 cells of ***IrpqSS.LPEG.AuNP13****,* ***IrpqSS.SPEG.AuNP13****,* ***IrpqSS.Zonyl.AuNP13*** *and* ***IrpqSH.Zonyl.AuNP13*** *at 0.6 nM for 24 hr collected on a Leica sp8 upright microscope using a 40x ceramic water dipping objective lens. Hoechst (blue) settings:* λ_{exc} *= 402,* λ_{em} *= 419 – 472 nm; Iridium(green):* λ_{exc} *= 458 nm,* λ_{em} *= 550 – 750 nm.*

Flow Cytometry scatter plots

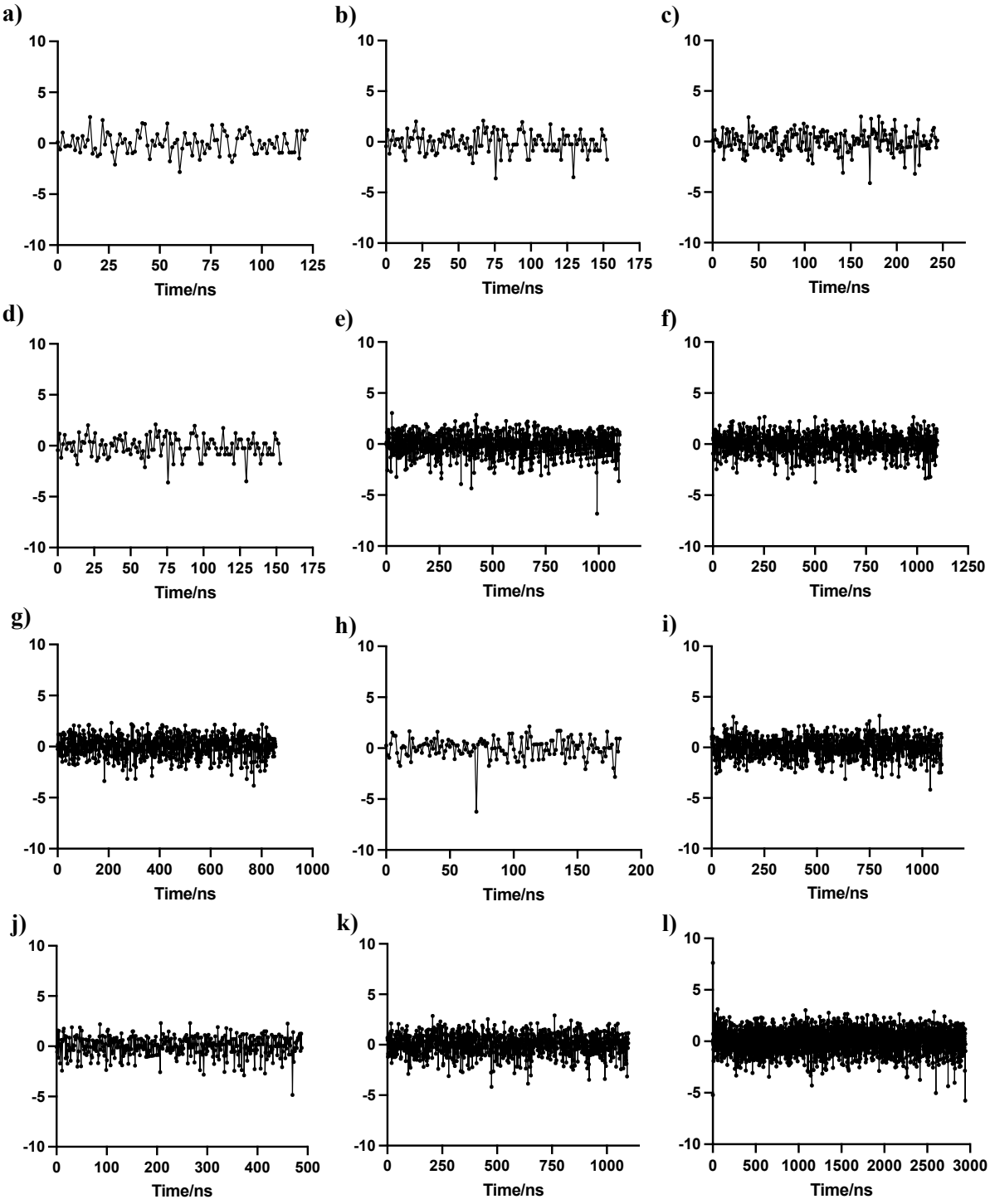


Supplementary Figure 3.10. Scatter plots (side scatter vs forward scatter) for ***a)*** *untreated cells (AuNP experiment),* ***b) IrpqSS.LPEG.AuNP13****,* ***c) IrpqSS.SPEG.AuNP13****,* ***d) IrpqSS.Zonyl.AuNP13****,* ***e) IrpqSH.Zonyl.AuNP13****,* ***f)*** *untreated cells (****Irpqbpy*** *experiment),* ***g) Irpqbpy*** *in MiaPaca-2 cells.*



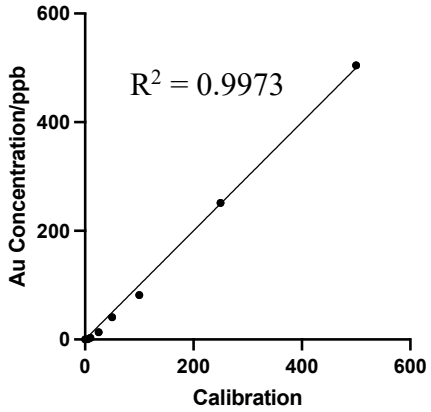
Supplementary Figure 3.11. Scatter plots (side scatter vs forward scatter) for ***a)*** *untreated cells (AuNP experiment),* ***b) IrpqSS.LPEG.AuNP13****,* ***c) IrpqSS.SPEG.AuNP13****,* ***d) IrpqSS.Zonyl.AuNP13****,* ***e) IrpqSH.Zonyl.AuNP13****,* ***f)*** *untreated cells (****Irpqbpy*** *experiment),* ***g) Irpqbpy*** *in CFPAC-1 cells.*

Residuals of Luminescence Lifetimes in cells



Supplementary Figure 3.12. Residuals of the fittings for the luminescent lifetimes in CFPAC-1 ***: a) IrpqSS.LPEG.AuNP13, b) IrpqSS.SPEG.AuNP13, c) IrpqSS.Zonyl.AuNP13, d) IrpqSS.TFD-S.AuNP13, e) IrpqSH.Zonyl.AuNP13, f) Irpqbpy*** *and in MiaPaca-2:* ***g) IrpqSS.LPEG.AuNP13, h) IrpqSS.SPEG.AuNP13, i) IrpqSS.Zonyl.AuNP13, j) IrpqSS.TFD-S.AuNP13, k) IrpqSH.Zonyl.AuNP13,***

ICP-MS calibrations and calculation of AuNP cell uptake



Supplementary Figure 3.13. Calibration curves for Au metal used in the ICP-MS analysis for the uptake of AuNPs in cells using the concentration of the gold content for each sample.

1) Convert the mean Au concentration (ppb) to gL^{-1}

$$1\ ppb = 1\ x\ 10^{-6}\ x\ gL^{-1}$$

2) Convert to gL^{-1}

$$1\ gL^{-1} = 1\ x\ 10^{-3}\ x\ mgL^{-1}$$

3) Total mass of Au in each sample was calculated by multiplying the concentration (mgL^{-1}) by the total volume, e.g. the sample volume was 5 mL, so the concentration (mgL^{-1}) was multiplied by 5.

4) The number of Au atoms was calculated by finding the ratio of the concentration (gmL^{-1}) to the atomic mass of Au (g/mol) and multiplying this ration by the Avogadro's constant (N_A).

$$number\ of\ Au\ atoms = (\frac{concentration(gmL^{-1})}{atomic\ mass\ of\ Au\ (gmol^{-1})})\ x\ N_A$$

5) The number of AuNPs was calculated by dividing the number of Au atoms in the sample by the number of Au atoms in 1 AuNP (Chapter 2, Section 2.4). For the AuNPs of size 15 ± 2 nm, the number of Au atoms in 1 AuNP was $1.04 \times 10^5 \pm 4.7 \times 10^4$.

$$number\ of\ AuNPs = \frac{number\ of\ gold\ atoms\ in\ sample}{1.04\ x\ 10^5}$$

6) The number of AuNPs per cell was calculated by dividing the number of AuNPs in the sample by the number of cells in the sample.

$$number\ of\ AuNPs\ per\ cell = \frac{number\ of\ AuNPs}{number\ of\ cells}$$

Chapter 4

4. Directional conjugation of anti-mesothelin antibodies to gold nanoparticles for diagnostic labelling of pancreatic cancer cells

4.1 Introduction

In this introduction, the different methods of antibody conjugation onto gold nanoparticle surfaces will be outlined, as well as the current research concerning antibodies that target overexpressed PDAC surface markers.

4.1.1 Directional conjugation of antibodies on gold nanoparticle surfaces

As mentioned in Chapter 1, Sections 1.1 – 1.3, many nanoconjugates have been used for studies of treatments for cancer, including PDAC (Pancreatic Ductal Adenocarcinoma). Antibody-AuNP nanoconjugates are one of them. Attachment of antibodies to AuNPs can happen due to hydrophobic interactions, ionic interactions and covalent bonding from dative bonding (Figure 4.1).[1] The non-covalent hydrophobic and ionic interactions of binding antibodies to AuNP surfaces have been studied with various antibodies[2-5], however the disadvantage of these techniques are that high concentrations of antibodies are required in the preparation process and the orientation of the antibodies on the AuNP surface is random. In addition, the antibodies can become detached from the AuNP surface in a biological medium.

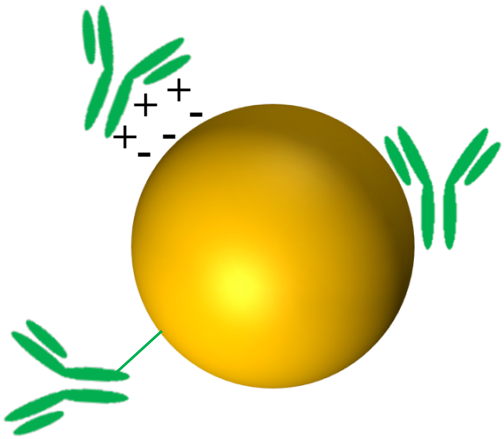


Figure 4.1. A schematic showing AuNP with the hydrophobic, ionic and covalent interactions with antibodies.

For covalent bonding, antibodies containing thiol groups can be directly attached to the AuNP surface by dative bonding a linker that allows a space between the antibody and the AuNP. For example, thiolated PEG linkers with carboxyl terminals have been used to attach antibodies and AuNPs together by EDC/NHS coupling[1, 6], where primary NH_2 groups over the whole antibody can be reacted with a maleimide functional group that is on the AuNP surface. This functional group on the surface of the AuNPs is created by reacting the carboxyl functional groups on the PEG linker on the AuNP surface with EDC, then maleimide. PEG can also increase the biocompatibility of the nanoconjugates due to the hydrophilic nature of PEG. Another linker method requires glycosylation of the antibody Fc region in order to attach a thiolated linker to the antibody.[7] This method allows the Fab region of the antibody to be available for binding to the target. This method requires a specific synthesis for the AuNPs that differs from the standard Turkevich method.[8]

4.1.2 Pancreatic cancer tumour markers

There are three kinds of cancer tumour markers – cell surface, transmembrane and intracellular[9]. Cell surface markers are the easiest to target because the targeting agent has free access to the surface marker. Transmembrane markers span the cell membrane and so the targeting agent must be able to enter the

membrane to reach the target. Intracellular cell markers are found inside the cell, in the cytoplasm or the nucleus, hence the targeting agent must not only enter the membrane but be internalised and if the marker is in the nucleus, cross the nuclear membrane.

In PDAC, more than a dozen cell surface tumour markers have been found over the years. CEA (Carcinoembryonic Antigen), a glycoprotein was first discovered by Gold and Freeman in 1965[10, 11], and hence it is one of the most widely used due to being the first tumour antigen described. Overexpression of CEA can also indicate colon, rectal, prostate, ovary, lung, thyroid, or liver cancers. Mesothelin, also a glycoprotein was first reported in 1992[12] and since.[13] It is overexpressed in mesothelioma, ovarian cancer, and others. The mesothelin tag has not been found in normal pancreas libraries according to Argani *et al.*[14] Therefore, as they state: "mesothelin overexpression in pancreatic adenocarcinoma has potential diagnostic, imaging, and therapeutic implications". Their research is supported by Hassan *et al.*[15] who reported that in 100% of the cases tested (18 in total), pancreatic adenocarcinomas showed mesothelin expression. In all cases, the adjacent normal pancreas did not stain for mesothelin.

EGFR (Epidermal Growth Factor Receptor) was first isolated in 1962 by Stanley Cohen[16] and it is present in other cancers including lung cancer, breast cancer and glioblastoma.[17] RON (Recepteur d'Origine Nantais) receptor tyrosine kinase was first reported in 1993[18, 19]. It has been shown to be linked to PDAC malignancy.[20] Prohibitin was reported in 2018[21] as a novel marker. There is evidence that prohibitin plays a role in proliferation, migration and invasion of certain PDAC cell lines, as silencing of prohibitin inhibited these behaviours in PDAC cell lines. S100A10 is a novel receptor reported in 2018.[22] In addition, other markers include CA 19-9 (serum carbohydrate antigen 19-9)[23] a serum marker, DUPAN 2[24], CEACAM[25], CD26[26] and Integrin $\alpha 3$.[27] Some transmembrane markers include MUC-1 and Her2-neu, which are overexpressed in PDAC cells.

4.1.3 Antibodies for pancreatic cancer targeting

There are many antibodies available for the targeting of cell surface antigens present in PDAC cells (Figure 4.2). Some considerations for choosing an antibody are whether it is monoclonal or polyclonal. Monoclonal antibodies have affinities for the same antigen and the same epitope within the antigen, which makes them very specific, as every antibody will bind to the same site on the antigen. Polyclonal antibodies bind to the same antigen but different epitopes within the antigen. This mixed population of antibodies is cheap to produce and may still bind even with small changes in the protein structure, unlike monoclonal ones. Another consideration is the type of antibody or the fragment (IgG, Fab, Fv and Fc) (Figure 4.3). Larger antibodies may hinder uptake into cells, especially when attached to a large AuNP. Smaller fragments could lack the functional groups needed for attachment to AuNPs (Section 4.1.1) but could penetrate tissues faster and may be degraded faster in the body.

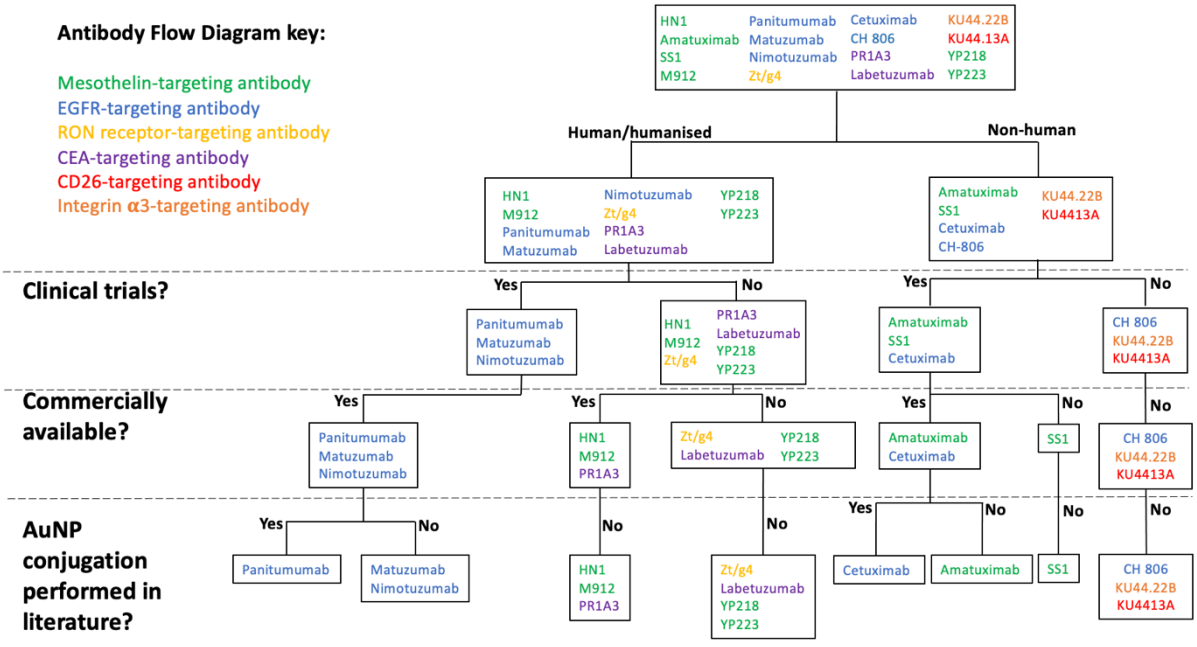


Figure 4.2. Flow diagram with PDAC-targeting antibodies and the selection methods for the type of antibody for various PDAC surface markers.

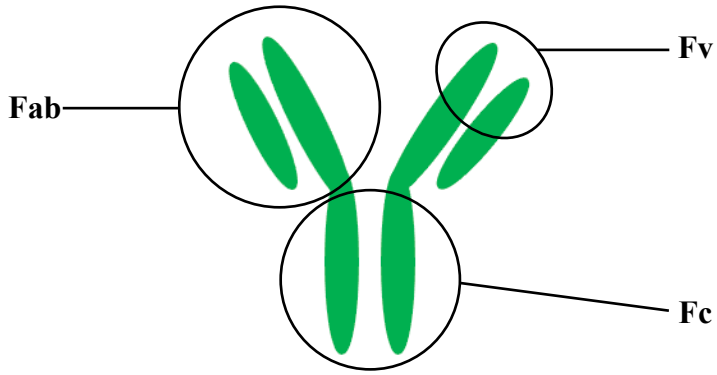


Figure 4.3. Diagram of an antibody with the different fragments circled and labelled. Fab = Fragment antigen binding, Fv = variable fragment, Fc = fragment crystallizable.

Immunogenicity is also an important consideration, as non-human antibodies are more likely to generate an immune response from the body viewing it as a "foreign object", however that is not always the case as will be shown, with some non-human antibodies that have reached clinical trials and show promising results. Fully human antibodies have been shown to be better due to their lower immunogenicity.[28] Another consideration is whether the antibody has been in clinical trials. Clinical trials provide further information on the behaviour of the antibody in the human body. Commercial availability of the antibodies is also important, especially in this project, where making the antibody was far out of the scope of the project. Lastly, whether the antibody has been studied for conjugation onto AuNPs is important to learn about the ability of different types of antibodies for conjugation to AuNPs. It would be almost futile to repeat studies already performed when there are many other antibodies to be studied.

From the different surface antigens mentioned before that are overexpressed in PDAC cell lines, some CEA targeting antibodies include PR1A3[29] and hMN-14 (labetuzumab).[30] hPRIA3 is a humanised antibody that has been shown to enhance CEA-specific cytotoxicity in colorectal cancer. Mesothelin-targeting antibodies include HN1[31], M912[32], MORAb-009 (Amatuximab)[33, 34], SS1[9] and YP218 and YP223.[35] HN1 and M912 are fully human antibodies, with HN1 as an IgG monoclonal antibody and

M912 in Fab, scFv and IgG forms. No clinical trials have been performed for either. Studies with M912 found that it binds to cells and kills them by ADCC (Antibody Dependent Cellular Cytotoxicity). The Fab, scFv and IgG forms were all able to recognise mesothelin. HN1 also has an ADCC effect on cells. Amatuximab is a chimeric antibody that causes ADCC in cells that overexpress mesothelin. Fv fragment SS1 also displays ADCC in cells. It is the same Fv fragment as for Amatuximab, and SS1 has also been in clinical trials as an immunotoxin SS1P (with PE38 toxin)[36], but in mesothelioma and ovarian cancers, not pancreatic. Amatuximab was also in phase 2 clinical trials against malignant mesothelioma (NCT01018784, NCT00711191) but the study was terminated due to business reasons, not safety reasons. MORAb-009, SS1P and HN1 bind to the same epitope of the mesothelin antigen.[35] M912 and MORAb-009 do not compete for binding to mesothelin[32] as MORAb-009 does not recognise mouse mesothelin[33] like m912 does, therefore the binding epitopes must be different. This is an indication that antibodies that bind to different epitopes can be used together in combination to target the same antigen without being in competition with one another. Hence MORAb-009 cannot be used in mouse models as m912 can be. YP218 and YP223 are humanised monoclonal antibodies that recognise different epitopes of mesothelin. Mesothelin antibodies have been used for the detection of mesothelin in pancreatic cancer cell supernatants by attaching mouse IgG antibodies to a gold surface by an alkanethiol monolayer[37]. This provides potential for use on AuNP surfaces.

EGFR-targeting antibodies include C225 (Cetuximab)[38], Panitumumab[39], Matuzumab[40], Nimotuzumab[41] and CH 806.[42] Cetuximab is a human/mouse IgG monoclonal antibody that has been approved by the FDA and has been used in clinical trials. Cetuximab has been reported as an AuNP conjugate and was effective in targeting cancer cell lines. It has also been in multiple clinical trials for pancreatic cancer (NCT00923299, NCT00042939, NCT00448838, NCT00305760, NCT00075686, NCT00408564, NCT00467116) and in combination with Trastuzumab, an anti-Her2/neu monoclonal antibody (NCT00599833). Panitumumab (NCT00004879, NCT00601627, NCT00550836) and Nimotuzumab (NCT00561990). No Matuzumab clinical trials have been performed with pancreatic cancer patients. CH 806 is a chimeric monoclonal antibody, but no PDAC studies have been conducted yet.

Cetuximab is the only antibody targeting PDAC cell lines that has been studied as an AuNP nanoconjugate. In 2008, the first report of the delivery of gemcitabine as a drug nanoconjugate, with AuNPs as the delivery vehicle[38] showed that the system could inhibit tumour proliferation and growth. AuNPs of 5 nm were incubated with cetuximab and gemcitabine and analysed by XPS to confirm attachment. The AuNPs with cetuximab were more effective in inhibiting tumour growth than those without cetuximab, and the presence of AuNPs was found to also decrease tumour growth due to the function of AuNPs as a delivery vehicle, delivering a toxic payload to the tumours. In 2010, 20 nm AuNPs conjugated with cetuximab induced hyperthermic apoptosis of PDAC cells when Radio Frequency (RF) energy was used to target the cells.[43] Hyperthermic cytotoxicity was not displayed in normal pancreatic tissues. Studies of the factors that contributed to successful targeting of the tumour cells with the cetuximab and AuNP delivery vehicle included the AuNP to antibody ratio, the surface area of the AuNP, the binding ability of the antibody to the target and the hydrodynamic diameter of the nanoconjugate[44]. In 2020, the importance of PEG as a stealth molecule was outlined[45], with thiolated PEG molecules of 550 or 1000 Da reducing the viability of PCC (Pancreatic cancer cells) and PSC (Pancreatic stellate cells) compared to the non-targeted nanoconjugates of AuNP and gemcitabine. PEG increased the circulation time of the AuNPs and the targeted delivery of gemcitabine in the nanoconjugates, allowing more time for the AuNPs to reach the tumours. Cell viability was shown to decrease the most with AuNPs conjugated with 1000 Da PEG, cetuximab and gemcitabine. The stability of cetuximab-AuNP nanoconjugates was proven over 24 months, with the structural integrity of the AuNPs maintained and cell apoptosis induced after EGFR receptor binding and cell internalisation.[46]

RON-receptor-targeting antibody is Zt/g4. It is a humanised IgG monoclonal antibody. Reported in 2018 as an antibody-drug conjugate[47] and in 2019 for evaluation for clinical trials[48], although no clinical trials have yet been conducted. The Zt/g4 antibody bound to the RON receptor without the influence of the MMAE drug that it was bound to. The tumour sizes of mice decreased in PDAC cell lines overexpressing RON receptor, due to ADC-mediated RON internalisation. Prohibitin antibodies are commercially available and peptide targets have been studied in clinical trials, however no clinical trials have been performed with pancreatic cancer. Integrin α3 antibody is KU44.22B, a mouse monoclonal

IgG antibody and CD26 antibody is a mouse monoclonal IgG antibody KU44.13A. Both were reported in 2020.[27] Although transmembrane antigens are not the focus of this study, antibodies for MUC-1 and Her2-neu, two overexpressed PDAC transmembrane markers are PankoMab™ (Glycotope, Germany) and Herceptin® (Genetech Inc., CA, USA) respectively.

The different antibodies available provide potential for different antibody coatings on AuNP surfaces, which could allow more efficient targeting and uptake of AuNPs into cells. For example, if a receptor has slow internalisation for a specific antibody, having a second antibody can ensure that the AuNP has another chance for uptake. In addition, non-competing binding sites of different antibodies to the same target would mean that the same surface marker could be targeted by different antibodies at the same time.

In this study, mesothelin was chosen as the surface antigen to target because it is overexpressed in other PDAC cell lines that EGFR is not expressed in, presenting potential for dual antibody conjugation onto single AuNPs to target multiple cell lines expressing different levels of surface markers in PDAC cells. In addition, anti-mesothelin immunotoxins have reached clinical trial stage (NCT01362790), although not with PDAC, showing that targeting mesothelin has been successful in the past. Anti-mesothelin antibodies has been used on gold surfaces, but not on AuNPs, as cetuximab has. But the gold surface work presents potential for use on AuNPs.

4.1.4 Chapter Summary

In this chapter, it will be shown that monodisperse luminescent **AuNP**s coated with mesothelin-targeting antibodies can be made and used for imaging in PDAC cell lines with the **IrpqSS** and **IrpqSH** complexes synthesised in Chapter 2, Section 2.2. The potential for these **AuNP**s for diagnostic labelling of cancer cell lines overexpressing mesothelin will be shown as well as the ability of the mesothelin-targeting antibodies to bind to and internalise in PDAC cells while attached to the **AuNP** delivery vehicle. In addition, the luminescent properties of the **IrpqSS** and **IrpqSH** complexes when on the AuNP surface will be outlined.

4.2 Synthesis and characterisation of IrpqSS- and IrpqSH-coated AuNP19s

AuNP19s were synthesised using a different method[7] from the standard Turkevich and Vossmeyer methods[8] used in Chapters 2 and 3. The method used allowed the attachment of directional linkers to antibodies. To obtain 1.1 nM of 18.5 ± 1.2 nm **AuNP19**s (Supplementary Figure 4.1). The directional conjugation ensures availability of the Fab region of the antibody by binding of the thiolated PEG linker (Sensopath Technologies, Cat No. SPT-0014B) to the Fc region of the antibody. This PEG linker binds only to glycosylated antibodies, so the glycosylation of the MAB32651 mesothelin-targeting antibody (**MAB**) from R&D Systems was confirmed with a Purpald test. The alcohol groups on the aldehyde were oxidised to form aldehydes which were reacted with Purpald (4-amino-3-hydrazino-5-mercapto-1,2,4-triazole), displaying a colour change from colourless to deep purple as a secondary unsaturated ring was formed on the Purpald molecule. 10 μL of **MAB**-linker solution 4 μM of **IrpqSS** and 7.5 μM of **IrpqSH** (Supplementary Figure 4.2, Supplementary Figure 4.3) was determined as the correct amount to add to the **AuNP19**s. LPEG (Poly(ethylene glycol) 2-mercaptoethyl ether acetic acid, average M_n 2100) was added after the **MAB**-linker coating and before adding **IrpqSS** or **IrpqSH** to ensured stabilisation of the **AuNP19**s. Five final **AuNP** samples were made: **MAB.IrpqSS.AuNP19**, **MAB.IrpqSH.AuNP19**, **IrpqSS.AuNP19**, **IrpqSH.AuNP19** (Figure 4.4) and **MAB.AuNP19**. **MAB.AuNP19** with **MAB** only and was made to investigate whether the iridium(III) complexes play a part in toxicity from the cell toxicity assays or the ROS assays (Section 4.5).

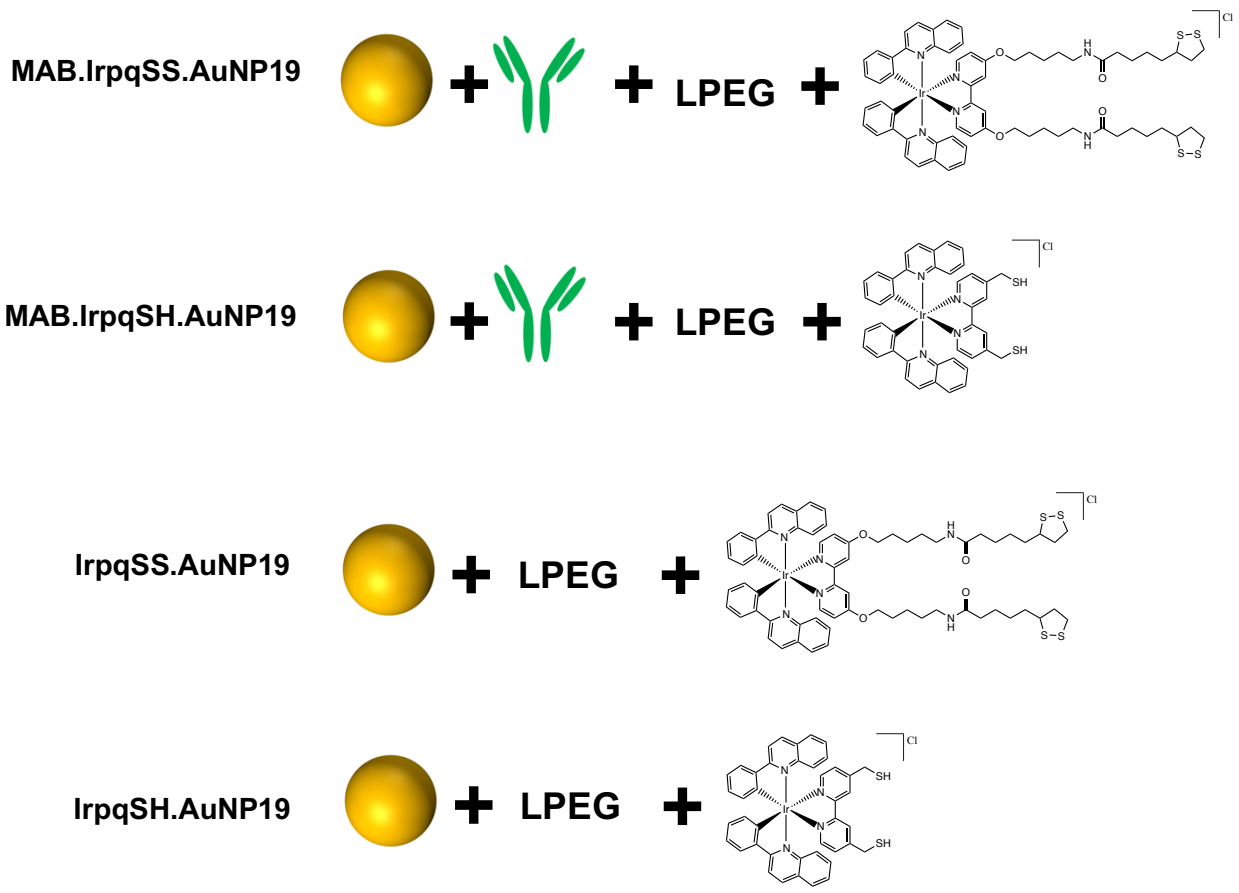


*Figure 4.4. Schematics of the formation of **MAB.IrpqSS.AuNP19**, **MAB.IrpqSH.AuNP19**, **IrpqSS.AuNP19** and **IrpqSH.AuNP19**.*

Surface modification of the AuNPs was confirmed by the SPR shift from the plain **AuNP19**s to the fully coated AuNPs (Figure 4.5, Table 4.1). 10K MWCO Pierce Protein Concentrators (0.5 mL) enabled the removal of any extra unbound iridium(III) complex or **LPEG** surfactant from the AuNP solution. DLS volume distribution increased from 19 ± 6 nm in the plain **AuNP19**s to 41 ± 20 nm and 41 ± 23 nm for **MAB.IrpqSS.AuNP19** and **MAB.IrpqSH.AuNP19** respectively (Figure 4.6, Table 4.2). In comparison, the samples without **MAB** had volume distribution values of 27 ± 9 nm and 30 ± 10 nm for **IrpqSS.AuNP19** and **IrpqSH.AuNP19** respectively. The size increase between the plain **AuNP19**s and the iridium-coated **AuNP19**s can be attributed to the sphere of H_2O. molecules around the AuNPs

that move with the sample as if they were a part of the sample (Chapter 1, Section 1.4.1). The increase between the iridium-coated AuNP19s and the **MAB**-coated AuNPs can be attributed to the **MAB** addition to the **AuNP19**s. Hence, **MAB** coating was confirmed by DLS size increase.

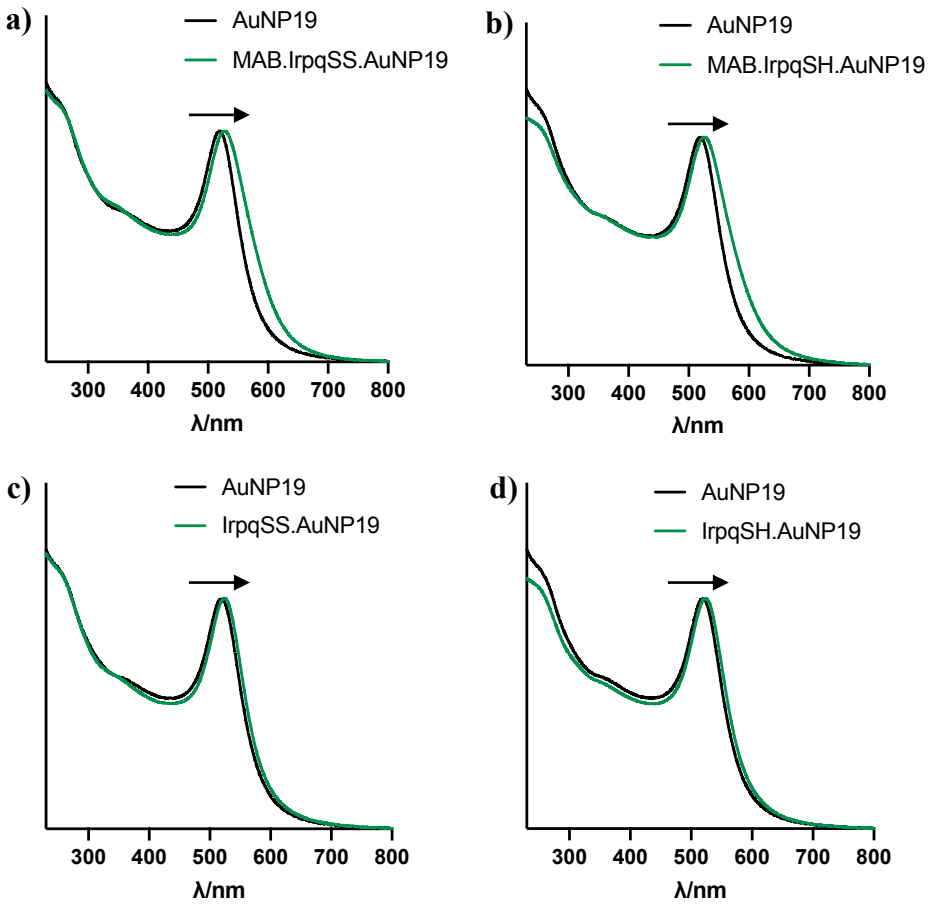


*Figure 4.5. Normalised UV-vis absorbance spectra (green) for **a) MAB.IrpqSS.AuNP19**, **b) MAB.IrpqSH.AuNP19**, **c) IrpqSS.AuNP19** and **d) IrpqSH.AuNP19**, with a red-shift in the SPR peak seen for all four samples compared to **AuNP19** (black), indicating modification of the **AuNP19** surface.*

	λ_{max}/nm	Shift/nm
AuNP19	519	0
MAB.IrpqSS.AuNP19	529	10
MAB.IrpqSH.AuNP19	528	9
IrpqSS.AuNP19	524	5
IrpqSH.AuNP19	524	5

*Table 4.1. UV-vis absorbance SPR shifts of the plain **AuNP19**s and the iridium-coated nanoparticles **MAB.IrpqSS.AuNP19**, **MAB.IrpqSH.AuNP19**, **IrpqSS.AuNP19** and **IrpqSH.AuNP19**.*

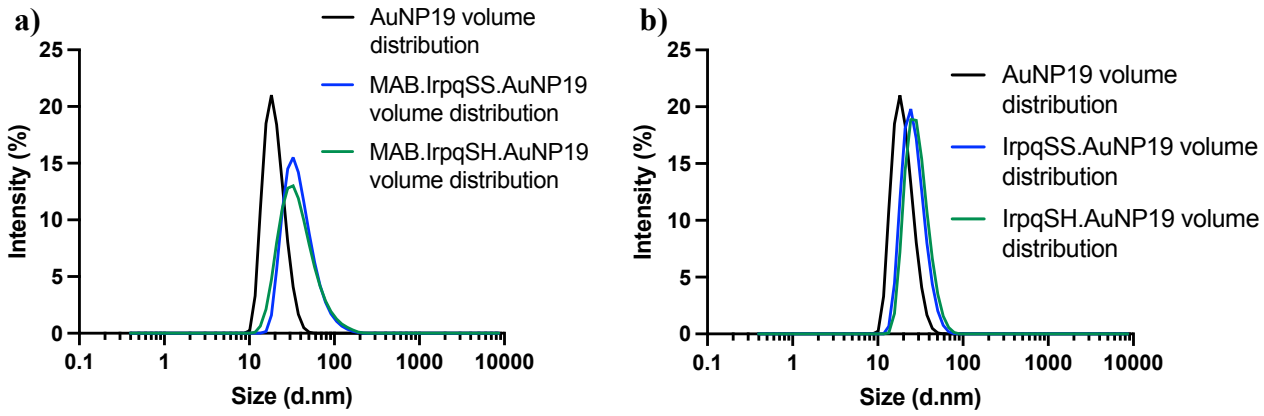


*Figure 4.6. DLS volume distribution histograms of **a) MAB.IrpqSS.AuNP19** and **MAB.IrpqSH.AuNP19** and **b) IrpqSS.AuNP19** and **IrpqSH.AuNP19** compared to that of plain AuNP19.*

	Number distribution (nm)	Volume distribution (nm)	Intensity distribution (nm)	PDI	Z-Average (nm)
AuNP19	15 ± 4	19 ± 6	25 ± 8	0.156	21 ± 0.007
MAB.IrpqSS.AuNP19	29 ± 9	41 ± 20	67 ± 31	0.232	51 ± 0.24
MAB.IrpqSH.AuNP19	26 ± 10	41 ± 23	72 ± 35	0.254	54 ± 0.17
IrpqSS.AuNP19	22 ± 6	27 ± 9	35 ± 11	0.16	30 ± 0.16
IrpqSH.AuNP19	24 ± 6	30 ± 10	39 ± 12	0.167	33 ± 0.09

*Table 4.2. DLS number distribution, volume distribution and intensity distribution sizes for **AuNP19, MAB.IrpqSS.AuNP19, MAB.IrpqSH.AuNP19, IrpqSS.AuNP19, IrpqSH.AuNP19**.*

A conjugate check process (Conjugation Check Kit (ab236554), Thermo Fisher) was used to confirm the binding of **MAB** to the **AuNP19**s (Figure 4.7) by a coloured line forming on the test strips when the antibody-AuNP nanoconjugate was successfully formed. The coloured line that formed was due to a line of protein A and G on the conjugate test strips that binds strongly to the Fc region of many IgG molecules. Hence, the red colour of the antibody-AuNP conjugate was concentrated at the test line for samples with the antibody. The monodispersity of the AuNPs in TEM was confirmed by images taken (Figure 4.8) and the diameters obtained for **MAB.IrpqSS.AuNP19**, **MAB.IrpqSH.AuNP19**, **IrpqSS.AuNP19** and **IrpqSH.AuNP19** were 19.4 ± 1.5 nm, 19.7 ± 1.0 nm, 19.7 ± 1.1 nm and 18.9 ± 1.6 nm respectively. The sizes were all within error of each other.

ICP-MS analysis of the iridium coating on the **AuNP19**s was too low to quantify in the system chosen except for **MAB.IrpqSS.AuNP19**, which had a coating of 1290 iridium(III) complexes per nanoparticle with a size of 18.5 ± 1.2nm. The error in the AuNP size would give an iridium coating from 1053 to

1553 complexes. The other three samples had a lower iridium(III) complex coating compared to **MAB.IrpqSS.AuNP19**.

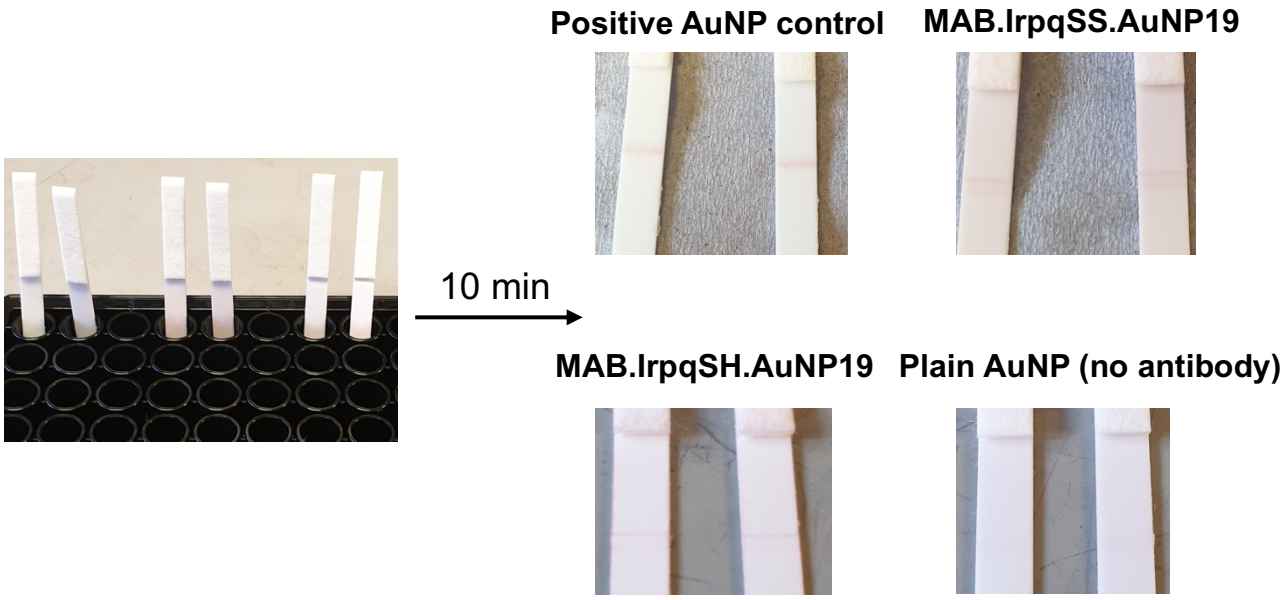


*Figure 4.7. Images showing the conjugate check (using Conjugation Check Kit (ab236554), Thermo Fisher) experiment for confirmation of binding of the antibody to the **AuNP19**s. The test was performed according to the product manual for **MAB.IrpqSS.AuNP19** and **MAB.IrpqSH.AuNP19**.*

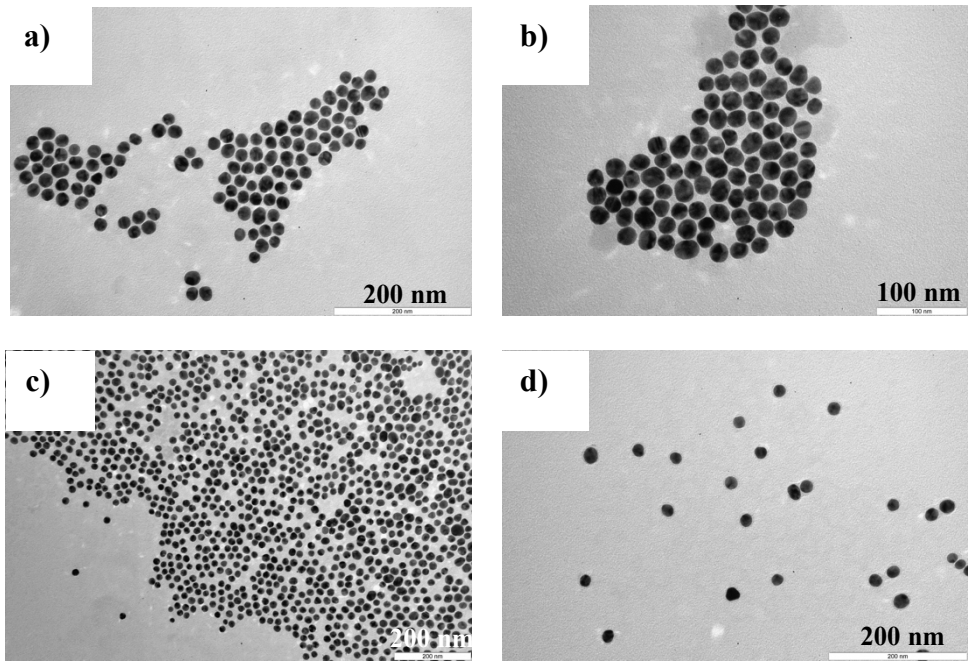


*Figure 4.8. TEM images of the different iridium-coated AuNPs: **a) MAB.IrpqSS.AuNP19**, **b) MAB.IrpqSH.AuNP19**, **c) IrpqSS.AuNP19** and **d) IrpqSH.AuNP19**, with sizes of 19.4 ± 1.5 nm, 19.7 ± 1.0 nm, 19.7 ± 1.1 nm and 18.9 ± 1.6 nm respectively.*

4.3 Photophysical characterisation of IrpqSS- and IrpqSH-coated AuNP19s

The emission of the AuNP samples was collected in H_2O to ensure suitable luminescence of the samples before commencing cell studies (Figure 4.9). The samples with the **IrpqSH** complex had a much lower emission than those with the **IrpqSS** complex, hence good emission not expected for the **IrpqSH**-coated AuNPs in cells (Section 4.5.2). A scattering peak from the gold in the **MAB.IrpqSH.AuNP19** and **IrpqSH.AuNP19** was seen (Figure 4.9b), further indicating the weak emission from **IrpqSH**, as this peak is not seen in emission spectra of AuNP samples with strong emission from the iridium(III) complexes (Figure 4.9a).

Luminescence lifetimes from **MAB.IrpqSH.AuNP19** and **IrpqSH.AuNP19** samples could not be collected due to low counts obtained from the samples. Luminescence lifetimes were obtained of 880 and 830 ns for **MAB.IrpqSS.AuNP19** and **IrpqSS.AuNP19** (Figure 4.10, Table 4.3, Supplementary Figure 4.5), which is a decrease from **IrpqSS** in H_2O at 1412 ns as seen from other AuNP samples discussed in Chapter 2, Section 2.7. As the long component of the lifetimes for **MAB.IrpqSS.AuNP19** and **IrpqSS.AuNP19** were within error of one another, it shows that the presence of the antibody did not significantly affect the luminescence lifetime.

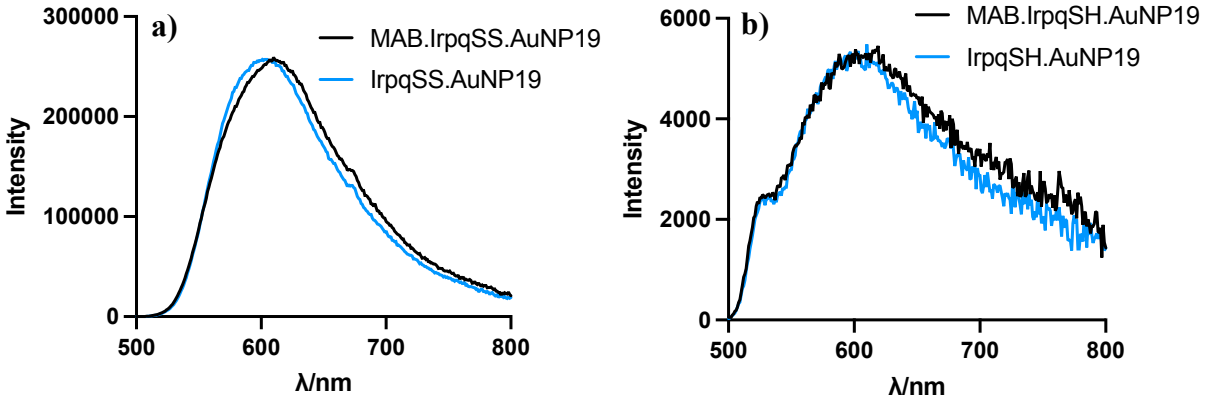


Figure 4.9. Emission spectra of the different AuNPs at 1 nM in H_2O: ***a) MAB.IrpqSS.AuNP19*** *(black) and* ***IrpqSS.AuNP19*** *(blue),* ***b) IrpqSH.MAB.AuNP19*** *(black) and* ***IrpqSH.AuNP19*** *(blue), UV-vis absorbance value at λ = 450nm was 0.5.*

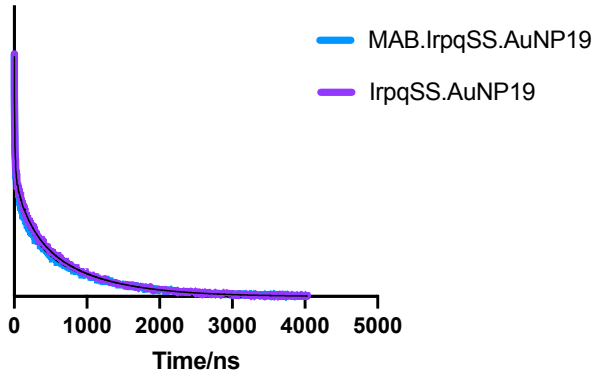


*Figure 4.10. Luminescence lifetime decay curves for **MAB.IrpqSS.AuNP19** and **IrpqSS.AuNP19** in H_2O at 1 nM, fitted with an IRF fitting of $\chi^2 < 1.2$.*

	MAB.IrpqSS.AuNP19		**IrpqSS.AuNP19**	
	%	**τ/ns**	**%**	**τ/ns**
Long component	63	**880**	69	**830**

*Table 4.3. Luminescence lifetime decay fitting numbers for the **MAB.IrpqSS.AuNP19** and **IrpqSS.AuNP19** samples at 1 nM in H_2O, fitted with an IRF fitting of $\chi^2 < 1.2$.*

4.4 Selection of pancreatic cancer cell lines for cell studies

BxPC-3, MiaPaca-2 and CFPAC-1 were analysed by qPCR in triplicates with three different primer pairs to obtain ΔCq values (quantitative cycle). The target was mesothelin (MSLN), a surface glycoprotein that is overexpressed in some PDAC cell lines. The ΔCq values represent the inverse of the receptor that is being targeted (Table 4.4). ΔCq values for BxPC-3 and CFPAC-1 across all 3 primer

pairs were lower than MiaPaca-2. Hence MiaPaca-2 was shown to have the lowest quantity of MSLN, as shown in previous studies testing for the overexpression of MSLN in PDAC cell lines.[49, 50]

	ΔCq value (MSLN primer pair #1)	**ΔCq value (MSLN primer pair #2)**	**ΔCq value (MSLN primer pair #3)**
BxPC-3	22.68	20.25	20.63
MiaPaca-2	24.09	24.08	25.55
CFPAC-1	22.17	18.24	18.44

Table 4.4. ΔCq values obtained from qPCR experiments on BxPc-3, MiaPaca-2 and CFPAC-1 cells performed with three different mesothelin (MSLN) primer pairs.

Although MiaPaca-2 had a lower expression of mesothelin, it still expresses mesothelin in low quantities and BxPC3 and CFPAC-1 overexpress it. Hence, mesothelin-related uptake could still be possible, although it would be very low due to the low expression of the marker. Panc-1, Capan-1, AsPc-1 and other PDAC cells also overexpress MSLN compared to MiaPaca-2, and HPDE (Human Pancreatic Duct Epithelial – a healthy pancreatic cell line), however these cell lines were not tested in this study due to lack of availability. MiaPaca2 and CFPAC-1 were chosen to use for this study because they were able to be grown in DMEM, whereas BxPC3 was grown in RPMI (Roswell Park Memorial Institute) media, so for consistency MiaPaca-2 and CFPAC-1 were the best for comparison. CFPAC-1 is a Cystic Fibrosis PDAC cell line and is a metastatic cell line[51, 52] obtained from the liver. MiaPaca-2 is a Primary Pancreatic Adenocarcinoma cell line.[52]

Confocal images of Allophycocyanin (APC)-tagged MSLN-targeting antibody (FAB32652A) showed increased uptake in the CFPAC-1 cells compared to the MiaPaca-2 cells, confirming the qPCR results of higher expression of mesothelin in CFPAC-1 compared to MiaPaca-2 (Figure 4.11, Figure 4.12).

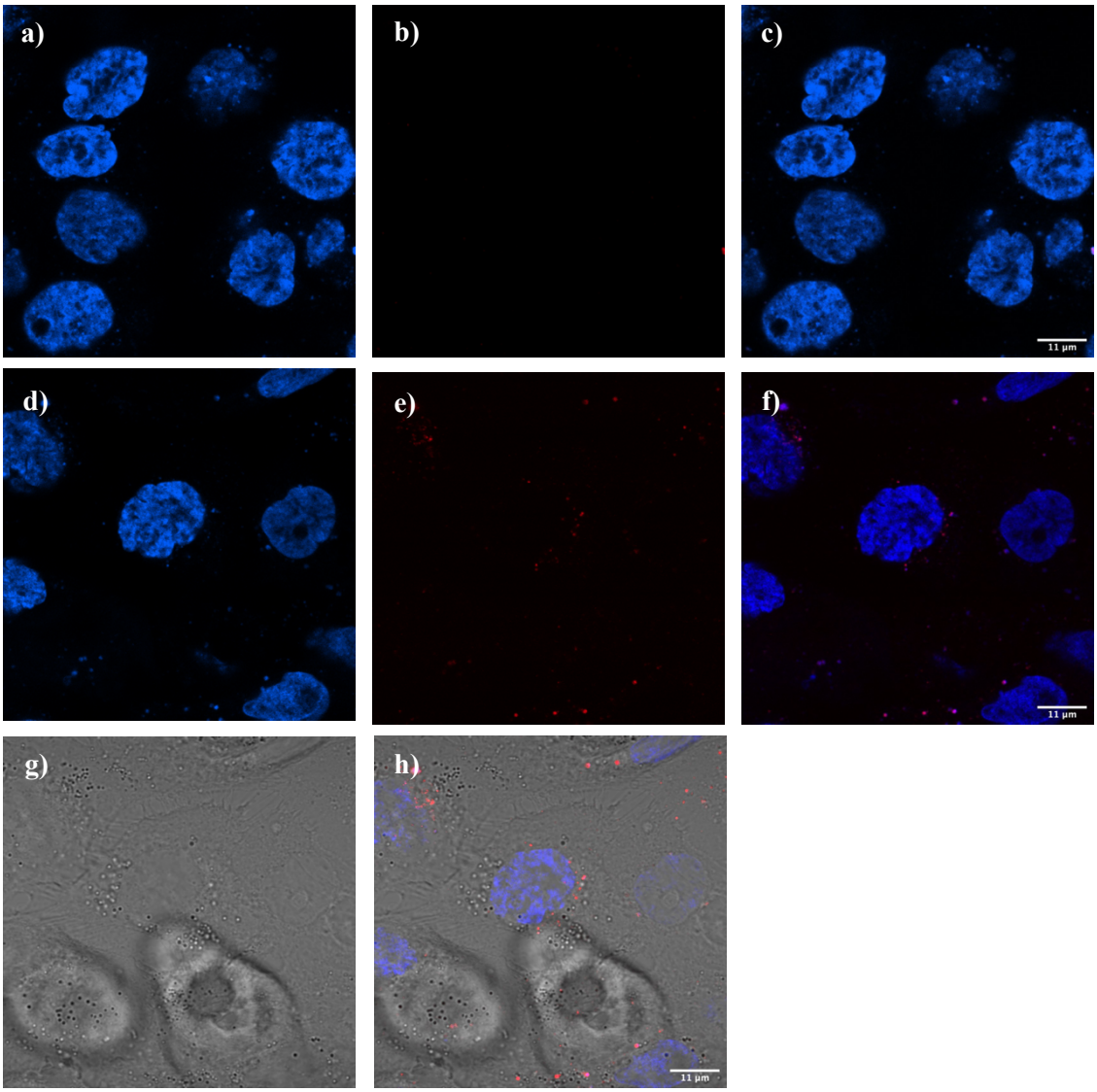


Figure 4.11. Confocal images at 5hr of fixed CFPAC-1 cells obtained from a Zeiss LSM900 microscope. ***a)*** *Hoechst staining of the nucleus in untreated cells,* λ_{exc} *= 405 nm,* λ_{em} *= 450 – 495 nm;* ***b)*** *APC-antibody red emission in untreated cells,* λ_{exc} *= 640 nm,* λ_{em} *= 600 – 700nm;* ***c)*** *overlay of* ***a)*** *and* ***b)****;* ***d)*** *Hoechst staining of the nucleus in APC-tagged antibody (10 µL)- treated cells,* λ_{exc} *= 405 nm,* λ_{em} *= 450 – 495 nm;* ***e)*** *APC-antibody red emission in APC-tagged antibody (10 µL)- treated cells,* λ_{exc} *= 640 nm,* λ_{em} *= 600 – 700nm;* ***f)*** *overlay of* ***d)*** *and* ***e)****;* ***g)*** *Transmitted light images of APC-tagged antibody (10 µL)- treated cells,* λ_{exc} *= 488 nm, ESID (Electronically switchable illumination and detection module);* ***h)*** *overlay of* ***f)*** *and* ***g)****.*

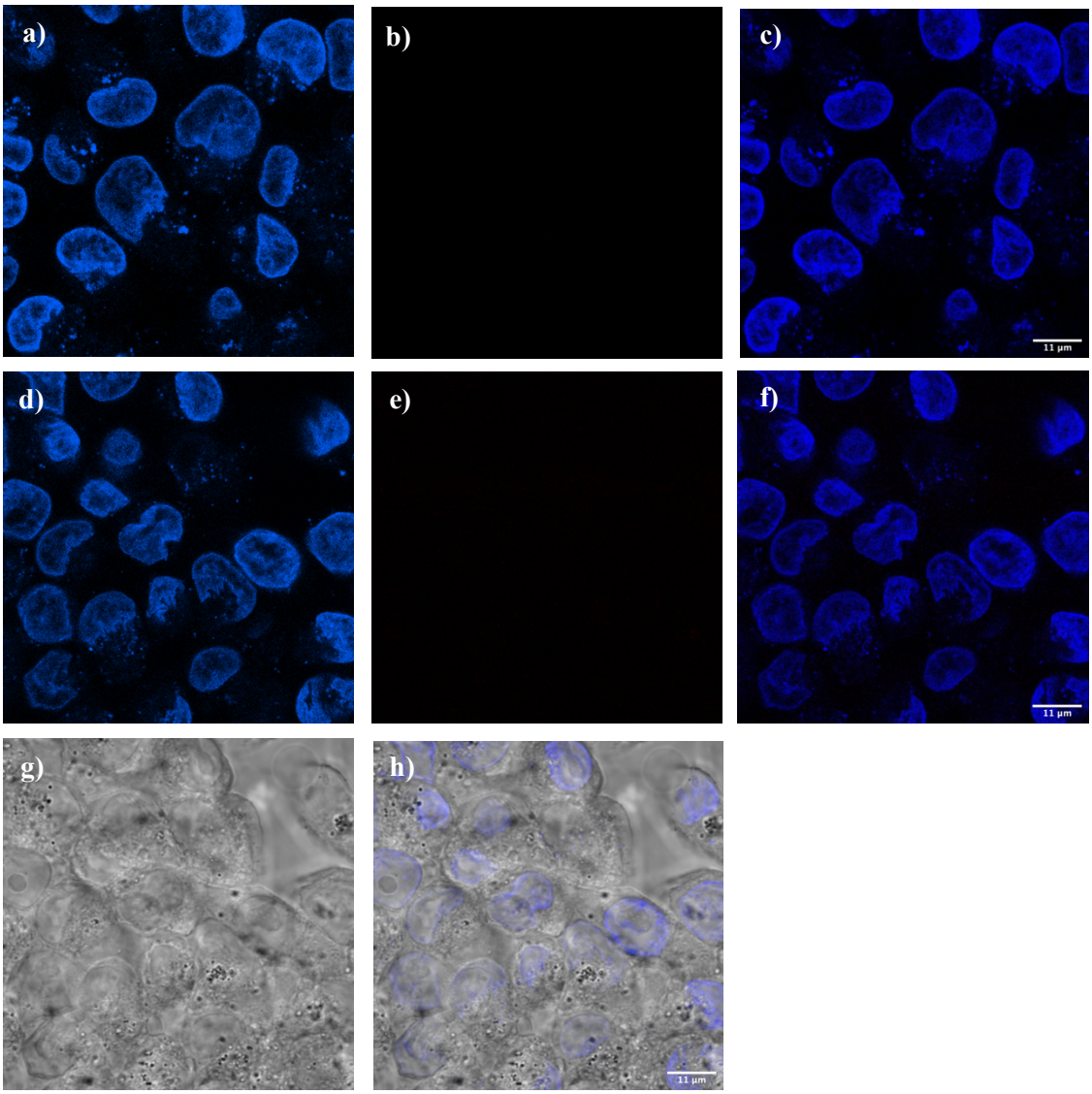


Figure 4.12. Confocal images at 5hr of fixed MiaPaca-2 cells obtained from a Zeiss LSM 900 microscope. ***a)*** *Hoechst staining of the nucleus in untreated cells,* λ_{exc} *= 405 nm,* λ_{em} *= 450 – 495 nm;* ***b)*** *APC-antibody red emission in untreated cells,* λ_{exc} *= 640 nm,* λ_{em} *= 600 – 700nm;* ***c)*** *overlay of* ***a)*** *and* ***b)****;* ***d)*** *Hoechst staining of the nucleus in APC-tagged antibody (10 µL)- treated cells,* λ_{exc} *= 405 nm,* λ_{em} *= 450 – 495 nm;* ***e)*** *APC-antibody red emission in APC-tagged antibody (10 µL)- treated cells,* λ_{exc} *= 640 nm,* λ_{em} *= 600 – 700nm;* ***f)*** *overlay of* ***d)*** *and* ***e)****;* ***g)*** *Transmitted light images of APC-tagged antibody (10 µL)- treated cells,* λ_{exc} *= 488 nm, ESID (Electronically switchable illumination and detection module);* ***h)*** *overlay of* ***f)*** *and* ***g)****.*

4.5 Uptake of AuNP19s in pancreatic cancer cells

4.5.1 Cell survival assays

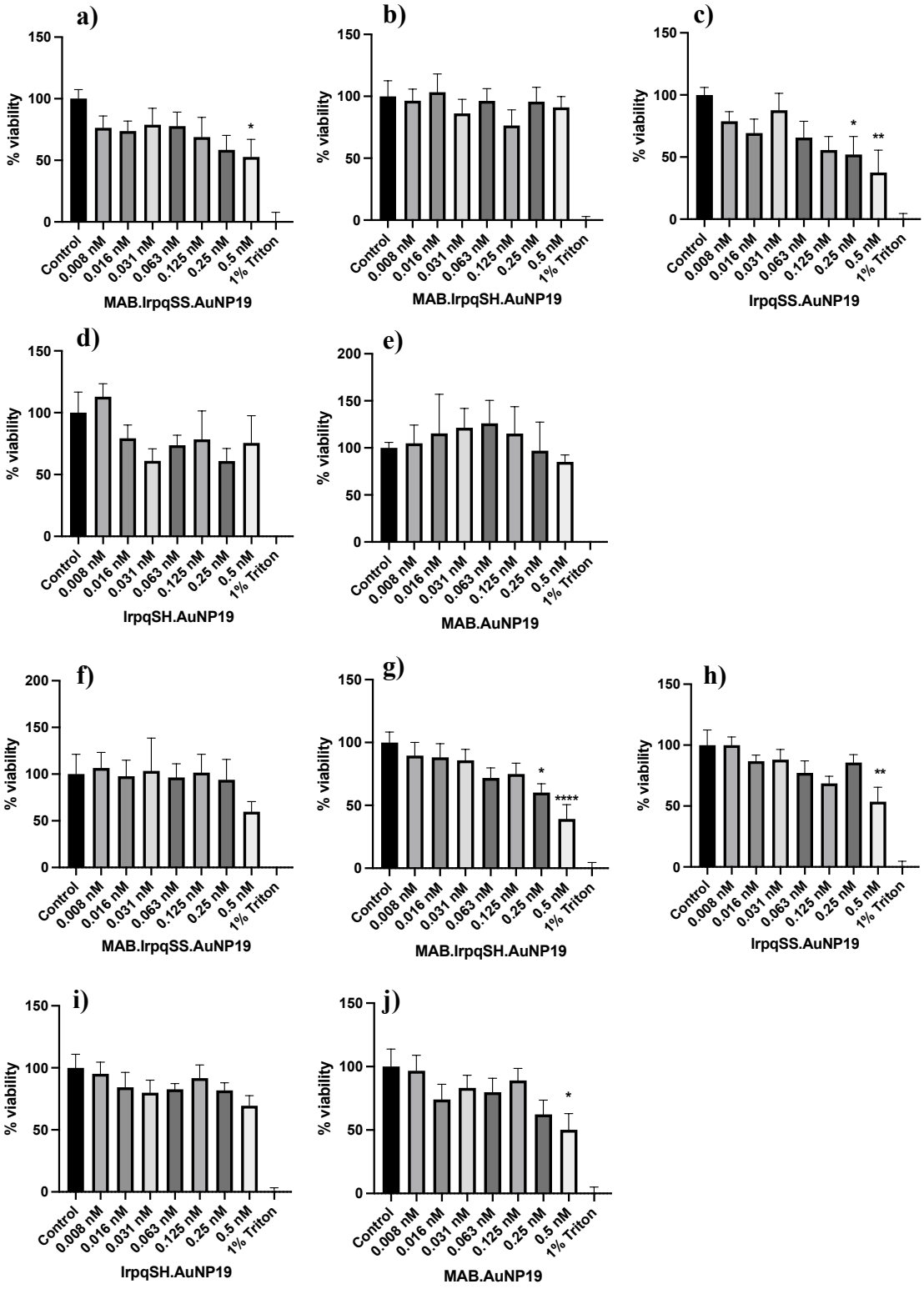


*Figure 4.13. MTT assays of the iridium-coated **AuNP19**s and **MAB**-coated **AuNP19**s. Mean of two experiments carried out in quintuplicates with untreated (control) cells and a 1% Triton positive controls. Samples were normalized to the 1% Triton signal. A maximum NP concentration of 0.5 nM was used in the CFPAC-1 cells (**a** – **e**) and the MiaPaca-2 (**f** - **j**) cells. P-value upper limits obtained from ANOVA analysis were represented by * = 0.0332, ** = 0.0021, *** = 0.002 and **** = 0.0001.*

MTT assays performed of the five AuNP samples showed that a concentration of 0.25 nM was a good concentration to use for comparative cell studies as a 0.5 nM concentration showed a statistically significant decreased in % cell viability from the untreated cells in two samples for CFPAC-1 and for three samples for MiaPaca-2. However, 0.25 nM was statistically different for only one sample in each cell line. To use a concentration that could be used to compare uptake across all samples with low toxicity and be seen under confocal, 0.25 nM was chosen (Supplementary Figure 4.4).

4.5.2 Confocal images

An AuNP concentration of 1 nM was at first used to test the luminescence in cells (Figure 4.14, Figure 4.15, Supplementary Figure 4.6, Supplementary Figure 4.7), due to a concentration of 0.25 nM determined by cell survival assays to be quite low compared to many studies performed before.[53] There was no visible damage to the cells at 1 nM under confocal. Quantification of the luminescence in the cells was performed with ImageJ by measuring the quantity of luminescent pixels in an image, and this was termed “average luminescence spots” (Figure 4.16). There was a statistically significant increase in brightness for MiaPaca-2 compared to CFPAC-1 for **MAB.IrpqSS.AuNP19** at 5 hr. However, there was no statistically significant difference in brightness for **MAB.IrpqSS.AuNP19** at 16 hr between cell lines, although in CFPAC-1 the luminescence was brighter. Between 5 hr and 16 hr there was a statistically significant increase in luminescence for the CFPAC-1 cells, however there was a decrease between 5 hr and 16 hr for the MiaPaca-2 cells.

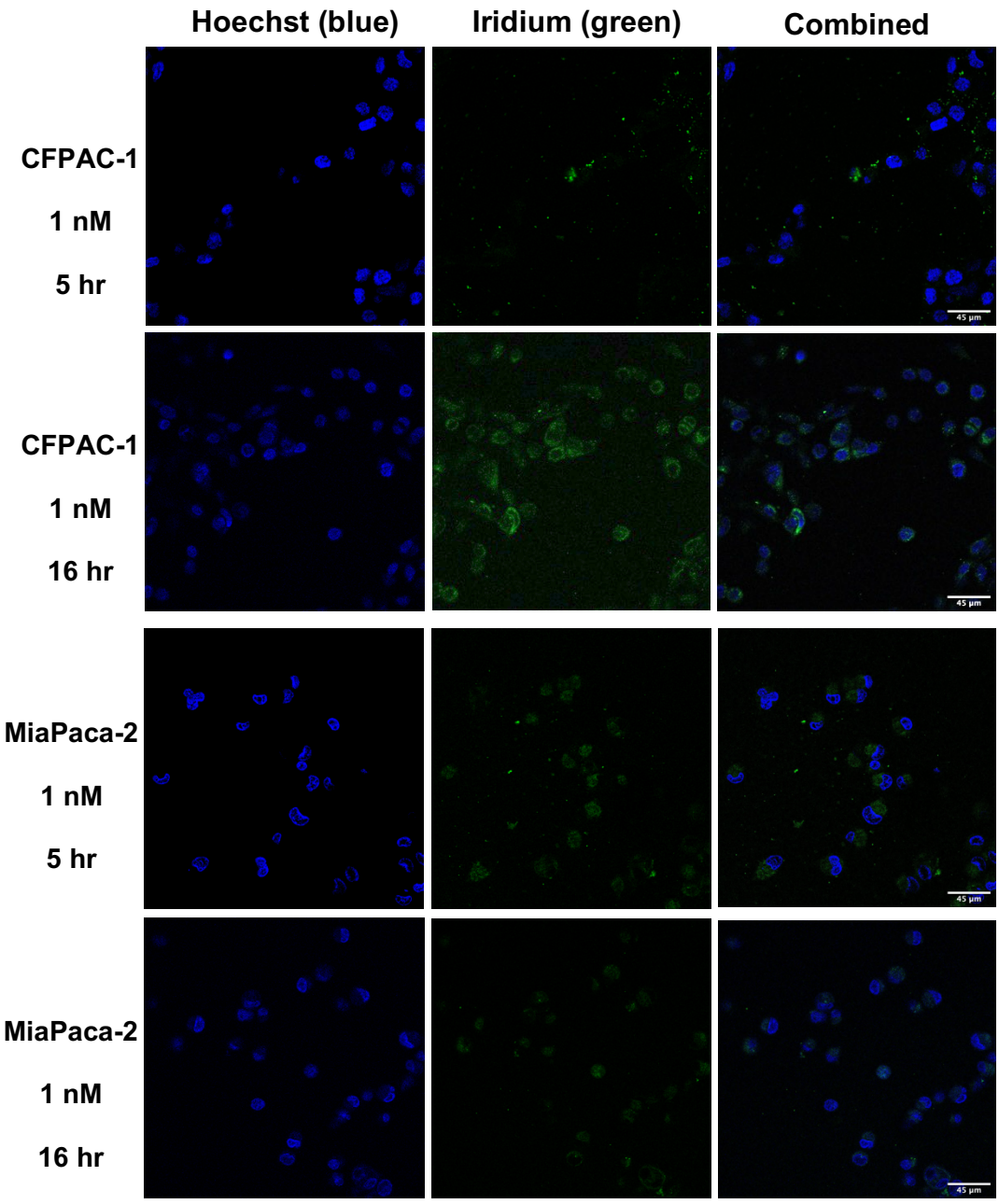


Figure 4.14. Confocal images of CFPAC-1 and MiaPaca-2 cells for ***MAB.IrpqSSAuNP19*** *at 1 nM on a Leica sp8 upright microscope using a 40x ceramic water dipping objective lens. Hoechst (blue) settings:* λ_{exc} *= 402,* λ_{em} *= 419 – 472 nm; Iridium(green):* λ_{exc} *= 458 nm,* λ_{em} *= 550 – 750 nm.*

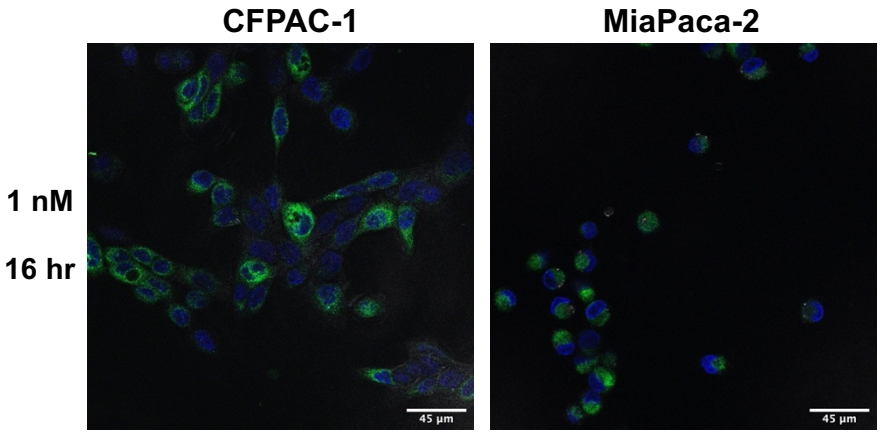


*Figure 4.15. Confocal images for **MAB.IrpqSH.AuNP19** at 1 nM on a Leica sp8 upright microscope using a 40x ceramic water dipping objective lens. Hoechst (blue) settings: λ_{exc} = 402, λ_{em} = 419 – 472 nm; Iridium(green): λ_{exc} = 458 nm, λ_{em} = 550 – 750 nm; Reflectance (grey): λ_{exc} = 633 nm, λ_{em} = 628 – 638 nm.*

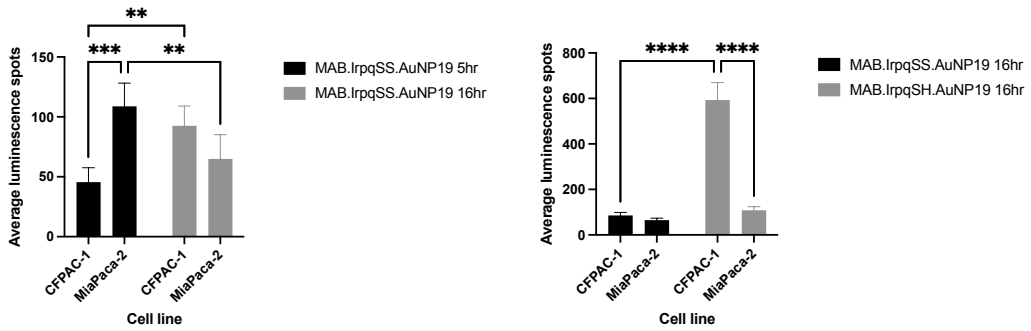


*Figure 4.16. Quantification of luminescence spots in cells obtained from confocal images, with an average of five cells measured for each sample. Results were analyzed using ANOVA to determine statistical significance, where the p-value upper limits obtained were represented by * = 0.0332, ** = 0.0021, *** = 0.002 and **** = 0.0001.*

The greater increase in luminescence for CFPAC-1 incubated with **MAB.IrpqSS.AuNP19** compared to MiaPaca-2 between 5 hr and 16 hr was expected due to the increased MSLN content in CFPAC-1 cells. However, the increased luminescence in MiaPaca-2 compared to CFPAC-1 at 5hr is most likely due to what was seen in Chapter 3, Section 3.4, where MiaPaca-2 cells have greater uptake of nanoparticles in general. Therefore, although the antibody may be targeting the Mesothelin receptor in CFPAC-1 at this timepoint, the faster uptake of MiaPaca-2 is seen here – more so than the targeting of the Mesothelin receptor.

There was a statistically significant increase in luminescence for CFPAC-1 compared to MiaPaca-2 at 16 hr for **MAB.IrpqSH.AuNP19** (Figure 4.15, Figure 4.16). The luminescence for **MAB.IrpqSH.AuNP19** was also statistically greater than **MAB.IrpqSS.AuNP19** in CFPAC-1 even though ICP-MS uptake studies (Section 4.5.4) showed that the uptake of the **MAB.IrpqSH.AuNP19** was not greater than that of **MAB.IrpqSS.AuNP19**. Since **IrpqSH**-coated AuNPs showed a much weaker luminescence in H_2O when characterised (Section 4.3), this was an interesting result, requiring further investigation, as in Chapter 3, Section 3.4.2, where the **IrpqSH**-coated **AuNP13**s also showed brighter than expected luminescence in the cells. Hence, a luminescence enhancement effect can also be seen for **IrpqSH**-coated AuNP19s as well (Section 4.5.7).

Images of the AuNP luminescence in cells under a Zeiss LSM900 confocal with a laser excitation of 488 nm were also collected due to unavailability of the Leica sp8 confocal microscope. Due to the excitation wavelength of the laser not being at the peak of the absorbance band for the iridium(III) complexes, the amount of light absorbed was reduced, however fluorescence were still seen at 1 nM (Supplementary Figure 4.8, Supplementary Figure 4.9, Supplementary Figure 4.10, Supplementary Figure 4.11) and 0.25 nM (Supplementary Figure 4.12, Supplementary Figure 4.13).

4.5.3 Flow Cytometry

Luminescence of cells was measured using flow cytometry at 16 hr with a 0.25 nM AuNP concentration (Figure 4.17, Supplementary Figure 4.14, Supplementary Figure 4.15), as this timepoint was the

timepoint that showed greater luminescence in CFPAC-1 cells for **MAB.IrpqSS.AuNP19** and **MAB.IrpqSH.AuNP19** in confocal at 1 nM incubation concentration, as expected due to the overexpression of mesothelin in CFPAC-1 compared to MiaPaca-2. The 0.25 nM concentration was also the best concentration for cell viability (Section 4.5.1). There was a statistically significant increase in luminescence intensity between CFPAC-1 and MiaPaca-2 for the four iridium-coated nanoparticles, which matched the data collected in Chapter 3, Section 3.4, where it was shown that MiaPaca-2 has a greater uptake of AuNPs compared to CFPAC-1 in general. The confocal images (Section 4.5.2) show that the CFPAC-1 cells have brighter luminescence at 16 hr than MiaPaca-2 for both **MAB.IrpqSS.AuNP19** and **MAB.IrpqSH.AuNP19**, however these results are not seen in flow cytometry. This could be due to a few reasons:

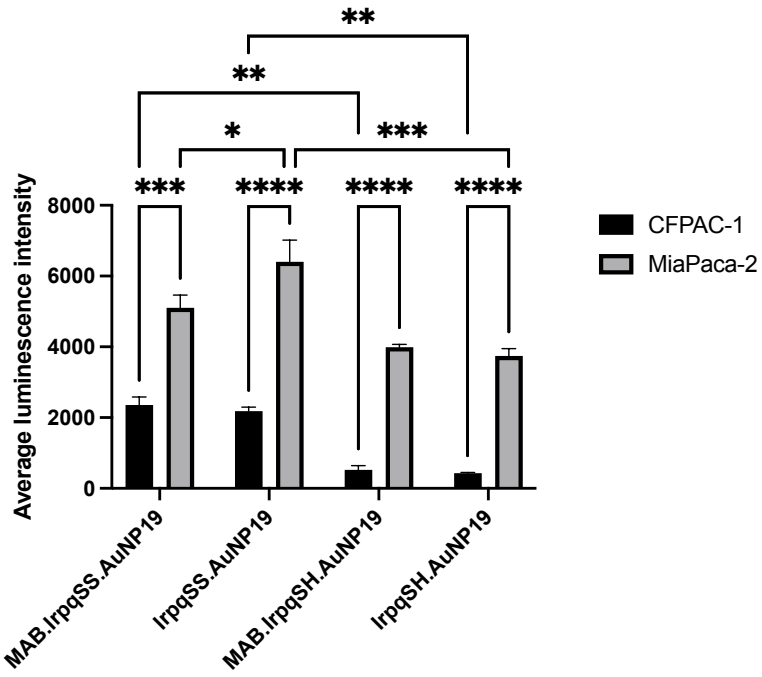


*Figure 4.17. Average fluorescence intensities from flow cytometry in CFPAC-1 and MiaPaca-2, where autofluorescence from the untreated cells was zeroed. Results were analyzed using ANOVA to determine statistical significance, where the p-value upper limits obtained were represented by * = 0.0332, ** = 0.0021, *** = 0.002 and **** = 0.0001.*

The first reason could be that the luminescence quantification of the confocal images was performed with nanoparticle incubation concentrations of 1 nM, whereas flow cytometry was performed with nanoparticle incubation concentrations of 0.25 nM. Studies have shown that antibody affinity/avidity is dependent on antibody concentration[54, 55], therefore the concentration of 0.25 nM used for the flow cytometry studies may not be the best concentration to see an antibody-binding effect.

The second reason could be due to confocal microscopy and flow cytometry being different techniques. Flow cytometry required trypsinization of the cells and centrifugation in the sample preparation method (Section 4.8.10), whereas confocal microscopy did not require this (Section 4.8.8). If the **MAB**-coated nanoparticles were targeting the cell membrane in CFPAC-1, but had not yet internalised, trypsinization would detach the cells from their surface during the cell detachment process and the centrifugation process would remove the nanoparticles them from the cell membrane, as antibody-antigen bonds are non-covalent and therefore reversible.[56] Therefore, any AuNPs bound to the membrane of cells and not internalised could be seen under confocal but are detached during trypsinization and centrifugation in flow cytometry, and they are not seen in the flow cytometry results. Further explanations as to why the different techniques result in different outcomes for the different samples will be explained in Section 4.5.4 and 4.5.5. Although the TrypLE step used in the flow cytometry sample preparation is gentler than using the Trypsin enzyme, TrypLE cleaves peptides like Trypsin does[57, 58] and can therefore cleave the antibody-antigen bonds, detaching any bound antibodies from the cell surface. Whether this was the case has not been studied in depth in this thesis but is a possible cause in the discrepancy between the confocal images and flow cytometry data.

4.5.4 ICP-MS gold quantification

The uptake of the AuNPs at 0.25 nM was quantified by measuring the gold content in both cell lines (Table 4.5, Figure 4.18). An ICP-MS calibration curve (Supplementary Figure 4.16) with $R^2 = 0.997$ did not show good fitting at low gold contents (< 100ppb). Hence, these ICP-MS results carry an error. However, as these samples were prepared on the same day with the same pipettes and analysed on the

same ICP-MS machine, the result obtained will be outlined in order that AuNP uptake can be discussed (Section 4.7).

Cell line	Sample	Average AuNPs per cell
CFPAC-1	**MAB.IrpqSS.AuNP19**	1055
	MAB.IrpqSH.AuNP19	205
	IrpqSS.AuNP19	188
	IrpqSH.AuNP19	181
MiaPaca-2	**MAB.IrpqSS.AuNP19**	2122
	MAB.IrpqSH.AuNP19	227
	IrpqSS.AuNP19	2316
	IrpqSH.AuNP19	103

Table 4.5. Table of ICP-MS average AuNP uptake values from the gold content in CFPAC-1 and MiaPaca-2 cells using an AuNP19 size of 19 nm NPs for calculating the AuNP uptake when cells were incubated with 0.25 nM of ***MAB.IrpqSS.AuNP19****,* ***MAB.IrpqSH.AuNP19****,* ***IrpqSS.AuNP19*** *and* ***IrpqSH.AuNP19****.*

The uptake of the **MAB**-coated AuNPs was greater in MiaPaca-2 compared to CFPAC-1 when comparing averages alone, however only **IrpqSS.AuNP19** had a statistically significant increase in uptake in MiaPaca-2 compared to CFPAC-1. This average increase in AuNP uptake between MiaPaca-2 and CFPAC-1 can explain the increased luminescence in flow cytometry in MiaPaca-2 cells compared to CFPAC-1, and is also seen in Chapter 3, Section 3.4, for the **AuNP13**s.

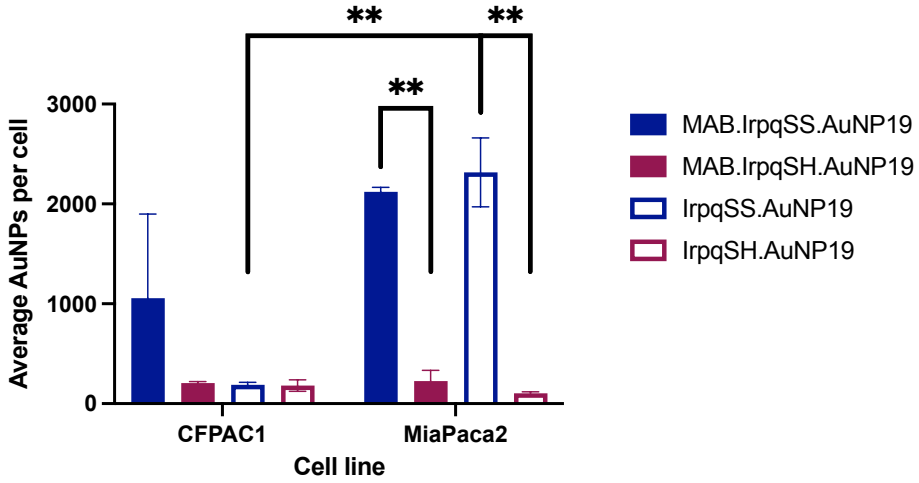


*Figure 4.18. Average AuNP uptake per cell obtained from ICP-MS gold content for MiaPaca-2 and CFPAC-1. The difference in uptakes was analyzed using ANOVA to determine statistical significance, where the p-value upper limits obtained were represented by * = 0.0332, ** = 0.0021, *** = 0.002 and **** = 0.0001.*

In CFPAC-1, none of the samples had statistically significant uptake compared to the others, showing that the presence of **MAB** at the surface is not affecting uptake for this cell line, despite CFPAC-1 overexpressing Mesothelin. The lack of significant difference in uptake between the **MAB**-coated AuNPs and the ones without **MAB** in CFPAC-1 can be explained like in Section 4.5.3. ICP-MS is like flow cytometry in the sense that they are techniques that require a cell suspension, so detachment of the cells was performed by TrypLE (Section 4.8.11). Therefore, any AuNP samples attached to the cell membrane would be detached as in flow cytometry, resulting in lower gold content in the CFPAC-1 cells incubated with **MAB**-coated AuNPs. This would explain the lower uptake seen in ICP-MS for **MAB.IrpqSS.AuNP19** and **MAB.IrpqSH.AuNP19** compared to MiaPaca-2. In Section 4.5.5, the localisation of the AuNP samples in the two PDAC cell lines will be shown and discussed to further explain this point.

In MiaPaca-2, the **MAB**-coated AuNPs did not have a statistically significant increase in uptake compared to the ones without **MAB**, as expected due to the low MSLN content of the cells, however **MAB.IrpqSS.AuNP19** and **IrpqSS.AuNP19** had an increased in uptake compared to their **IrpqSH**-

coated counterparts. This shows that the iridium(III) complex influences the uptake mechanism of the nanoparticles in MiaPaca-2 cell lines, as **IrpqSS** and **IrpqSH** have different chain lengths (long and short respectively). The uptake of the **IrpqSH**-coated **AuNP19**s in MiaPaca-2 was significantly lower compared to the **IrpqSS**-coated AuNPs (Figure 4.18), however comparably bright luminescence was seen under confocal (Figure 4.15, Figure 4.16), even though **IrpqSH** has a lower quantum yield than **IrpqSS**. Hence the luminescence enhancement effect mentioned previously and in Chapter 3, Section 3.4.6, is shown further by these ICP-MS values. In Section 4.5.7, the luminescence enhancement will be discussed. The TEM sizes for the **AuNP19**s was 18.5 ± 1.2 nm, hence with the error in the AuNP size would give an **MAB.IrpqSS.AuNP19** uptake in CFPAC-1 of between 947 to 11,241 particles and between 1907 to 2813 particles in MiaPaca-2. The **MAB.IrpqSH.AuNP19** uptake in CFPAC-1 was between 184 to 271 particles and between 204 to 301 particles in MiaPaca-2. The **IrpqSS.AuNP19** uptake in CFPAC-1 was between 169 to 249 particles and between 2081 to 3069 particles in MiaPaca-2. The **IrpqSH.AuNP19** uptake in CFPAC-1 was between 163 to 240 particles and between 93 to 137 particles in MiaPaca-2.

4.5.5 TEM localisation of gold nanoparticles

As outlined in Chapter 3, Section 3.1.3, TEM can be used as initial studies to identify the location of particles in sub-cellular organelles. The nucleus, mitochondria, lysosomes, Golgi apparatus, autophagic vacuoles, lamellar bodies and endoplasmic reticulum can be identified by TEM. Identification of these sub-cellular organelles provides a basis for further studies such as fractionation or staining cells for co-localisation of luminescence in confocal. Hence, these TEM images shown are the initial studies that indicate possible location in the organelles identified. The nucleus was the largest organelle, and easy to identify. The mitochondria were identified by finger-like membranes within the organelle. Lysosomes were round structures mainly ~500 nm or less in size. The Golgi apparatus was curved in shape. Autophagic vacuoles were identified by their distorted shape and appearance of fusion of multiple organelles together. The lamellar bodies had multiple membranes – one within the other, and the endoplasmic reticulum was identified by finger-like structures present around the nucleus.

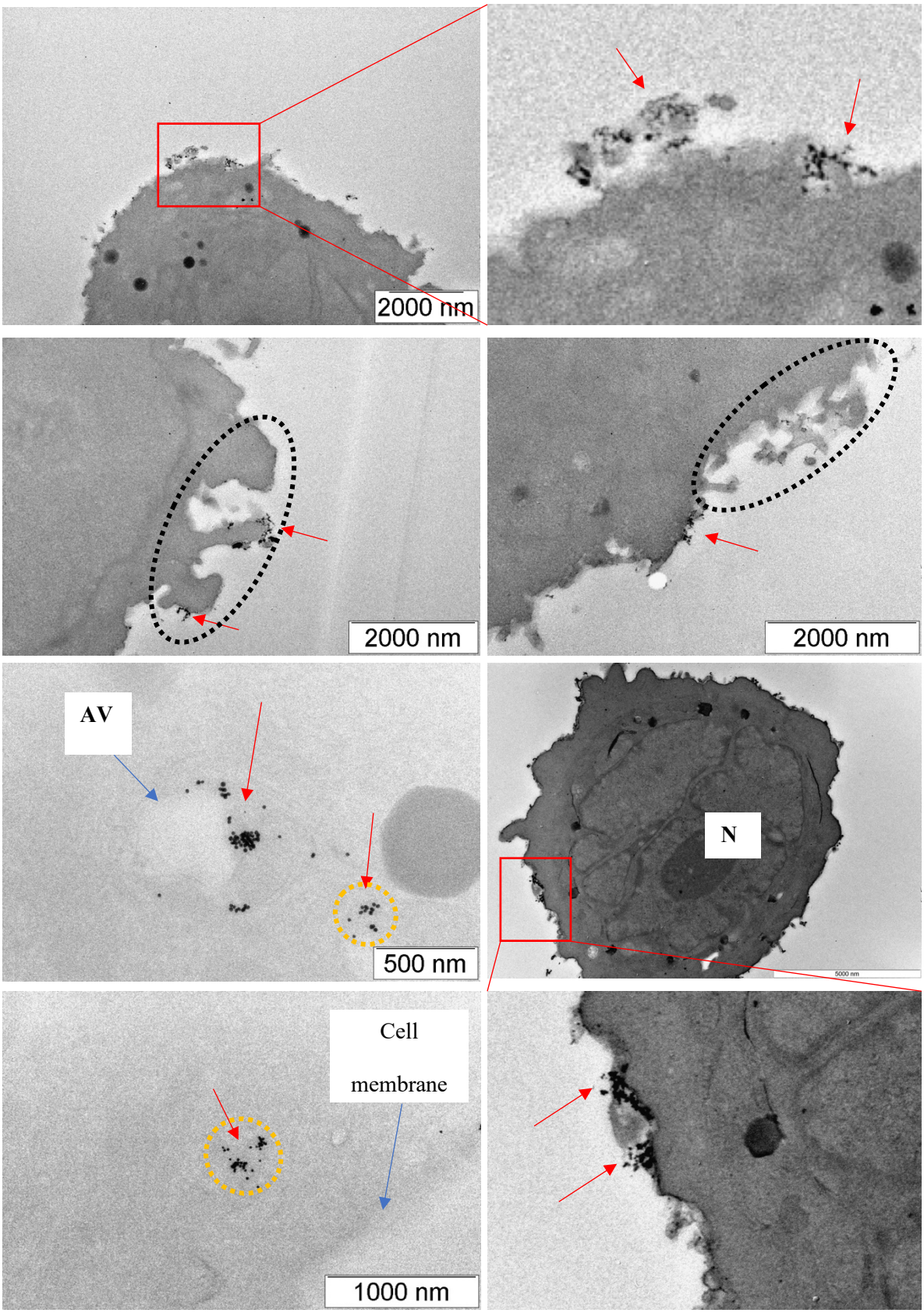


*Figure 4.19. TEM images of CFPAC-1 cells incubated with 0.25 nM of **MAB.IrpqSS.AuNP19**s for 16 hr. Red arrows show the location of **AuNP**s in the cells, with the red boxes showing the magnification in the cells, **AV** indicating autophagic vacuoles and **N** indicating the nucleus. Black dotted lines represent ruffled membranes and yellow dotted lines represent poorly defined endosomal membranes.*

The TEM images for **MAB.IrpqSS.AuNP19** in CFPAC-1 at 16 hr showed that they are located mainly on the membrane of the cells, although internalisation did occur (Figure 4.19). Protrusions from the cell membrane indicated some uptake due to micropinocytosis or another active endocytosis method[53]. The slow uptake at 16 hr for the particles bound to the membrane could be due to slow internalisation of MSLN into vesicles, probably through endocytosis that has been previously shown[59, 60], as little uptake at 6 hr was seen in previous studies with MSLN-targeting antibodies. No particles were seen in the nucleus. In MiaPaca-2, the **MAB.IrpqSS.AuNP19** was not found on the membrane of the cells but was internalised into the cytoplasm of the cells (Figure 4.20). This shows that the **MAB.IrpqSS.AuNP19**s were not targeting the mesothelin surface protein as in CFPAC-1, and were mainly taken up using another method of internalisation, otherwise the particles would have also been localised on the membrane of the cells as in CFPAC-1. **MAB.IrpqSS.AuNP19** were mostly located in the darker round sub-cellular components in the TEM images, most likely lysosomes. No particles were seen in the nucleus.

IrpqSS.AuNP19 in CFPAC-1 were in possible endosomal compartments with poorly defined membranes[53] (Figure 4.21). No particles were seen in the nucleus. Larger darker vacuoles in the cell did not contain these particles, showing that the uptake of these particles may be specific to the endosomal compartments. In MiaPaca-2, **IrpqSS.AuNP19** was found mainly in multi-membrane sub-cellular organelles (Figure 4.22) which could be lamellar bodies. Particles were also found in possible lysosomes and autophagic vacuoles. The different localisation of the particles in the two cell lines indicate different methods of uptake between the two cell lines. No particles were seen in the nucleus.

A few particles of **MAB.IrpqSH.AuNP19** were found on the membrane of the CFPAC-1 cells (Figure 4.23), though not as many as for **MAB.IrpqSS.AuNP19**. This shows that the iridium(III) complex may play a role in the uptake of the AuNPs, as ICP-MS also showed decreased uptake (though not significant) in CFPAC-1 for **MAB.IrpqSH.AuNP19** compared to **MAB.IrpqSS.AuNP19**, and also decreased uptake (significant) in MiaPaca-2 of **MAB.IrpqSH.AuNP19** compared to **MAB.IrpqSS.AuNP19** (Figure 4.18). Membrane ruffling was seen in the CFPAC-1 cells indicating

possible micropinocytosis or other active endocytosis method. Some particles were also located in endosomes with poorly defined membranes. **MAB.IrpqSH.AuNP19** in MiaPaca-2 were found in possible lysosomes, lamella bodies and autophagic vacuoles (Figure 4.24). No particles were seen in the nucleus.

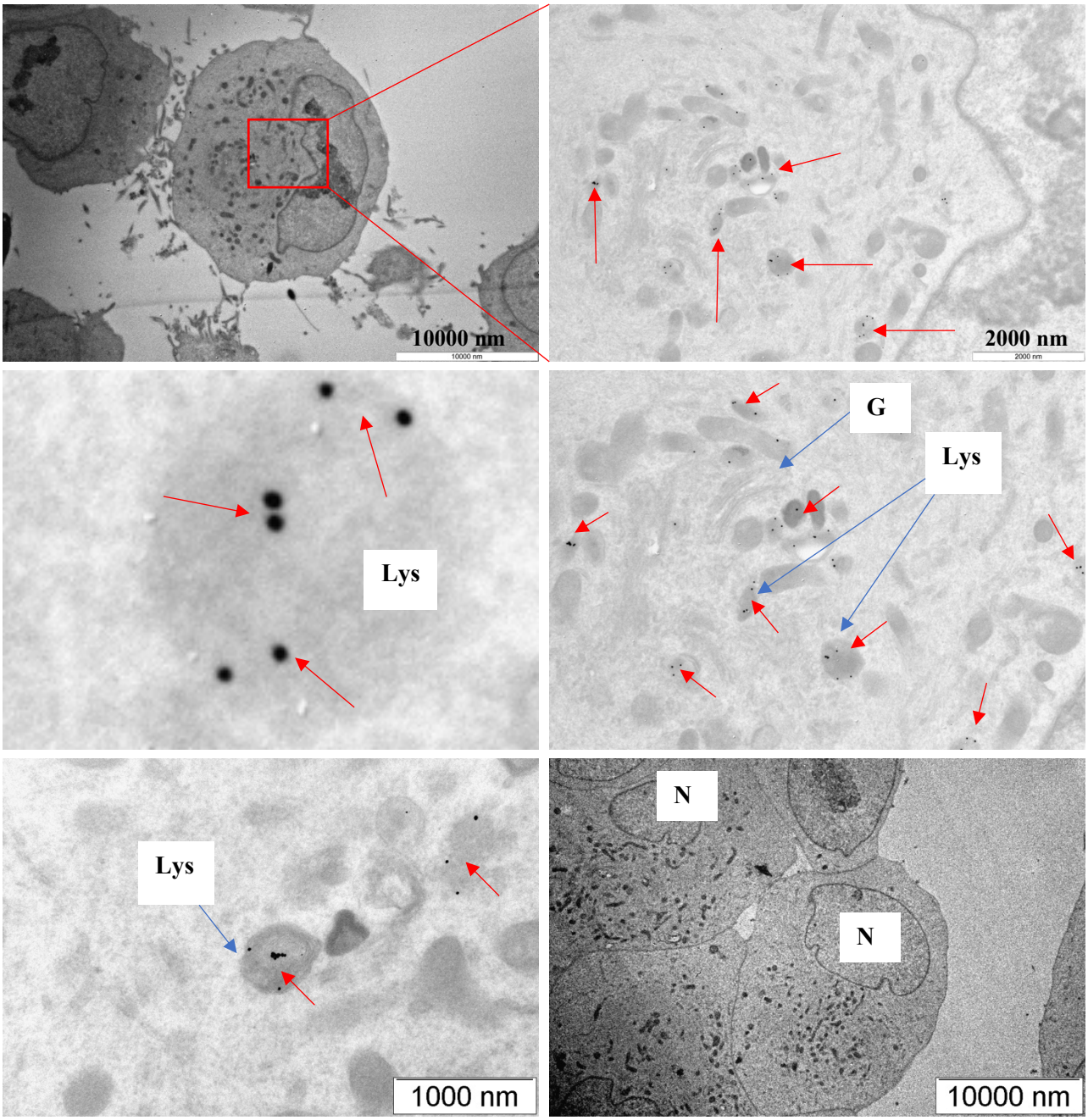


*Figure 4.20. TEM images of MiaPaca-2 cells incubated with 0.25 nM of **MAB.IrpqSS.AuNP19**s for 16 hr. Red arrows show the location of **AuNP**s in the cells, with the red boxes showing the magnification in the cells, **Lys** indicating the lysosomes, **G** indicating the Golgi apparatus and **N** indicating the nucleus.*

In CFPAC-1 **IrpqSH.AuNP19** were in possible autophagic vacuoles and endosomal compartments with weak membranes. In MiaPac-2, **IrpqSH.AuNP19** were in possible lysosomes, autophagic vacuoles and mitochondria. No particles were seen in the nucleus.

From all the TEM results, most particles were in possible lysosomes in MiaPaca-2 cells, whereas in CFPAC-1 they were located mainly in possible endosomal compartments or on the cell membrane for the **MAB**-coated AuNPs. In addition, conformational changes of the cell membrane due to micropinocytosis or other active endocytosis methods were seen in CFPAC-1. In the micropinocytosis process, which is a unique from of endocytosis[61], the particles are transported in endocytic compartments, so this could explain the location of the particles in CFPAC-1 seen in TEM. Membrane ruffling was not predominantly seen in the MiaPaca-2 cells, indicating that micropinocytosis was not the primary method of particle uptake[62, 63]. Due to the low levels of MSLN on the surface of the cells, antibody-mediated uptake would have been very low and so passive uptake and translocation or another endocytosis method would be the most likely method of uptake for the MiaPaca-2 cells. So, the particles in MiaPaca-2 were seen mainly in possible lysosomes.

The TEM results have shown why the confocal images, flow cytometry and ICP-MS show the results that they do. Flow cytometry and ICP-MS involve detachment of cells by trypsinization to form a cell suspension. The trypsin enzyme would dislodge the AuNPs on the cell membrane by breaking the peptide bonds and non-covalent interactions, causing the results in flow cytometry and ICP-MS to be lower than expected for the **MAB**-coated AuNPs in CFPAC-1. This would explain the increased uptake in MiaPaca-2 compared for CFPAC-1 in ICP-MS and flow cytometry. ICP-MS and flow cytometry are not able to give us information as to the targeting of the mesothelin, since mesothelin is a surface protein with slow internalisation, as has been shown in previous studies. As seen from the TEM images, **MAB.IrpqSS.AuNP19** and **MAB.IrpqSH.AuNP19** are located mainly at the surface of the cells in CFPAC-1, whereas in MiaPaca-2, the AuNPs are internalised well and are located within the cytoplasm. It may be that the low MSLN-expressing cell line MiaPaca-2 is the wrong cell line for this study, as it

takes up nanoparticles at a faster rate than the higher MSLN-expressing cell CFPAC-1 (Chapter 3, Section 3.4), so this could be competing with the antibody targeting.

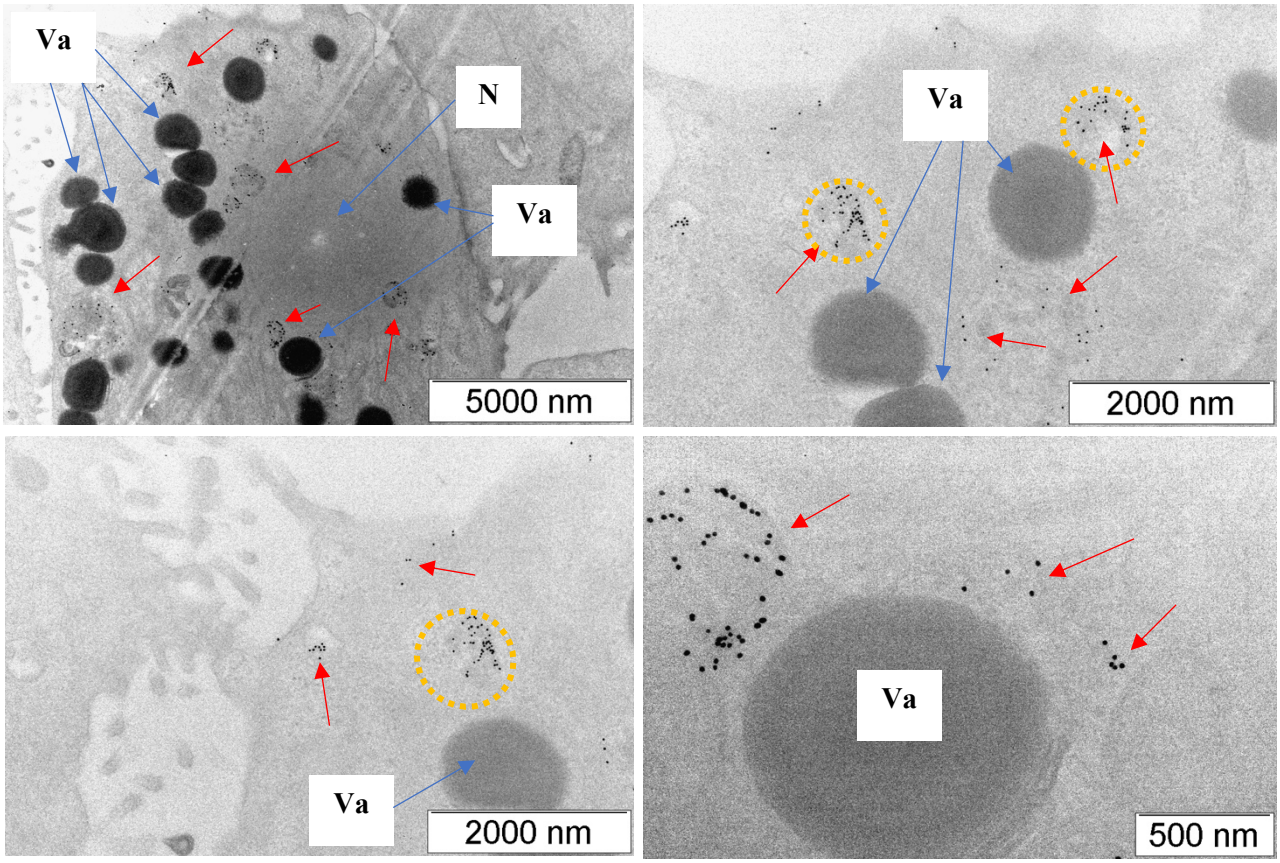


*Figure 4.21. TEM images of CFPAC-1 cells incubated with 0.25 nM of **IrpqSS.AuNP19**s for 16 hr. Red arrows show the location of **AuNP**s in the cells, with **Va** indicating the vacuoles and **N** indicating the nucleus. Yellow dotted lines represent poorly defined endosomal membranes.*

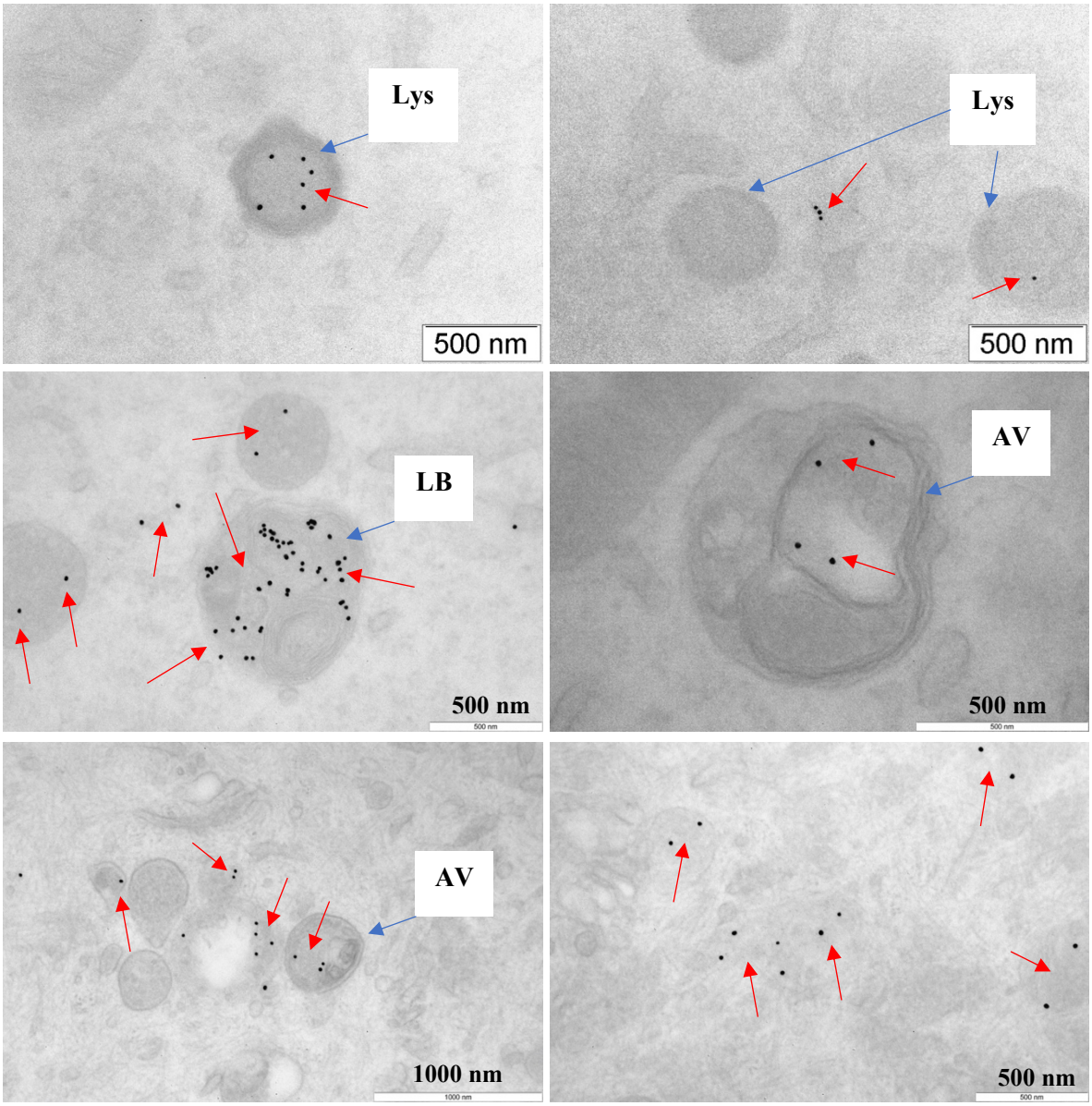


*Figure 4.22. TEM images of MiaPaca-2 cells incubated with 0.25 nM of **IrpqSS.AuNP19**s for 16 hr. Red arrows show the location of **AuNP**s in the cells, with **LB** indicating the lamella bodies and **AV** indicating autophagic vacuoles.*

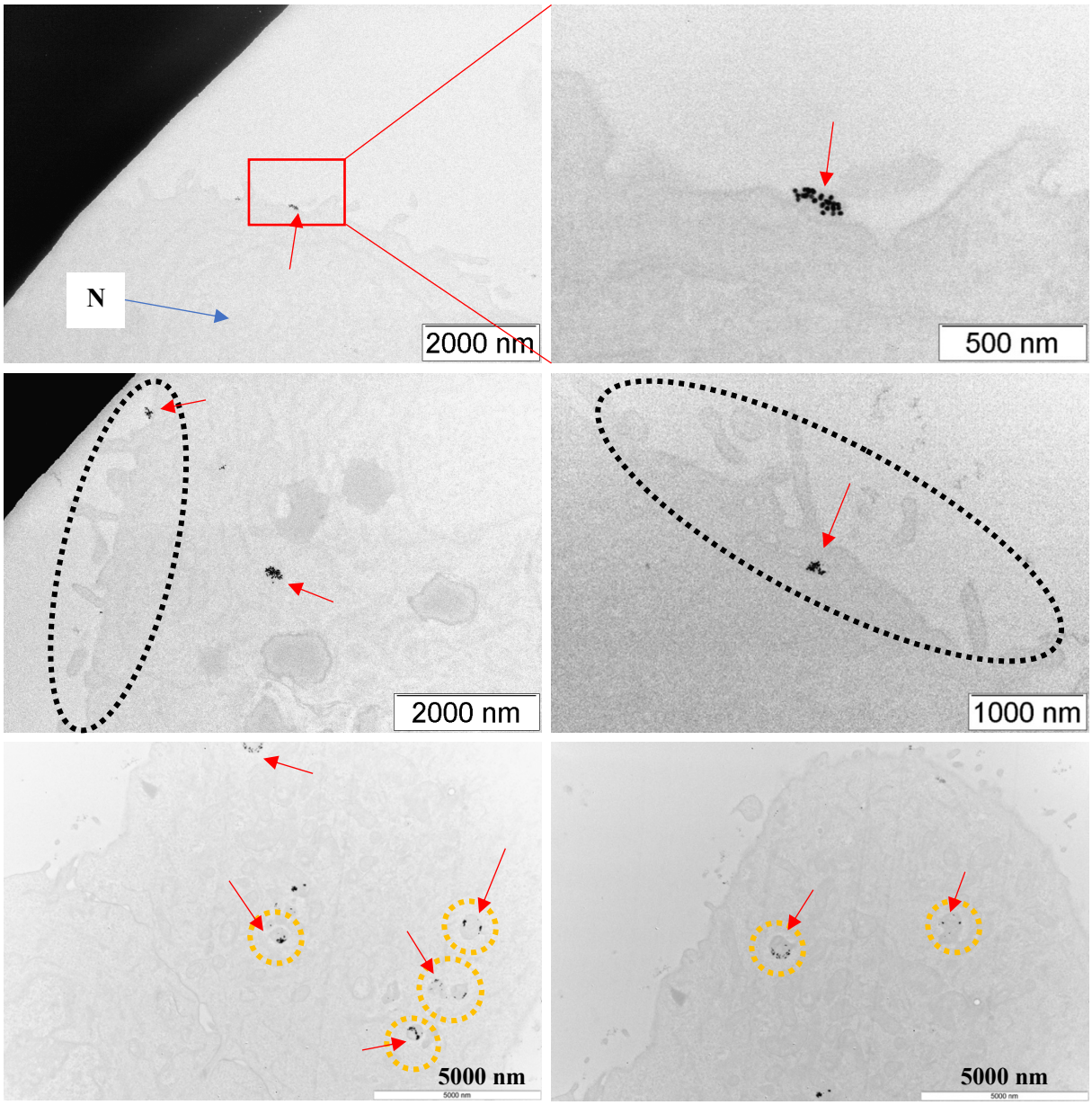


*Figure 4.23. TEM images of CFPAC-1 cells incubated with 0.25 nM of **MAB.IrpqSH.AuNP19**s for 16 hr. Red arrows show the location of **AuNP**s in the cells, with **N** indicating the nucleus. Black dotted lines represent ruffled membranes and yellow dotted lines represent poorly defined endosomal membranes.*

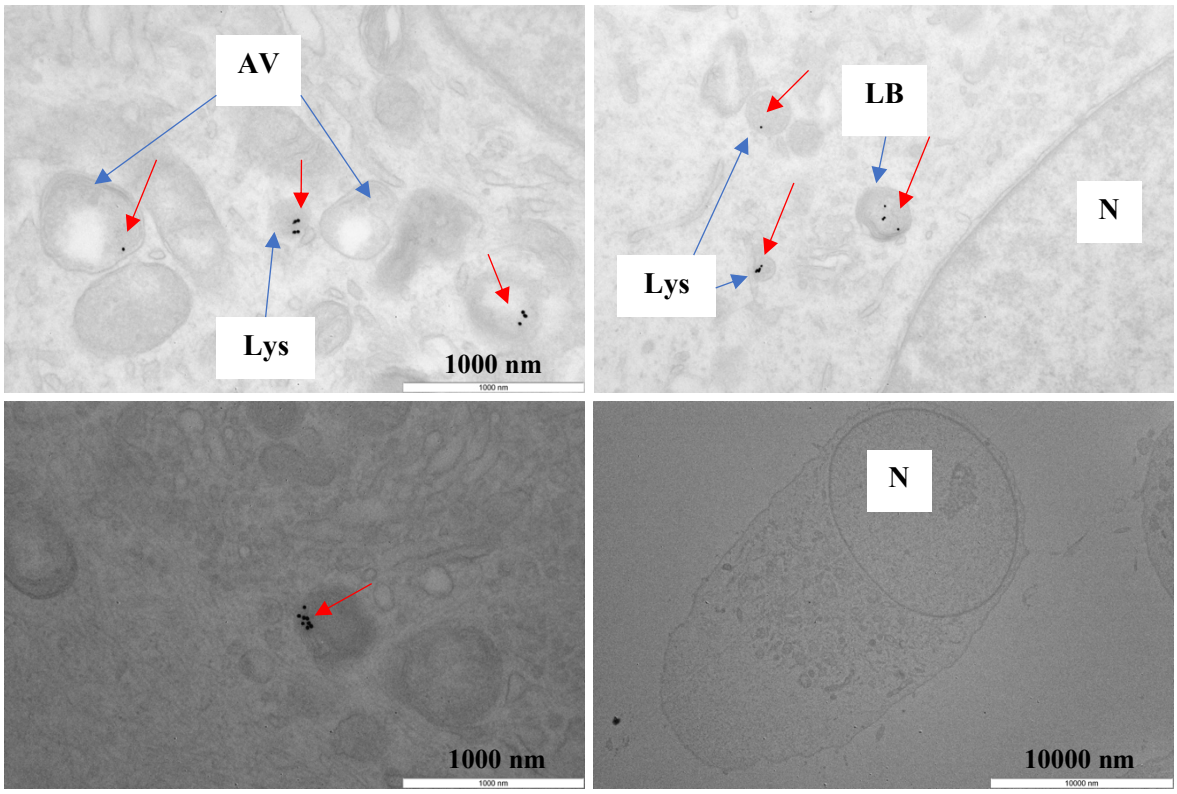


*Figure 4.24. TEM images of MiaPaca-2 cells incubated with 0.25 nM of **MAB.IrpqSH.AuNP19**s for 16 hr. Red arrows show the location of **AuNP**s in the cells, with **LB** indicating the lamella bodies, **Lys** indicating the lysosomes, **AV** indicating the autophagic vacuoles and **N** indicating the nucleus.*

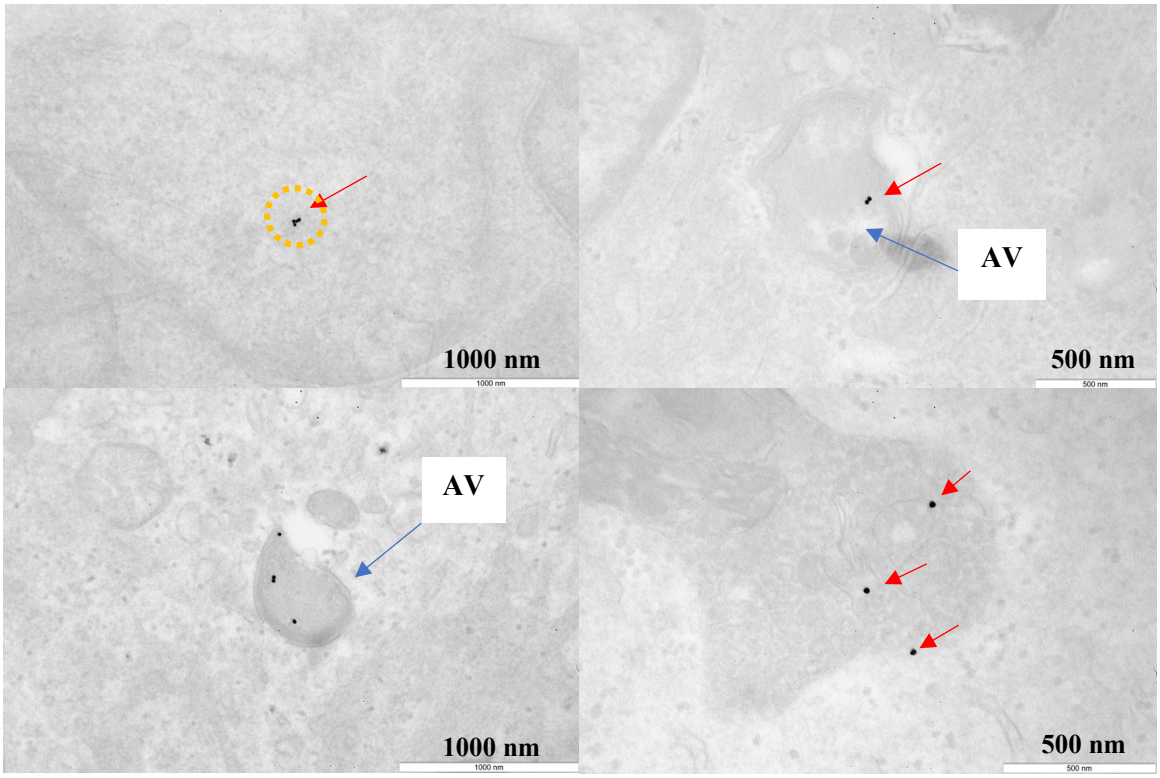


*Figure 4.25. TEM images of CFPAC-1 cells incubated with 0.25 nM of **IrpqSH.AuNP19**s for 16 hr. Red arrows show the location of **AuNP**s in the cells, with **AV** indicating the autophagic vacuoles and **N** indicating the nucleus. Yellow dotted lines represent poorly defined endosomal membranes.*

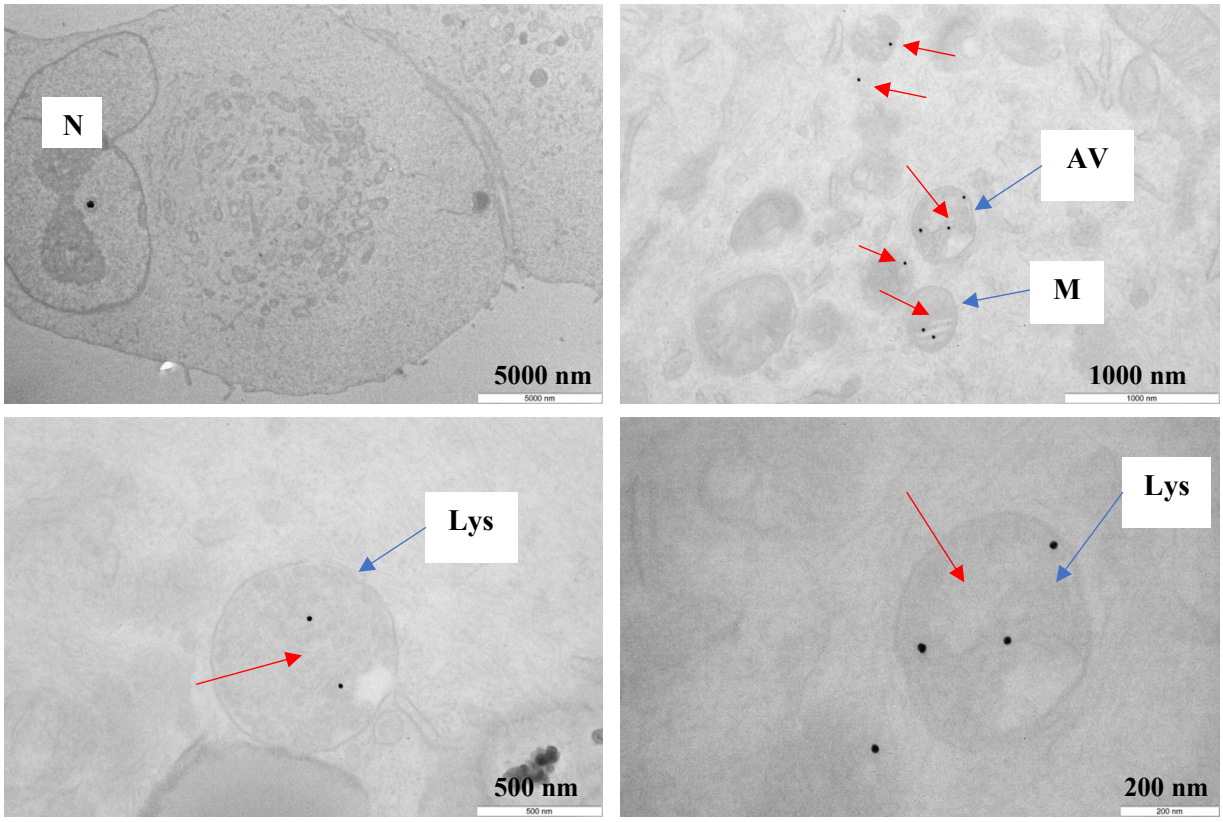


*Figure 4.26. TEM images of MiaPaca-2 cells incubated with 0.25 nM of **IrpqSH.AuNP19**s for 16 hr. Red arrows show the location of **AuNP**s in the cells, with **AV** indicating autophagic vacuoles, **M** indicating the mitochondria, **Lys** indicating the lysosomes and **N** indicating the nucleus.*

4.5.6 Reactive Oxygen Species (ROS) assays

A DCFDA (2',7'-dichlorodihydrofluorescein diacetate) assay was performed for **MAB.IrpqSS.AuNP19**, **MAB.IrpqSH.AuNP19**, **IrpqSS.AuNP19**, **IrpqSH.AuNP19** and **MAB.AuNP19** at a concentration of 0.25 nM and for **Irpqbpy** at a concentration of 0.75 μM for 16 hr. No statistically significant difference was found between the different treatments, indicating that these samples do not generate ROS at a concentration of 0.25 nM. Even **Irpqbpy** did not generate ROS at a concentration of 0.75 μM. Higher sample concentrations may be needed to generate ROS, as these

concentrations were chosen for the cell studies due to showing low cytotoxicity in both cell lines. The confocal images (Section 4.5.2) of the cells with 1 nM AuNP incubation also did not show a visual damage of the cells, so 1 nM may be a concentration suitable to generate ROS in cells.

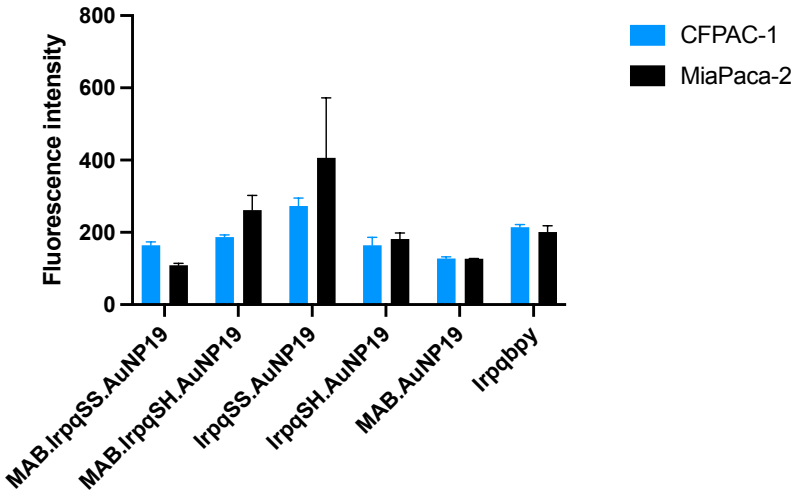


*Figure 4.27. DCFDA (2',7'-dichlorodihydrofluorescein diacetate) assay of CFPAC-1 and MiaPaca-2 cells when incubated with **MAB.IrpqSS.AuNP19**, **MAB.IrpqSH.AuNP19**, **IrpqSS.AuNP19** and **IrpqSH.AuNP19** at 0.25 nM and **Irpqbpy** at 0.75 μM for 16 hr. A positive control of hydrogen peroxide was used.*

4.5.7 Effect of gold nanoparticle interaction with cell media

As discussed in Chapter 3, Section 3.4.6, the AuNPs can interact with the hydrophobic environment created by aromatic amino acids in unsupplemented DMEM to have an increased luminescence. As seen in Figure 4.15, **MAB.IrpqSH.AuNP19** had even brighter luminescence than **MAB.IrpqSS.AuNP19** despite having a weaker emission profile, and a smaller uptake by ICP-MS. However, Table 4.6 shows the area of the AuNP emission profile in DMEM, and the greatest increase in the emission was in **IrpqSH.AuNP19**, showing a percentage increase between H_2O to DMEM of 14186%. **MAB.IrpqSS.AuNP19** showed a percentage increase between H_2O to DMEM of 3406%, **MAB.IrpqSH.AuNP19** showed 11793% and **IrpqSS.AuNP19** showed 4372%.

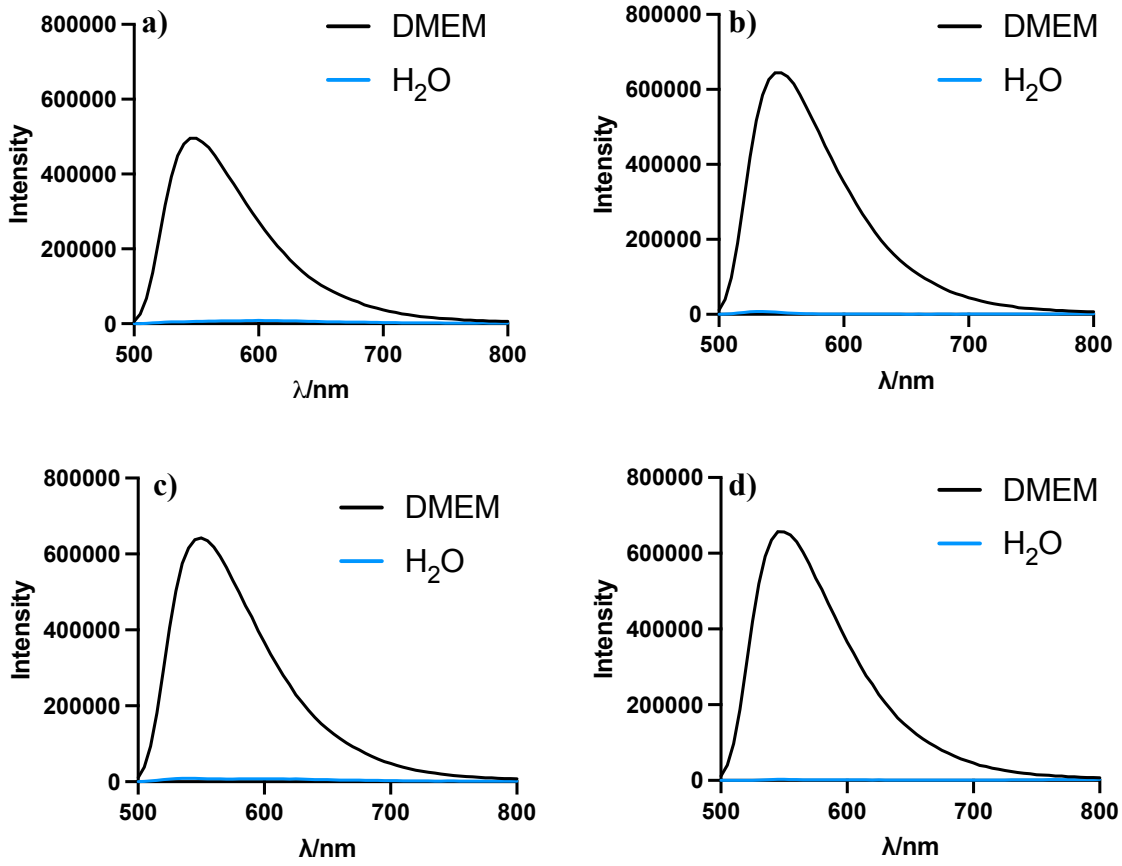


*Figure 4.28. Emission spectra for different coated **AuNP19**s at 0.05 nM: **a) MAB.IrpqSS.AuNP19**, **b) MAB.IrpqSH.AuNP19**, **c) IrpqSS.AuNP19** and **d) IrpqSH.AuNP19** in DMEM (black) and H_2O (blue).*

It was not fully concluded why the **IrpqSH**-coated AuNPs seem to be the ones showing this significantly improved imaging effect in confocal. One reason may be due to the sulphur groups in **IrpqSH** that can form hydrogen bonds in polar environments, increase luminescence quenching[64, 65]. When the polar environment is removed from the interaction with hydrophobic environments, this could be leading to enhanced luminescence.

	Area under curve			
	MAB.IrpqSS. AuNP19	**MAB.IrpqSH. AuNP19**	**IrpqSS.AuNP19**	**IrpqSH.AuNP19**
H_2O	1,360,145	519,161	1,436,788	443,276
DMEM	47,690,487	61,742,665	62,818,497	63,325,766

*Table 4.6. Area under curve of the emission spectra for the AuNP solutions in H_2O and DMEM for **MAB.IrpqSS.AuNP19**, **MAB.IrpqSH.AuNP19**, **IrpqSS.AuNP19** and **IrpqSH.AuNP19** at 0.05 nM. Stock AuNP solutions of 5 nM were diluted by a factor of 100 to achieve the final solutions in H_2O and phenol red-free DMEM.*

4.6 Conclusions

Confocal images of CFPAC-1 and MiaPaca-2 cells incubated with AuNP samples show that **AuNP19**s coated with **IrpqSS** and **IrpqSH** complexes are suitable for imaging in cells and that increased luminescence was seen in CFPAC-1 of **MAB**-coated AuNPs compared to MiaPaca-2 at 16hr. Flow cytometry confirmed the increase in cellular AuNP luminescence in MiaPaca-2 cells compared to CFPAC-1 cells, matching findings seen in Chapter 3, Section 3.4. ICP-MS quantification of AuNP uptake showed that CFPAC-1 did not show any statistically significant different in uptake between the samples, but MiaPaca-2 cells had greater uptake of AuNPs compared to CFPAC-1. **MAB.IrpqSS.AuNP19** had comparable uptake to **IrpqSS.AuNP19** and **MAB.IrpqSH.AuNP19** had significantly less uptake than **MAB.IrpqSS.AuNP19**, but comparable uptake to **IrpqSH.AuNP19** in MiaPaca-2 cells, indicating the influence of the different iridium(III) complexes in cell uptake.

MAB.IrpqSS.AuNP19 and **MAB.IrpqSH.AuNP19** are localised on the surface of CFPAC-1 cells but not on the surface of MiaPaca-2 cells from the TEM images, confirming binding of the **MAB**-coated AuNPs to the cell surface MSLN antigen. CFPAC-1 cells seem take up AuNPs by micropinocytosis or another active endocytosis method, leading to localisation in endosomal compartments, however

MiaPaca-2 cells seem to take up AuNPs by passive uptake and translocation, leading to location in lysosomes. TEM images indicate that **MAB.IrpqSS.AuNP19** and **MAB.IrpqSH.AuNP19** have potential for diagnostic labelling for cancer cell lines due to binding to the surface of CFPAC-1 cells that overexpress MSLN. The ROS generation in both cell lines was not as much as expected, and there was no statistically significant difference in ROS between the samples in each cell line, indicating that the sample concentrations of 0.25 nM for the AuNPs and 0.75 μM for **Irpqbpy** was too low to generate ROS in cells. In addition, good localisation of AuNPs in mitochondria was not seen, so mitochondria were not affected by the AuNP samples at the concentration used.

4.7 Further Studies

Further studies in addition to the experiments outlined in this chapter would provide better conclusions for the **MAB**-AuNP nanocomposite uptake. ROS assays at different concentrations would be necessary, because a concentration of 0.25 nM was non-toxic to the samples overall as shown by the MTT assays, so a higher concentration was probably needed to see an impact of high ROS levels in the cells. In addition, comet assays would provide information about the DNA damage in cells at different concentrations, as DNA damage could be occurring from different methods other than ROS. ICP-MS uptake studies of **MAB.AuNP19**s without iridium(III) complexes would provide further indication as to the influence of **IrpqSS** and **IrpqSH** on the uptake of the AuNPs in the cells.

Fractionation of the cells into different sub-cellular components and analysis of these different components by ICP-MS would provide more information to confirm the localisation seen in the TEM images. Studies in spheroid cell cultures[66-68] would provide better information on AuNP uptake in 3D tumours as spheroids are more representative of the tumour site, as they can replicate the dense stroma seen in PDAC tumours. Chemotherapy-resistant 3D spheroids containing rich matrices have shown to be an improved model for testing samples compared to 2D cell lines[69]. Also, studies with different cell lines that have comparable speed of AuNP uptake would give a better comparison and conclusions

about the uptake of the particles in cells, as MiaPaca-2 has already shown increased uptake of AuNPs in cells in Chapter 3 compared to CFPAC-1. Repeating the experiments in this chapter with a different mesothelin antibody would allow determination of the best anti-mesothelin antibody to use, as some may have better uptake than others due to targeting different epitopes of mesothelin. The samples prepared for ICP-MS uptake studies contained 2 x 10^6 cells. Repeating the experiment with a higher number of cells (~10 x 10^6 cells per sample) would allow the gold concentration to be in a good range on the calibration curve, ensuring reliability of data.

4.8 Experimental

All chemicals and consumables were obtained from Sigma Aldrich, Thermo Fisher Scientific and Greiner Bio One Ltd, unless otherwise stated.

4.8.1 Colloidal AuNP synthesis *(AuNP19)*

The synthesis followed a previously studied protocol for NPs of this size[7]. $HAuCl_4 \bullet 3H_2O$ (10 mg, 0.025 mmol) was dissolved in MilliQ H_2O (100 mL) to make a 0.25 mM solution. This was refluxed at 150 ^oC while stirring for 15 minutes. Trisodium citrate dihydrate (21.4 mg, 0.073 mmol) was dissolved in MilliQ H_2O (1.88 mL) to make a 38.70 mM solution This was quickly added to the hot $HAuCl_4$ solution. The colour of the reaction mixture changed from clear yellow to dark blue to red pink. The reflux was continued for a further 15 mins in the dark, then the reaction was stirred and cooled to room temperature for 1 hr to make 100 mL of 1.1 ± 0.1 nM **AuNP19**s. λ_{max} (H_2O) = 519 nm (SPR), ζ-potential = -37.3 mV, Diameter = 15 ± 4 nm (DLS number distribution), PDI = 0.156.

4.8.2 Attachment of antibodies to a directional PEG linker

MAB32651 mesothelin-targeting antibody from R&D Systems was confirmed to be glycosylated by performing the Purpald test. 100 μg of MAB32651 was suspended in 100 μL 0f $Na_2HPO_4 \bullet 2H_2O$ (100mM). This was mixed with 10 μL $NaIO_4$ (100mM) and incubated in the dark at r.t. for 30 mins.

This was quenched with 500 μL of PBS (0.1 mM). 20 μL of this solution was added to 60 μL of freshly prepared Purpald solution (10 mg/ mL in 1 M NaOH). After a few minutes, a deep purple colour was seen, indicating the presence of aldehydes in the antibody. 2 μL of PEG linker (Sensopath Technologies, Cat No. SPT-0014B) solution (46.5 mM) was added to the remaining antibody solution, and this was incubated at r.t. for 1 hr. The solution was centrifuged for 5 mins at 4 °C at 9000 rpm, then resuspended in 500 μL PBS (0.01 M) and stored at 4 °C in the dark.

4.8.3 Coating of *AuNP19*s with antibody-linker solution

The antibody-linker solution was added to 1 mL of 1.10 nM **AuNP19** in 2μL aliquots until aggregation had occurred. From the binding curve plotted of UV-vis absorbance SPR shift vs. volume of antibody-linker solution, the optimal volume of antibody-linker solution was determined. This optimal volume was added to a fresh solution of 1 mL of 1.10 nM **AuNP19**s and this was stirred in the dark at r.t. for 20 minutes. 2 μL of **LPEG** (Poly(ethylene glycol) 2-mercaptoethyl ether acetic acid, average M_n 2100), obtained from Sigma Aldrich, was added to the AuNPs and the NPs were stirred for a further 20 minutes. The AuNP solution was transferred to 10K MWCO Pierce Protein Concentrators (0.5 mL) and centrifuged twice at r.t. and 11000 rpm for 5 mins. The NPs were resuspended in 1 mL of MilliQ H_2O to obtain 1.1 nM of **MAB** (Monoclonal Mesothelin Antibody)**.AuNP19**s. If further addition of **IrpqSS** and **IrpqSH** were required, purification with the Pierce Protein Concentrators was not performed, and the addition with the complexes was carried out as outlined in Section 4.8.4.

4.8.4 Coating of MAB.AuNP19s with IrpqSS and IrpqSH complexes

Solutions of **IrpqSS** and **IrpqSH** in MeOH were added to 1 mL of 1.10 nM **MAB.AuNP19** in 2μL aliquots until aggregation had occurred. From the binding curve plotted of UV-vis absorbance SPR shift vs. concentration of iridium(III) complex solution, the optimal concentration of iridium(III) complex to add was determined. To a fresh solution of 1 mL of 1.10 nM **MAB.AuNP19**, the optimal iridium(III) complex concentration was added and stirred at 20 mins. The AuNP solution was transferred to 10K MWCO Pierce Protein Concentrators (0.5 mL) and centrifuged twice at r.t. and 11000 rpm for 5 mins.

The NPs were resuspended in 1 mL of MilliQ H_2O to obtain 1.0 nM ± 0.1 nM of **MAB.IrpqSS.AuNP19,** λ_{max} (H_2O) = 529 nm (SPR), ζ-potential = -42.3 mV, Diameter = 29 ± 9 nm (DLS number distribution), PDI = 0.232; and 1.0 ± 0.1 nM of **MAB.IrpqSH.AuNP19**, λ_{max} (H_2O) = 528 nm (SPR), ζ-potential = -31.6 mV, Diameter = 26 ± 10 nm (DLS number distribution), PDI = 0.254.

4.8.5 Preparing samples for ICP-MS analysis of AuNPs

Fresh aqua regia was made up from TraceSelect HNO_3 and HCl in a 1:3 ratio. The NP samples were digested in the aqua regia until the solution was clear. The solution was diluted with 4% HNO_3 solution (in ultrapure H_2O) to create a 5mL solution. This solution was diluted further to a 1:10, 1:20, 1:50 or 1:100 solution, as the experiment required. The solutions were transferred in 16.5mL polypropylene tubes to the School of Chemistry at the University of Warwick for ICP-MS analysis of gold and iridium content. Samples were run on a 7500cx ICPMS instrument with an Agilent integrated auto-sampler. PlasmaCal calibration standards were obtained from QMX laboratories. Calibration curves were fitted to R^2 values of >0.998 and the standard solutions of gold used were 0, 5, 10, 25, 50, 100, 250 and 500 and 1000 ppb.

4.8.6 Cell Culture

MiaPaca-2 and CFPAC-1 pancreatic cancer cells were cultured in vented cap T-75 flasks at 37 ºC in 5% CO_2. The cell monolayer was grown in Dulbecco's modified Eagle medium (DMEM), supplemented with 10% fetal bovine serum (FBS), 1% of Penicillin-Streptomycin (100X) and 1% of Eagle's Minimal Essential Medium (MEM) Non-Essential Amino Acid. The cells were sub-cultured when at high cell confluency, using TrypLE Express enzyme (10 mins) to detach the cells. Much of this was performed with the assistance of Garret Rochford.

4.8.7 MTT assays

MiaPaca-2 and CFPAC-1 cells were counted using a Haemocytometer and seeded at a density of 5000 cells per well onto 96-well plates. The cells were adhered to the plates overnight at 37 ºC in 5% CO_2.

The treatment samples were added at different dilutions to the wells in repeats and incubated for 24 hr at 37 ^{o}C in 5% CO_2. A positive 1% Triton control in PBS was also added to the cells for the 24 hr incubations. All cell media was removed and the NPs in each well were incubated with 3-(4,5-dimethylthiazol-2-yl)-2,5-diphenyl tetrazolium bromide (5 mg/10 mL) in phenol red-free DMEM with 10% PBS. The cells were incubated at 37 oC in 5% CO2 for 3-4 hrs, then the media was completely removed, DMSO was added to each well and the absorbances of the plates at 595 nm was measured using a Tecan Infinite 200 Pro plate reader. Samples were normalized to the 1% Triton signal.

4.8.8 Confocal Microscopy Imaging

MiaPaca-2 and CFPAC-1 cells were counted using a Haemocytometer and seeded at a density of 100,000 cells onto 35 mm CELLview dishes with a 10 mm glass insert, or 35 mm cell culture dishes without glass inserts. The cells were adhered to the dish overnight at 37 ^{o}C in 5% CO_2. The treatment samples were added to the dish to obtain the final desired concentration, and the cells were incubated for the desired timescale at 37 ^{o}C in 5% CO_2. DMEM without phenol-red was used to incubate the cells. Cells were stained with Hoechst 33342, at a final concentration of 20 nM for at least 15 minutes before imaging. For live cell imaging, the cells were imaged without washing, however for fixed cell imaging, the cells were washed twice with PBS and fixed with paraformaldehyde (4% in PBS) for 20 minutes. The paraformaldehyde was washed twice with PBS and the cells imaged in PBS. Confocal images and z-stacks were collected on a Leica SP8 upright microscope using a 40x ceramic water dipping objective lens, and on a Zeiss LSM900 inverted confocal microscope with Airyscan using a 63x oil immersion objective lens. Images were acquired using fluorescence, reflectance and transmission mode. For the fluorescence channels on the Leica SP8 upright microscope, the settings used were: Hoechst (blue): λ_{exc} = 405 nm, λ_{em} = 419 – 472 nm, treatment sample luminescence (green): λ_{exc} = 458 nm, λ_{em} = 550 – 750 nm. For the fluorescence channels on the Zeiss LSM900 inverted confocal microscope, the settings used were: Hoechst (blue): λ_{exc} = 405 nm, λ_{em} = 400 – 495 nm, treatment sample luminescence (green): λ_{exc} = 488 nm, λ_{em} = 500 – 700 nm. All the images were processed with ImageJ.

4.8.9 Transmission Electron Microscopy

MiaPaca-2 and CFPAC-1 cells were counted using a Haemocytometer and seeded at a density of 100,000 cells onto sterilised 13 mm glass coverslips that were placed in wells of six-well plates. The cells were adhered to the slips overnight at 37 ºC in 5% CO_2. The AuNPs were added to the cells at the required concentration and incubated for 24 hr at 37 ºC in 5% CO_2. The cells were rinsed twice with PBS and fixed with glutaraldehyde (2.5% in 0.1 M PBS) for 24 hr at 4 ºC. Samples were processed at the Centre for Electron Microscopy at the University of Birmingham. Ultrathin sections of the cells were cut and loaded onto Formvar Carbon support films. Images were acquired using a Joel 1400 Bio Electron Microscope and the images were analysed by ImageJ software. All this was done with the assistance of Theresa Morris.

4.8.10 Flow Cytometry

MiaPaca-2 and CFPAC-1 cells were counted using a Haemocytometer and seeded at a density of 100,000 cells per well in six-well plates. The cells were adhered overnight at 37 ºC in 5% CO_2. The cells were incubated with the desired concentration of AuNPs in phenol red-free DMEM for 24hr at 37 ºC in 5% CO_2. The cells were washed twice with PBS, then detached with TrypLE Express enzyme. The cells were centrifuged for 5 mins at 1500g to produce cell pellets that were resuspended in 200 μL of PBS (1% FBS). The samples were run on a Beckman Coulter CytoFLEX Flow Cytometer using the Violet610 channel, with a 405 nm laser and an emission detection range of 590 – 630 nm.

4.8.11 Preparing samples for ICP-MS analysis of AuNPs in cells

MiaPaca-2 and CFPAC-1 cells were counted using a Haemocytometer and seeded at a density of 2 x 10^6 cells per well in six-well plates. The cells were adhered overnight at 37 ºC in 5% CO_2. The cells were incubated with the desired concentration of AuNPs in duplicates in phenol red-free DMEM for the required timescale at 37 ºC in 5% CO_2. The cells were washed twice with PBS, then detached with TrypLE Express enzyme. The cells were centrifuged for 5 mins at 1500g to produce cell pellets that were resuspended in PBS (1mL). The cells were counted again using a Haemocytometer. The cells in

PBS were digested overnight in ultrapure HNO_3 while being stirred and heated. Then the digested samples were diluted with 4% HNO_3 in ultrapure H_2O to a final volume of 5 mL. ICP-MS measurements in duplicates of the gold content in the cell samples were run on a 7500cx ICPMS instrument with an Agilent integrated auto-sampler at the Chemistry department at the University of Warwick. PlasmaCal calibration standards were obtained from QMX laboratories. Calibration curves were fitted to R^2 values of >0.997 and the standard solutions of gold used were 0, 5, 10, 25, 50, 100, 250 and 500 ppb.

4.8.12 Reactive Oxygen Species (ROS) assay

MiaPaca-2 and CFPAC-1 cells were counted using a Haemocytometer and seeded at a density of 2500 cells per well in 96-well plates with phenol red-free DMEM. The cells were adhered overnight at 37 ºC in 5% CO_2. The cells were incubated with the desired concentration of treatment samples in duplicates for 16 hr at 37 ºC in 5% CO_2 in phenol red-free DMEM. H_2O_2 (1%) in DMEM and untreated cells (DMEM only) were used as controls, and the positive control was hydrogen peroxide. 45 mins before the incubation time was completed, the cells were incubated with 20 μM of DCFDA (2',7'-dichlorodihydrofluorescein diacetate) solution and read on a fluorescent plate reader with ex/em of 485/535 nm. The samples were normalised to the untreated cells.

4.8.13 qPCR of BxPC-3, MiaPaca-2 and CFPAC-1 cell lines

RNA was extracted from BxPC-3, MiaPaca-2 and CFPAC-1 cell lines. A Nanodrop Spectrophotometer was used to calculate the RNA concentration, using nuclease-free H_2O as a background solvent. BxPC3 RNA concentration was found to be 618.1 ng/uL, in MiaPaca-2 it was found to be 1276 ng/uL and in CFPAC-1 it was found to be 443.0 ng/uL. Solutions of 100 ng/uL in 20uL were made up in nuclease-free H_2O. A Bioline Tetro cDNA synthesis kit protocol was used to create an SYBR green qPCR Mastermix, and three solutions of Master Mix containing the RNA for the three cell lines was transferred for a PCR machine for 30 mins. In the meantime, three different mesothelin (MSLN) primer pairs were made up to 100 μM. This was diluted to 5 μM in nuclease-free H_2O. The Mastermix, forward and reverse primers, ROX reference dye, cDNA and nuclease-free H2O were combined on a PCR plate

for each cell line and each primer pair, and the PCR plate read on a PCR plate reader to obtain the ΔCq values for MSLN for each cell line. MSLN primer sequences were as follows: Human MSLN primer pair 1 forward sequence: ATTGAGGAAACCGAGGCAGA and reverse sequence: TGAAGAGCAGGAACAGGAGG. Human MSLN primer pair 2 forward sequence: GGAAGTGGAGAAGACAGCCT and reverse sequence: CTCGTAGGTGAAGGGGATGG. Human MSLN primer pair 3 forward sequence: GACACCCTAGACACCCTGAC and reverse sequence: ATGTTCTGGAAAGCAAGGCG. All this was done with the assistance of Marium Rana.

4.9 References

1. M. H. Jazayeri, H. Amani, A. A. Pourfatollah, H. Pazoki-Toroudi and B. Sedighimoghaddam, *Sens. Bio-Sens. Res.*, 2016, **9**, 17-22.
2. Y. Qian, M. Qiu, Q. Wu, Y. Tian, Y. Zhang, N. Gu, S. Li, L. Xu and R. Yin, *Sci. Rep.*, 2014, **4**, 7490.
3. J. Ljungblad, 2009.
4. R. G. Rayavarapu, W. Petersen, C. Ungureanu, J. N. Post, T. G. van Leeuwen and S. Manohar, *Int. J. Biomed. Imaging*, 2007, **2007**, 29817.
5. Z. Zhang, S. Wang, H. Xu, B. Wang and C. Yao, *J. Biomed. Opt.*, 2015, **20**, 51043.
6. R. T. Busch, F. Karim, J. Weis, Y. Sun, C. Zhao and E. S. Vasquez, *ACS Omega*, 2019, **4**, 15269-15279.
7. S. Kumar, J. Aaron and K. Sokolov, *Nat. Protoc.*, 2008, **3**, 314-314.
8. F. Schulz, T. Homolka, N. G. Bastús, V. Puntes, H. Weller and T. Vossmeyer, *Langmuir*, 2014, **30**, 10779-10784.
9. L. F. Dodson, W. G. Hawkins and P. Goedegebuure, *Immunotherapy*, 2011, **3**, 517-537.
10. P. Gold and S. O. Freedman, *J. Exp. Med.*, 1965, **121**, 439-462.
11. D. M. Thomson, J. Krupey, S. O. Freedman and P. Gold, *Proc. Natl. Acad. Sci. U. S. A.*, 1969, **64**, 161-167.
12. K. Chang, I. Pastan and M. C. Willingham, *Int. J. Cancer*, 1992, **50**, 373-381.
13. D. M. McCarthy, A. Maitra, P. Argani, A. E. Rader, D. O. Faigel, N. T. van Heek, R. H. Hruban and R. E. Wilentz, *Appl. Immunohistochem. Mol. Morphol.*, 2003, **11**, 238-243.

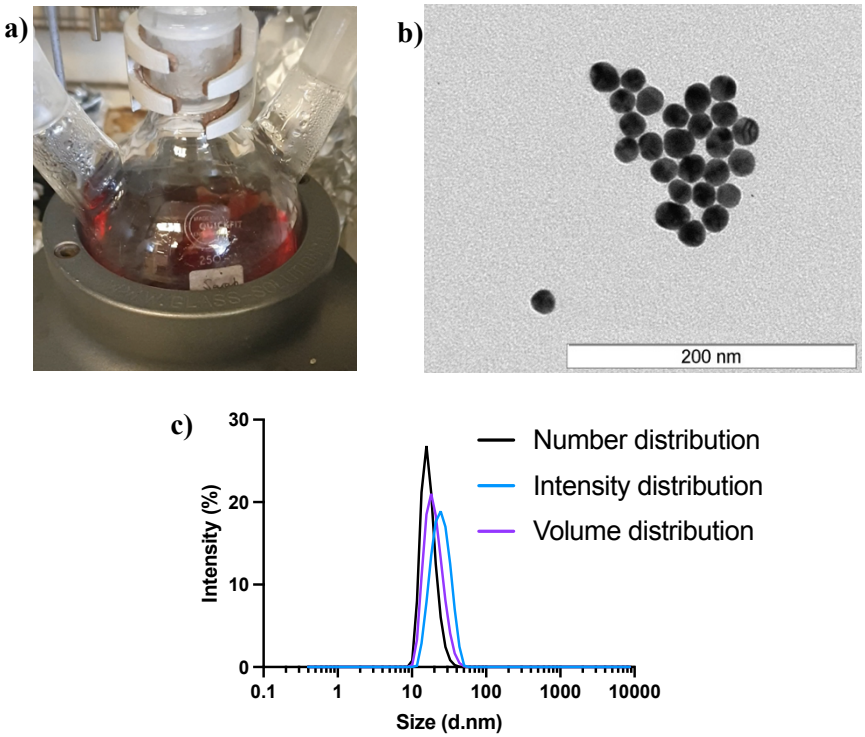
14. P. Argani, C. Iacobuzio-Donahue, B. Ryu, C. Rosty, M. Goggins, R. E. Wilentz, S. R. Murugesan, S. D. Leach, E. Jaffee, C. J. Yeo, J. L. Cameron, S. E. Kern and R. H. Hruban, *Clin. Cancer Res.*, 2001, **7**, 3862-3868.
15. R. Hassan, Z. G. Laszik, M. Lerner, M. Raffeld, R. Postier and D. Brackett, *Am. J. Clin. Pathol.*, 2005, **124**, 838-845.
16. S. Cohen, *J. Biol. Chem.*, 2008, **283**, 33793-33797.
17. S. Sigismund, D. Avanzato and L. Lanzetti, *Mol. Oncol.*, 2018, **12**, 3-20.
18. S. S. Padhye, S. Guin, H.-P. Yao, Y.-Q. Zhou, R. Zhang and M.-H. Wang, *Mol. Pharm.*, 2011, **8**, 2310-2319.
19. C. Ronsin, F. Muscatelli, M. G. Mattei and R. Breathnach, *Oncogene*, 1993, **8**, 1195-1202.
20. H. P. Yao, Y. Q. Zhou, R. Zhang and M. H. Wang, *Nat. Rev. Cancer*, 2013, **13**, 466-481.
21. W. Wang, L. Xu, Y. Yang, L. Dong, B. Zhao, J. Lu, T. Zhang and Y. Zhao, *Clin. Transl. Gastroenterol.*, 2018, **9**, 178.
22. M. Bydoun, A. Sterea, H. Liptay, A. Uzans, W.-Y. Huang, G. J. Rodrigues, I. C. G. Weaver, H. Gu and D. M. Waisman, *Mol. Oncol.*, 2018, **12**, 1895-1916.
23. S. Salleh, A. Thyagarajan and R. P. Sahu, *J. cancer metastatis treat.*, 2020, **6**, 31.
24. S. Kawa, H. Oguchi, T. Kobayashi, M. Tokoo, S. Furuta, M. Kanai and T. Homma, *Br. J. Cancer*, 1991, **64**, 899-902.
25. F. Gebauer, D. Wicklein, J. Horst, P. Sundermann, H. Maar, T. Streichert, M. Tachezy, J. R. Izbicki, M. Bockhorn and U. Schumacher, *PLoS One*, 2014, **9**, e113023.
26. L. Yan, X. Tian, C. Ye, X. Guan, B. Dong, M. Zhao, J. Wu and C. Hao, *Onco Targets Ther.*, 2020, **13**, 12615-12623.
27. G. A. Arias-Pinilla, A. G. Dalgleish, S. Mudan, I. Bagwan, A. J. Walker and H. Modjtahedi, *Sci. Rep.*, 2020, **10**, 537.
28. G. A. Huls, I. A. Heijnen, M. E. Cuomo, J. C. Koningsberger, L. Wiegman, E. Boel, A. R. van der Vuurst de Vries, S. A. Loyson, W. Helfrich, G. P. van Berge Henegouwen, M. van Meijer, J. de Kruif and T. Logtenberg, *Nat. Biotechnol.*, 1999, **17**, 276-281.
29. P. Conaghan, S. Ashraf, M. Tytherleigh, J. Wilding, E. Tchilian, D. Bicknell, N. J. Mortensen and W. Bodmer, *Br. J. Cancer*, 2008, **98**, 1217-1225.
30. R. M. Sharkey, G. Hajjar, D. Yeldell, A. Brenner, J. Burton, A. Rubin and D. M. Goldenberg, *J. Nucl. Med.*, 2005, **46**, 620-633.
31. M. Ho, M. Feng, R. J. Fisher, C. Rader and I. Pastan, *Int. J. Cancer*, 2011, **128**, 2020-2030.
32. Y. Feng, X. Xiao, Z. Zhu, E. Streaker, M. Ho, I. Pastan and D. S. Dimitrov, *Mol. Cancer Ther.*, 2009, **8**, 1113-1118.
33. R. Hassan, W. Ebel, E. L. Routhier, R. Patel, J. B. Kline, J. Zhang, Q. Chao, S. Jacob, H. Turchin, L. Gibbs, M. D. Phillips, S. Mudali, C. Iacobuzio-Donahue, E. M. Jaffee, M. Moreno, I. Pastan, P. M. Sass, N. C. Nicolaides and L. Grasso, *Cancer Immun.*, 2007, **7**, 20.

34. P. Baldo and S. Cecco, *Onco Targets Ther.*, 2017, **10**, 5337-5353.
35. Y.-F. Zhang, Y. Phung, W. Gao, S. Kawa, R. Hassan, I. Pastan and M. Ho, *Sci. Rep.*, 2015, **5**, 9928.
36. I. Pastan, R. Hassan, D. J. FitzGerald and R. J. Kreitman, *Annu. Rev. Med.*, 2007, **58**, 221-237.
37. C. D. Corso, D. D. Stubbs, S.-H. Lee, M. Goggins, R. H. Hruban and W. D. Hunt, *Cancer Detect. Prev.*, 2006, **30**, 180-187.
38. C. R. Patra, R. Bhattacharya, E. Wang, A. Katarya, J. S. Lau, S. Dutta, M. Muders, S. Wang, S. A. Buhrow, S. L. Safgren, M. J. Yaszemski, J. M. Reid, M. M. Ames, P. Mukherjee and D. Mukhopadhyay, *Cancer Res.*, 2008, **68**, 1970-1978.
39. M. Peeters, J. Balfour and D. Arnold, *Aliment. Pharmacol. Ther.*, 2008, **28**, 269-281.
40. U. Graeven, B. Kremer, T. Südhoff, B. Killing, F. Rojo, D. Weber, J. Tillner, C. Ünal and W. Schmiegel, *Br. J. Cancer*, 2006, **94**, 1293-1299.
41. M. S. Ramakrishnan, A. Eswaraiah, T. Crombet, P. Piedra, G. Saurez, H. Iyer and A. S. Arvind, *MAbs*, 2009, **1**, 41-48.
42. C. Panousis, V. M. Rayzman, T. G. Johns, C. Renner, Z. Liu, G. Cartwright, F. T. Lee, D. Wang, H. Gan, D. Cao, A. Kypridis, F. E. Smyth, M. W. Brechbiel, A. W. Burgess, L. J. Old and A. M. Scott, *Br. J. Cancer*, 2005, **92**, 1069-1077.
43. E. S. Glazer, K. L. Massey, C. Zhu and S. A. Curley, *Surgery*, 2010, **148**, 319-324.
44. J. A. Khan, R. A. Kudgus, A. Szabolcs, S. Dutta, E. Wang, S. Cao, G. L. Curran, V. Shah, S. Curley, D. Mukhopadhyay, J. D. Robertson, R. Bhattacharya and P. Mukherjee, *PLoS One*, 2011, **6**, e20347-e20347.
45. C. K. Elechalawar, M. N. Hossen, P. Shankarappa, C. J. Peer, W. D. Figg, J. D. Robertson, R. Bhattacharya and P. Mukherjee, *Int. J. Nanomedicine*, 2020, **15**, 991-1003.
46. L. M. Andrade, E. M. N. Martins, A. F. Versiani, D. S. Reis, F. G. da Fonseca, I. P. d. Souza, R. M. Paniago, E. Pereira-Maia and L. O. Ladeira, *Mater. Sci. Eng. C.*, 2020, **107**, 110203-110203.
47. H.-P. Yao, L. Feng, T.-H. Weng, C.-Y. Hu, S. R. Suthe, A. G. M. Mostofa, L.-H. Chen, Z.-G. Wu, W.-L. Wang and M.-H. Wang, *Mol. Pharm.*, 2018, **15**, 3260-3271.
48. H. P. Yao, L. Feng, S. R. Suthe, L. H. Chen, T. H. Weng, C. Y. Hu, E. S. Jun, Z. G. Wu, W. L. Wang, S. C. Kim, X. M. Tong and M. H. Wang, *J. Immunother. Cancer*, 2019, **7**, 75.
49. M. Li, U. Bharadwaj, R. Zhang, S. Zhang, H. Mu, W. E. Fisher, F. C. Brunicardi, C. Chen and Q. Yao, *Mol. Cancer Ther.*, 2008, **7**, 286-296.
50. U. Bharadwaj, C. Marin-Muller, M. Li, C. Chen and Q. Yao, *Carcinogenesis*, 2011, **32**, 1013-1024.
51. R. A. Schoumacher, J. Ram, M. C. Iannuzzi, N. A. Bradbury, R. W. Wallace, C. T. Hon, D. R. Kelly, S. M. Schmid, F. B. Gelder, T. A. Rado and et al., *Proc. Natl. Acad. Sci. U. S. A.*, 1990, **87**, 4012-4016.

52. E. L. Deer, J. González-Hernández, J. D. Coursen, J. E. Shea, J. Ngatia, C. L. Scaife, M. A. Firpo and S. J. Mulvihill, *Pancreas*, 2010, **39**, 425-435.
53. A. N. Dosumu, S. Claire, L. S. Watson, P. M. Girio, S. A. M. Osborne, Z. Pikramenou and N. J. Hodges, *JACS Au*, 2021, **1**, 174-186.
54. A. P. Chimalakonda, R. Yadav and P. Marathe, *AAPS J.*, 2013, **15**, 717-727.
55. T. Dunlap and Y. Cao, *Front. Pharmacol.*, 2022, **13**.
56. C. J. van Oss, R. J. Good and M. K. Chaudhury, *J. Chromatogr.*, 1986, **376**, 111-119.
57. K. Tsuji, M. Ojima, K. Otabe, M. Horie, H. Koga, I. Sekiya and T. Muneta, *Cell Transplant.*, 2017, **26**, 1089-1102.
58. J. V. Olsen, S.-E. Ong and M. Mann, *Mol. Cell. Proteomics*, 2004, **3**, 608-614.
59. X.-Y. Zhao, B. Subramanyam, N. Sarapa, S. Golfier and H. Dinter, *Clin. Cancer Drugs*, 2016, **3**, 76-86.
60. A. G. T. Terwisscha van Scheltinga, A. Ogasawara, G. Pacheco, A. N. Vanderbilt, J. N. Tinianow, N. Gupta, D. Li, R. Firestein, J. Marik, S. J. Scales and S.-P. Williams, *Mol. Cancer Ther.*, 2017, **16**, 134.
61. X. P. Lin, J. D. Mintern and P. A. Gleeson, *Membranes*, 2020, **10**.
62. Y. Wei, T. Tang and H. Pang, *Nat. Commun.*, 2019, **10**.
63. M. Sousa de Almeida, E. Susnik, B. Drasler, P. Taladriz-Blanco, A. Petri-Fink and B. Rothen-Rutishauser, *Chem. Soc. Rev.*, 2021, **50**, 5397-5434.
64. M. M. H. Khalil, F. C. De Schryver, H. Keller and J. M. Lehn, *Supramol. Sci.*, 1995, **2**, 175-182.
65. L. A. H. van Bergen, M. Alonso, A. Palló, L. Nilsson, F. De Proft and J. Messens, *Sci. Rep.*, 2016, **6**, 30369.
66. M. Durymanov, C. Kroll, A. Permyakova, E. O'Neill, R. Sulaiman, M. Person and J. Reineke, *Transl. Oncol.*, 2019, **12**, 180-189.
67. M. Durymanov, C. Kroll, A. Permyakova and J. Reineke, *Mol. Pharm.*, 2019, **16**, 1074-1082.
68. M. J. Ware, V. Keshishian, J. J. Law, J. C. Ho, C. A. Favela, P. Rees, B. Smith, S. Mohammad, R. F. Hwang, K. Rajapakshe, C. Coarfa, S. Huang, D. P. Edwards, S. J. Corr, B. Godin and S. A. Curley, *Biomaterials*, 2016, **108**, 129-142.
69. P. Longati, X. Jia, J. Eimer, A. Wagman, M.-R. Witt, S. Rehnmark, C. Verbeke, R. Toftgård, M. Löhr and R. L. Heuchel, *BMC Cancer*, 2013, **13**, 95.

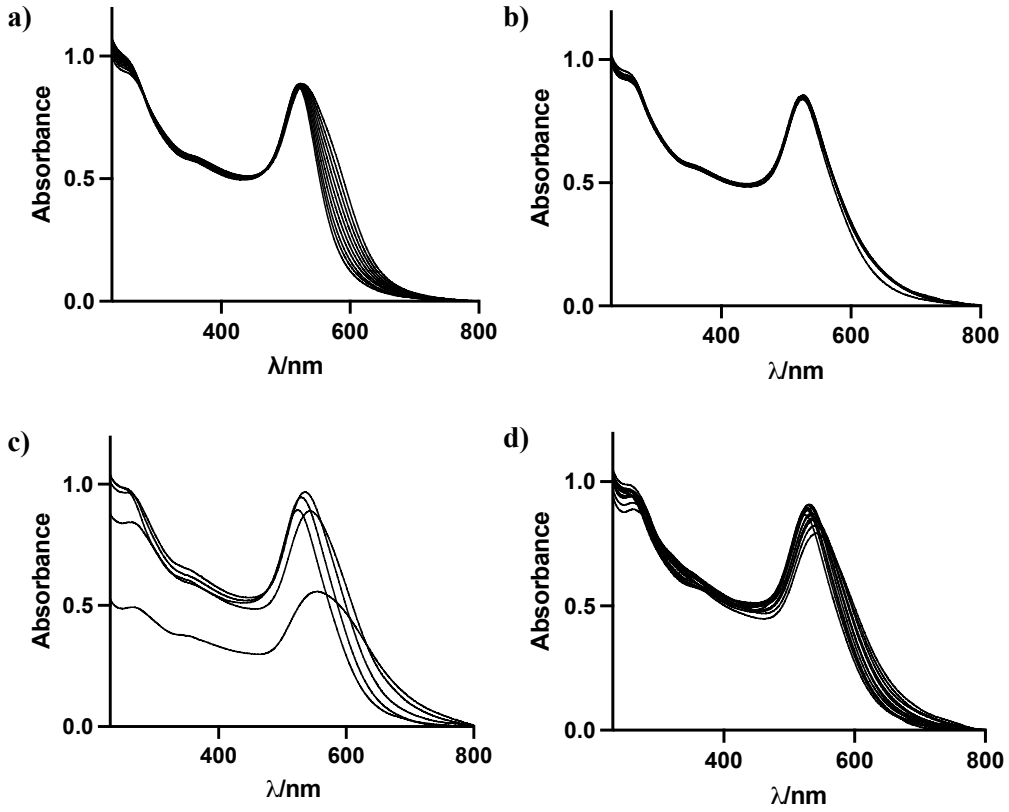
4.10 Appendix

AuNP19 synthesis

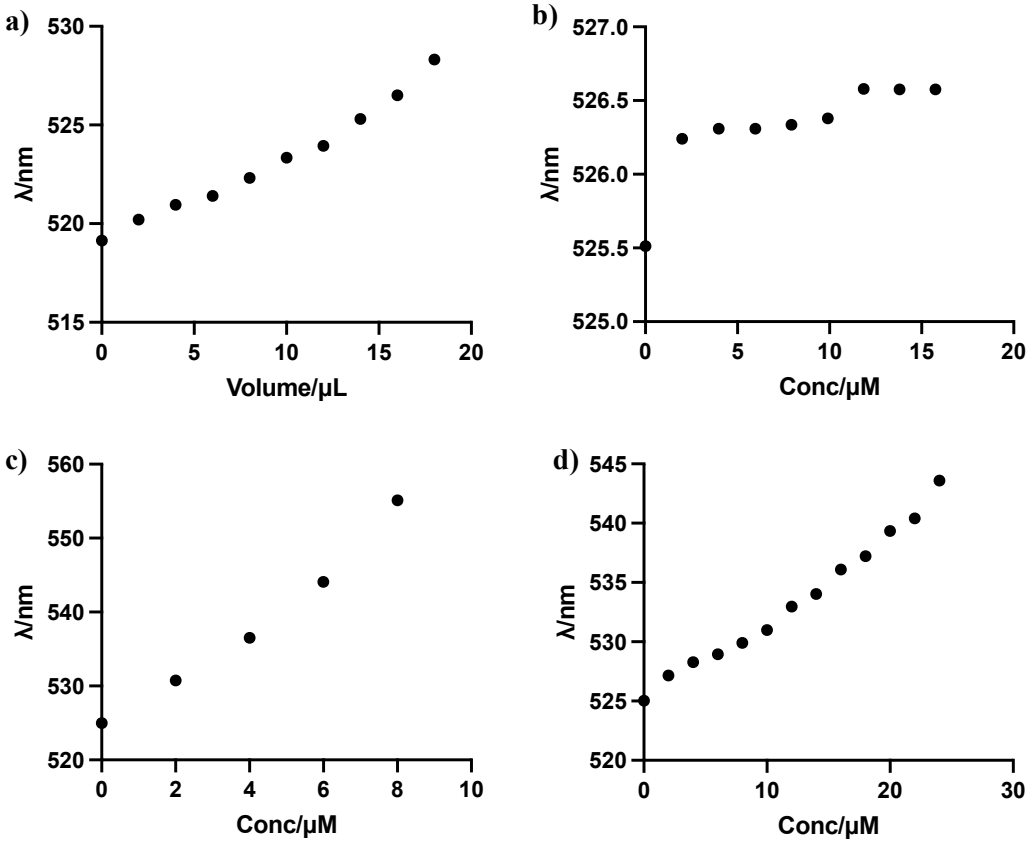


Supplementary Figure 4.1. Image displaying the pink colour of the AuNP19s forming in ***a)****, the TEM image of the* ***AuNP19****s giving a volume distribution value of 18.5 ± 1.2 nm in* ***b)*** *and DLS number, volume and intensity distribution histograms of the AuNP19s in* ***c)****.*

UV-vis absorbance spectra for coating of the AuNP19s

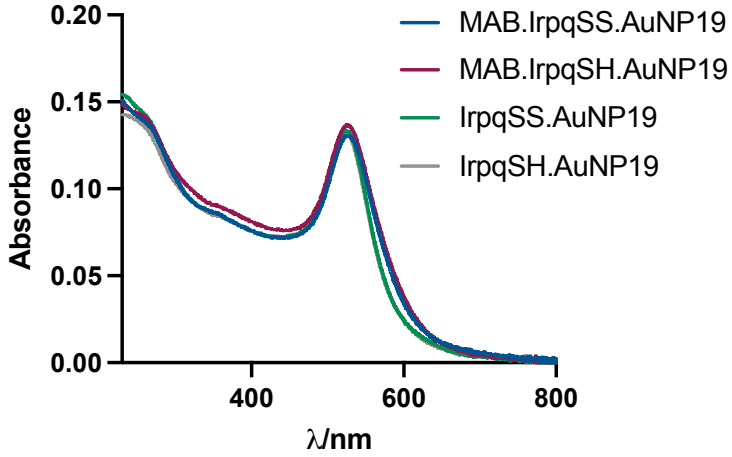


Supplementary Figure 4.2. UV-vis absorbance spectra showing the SPR shifts for ***a) MAB*** *additions (18 μL maximum) onto 1.1 nM* ***AuNP19****,* ***b) LPEG*** *addition (16 μM maximum) onto 1.1 nM* ***MAB.AuNP19****,* ***c) IrpqSS*** *addition (8 μM maximum) onto* ***MAB.AuNP19*** *and* ***d) IrpqSH*** *addition (24 μM maximum) onto* ***MAB.AuNP19****.*



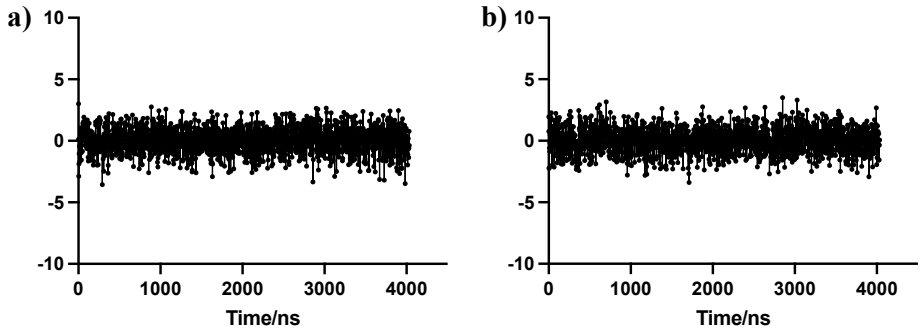
Supplementary Figure 4.3. Binding curves of SPR wavelength vs volume/concentration for ***a) MAB*** *antibody onto* ***AuNP19****,* ***b) LPEG*** *onto* ***MAB.AuNP19****,* ***c) IrpqSS*** *onto* ***MAB.AuNP19*** *and* ***d) IrpqSH*** *onto* ***MAB.AuNP19****.*

UV-vis absorbance spectra for cell studies



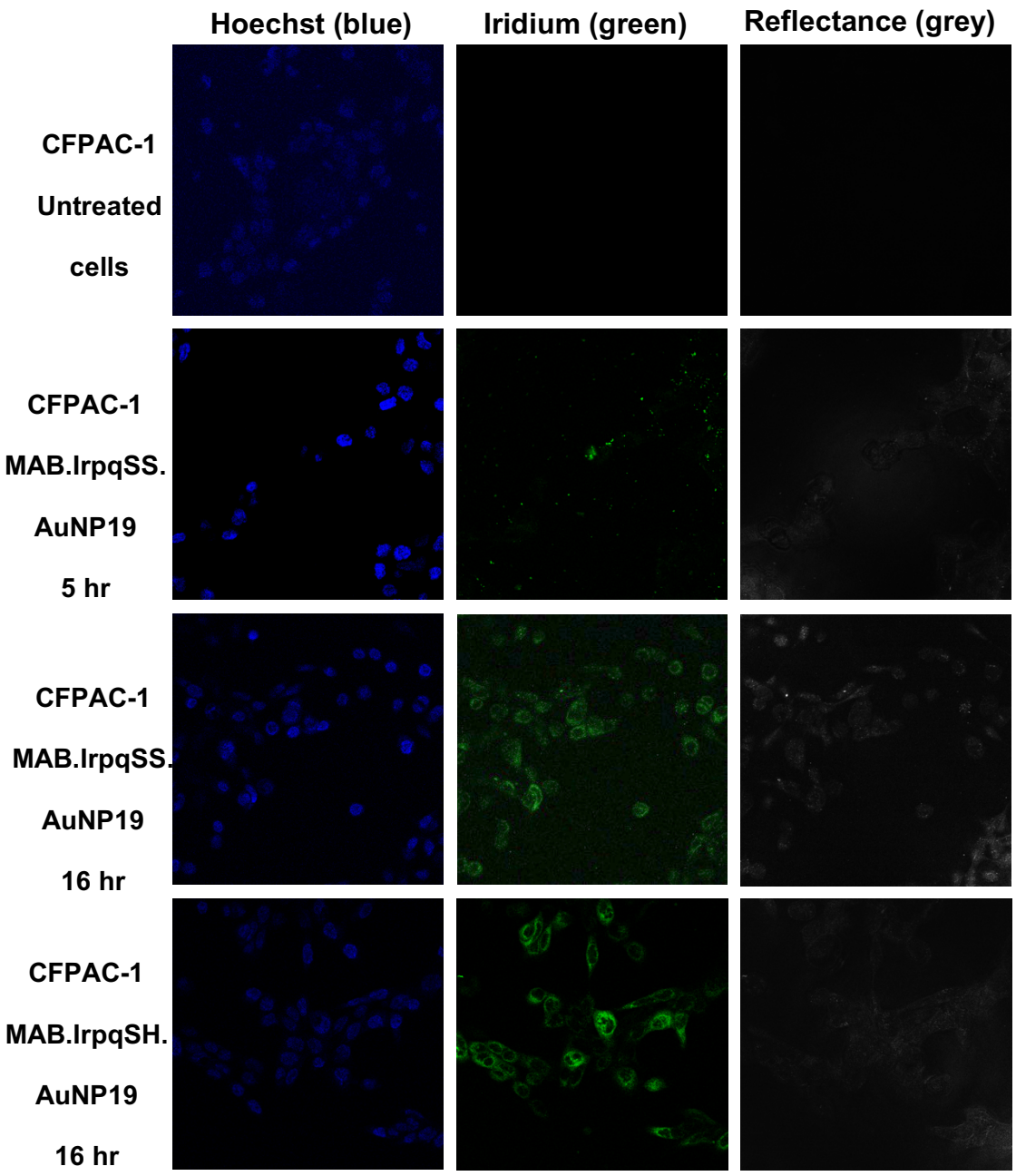
*Supplementary Figure 4.4. UV-vis absorbance spectra of **MAB.IrpqSS.AuNP19**, **MAB.IrpqSH.AuNP19**, **IrpqSS.AuNP19** and **IrpqSH.AuNP19** in H_2O at 0.2 nM (10% dilution from 2 nM), used for cell studies.*

Luminescence lifetime residuals for the iridium-coated AuNP19s

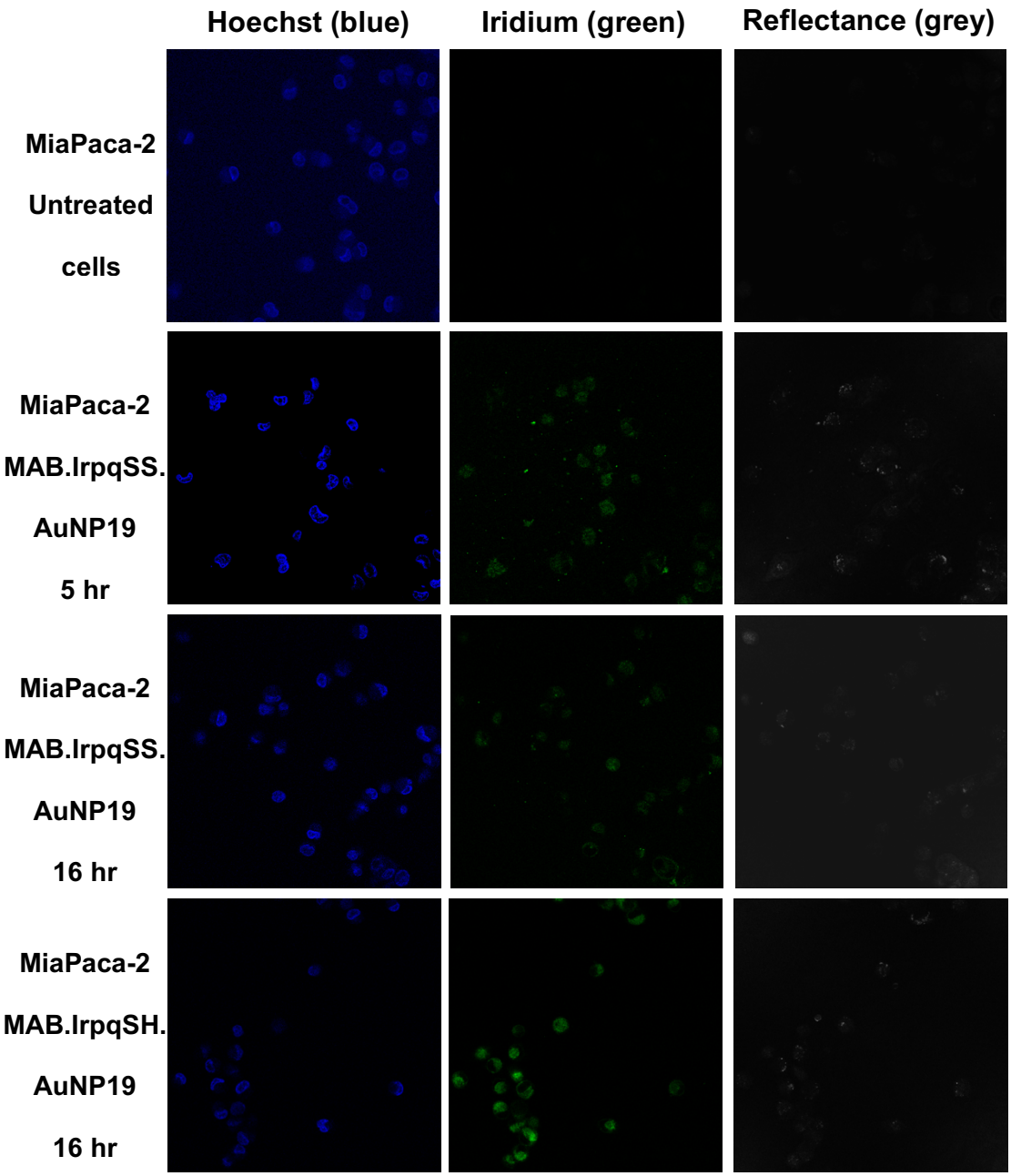


*Supplementary Figure 4.5. Luminescence lifetime residuals for **a) MAB.IrpqSS.AuNP19** and **b) IrpqSS.AuNP19** at 1 nM, with lifetime decay curves fitted with IRF fitting of $\chi^2 < 1.2$.*

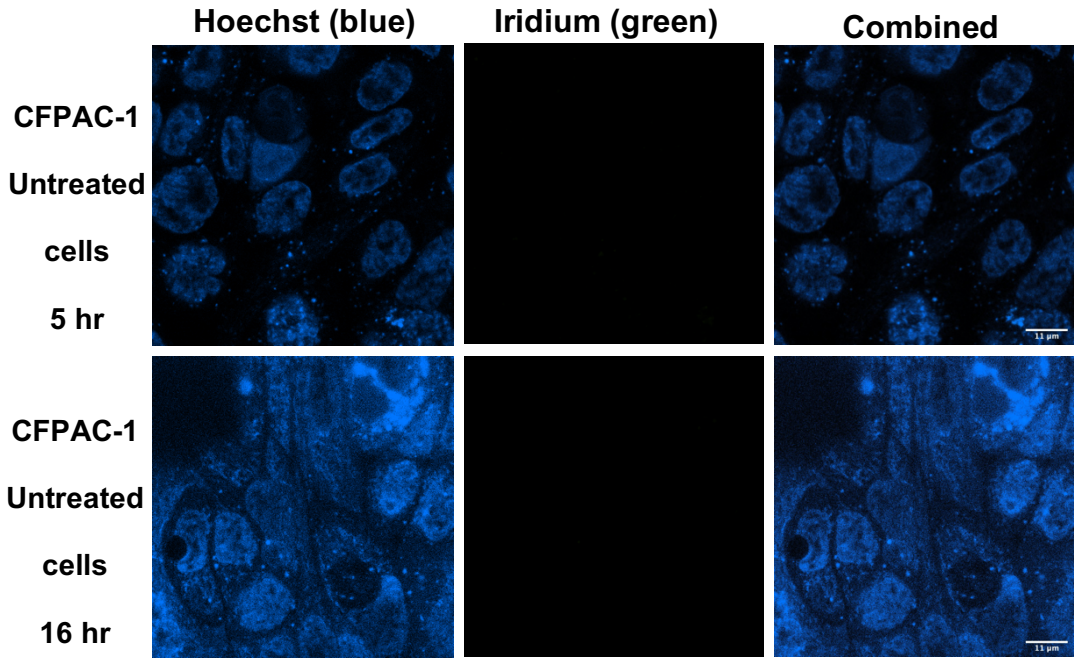
Confocal images



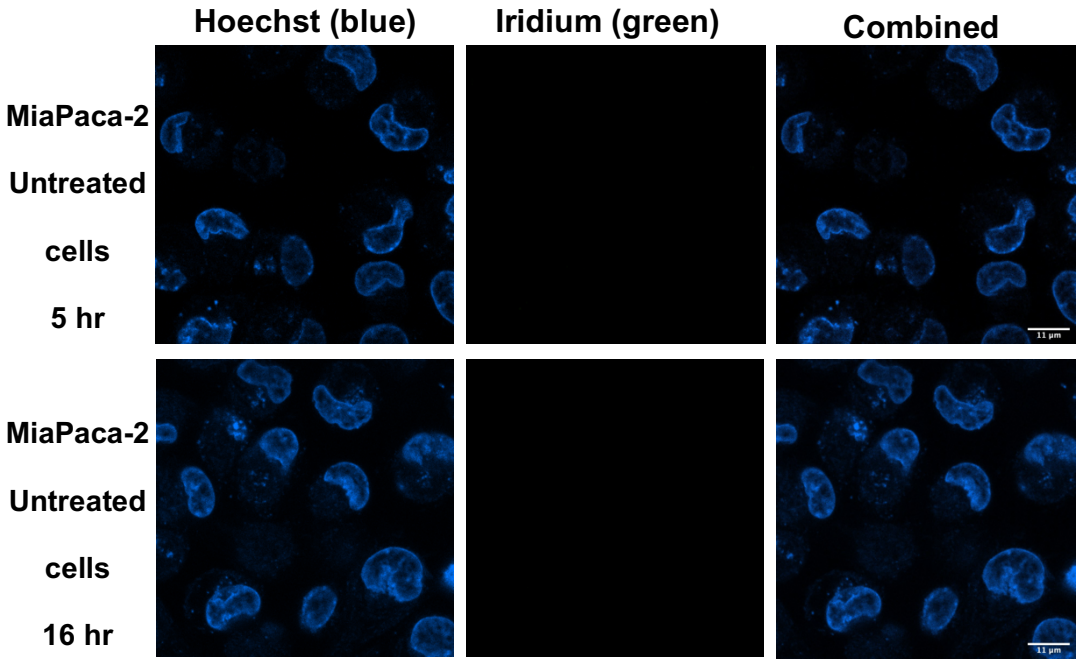
Supplementary Figure 4.6. Confocal images with separate channels for untreated CFPAC-1 cells, CFPAC-1 cells with 1 nM ***MAB.IrpqSS.AuNP19*** *at 5 hr and 16 hr, 1 nM* ***MAB.IrpqSH.AuNP19*** *at 16 hr on a Leica sp8 upright microscope using a 40x ceramic water dipping objective lens. Hoechst (blue) settings:* λ_{exc} *= 402,* λ_{em} *= 419 – 472 nm; Iridium(green):* λ_{exc} *= 458 nm,* λ_{em} *= 550 – 750 nm; Reflectance (grey):* λ_{exc} *= 633 nm,* λ_{em} *= 628 – 638 nm.*



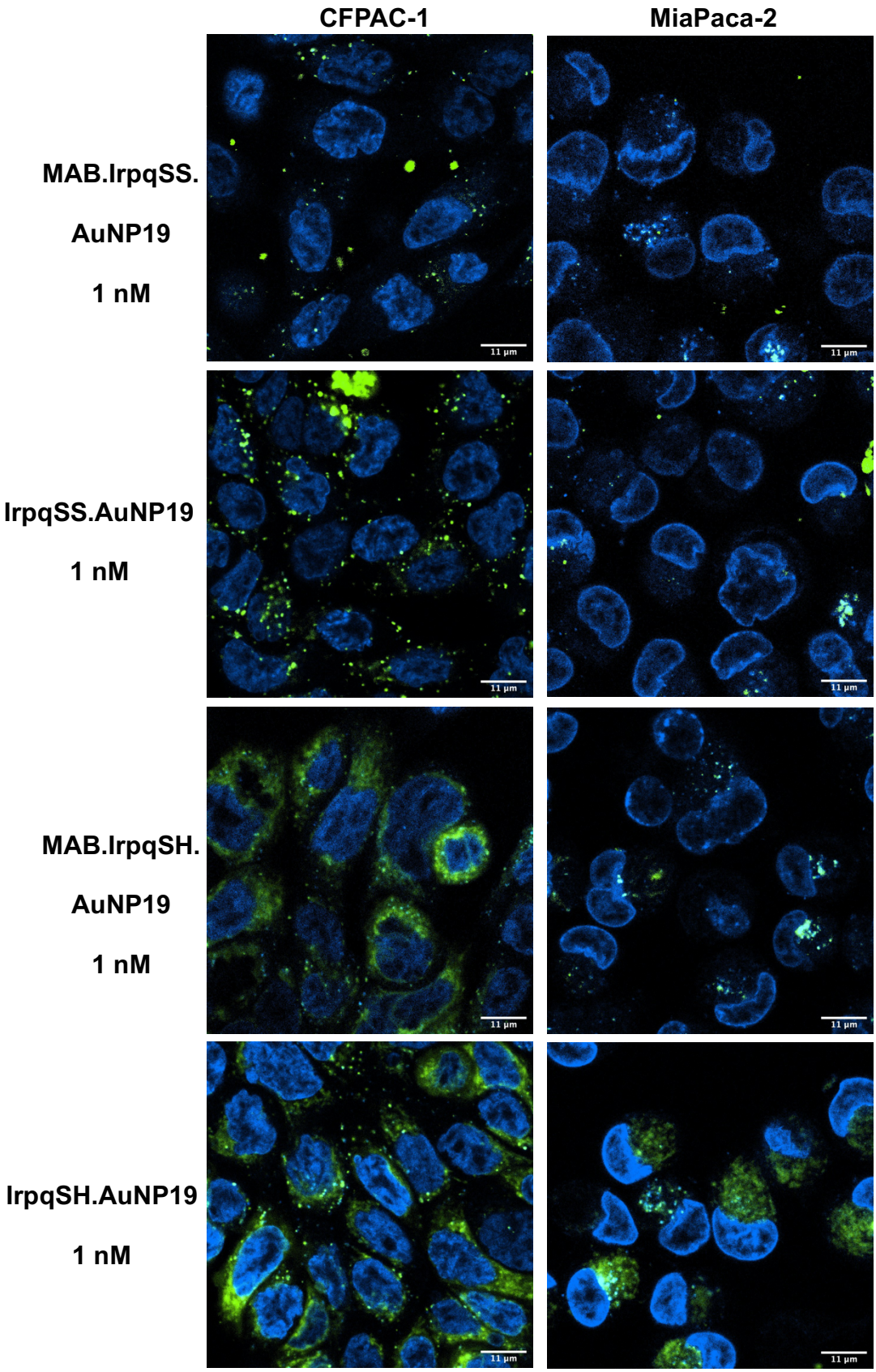
Supplementary Figure 4.7. Confocal images with separate channels for untreated MiaPaca-2 cells, MiaPaca-2 cells with 1 nM ***MAB.IrpqSS.AuNP19*** *at 5 hr and 16 hr, 1 nM* ***MAB.IrpqSH.AuNP19*** *at 16 hr on a Leica sp8 upright microscope using a 40x ceramic water dipping objective lens. Hoechst (blue) settings:* λ_{exc} *= 402,* λ_{em} *= 419 – 472 nm; Iridium(green):* λ_{exc} *= 458 nm,* λ_{em} *= 550 – 750 nm; Reflectance (grey):* λ_{exc} *= 633 nm,* λ_{em} *= 628 – 638 nm.*



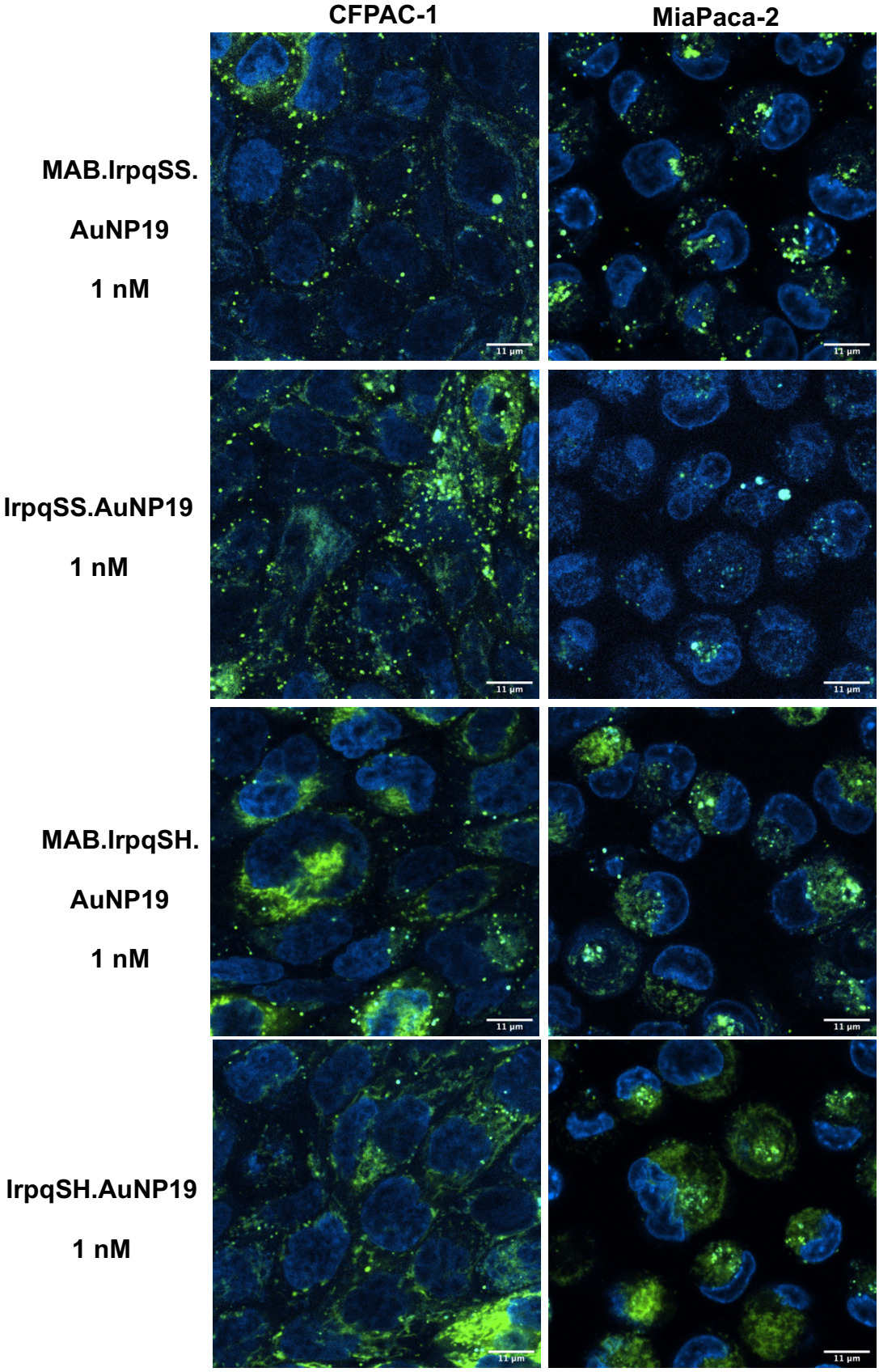
Supplementary Figure 4.8. Confocal images of untreated CFPAC-1 cells incubated for 5 hr and 16 hr. Images obtained on a Zeiss LSM900 inverted microscope using a 63x oil immersion objective lens. Hoechst (blue) settings: λ_{exc} = 402, λ_{em} = 450 - 495 nm; Iridium(green): λ_{exc} = 488 nm, λ_{em} = 500 – 700 nm.



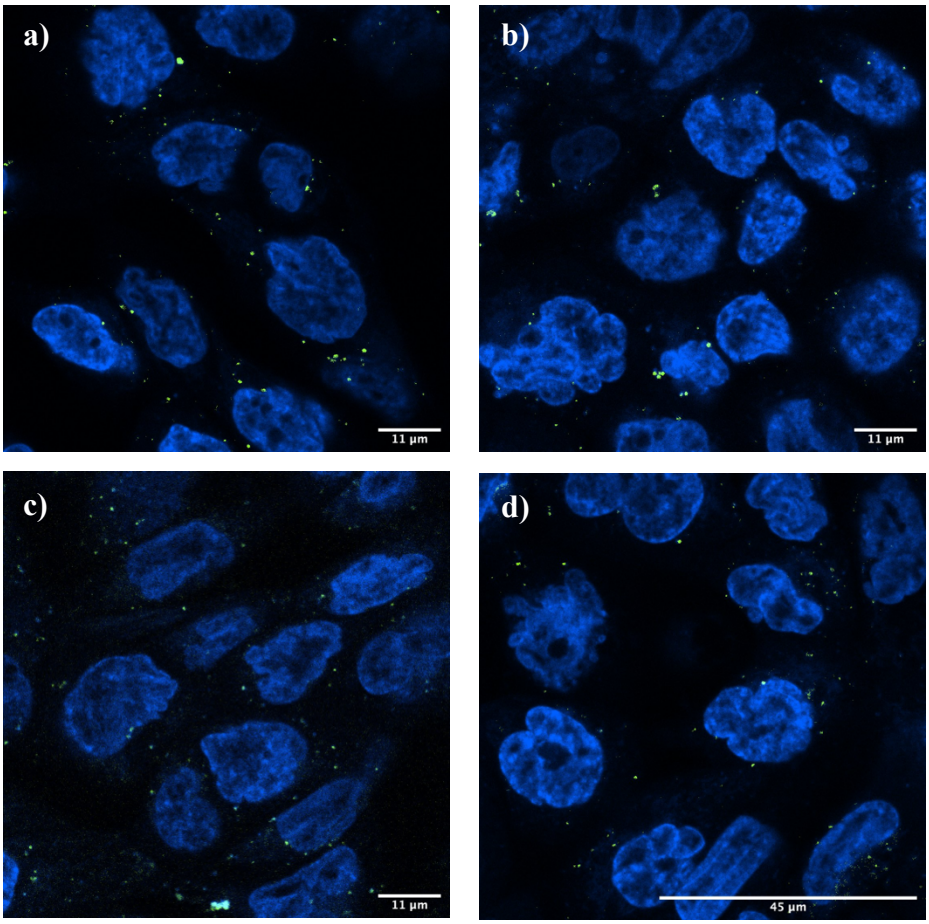
Supplementary Figure 4.9. Confocal images of untreated MiaPaca-2 cells incubated for 5 hr and 16 hr. Images obtained on a Zeiss LSM900 inverted microscope using a 63x oil immersion objective lens. Hoechst (blue) settings: λ_{exc} = 402, λ_{em} = 450 - 495 nm; Iridium(green): λ_{exc} = 488 nm, λ_{em} = 500 – 700 nm.



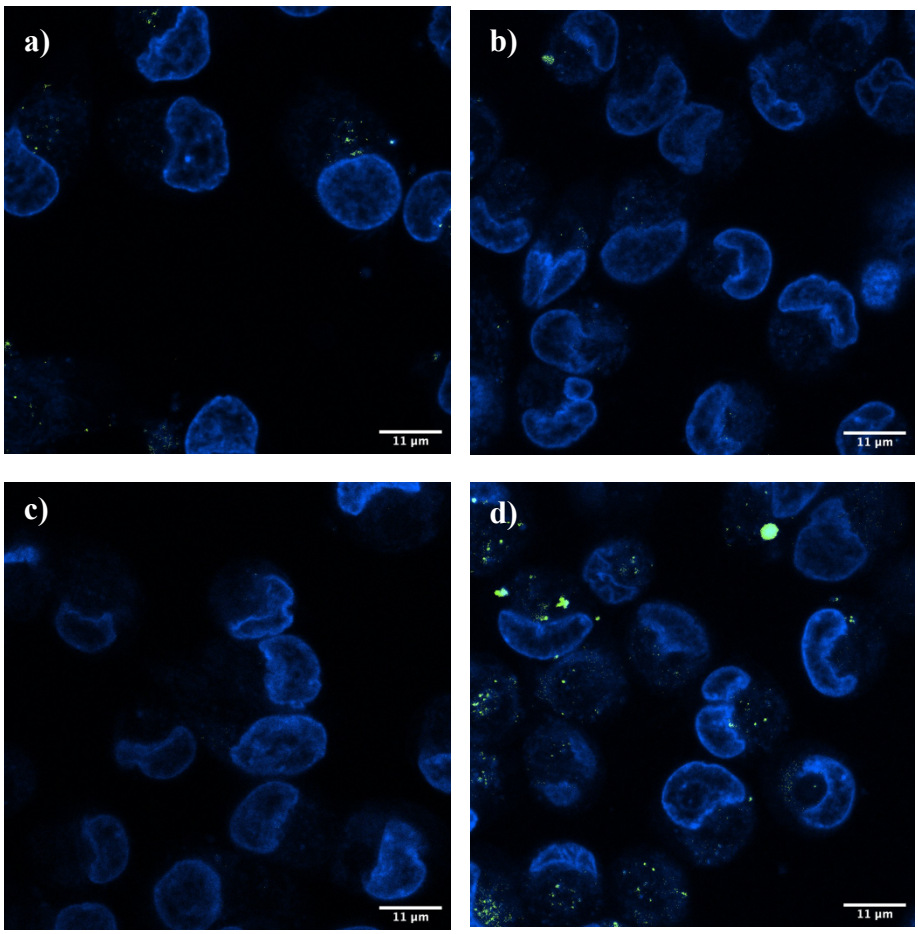
Supplementary Figure 4.10. Confocal images of CFPAC-1 cells (left) and MiaPaca-2 cells (right) incubated for 5 hr with 1 nM of ***MAB.IrpqSS.AuNP19***, ***MAB.IrpqSH.AuNP19***, ***IrpqSS.AuNP19*** *and* ***IrpqSH.AuNP19****. Images obtained on a Zeiss LSM900 inverted microscope using a 63x oil immersion objective lens. Hoechst (blue) settings:* λ_{exc} *= 402,* λ_{em} *= 450 - 495 nm; Iridium(green):* λ_{exc} *= 488 nm,* λ_{em} *= 500 – 700 nm.*



Supplementary Figure 4.11. Confocal images of CFPAC-1 cells (left) and MiaPaca-2 cells (right) incubated for 16 hr with 1 nM of ***MAB.IrpqSS.AuNP19****,* ***MAB.IrpqSH.AuNP19****,* ***IrpqSS.AuNP19*** *and* ***IrpqSH.AuNP19****. Images obtained on a Zeiss LSM900 inverted microscope using a 63x oil immersion objective lens. Hoechst (blue) settings:* λ_{exc} *= 402,* λ_{em} *= 450 - 495 nm; Iridium(green):* λ_{exc} *= 488 nm,* λ_{em} *= 500 – 700 nm.*

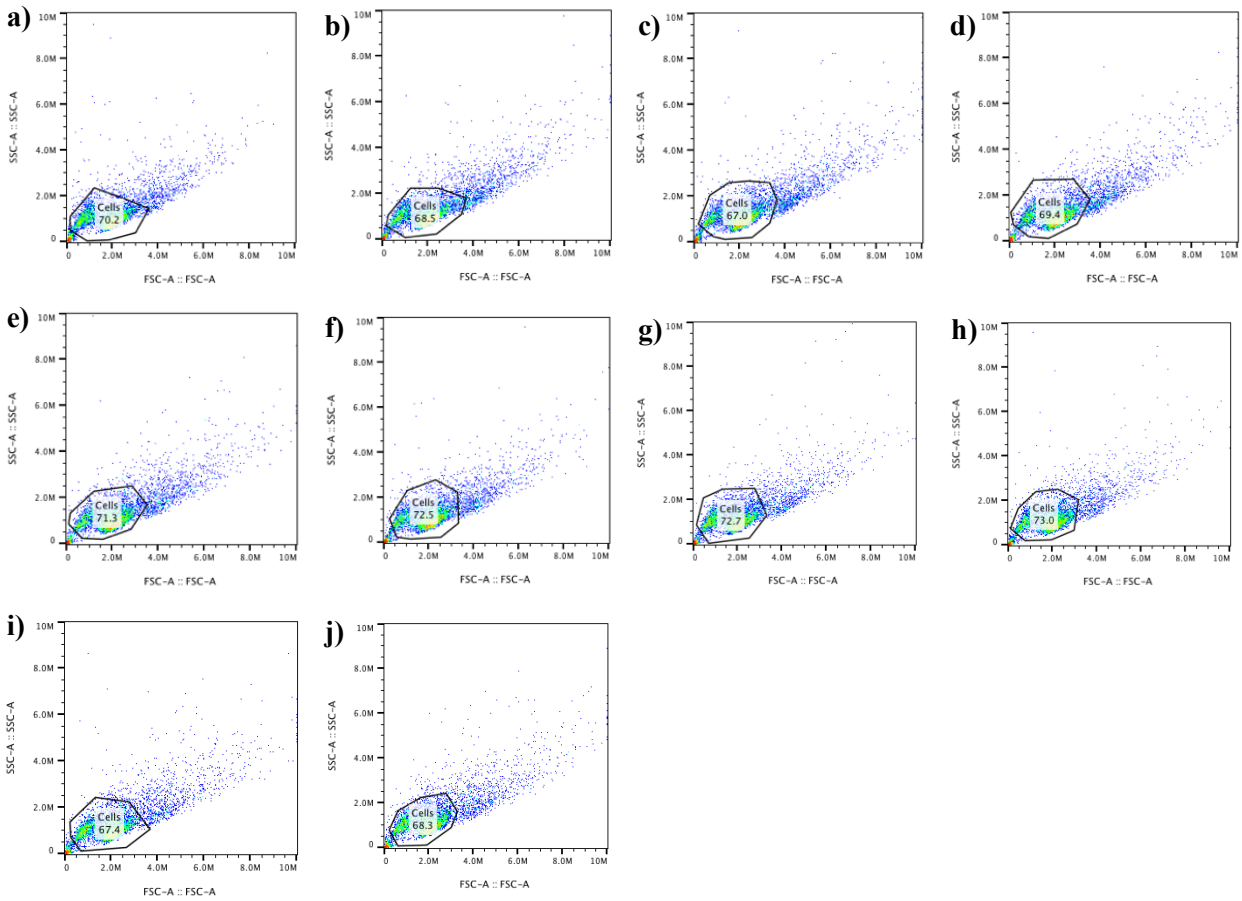


Supplementary Figure 4.12. Confocal images of CFPAC-1 cells incubated for 16 hr with 0.25 nM of ***a) MAB.IrpqSS.AuNP19****,* ***b) MAB.IrpqSH.AuNP19****,* ***c) IrpqSS.AuNP19*** *and* ***d) IrpqSH.AuNP19****. Images obtained on a Zeiss LSM900 inverted microscope using a 63x oil immersion objective lens. Hoechst (blue) settings:* λ_{exc} *= 402,* λ_{em} *= 450 - 495 nm; Iridium(green):* λ_{exc} *= 488 nm,* λ_{em} *= 500 – 700 nm.*

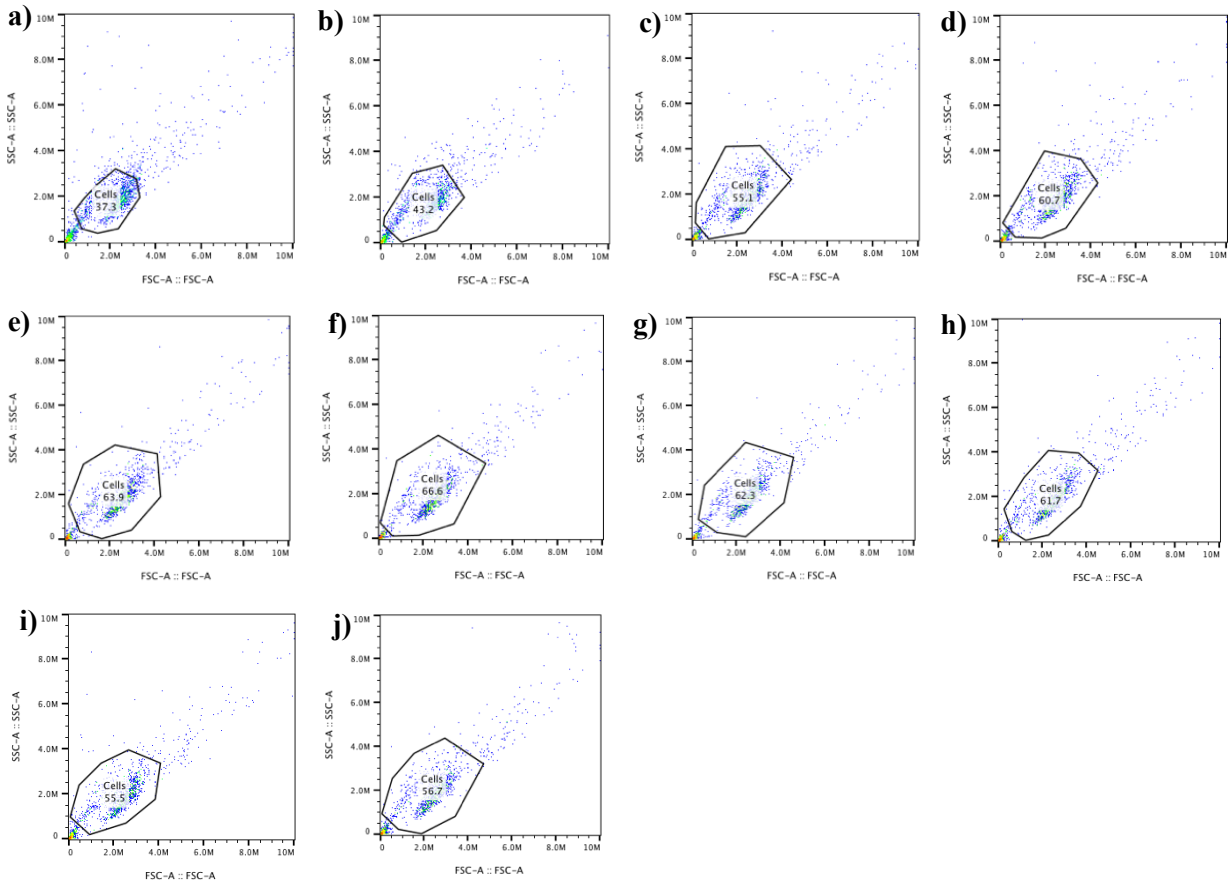


Supplementary Figure 4.13. Confocal images of MiaPaca-2 cells incubated for 16 hr with 0.25 nM of ***a) MAB.IrpqSS.AuNP19****,* ***b) MAB.IrpqSH.AuNP19****,* ***c) IrpqSS.AuNP19*** *and* ***d) IrpqSH.AuNP19****. Images obtained on a Zeiss LSM900 inverted microscope using a 63x oil immersion objective lens. Hoechst (blue) settings:* λ_{exc} *= 402,* λ_{em} *= 450 - 495 nm; Iridium(green):* λ_{exc} *= 488 nm,* λ_{em} *= 500 – 700 nm.*

Flow Cytometry scatter plots

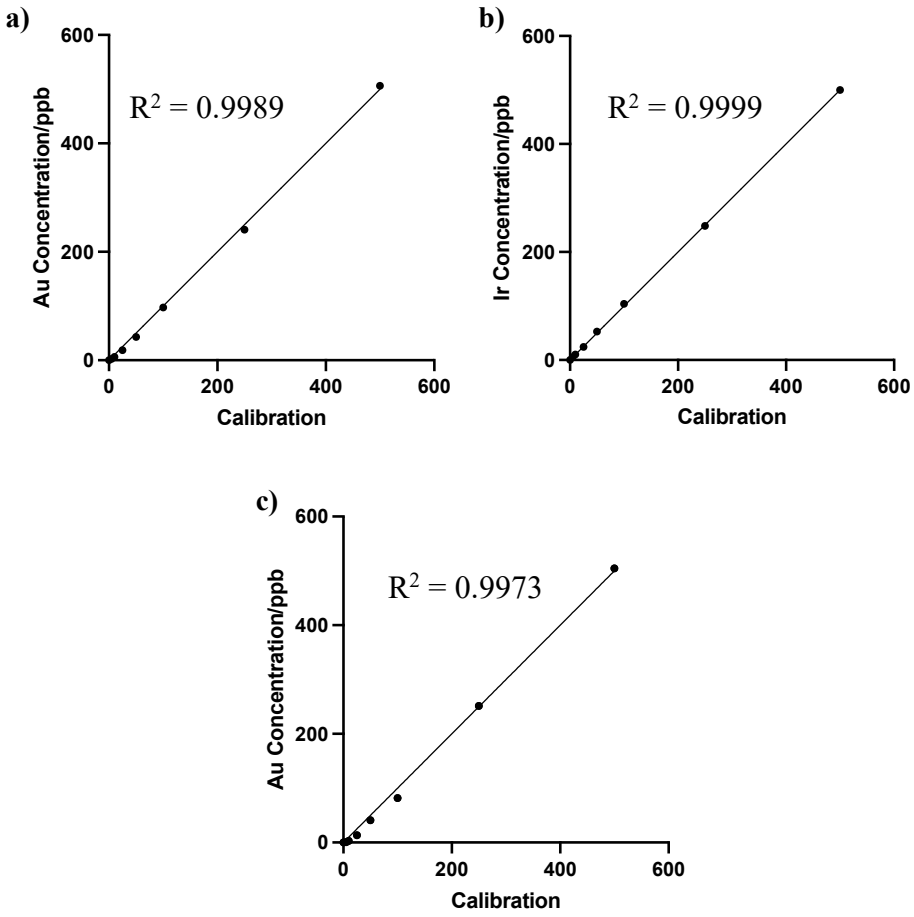


*Supplementary Figure 4.14. Flow cytometry scatter plots of side scatter (SSC) vs. forward scatter (FSC) in CFPAC-1 cells for untreated cells (**a** & **b**), **MAB.IrpqSS.AuNP19** (**c** & **d**), **MAB.IrpqSH.AuNP19** (**e** & **f**), **IrpqSS.AuNP19** (**g** & **h**) and **IrpqSH.AuNP19** (**i** & **j**).*



*Supplementary Figure 4.15. Flow cytometry scatter plots of side scatter (SSC) vs. FSC (FSC) in MiaPaca-2 cells for untreated cells (**a** & **b**), **MAB.IrpqSS.AuNP19** (**c** & **d**), **MAB.IrpqSH.AuNP19** (**e** & **f**), **IrpqSS.AuNP19** (**g** & **h**) and **IrpqSH.AuNP19** (**i** & **j**).*

ICP-MS calibrations and calculations



*Supplementary Figure 4.16. Calibration curves for Au (**a**) and Ir (**b**) used in the ICP-MS analysis for iridium(III) complex coating of **AuNP19**s and calibration curve for Au (**c**) used in the ICP-MS analysis for the uptake of **AuNP19**s in cells.*

ICP-MS calculations for the iridium coating on the AuNP19 samples:

1) Calculate the ratio of iridium atoms to gold atoms. Ratio = Ir conc (ppb):Au conc (ppb)

2) Calculate the number of metal complexes by multiplying the ratio of Ir:Au by the number of atoms in 1 AuNP

$$number\ of\ Ir\ complexes = number\ of\ atoms\ in\ 1\ AuNP\ x\ Ir{:}\ Au\ ratio$$

ICP-MS calculations for the AuNP uptake in the cell lines:

1) Convert the mean Au concentration (ppb) to gL^{-1}

$$1\ ppb = 1\ x\ 10^{-6}\ x\ gL^{-1}$$

2) Convert to gL^{-1}

$$1\ gL^{-1} = 1\ x\ 10^{-3}\ x\ mgL^{-1}$$

3) Total mass of Au in each sample was calculated by multiplying the concentration (mgL^{-1}) by the total volume, e.g. the sample volume was 5 mL, so the concentration (mgL^{-1}) was multiplied by 5.

4) The number of Au atoms was calculated by finding the ratio of the concentration (gmL^{-1}) to the atomic mass of Au (g/mol) and multiplying this ration by the Avogadro's constant (N_A).

$$number\ of\ Au\ atoms = \left(\frac{concentration(gmL^{-1})}{atomic\ mass\ of\ Au\ (gmol^{-1})}\right)\ x\ N_A$$

5) The number of AuNPs was calculated by dividing the number of Au atoms in the sample by the number of Au atoms in 1 AuNP. For the AuNPs of size 18.5 ± 1.2 nm, the number of Au atoms in 1 AuNP was $2.0 \times 10^5 \pm 4.1 \times 10^4$.

$$number\ of\ AuNPs = \frac{number\ of\ gold\ atoms\ in\ sample}{2.0\ x\ 10^5}$$

6) The number of AuNPs per cell was calculated by dividing the number of AuNPs in the sample by the number of cells in the sample.

$$number\ of\ AuNPs\ per\ cell = \frac{number\ of\ AuNPs}{number\ of\ cells}$$

5. General Conclusions

IrpqSS- and **IrpqSH**-functionalised **AuNP13**s were monodisperse and luminescent in H_2O suspensions. Good dispersion was seen in TEM and PDI values were low. A novel surfactant **TFD-S** also promoted binding of the iridium(III) complexes to the gold surfaces. The 440 nm excitation peak for all samples in free probe and on the AuNP surface represented an MLCT band in the visible region, providing promising grounds for future studies in two-photon excitation using NIR light. **IrpqSS** and **IrpqSH** and **Irpqbpy** displayed a trend in their values of luminescence lifetimes and quantum yields while varying solvent polarity. In more polar solvents, the quantum yield decreased while the luminescence lifetime increased. When on the surface of the AuNPs, around 600 metal complexes were found to be on the surface. This value varied depending on the type of surfactant in the sample. Investigating the role of surfactants in cell imaging of pancreatic cancer cell lines showed that in CFPAC-1 cells, no surfactant promoted a brighter luminescence than the others, although **TFD-S** was seen to promote the best AuNP uptake of all samples. In MiaPaca-2 cells, **SPEG** surfactant was the worst for imaging properties and **LPEG** and **Zonyl** the best. **LPEG** also showed the best **AuNP** uptake in cells. **IrpqSS.TFD-S.AuNP13** uptake in both cell lines was very good, even at an incubation concentration of 0.4 nM compared to the other AuNP samples at 0.6 nM. As **TFD-S** was a synthesised surfactant, this provides potential for investigation into other perfluorinated surfactants that could be engineered to improve uptake of AuNPs into cells by modifying the synthetic methods used to produce them. PEG-coated AuNPs were observed to go to the nucleus, while perfluorinated surfactant-coated AuNPs remain within the cytoplasm in sub-cellular organelles due to differences in lipophilicity. **IrpqSS**- and **IrpqSH**-functionalised **AuNP19**s were also monodisperse and luminescent in H_2O suspensions, indicating suitability as imaging agents. Targeting of a mesothelin surface marker with a monoclonal antibody showed that the antibody-coated particles provide potential for diagnostics agents, as the antibody-coated particles bound to the membrane of cells and had slow internalisation at 16 hr, whereas this was not seen in the samples without antibody. Cell analysis techniques requiring detachment of the cells from a surface were found to show decreased uptake/luminescence intensity of antibody-coated AuNP-treated cells due to possible removal of particle samples from the membrane

during the sample preparation process. Hence, static analytical techniques such as confocal microscopy may be better to quantify differences in luminescence intensity compared to flow cytometry for example, which requires a cell suspension. CFPAC-1 cells seem take up AuNPs by micropinocytosis or other endocytosis methods, leading to localisation in endosomal compartments, however MiaPaca-2 cells seem to take up AuNPs by passive uptake and translocation, leading to location in lysosomes. The **AuNP19** and **Irpqbpy** complex concentrations used in the cell studies, which were also used in the ROS assays did not show any statistically significant difference between all samples, indicating that the concentration may be too low to generate ROS in cells. Altogether, the findings show that novel iridium(III) complexes and novel antibody-AuNP conjugates can be combined in one delivery vehicle for imaging and targeting in pancreatic cancer cells.